Alternative Design of Pt-based Catalysts: an X-ray Spectroscopic View

Alternatief Ontwerp van Pt-gebaseerde Katalysatoren: een X-stralenspectroscopische Kijk

Matthias Filez

Promotoren: Prof. dr. ir. G. B. Marin, Prof. dr. C. Detavernier
Proefschrift ingediend tot het behalen van de graad van
Doctor in de Ingenieurswetenschappen: Chemische Technologie

Vakgroep Chemische Proceskunde en Technische Chemie
Voorzitter: Prof. dr. ir. G. B. Marin
Faculteit Ingenieurswetenschappen en Architectuur
Academiejaar 2014 – 2015

UNIVERSITEIT GENT

Examination committee

Promoters:

Prof. dr. ir. Guy B. Marin	Ghent University, Belgium (EA12)	
Prof. dr. Christophe Detavernier*	Ghent University, Belgium (WE04)	

Other members of the examination committee:

Prof. dr. Sylvain Cristol*	Lille University, France	
Dr. Vladimir V. Galvita	Ghent University, Belgium (EA12)	
Dr. Hilde Poelman*	Ghent University, Belgium (EA12)	Secretary
Prof. dr. Marie-Françoise Reyniers	Ghent University, Belgium (EA12)	
Prof. dr. ir. Mark Saeys	Ghent University, Belgium (EA12)	
Prof. dr. ir. Rik Van de Walle	Ghent University, Belgium (EA06)	Chairman
Prof. dr. Laszlo Vincze*	Ghent University, Belgium (WE08)	

* Members of the reading committee

This work was supported by the Fund for Scientific Research Flanders (FWO) in supplying financing of FWO-project G.0209.11, travel costs and beam times at the DUBBLE beam line of the ESRF.

Laboratory for Chemical Technology

Department of Chemical Engineering and Technical Chemistry

Ghent University

Technologiepark 914, B-9052 Ghent, Belgium

UNIVERSITEIT GENT

Dedicated to my father…

Acknowledgments

Four years ago, I initiated my PhD at the Laboratory for Chemical Technology. Being a fresh chemical engineer with physics background, I would ‘go to synchrotrons – like CERN! – to shoot X-rays on catalysts’, as Hilde explained me when we met for the first time. This convincing sentence was the starting point of a challenging and extremely instructive research experience. The gained insights and yielded scientific results are not the consequence of a lonely effort, but rather the product of close teamwork. For of this reason, I would like to take the opportunity to thank a number of people.

First of all, my sincerest gratitude goes to my promoter Prof. Marin, for giving me the opportunity to start my PhD at the LCT. Your broad knowledge, eye for detail and intellectual refinement will always be an example to me in my future career. In addition, I would like to thank my promoter Prof. Detavernier for sharing all the useful insights and motivating comments.

Hilde, you introduced me into the world of research and guided me over all the mountains that had to be overcome. Besides my colleague you are also my mentor and counselor. Your door was always open to me for discussion and advise. Your positivism, diplomacy, honesty and motivating power stimulated me a lot to yield the best possible results, both personally and scientifically. Thanks a lot for everything.

Vladimir, you are the most gentle person I ever met. You are the scientific brain of many projects which are currently investigated in our lab. You cherish a true passion for science, which you can spread like a virus to your colleagues. I will never forget the moment that we observed H spill over on our catalyst, at 4.30 am at the synchrotron… Or that time you synthesized new catalysts during the night shifts.

Evgeniy, *quintessential* words are inadequate for describing our intensive collaboration. We discussed a lot, *triggering* the *fabrication* of *multifarious* ideas: we have

learned so much! I still remember those unique moments when we talked about ‘attacking the scientific community from all sides’ with our results. When you didn’t like what I wrote, you polished the text until it was perfect. Your open communication and intelligence increased the quality of our research. I really appreciated the efforts of Chris for proofreading some of our manuscripts.

Together we formed a strong and complementary team. Only a few people understand what WIWI samples are, a result of our close teamwork during day and night at the synchrotron and in the LCT. Furthermore, I would like to thank all other colleagues who contributed to synchrotron beam times: Kristof, Aditya, Kostas, Ricardo, Eduardo, Ranjith, Jolien, Christophe, Kilian. My gratitude goes to all colleagues with which we had good discussions: all members of the weekly seminar group organized by Vladimir and Hilde; Stephanie Saerens, Maarten Sabbe and Prof. Reyniers. Chetan, Aditya, Rakesh, we had so many funny moments in our office and we always worked in a good and informal atmosphere. Thanks a lot!

Colleagues from the CoCooN research group, thank you for our nice collaboration. Ranjith, you were always ready to do more experiments. When we asked you whether it was possible to coat ‘some grams’ of catalyst – which I now know is a lot of work – you made it a priority in your busy working schedule. Jolien, your scientific skills and attitude are an example to me. Our synchrotron campaigns would not have been the same without you. Furthermore, I would like to thank Vitaliy Bliznuk for TEM, Nico De Roo for XPS, and Olivier Janssens for XRD measurements. Thanks to the colleagues from EMAT (UAntwerp) for providing high-quality TEM measurements: Maria Meledina, Stuart Turner, Prof. Van Tendeloo. Thanks to Prof. Bell from UC Berkeley for his thoughts about our manuscript.

My gratitude goes to several beamline scientists: Emiliano Fonda and Valérie Briois from SAMBA/ROCK (SOLEIL, Paris), Sergey Nikitenko, Dipanjan Banerjee, Alessandro Longo and Wim Bras from DUBBLE (ESRF, Grenoble) and Olga Safonova and Maarten Nachtegaal from SuperXAS (SLS, PSI, Villigen). Special thanks goes to the technical staff of

the LCT, which always provided the best possible service. Marcel, Georges, thanks a lot for the nice talks we had about everyday life. Petra, Sarah, Kevin, Kim, thank you a lot for your administrative work.

Besides my colleagues, I would like to acknowledge my friends from Ghent (Arne, Anne, Joke, Kim, Steven, Pieter, and so many other musicians from GUHO) and Leuven (Chini, Heps, Wim, Herbert, Brecht, Benoit, Davy, Sara, Lou, Denis, Martien, Samme, Bieke, Nele, Babs, Sofie, and all others which are not in this short list). Thanks for the multitude of happy moments we shared together.

Naast de vele vrienden en collega's die mij hebben gesteund, wil ik graag mijn hele familie oprecht bedanken voor de waarden die ze mij hebben meegegeven in de loop van mijn opvoeding en voor de zorg die ze aan mij hebben besteed. Speciale dank aan mijn meter Mamie voor de vele kaarsjes die je hebt ontstoken om mij te doen slagen op de vele examens die ik heb afgelegd. Oma, je bent net uit ons leven ontglipt maar je zal voor altijd in mijn gedachten blijven als een zeer sterke vrouw die me enorm veel waarden heeft bijgebracht tijdens mijn opvoeding. Je bent nu tot rust gekomen en verenigd met Opa. Papie, bedankt voor alle mooie herinneringen dewelke we zullen blijven koesteren.

Bedankt aan het zogenaamde 'mijlpaalteam' voor het warm onthaal dat ik mocht ervaren tijdens de afgelopen jaren. Ik heb het geluk deel te mogen uitmaken van jullie hecht en warm nest, en dat is voor mij een uitzonderlijk genoegen. Dank aan Ivo en Lut voor hun oprechte bezorgdheid gedurende de afgelopen jaren over het verloop van mijn doctoraat en het 'meten'.

Mama, je bent sinds mijn eerste levensdag de steunpilaar in mijn leven. Je kent me door en door en voelt onmiddellijk aan hoe het met mij gaat en hoe hierop in te spelen. Zonder jouw steun was ik er – echt! – niet geraakt. Bedankt voor de onvoorwaardelijke ruggengraat die je voor me was de afgelopen jaren. Been, we hebben samen veel gespeeld – als pubers veel ruzie gemaakt! – en een mooie kindertijd beleefd. Als student waren we

elkaars trouwste studiemakkers en konden we bij elkaar steeds steun vinden. Je bent iemand waarop ik kan rekenen, dag en nacht.

Papa, jouw verlies blijft moeilijk, maar verdriet is omgezet in het terugblikken naar de prachtige momenten die we samen hebben beleefd. Samen reizen, samen muziek spelen, samen eten, samen vanalles. Je punctualiteit, discipline en werkijver gecombineerd met je interne zachtheid zal voor mij een voorbeeld zijn voor de rest van mijn leven. Jouw grootste wens was ons geluk en welvaren, waarbij studie een belangrijke pijler was. Om deze reden draag ik dit werk aan jou op, omdat je fier zou zijn op mijn prestatie.

Annemie, jij bent de laatste in het lijstje, maar in mijn leven de meest belangrijke. Toen ik je als student leerde kennen, heb je me geleerd om mijn dromen na te streven en deze te realiseren. Zo ook dit doctoraat. Het geleverde werk is mede tot stand gekomen door jouw onvoorwaardelijke steun en advies. Je bent meesterlijk goed in mij uit m’n onderzoeks-stulp te halen, en mij hierdoor de broodnodige ontspanning te bieden. Bedankt om voor mij te zorgen in ieder opzicht, gaande van bemoedigingen tot de meer alledaagse zaken. Je maakt me gelukkig!

Matthias

Ghent, May 2015

Contents

Samenvatting

De recente exploitatie van schaliegasreserves heeft een revolutie teweeggebracht in de chemische industrie, met als gevolg het ontstaan van een sterke vraag naar zeer zuiver propyleen. Selectieve katalytische dehydrogenatie van propaan kan een oplossing bieden om aan deze marktvraag te voldoen. Bijvoorbeeld, gedragen bimetallische Pt-In en Pt-Ga nanokatalysatoren spreiden een superieure katalytische activiteit tentoon tijdens propaan dehydrogenatie tot zeer zuiver propyleen. Echter, om deze katalysatoren economisch rendabel te maken voor industrieel gebruik dienen goedkopere/eenvoudigere synthesemethoden te worden ontwikkeld die toelaten om de Pt-fase met hoge precisie vorm te geven. In het kader van dit proefschrift zijn twee nieuwe strategieën verkend en onderzocht: katalysatorvorming of basis van (1) dubbele-laag hydroxidematerialen (DLH) en met behulp van (2) atomaire-laagdepositie (ALD).

De belangrijkste techniek die wordt gebruikt voor dit onderzoek is X-stralen absorptiespectroscopie (XAS). Complementair aan conventionele XAS-methoden wordt multi-resolutie wavelet-gebaseerde XAS-analyse toegepast tijdens *in situ* vormingsprocessen van Pt-M katalysatoren (M = In, Ga) aan de Pt L_{III} absorptierand. Wavelet transformatie (WT) van het XAS-signaal laat toe om gelijktijdig het type nabuur van Pt te discrimineren alsook de ruimtelijke positie van deze nabuur rond Pt te bepalen. In dit werk wordt aangetoond dat WT XAS een handig instrument is om een snellere en meer grondige XAS-analyse in de hand te werken, vooral wanneer meerdere atomaire types het X-stralen absorberend element omringen – zoals tijdens vormingsprocessen van katalysatoren. De voor- en nadelen van WT XAS worden gedemonstreerd tijdens het *in situ* vormingsproces van Pt-In katalysatoren.

In dit proefschrift wordt initieel de vorming van DLH-afgeleide Pt-M/Mg(M)(Al)O_x katalysatoren bestudeerd (M = In, Ga). De vorming van dergelijke katalysatoren is bewerkstelligd door – eerst – het legeringselement M in de Mg,Al-DHL lagen te incorporeren

tijdens co-precipitatie, hetgeen gestructureerde materialen oplevert die zijn opgebouwd uit gestapelde 2D Mg(M)(Al)$(OH)_2$ lagen. Tijdens calcinatie transformeren deze 2D DHLs naar 3D MgO-type Mg(M)(Al)O_x gemengde metaal oxides (GMOs). Vervolgens worden Pt$(acac)_2$ precursoren geïmpregneerd op deze Mg(M)(Al)O_x dragers, hetgeen resulteert in de vorming van gelegeerde Pt-M/Mg(M)(Al)O_x katalysatoren na calcinatie en H_2 reductie tot 650 °C. Het direct inbouwen van de promotor M in de Mg,Al-DLH structuur vereenvoudigt het katalysator vormingsproces, aangezien het aantal synthesestappen wordt gereduceerd in vergelijking met conventionele dubbele impregnatie van Pt en M op Mg(Al)O_x. Hoewel deze methode efficiënt is, zijn de optredende mechanismen van Pt nanodeeltjes- en Pt-M legeringvorming tijdens het vormingsproces van deze katalysatoren niet voldoende begrepen. Om deze reden is uitgebreid onderzoek gevoerd om de mechanismen die op atomaire schaal optreden, en het Pt-Ga/Mg(Ga)(Al)O_x vormingsproces aansturen, te ontrafelen.

Het vormingsproces is gevolgd aan de hand van *in situ* XAS data, die zijn opgemeten tijdens calcinatie en H_2 reductie van Pt$(acac)_2$/Mg(Ga)(Al)O_x. Calcinatie tot 350 °C leidt tot decompositie van de precursorliganden, hetgeen atomair gedispergeerde Pt^{4+} species op het Mg(Ga)(Al)O_x drageroppervlak oplevert. Calcinatie op 650 °C veroorzaakt het thermisch breken van sterke Pt-O dragerbindingen, resulterend in migratie van Pt over het drageroppervlak en Pt deeltjesvorming. H_2 reductie induceert Pt sintering, gevolgd door Pt-Ga legeringvorming tussen 450 °C en 650 °C. Dit laatste proces van Pt-Ga legeringvorming bestaat uit de volgende stappen: (1) Pt promoot dissociatieve chemisorptie van H_2 op zijn nanodeeltje oppervlak, (2) Pt-gedissocieerde H loopt over naar de Mg(Ga)(Al)O_x drager, (3) H verplaatst zich over lange afstand over het drageroppervlak en (4) reduceert Ga^{3+} partieel in $Ga^{\delta+}O_x$ species, (5) matig mobiel $Ga^{\delta+}O_x$ ondergaat korte afstand transport naar Pt deeltjes, (6) Pt promoot de reductie van $Ga^{\delta+}O_x$ naar Ga^0 en stabiliseert Ga in Pt-Ga nanolegeringen. Naast deze resultaten worden ook de aard en het gedrag van H tijdens Pt-Ga legeringvorming bestudeerd.

De hierboven beschreven syntheseroute – gebruik makend van $Mg(M)(Al)O_x$ dragers – is verder verbeterd door beide legeringselementen, M én Pt, te incorporeren in de DLH structuur, hetgeen $Mg(Pt)(M)(Al)O_x$ GMOs oplevert na calcinatie van Mg,Al,Pt,M-DLHs. Wanneer deze Pt,M-geïncorporeerde GMOs worden gereduceerd in H_2 tot 650 °C, dan worden gedispergeerde Pt-M nanodeeltjes gevormd op de $Mg(Pt)(M)(Al)O_x$ drager. Deze katalysatoren vertonen een hogere activiteit voor propaan dehydrogenatie in vergelijking met hun Pt-M/$Mg(M)(Al)O_x$ analoog. Dergelijke Pt-M katalysatoren, gesynthetiseerd in één pot, zijn bijgevolg erg aantrekkelijk voor industrieel gebruik door hun eenvoudig vormingsproces en superieure katalytische activiteit.

Naast DLH-gebaseerde katalysatorsynthese is het potentieel van ALD voor de vorming van Pt-In bimetallische katalysatoren onderzocht als tweede synthesestrategie. Als eerste stap is het nucleatiegedrag van Pt op SiO_2 bestudeerd tijdens $MeCpPtMe_3/O_3$ ALD met behulp van een nieuwe *in situ* XRF-XAS-methodologie. Naast de Pt nanostructuur (XAS) en de afgezette hoeveel Pt (XRF) kan ook de evolutie van de concentratie van Pt nuclei op het SiO_2 oppervlak evenals hun grootte worden opgevolgd tijdens het Pt ALD proces. Dit resulteert in de directe observatie van fenomenen zoals nucleatie, sintering en deeltjesgroei door ALD afzetting. Als volgende stap naar bimetaalsynthese worden $MeCpPtMe_3/O_3$ en $In(TMHD)_3/O_2$ plasma ALD gecombineerd voor het produceren van twee verschillende nanocomposieten, namelijk Pt/In_2O_3 en $In(Pt)O_x$. Ter vorming van Pt/In_2O_3 (analoog van $Pt/Mg(In)(Al)O_x$) wordt depositie van Pt uitgevoerd op een eerder afgezette In_2O_3 laag. $In(Pt)O_x$ (analoog van $Mg(Pt)(In)(Al)O_x$) daarentegen is afgezet door afwisselende depositie van In_2O_3 en Pt, hetgeen resulteert in een Pt-gedopeerde In_2O_3 laag. Bij beide types ALD-gebaseerde nanocomposieten wordt de reductie van In_2O_3 gepromoot door Pt (~ 360 °C) en vindt Pt-In legeringvorming plaats beneden de In_2O_3 reductietemperatuur (~ 420 °C). Voor Pt/In_2O_3 verloopt Pt-In legeringvorming door graduele In-verrijking van de Pt-fase tijdens temperatuur-geprogrammeerde H_2 reductie. Initieel wordt In substitutioneel opgenomen in de vlak-gecentreerde kubische structuur van Pt, resulterend in een Pt-In vaste metaaloplossing.

Deze laatste evolueert naar een Pt_3In of meer In-rijke intermetallische legering, afhankelijk van de verhouding van initieel afgezet In/Pt. Daarentegen levert H_2 reductie van $In(Pt)O_x$ meteen de meest In-rijke In_7Pt_3 intermetallische legering op door de sterke aanwezigheid van In rond Pt in de initiële $In(Pt)O_x$ laag.

De grootste uitdaging voor toekomstig onderzoek naar DLH-gebaseerde katalysatoren bestaat in het verkrijgen van de structuur-activiteitsrelatie tussen de Pt-M nanodeeltjestructuur en -samenstelling enerzijds en de activiteit voor propaan dehydrogenatie anderzijds. Voor ALD-gebaseerde materialen dient de gedemonstreerde methodologie te worden gerealiseerd op de atomaire schaal, en zou de graad van controle over de legering samenstelling moeten worden afgetoetst. Het dient opgemerkt dat bimetaal ALD veel potentieel heeft om fundamentele vragen in de katalyse het beantwoorden, gezien de methodologie in staat is om modelkatalysatoren te produceren.

Summary

Recently, the widespread exploitation of shale gas reserves has revolutionized chemical industry, thereby creating a strong need for high-purity propylene. Selective catalytic propane dehydrogenation can provide the key solution for meeting this market demand. For example, bimetallic Pt-In and Pt-Ga supported nanocatalysts exhibit superior performance during propane dehydrogenation into high-purity propylene. However, to make these catalysts economically rentable for industrial use, more cheap/simple synthesis methods should be developed which allow for precisely shaping the Pt phase. In this dissertation, two novel strategies have been explored and investigated: catalyst formation based on (1) layered double hydroxide (LDH) materials, and (2) via the method of atomic layer deposition (ALD).

The main characterization technique employed for this research concerns X-ray absorption spectroscopy (XAS). Multi-resolution wavelet-based XAS analysis is applied during the *in situ* formation of the Pt-M catalysts (M = In, Ga) at the Pt L_{III} absorption edge to complement conventional XAS methods. Wavelet transformed (WT) XAS allows for the simultaneous elemental discrimination and spatial localization of the atomic neighbors around Pt. Especially when multiple atomic types surround the X-ray absorber – such as during catalyst formation processes – WT XAS is shown to be a handy tool for triggering more rapid and profound XAS analysis. The advantages and drawbacks of WT XAS are demonstrated during the *in situ* formation of Pt-In catalysts.

In this dissertation, initially, the formation of LDH-derived Pt-M/Mg(M)(Al)O_x catalysts is studied (M = In, Ga). The formation of such Pt-M/Mg(M)(Al)O_x (M = In, Ga) catalysts is effectuated by – first – incorporating the promoting element M inside the Mg,Al-LDH layers during co-precipitation, yielding structured materials consisting of stacked Mg(M)(Al)$(OH)_2$ 2D sheets. Upon calcination, these 2D LDHs transform to 3D MgO-type Mg(M)(Al)O_x mixed metal oxides (MMOs). Subsequently, Pt$(acac)_2$ precursors are

impregnated on these Mg(M)(Al)O_x supports, resulting in the formation of alloyed Pt-M/Mg(M)(Al)O_x catalysts after calcination and H_2 reduction to 650 °C. The direct incorporation of M inside the Mg,Al-LDH structure simplifies the catalyst formation process, as the number of synthesis steps is reduced compared to conventional double impregnation of Pt and M on Mg(Al)O_x. In spite of the method's efficiency, the mechanisms of Pt nanoparticle formation and Pt-M alloying which occur during catalyst formation are not sufficiently understood. Therefore, an extensive investigation is performed to unravel the atomic scale events which steer the formation of Pt-Ga/Mg(Ga)(Al)O_x catalysts.

The formation process is followed in detail by means of *in situ* XAS data, recorded during calcination and temperature programmed H_2 reduction of Pt(acac)$_2$/Mg(Ga)(Al)O_x. Calcination to 350 °C results in the decomposition of the precursor ligands, yielding atomically dispersed Pt^{4+} species on the Mg(Ga)(Al)O_x support surface. Calcination at 650 °C thermally activates the scission of strong Pt-O support bonds, resulting in Pt surface migration and cluster formation. Gas switching to H_2 induces Pt sintering which is followed by Pt-Ga alloying between 450 °C and 650 °C. The latter Pt-Ga alloying process consists of the following steps: (1) Pt promotes the dissociative chemisorption of H_2 on its cluster surface, (2) Pt-dissociated H spills over to the Mg(Ga)(Al)O_x support, (3) H undergoes long range transport over the support surface and (4) partially reduces Ga^{3+} sites into $Ga^{\delta+}O_x$ species, (5) moderately mobile $Ga^{\delta+}O_x$ undergoes short range transport to Pt clusters, (6) Pt promotes the reduction of $Ga^{\delta+}O_x$ into Ga^0 on condition of stabilization of Ga inside Pt-Ga nanoalloys. Besides these results, the nature and behavior of H during Pt-Ga alloying are investigated.

The above described synthesis routine – using Mg(M)(Al)O_x supports – is further improved by introducing both alloying elements, M ànd Pt, into the LDH support, yielding Mg(Pt)(M)(Al)O_x MMOs after Mg,Al,Pt,M-LDH calcination. When these Pt,M-incorporated MMOs are H_2 reduced to 650 °C, well-dispersed Pt-M nanoparticles on Mg(Pt)(M)(Al)O_x are obtained. These catalysts display higher propane dehydrogenation activity relative to their Pt-

M/Mg(M)(Al)O_x analogs. In combination, the one-pot synthesized Pt-M catalysts are highly attractive for industrial use, owing to their facile formation and superior performance.

Besides LDH-based catalyst synthesis, the potential of ALD for the tailored formation of Pt-In bimetallic catalysts is explored as second synthesis strategy. As a first step, the nucleation behavior of Pt on SiO_2 is studied during $MeCpPtMe_3/O_3$ ALD by a novel *in situ* XRF-XAS methodology. Besides the Pt cluster structure (XAS) and the Pt amount deposited (XRF), the concentration of Pt nuclei on the SiO_2 surface as well as their cluster size evolution can be monitored during Pt ALD (XRF-XAS). This results in the direct observation of nucleation, sintering and cluster growth events during ALD deposition. As a next step toward bimetallic synthesis, $MeCpPtMe_3/O_3$ and $In(TMHD)_3/O_2$ plasma ALD are combined for tailoring two different nanocomposites, namely Pt/In_2O_3 and In(Pt)O_x. For Pt/In_2O_3 (analog of Pt/Mg(In)(Al)O_x), Pt is deposited on top of a separately deposited In_2O_3 layer. In contrast, In(Pt)O_x (analog of Mg(Pt)(In)(Al)O_x) is deposited by alternating depositions of In_2O_3 and Pt, yielding a Pt-doped In_2O_3 layer. For both ALD nanocomposites, Pt promotes the reduction of In_2O_3 (~ 360 °C), inducing Pt-In alloying below In_2O_3 reduction temperatures (~ 420 °C). For Pt/In_2O_3, Pt-In alloying during H_2 temperature programmed reduction is established by the gradual In-enrichment of the Pt phase. Initially, In is inserted in fcc Pt, yielding a Pt-In solid solution, which evolves to Pt_3In or more In-rich intermetallic compounds depending on the initially deposited In/Pt ratio. In contrast, H_2 reduction of In(Pt)O_x directly yields the most In-rich In_7Pt_3 alloy due to the high In abundance around Pt.

The major challenge for future research in LDH-derived catalysts consist of establishing the structure-performance relation between the Pt-M nanoparticle structure and composition on the one hand and the propane dehydrogenation performance on the other hand. For the ALD-based approach, the methodology should be scaled down to the atomic scale level and the limits of compositional control should be evaluated. Finally, the ALD methodology has high potential for answering more fundamental questions in catalysis in general, as it can produce tailored model catalysts.

List of symbols

Roman symbols

A	LDH interlayer anion
a	Charge of 2D sheets in LDH, equivalent to the fraction of M^{3+} cations in the brucite-type LDH layers: $[M^{3+}]/([M^{3+}] + [M^{2+}])$ (-)
A_{Al}	Atomic mass of Al (amu)
A_{Ga}	Atomic mass of Ga (amu)
a_{HT}	Cell parameter of LDH, equals average metal-metal distance in 2D HT layer (nm)
$A_j(k)$	Amplitude factor of j^{th} photoelectron scattering path contribution (-)
A_{Mg}	Atomic mass of Mg (amu)
a_{MgO}	MgO lattice parameter (nm)
A_O	Atomic mass of O (amu)
A_{Pt}	Atomic mass of Pt (amu)
c	Parameter which shifts the wavelet over k-space ($Å^{-1}$)
c_f^i	Calibration coefficient of gas i (i = H_2 or He)
c_{HT}	LDH interlayer spacing (nm)
C_i	Constants in V(E) function (i = 0, 1, 2) (-)
d	Parameter which alters the wavelength of the wavelet, termed 'scaling parameter' (-)
D	Effective diffusion coefficient ($m^2\ s^{-1}$)
$d_{003,HT}$	(003) LDH basal plane spacing (nm)
$d_{110,HT}$	(110) LDH intralayer spacing (nm)
D_i	Effective diffusion coefficient for gas i ($m^2\ s^{-1}$)

D_{ref}	Reference effective diffusion coefficient ($m^2\ s^{-1}$)
E	X-ray energy (eV)
ê	Electric field polarization vector of a photon
E_0	Absorption edge energy (eV)
ΔE_0	Photoelectron energy origin correction (eV)
$E_{binding}$	Electron binding energy (eV)
E_{kin}	Electron kinetic energy (eV)
F_{H_2}	H_2 exit-flow rate (mol/s)
$f_j(k)$	Photoelectron backscattering amplitude function of material shell j around the X-ray absorber (Å)
$F_j^{eff}(k)$	Effective photoelectron backscattering amplitude function of scattering path j (Å)
$F_{propane,0}$	Propane exit-flow rate (mol/s)
h	Planck constant (eV s)
ΔH_{298}^0	Standard enthalpy of reaction (kJ mol^{-1})
h_{HT}	LDH interlayer distance (nm)
I_0	Incoming X-ray intensity (s^{-1})
I_e	Electron yield (s^{-1})
I_f	X-ray fluorescence intensity or fluorescence yield (s^{-1})
I_t	Transmitted X-ray intensity (s^{-1})
k	Photoelectron wavenumber ($Å^{-1}$)
Δk	k-space fitting range ($Å^{-1}$)
Δk	k-space resolution of the wavelet transformed XAS signal ($Å^{-1}$)
k_{max}	Maximum value of the k-range which is selected for transformation ($Å^{-1}$)
k_{min}	Minimum value of the k-range which is selected for transformation ($Å^{-1}$)
l	Orbital quantum number (-)
L_{cat}	Length of the catalyst zone (m)

L_{in2}	Length of the inert zone downstream of the catalyst zone (m)
M	Metal
m	Stoichiometric concentration of H_2O (-)
$\boldsymbol{m}$	Photoelectron scattering path degeneracy (-)
m_e	Electron mass (kg)
M_i	Molar mass of gas i (kg mol^{-1})
M_{ref}	Molar mass of reference gas (kg mol^{-1})
M_s	Support metal
n	Charge of compensation interlayer anions (-)
n_c	Cauchy order (-)
N_{H_2}	Injected moles of H_2 (mol)
N_{idp}	Number of independent points (-)
N_j	Number of equivalent scattering paths j (MS), or coordination number j (SS) (-)
N_{NN1}	Sum of $N_{Pt,NN1}$ and $N_{O,NN1}$ (-)
$N_{O,NN1}$	Pt-O nearest neighbor coordination number (equals N_{Pt-O}) (-)
N_p	Number of moles per pulse (mol)
N_{par}	Number of parameters used for the fit (-)
$N_{Pt,NNi}$	Pt-Pt i^{th} nearest neighbor coordination number (i = 1 – 4, $N_{Pt,NN1}$ equals N_{Pt-Pt}) (-)
N_{Pt-Cl}	Pt-Cl coordination number (-)
N_{Pt-Ga}	Pt-Ga coordination number (-)
N_{Pt-In}	Pt-In coordination number (-)
N_{Pt-Mg}	Pt-Mg coordination number (-)
N_{Pt-O}	Pt-O coordination number (-)
N_{Pt-Ol}	Pt-O_l coordination number (-)
N_{Pt-Pt}	Pt-Pt coordination number (-)

N_{pts}	Number of data points used for data fitting (-)
p	Electron impulse ($kg^{1/2}$ $eV^{1/2}$)
p	Sorption pressure (Pa)
ΔP	Pressure drop in the feed volume over the microreactor bed (kPa)
p^0	Standard vapor pressure (Pa)
$P_{propane,0}$	Propane partial pressure (Pa)
q	Photoelectron wavenumber (inverse Fourier transformed space) ($Å^{-1}$)
r	Coordinate vector of the electron
R	Radial distance from the X-ray absorber (Å)
R	Universal gas constant (J mol^{-1} K^{-1})
ΔR	R-space fitting range ($Å^{-(z+1)}$)
ΔR	R-space resolution of the wavelet transformed XAS signal ($Å^{-(z+1)}$)
$R-factor$	Fractional sum of squared residuals of misfit (-)
R_{eff}	Effective absorber-scatterer pair interatomic distance (Å)
R_{H_2}	Adsorption rate of H_2 on sample surface (mol s^{-1})
R_j	Half-path length of photoelectron scattering path j (MS), or interatomic distance j (SS) (Å)
$R_{O,NN1}$	Pt-O nearest neighbor distance (equals R_{Pt-O}) (Å)
$R_{Pt,NNi}$	Pt-Pt i^{th} nearest neighbor distance (i = 1 – 4, $R_{Pt,NN1}$ equals R_{Pt-Pt}) (Å)
R_{Pt-Cl}	Pt-Cl interatomic distance (Å)
R_{Pt-Ga}	Pt-Ga interatomic distance (Å)
R_{Pt-In}	Pt-In interatomic distance (Å)
R_{Pt-Mg}	Pt-Mg interatomic distance (Å)
R_{Pt-O}	Pt-O interatomic distance (Å)
R_{Pt-Ol}	Pt-O_l interatomic distance (Å)
R_{Pt-Pt}	Pt-Pt interatomic distance (Å)
S_0^2	amplitude reduction factor (-)

STY	Site-time yield (mol s^{-1} mol_{Pt}^{-1})
t	Real time (s)
T	Temperature (K)
T_{ref}	Reference temperature (K)
V(E)	Victoreen function
V_f	Feed volume (ml)
W_{cat}	Catalyst mass (kg_{cat})
z	k-weight to the EXAFS signal (-)

Greek symbols

α	Isotropic thermal expansion coefficient (-)
δ	Oxidation state intermediate to 3+ and 0 (-)
$\delta_j(k)$	Phase shift for photoelectron scattering path j (-)
ϵ	Measurement uncertainty ($Å^{-(z+1)}$)
ε	Bed porosity (-)
θ	X-ray angle of incidence (°)
θ_H	H uptake (mmol/m²)
λ(k)	energy dependent mean-free path distance of the photoelectron (Å)
λ_{el}	De Broglie wavelength (m^{-1})
μ(E)	Linear absorption coefficient (m^{-1})
$\mu_0(E)$	Atomic background function (m^{-1})
ν	X-ray photon frequency (s^{-1})
$\boldsymbol{\nu}$	Number of free parameters (-)
$\sigma^{(3)}$	Third cumulant (Å³)
σ_j^2	Squared Debye-Waller (DW) bond length disorder factor for photoelectron scattering path j (Å²)
$\sigma^2_{O,NN1}$	Pt-O nearest neighbor Debye-Waller disorder factor (equals σ^2_{Pt-O}) (Å²)

$\sigma^{(3)}_{Pt,NN1}$	Third cumulant for the first Pt-Pt nearest neighbors (Å³)
$\sigma^2_{Pt,NNi}$	Pt-Pt ith nearest neighbor Debye-Waller disorder factor (i = 1 – 4, $\sigma^2_{Pt,NN1}$ equals σ^2_{Pt-Pt}) (Å²)
σ^2_{Pt-Ga}	Debye-Waller disorder factor for Pt-Ga neighbors (Å²)
σ^2_{Pt-In}	Debye-Waller disorder factor for Pt-In neighbors (Å²)
σ^2_{Pt-Mg}	Debye-Waller disorder factor for Pt-Mg neighbors (Å²)
σ^2_{Pt-O}	Debye-Waller disorder factor for Pt-O neighbors (Å²)
σ^2_{Pt-Pt}	Debye-Waller disorder factor for Pt-Pt neighbors (Å²)
σ^2_{Pt-X}	Debye-Waller disorder factor for Pt-X neighbors (X = O, O_l, Pt, Mg) (Å²)
τ	Dimensionless time (-)
$\Phi_j(k)$	Phase factor of jth photoelectron scattering path contribution (-)
χ^2	Chi-squared objective function (-)
$\chi(E)$	EXAFS signal in E-space (-)
$\chi(k)$	EXAFS signal in k-space (-)
$\chi(R)$	EXAFS signal in R-space (Å$^{-(z+1)}$)
$\chi_e(R_i)$	Complex Fourier transformed experimental $\chi(k)$ signal (Å$^{-(z+1)}$)
$\chi_j(k)$	jth contribution to the total EXAFS signal (-)
$\chi_t(R_i)$	Complex Fourier transformed theoretical $\chi(k)$ signal (Å$^{-(z+1)}$)
${\chi_\nu}^2$	Reduced chi-squared $\chi^2/\boldsymbol{\nu}$ (-)
ψ	Mother wavelet function
$\|\psi_f\rangle$	Final electron wave function
$\|\psi_i\rangle$	Initial electron wave function

Abbreviations and acronyms

acac	Acetylacetonate
ALD	Atomic layer deposition
at%	Atom percent

BET	Brunauer–Emmett–Teller
CCR	Continuous catalyst regenerator
CoCooN	Conformal Coating of Nanomaterials
DUBBLE	Dutch Belgian BeamLine
DW	Debye-Waller
EDX	Energy dispersive X-rays
EML	Equivalent monolayers
ESRF	European Synchrotron Radiation Facility
EXAFS	Extended X-ray absorption fine structure
FCC	Fluid catalytic cracking
fcc	Face-centered cubic
FT	Fourier transformation
FTO	Fischer-Tropsch-to-olefins
HAADF-STEM	High angle annular dark field scanning transmission electron microscopy
HT	Hydrotalcite, synonym of LDH
ICP-AES	Inductively coupled plasma atomic emission spectrometry
LCF	Linear combination fitting
LCT	Laboratory for Chemical Technology
LDH	Layered double hydroxides, synonym of HT
$MeCpPtMe_3$	(methylcyclopentadienyl)trimethylplatinum
MMO	Mixed metal oxides
MS	Multiple scattering
MTO	Methanol-to-olefins
NGL	Natural gas liquids
PDH	Propane dehydrogenation
QMS	Quadrupole mass spectrometer
QXAS	Quick X-ray absorption spectroscopy

S/N	Signal-to-noise
SAMBA	Spectroscopy applied to material based on absorption
SLS	Swiss Light Source
SOLEIL	Source optimisée de lumière d'énergie intermédiaire du Laboratoire pour l'utilisation du rayonnement électromagnétique
SS	Single scattering
STEM-DF	Scanning transmission electron microscopy – dark field
TAP	Temporal analysis of products
TEM	Transmission electron microscopy
TMA	trimethylaluminium
TMHD	Tris(2,2,6,6-tetramethyl-3,5-heptanedionato)
TPR	Temperature programmed reduction
WI	Wet impregnation
WL	White line
WT	Wavelet transformation
wt%	Weight percent
XAFS	X-ray absorption fine structure
XANES	X-ray absorption near edge structure
XAS	X-ray absorption spectroscopy
XMT	X-ray microtomography
XPS	X-ray photoemission spectroscopy
XRD	X-ray diffraction
XRF	X-ray fluorescence
XRR	X-ray reflectivity

Chapter 1. Introduction

Light olefins are of utmost importance for chemical industry as they function as building blocks, in particular for polymer production. Recently, the improved exploitation of novel shale gas feedstocks triggered significant changes in light olefin availability. For example, the supply of propylene has drastically decreased, necessitating the search for efficient and economically viable on-purpose production alternatives. In current economic conditions, catalytic propane dehydrogenation (PDH) offers a suitable solution to meet the increasing market demand for propylene. Supported Pt nanoparticles alloyed with In, Ga or Sn have proven to be highly selective dehydrogenation catalysts for transforming propane into propylene. However, the formation mechanisms and functioning of the current generation of bimetallic Pt-based dehydrogenation catalysts are not fully understood. This lack of knowledge hinders manipulation during catalyst formation in view of catalyst optimization, eventually yielding increased catalyst stability combined with superior performance. In addition, more cheap, scalable and efficient synthesis protocols are highly desired which also allow tailoring of the bimetallic nanoparticle size and composition with unprecedented precision. In this work, the atomic scale mechanisms governing the formation of novel layered double hydroxide (LDH)- and atomic layer deposition (ALD)-derived PDH catalysts are scrutinized in the course of catalyst synthesis and formation.

1.1 Economic climate

During the past decade, the global consumption of ethylene (ethene) and propylene (propene) has gradually increased with about 4% on a yearly basis.[1] This consumption increase is expected to persist in the coming years owing to the growing middle class in countries under development. In general, light olefin consumption is an indicator of economic activity as these compounds are essential units for the production of more complex chemicals which are widely used in all branches of the economy.[2-5] The relative ethylene, propylene and butylene consumptions amount to about 60%, 30% and 10% respectively, and result into the production of around 35% polyethylene, 25% polypropylene, 10% oxygenates, 20% intermediates – such as ethylbenzene – and 10% others.[6]

Nowadays, the vast majority of light olefins is obtained by steam cracking and fluid catalytic cracking (FCC) of naphtha and light diesels.[1] These technologies are however energy intensive as cracking processes are operated at high temperatures – steam cracking typically at 850 °C. In addition, the depleting petroleum reserves cause a persistent increase in the cost of the cracking feed, further increasing the total operational cost. Besides these issues, petroleum-based cracking processes are non-selective, as they show low selectivity towards specific olefins.[7] These elements have stimulated the chemical industry to transform current technologies to more efficient and energy favorable processes which utilize more economical feedstocks.

In recent years, hydraulic fracturing techniques have improved to such extent that shale gas reserves can be extracted in an economic way. The great availability and exploitation of shale gas reserves has resulted in a 75% drop of the natural gas prices compared to 2005.[8, 9] For this reason, shale gas – as a novel source of natural gas – has become an increasingly attractive feedstock for the production of a variety of chemicals and transportation fuels. For example, the production of light olefins can be achieved by a train of

processes which make use of natural (shale) gas: steam reforming of natural gas into synthesis gas, followed either by direct Fisher-Tropsch-to-olefins (FTO) or by methanol-to-olefins (MTO) using an intermediate step for methanol synthesis from syngas.[10, 11]

Depending on the location of exploitation, shale gas contains a significant fraction of natural gas liquids (NGL) – around 1 - 10% ethane and 0 - 3% propane – which can be separated with relative ease from the remaining gas phase compounds – methane (60 - 97%), carbon oxides (0.5 - 5%) and nitrogen (0 - 30%).[12] The wide availability and easy extraction of shale-gas-derived NLG therefore allows it to replace naphtha as cheap alternative feed for steam cracking. Indeed, besides the construction of novel ethane steam crackers in previous years, naphtha crackers have been disassembled or rebuilt to ethane crackers.[13] The latter process does not only allow the use of cheap feeds, but also displays high selectivity towards ethylene.[7]

Ethane steam cracking only produces trace amounts of propylene. In contrast, more expensive naphtha-based steam cracking yields considerable amounts of propylene. The shift from naphtha-based to ethane-based steam cracking therefore caused a sharp drop in the propylene supply, while its demand only increased.[14] In current economic perspective, the selective production of propylene is therefore highly-profitable. As catalytic propane dehydrogenation offers high selectivity towards propylene (> 90%) compared to other processes, the further development and optimization of dehydrogenation catalysts is stringent.

1.2 Dehydrogenation catalyst selection

Two major types of catalytic alkane dehydrogenation processes are currently available: (1) non-oxidative dehydrogenation and (2) CO_2- or O_2-assisted oxidative dehydrogenation.[7] Non-oxidative dehydrogenation ($C_3H_8 = C_3H_6 + H_2$) is an endothermic process (ΔH^0_{298} = 124.3 kJ mol^{-1}) which is thermodynamically limited. To obtain high conversions (> 50%), high temperatures and low paraffin partial pressures are required,

necessitating typical reaction temperatures of 550 – 750 °C. In contrast, oxidative dehydrogenation is not a thermodynamically limited process, allowing full conversion for optimized reaction conditions, as the H_2 product is removed by the oxidizing agent ($CO_2 + H_2 = CO + H_2O$ or $½ O_2 + H_2 = H_2O$). Both CO_2- and O_2-assisted oxidative dehydrogenation processes impose difficulties during operation. For example, O_2-assisted oxidative dehydrogenation entails significant risk for over-oxidizing the produced olefins, thereby cancelling the advantage of supplying O_2 to increase conversion. CO_2-assisted oxidative dehydrogenation can result in additional coke formation and competitive adsorption on catalyst sites, both influencing the dehydrogenation performance.[7] Because of these operational challenges, this work's focus is on non-oxidative catalytic dehydrogenation.

Within the family of non-oxidative dehydrogenation catalysts, a multitude of materials have been studied, including bimetallic Pt-Sn-based catalysts as well as CrO_x-, VO_x-, MoO_x-, GaO_x-, InO_x- and FeO_x-based oxide materials.[7] Two patented processes are currently being used in chemical industry, namely Catofin (CB&I Lummus) and Oleflex (UOP).[15, 16] The Catofin process employs CrO_x/Al_2O_3 catalysts inserted in a series of parallel adiabatic fixed bed reactors, run at 575 °C and pressures of 0.2 – 0.5 bar. Because of rapid coke formation on this type of catalysts, a single fixed bed reactor undergoes cyclic reaction, regeneration and purging (15 – 30 min/cycle), making multiple parallel fixed bed reactors necessary to provide continuous product flows. The Oleflex process uses Pt-Sn-based catalysts which are operated at 525 – 705 °C under 1 – 3 bar. The preheated gas feed passes through a number of fluidized bed reactors, which are connected in series. Similarly, the catalyst travels through this series of reactors and is finally recovered in a continuous catalyst regenerator (CCR), which burns off all coke and redisperses Pt-Sn clusters by adding a chlorine-air mixture.

A performance evaluation of the above-mentioned dehydrogenation catalysts shows that metallic Pt-based catalysts have similar propylene yield compared to metal oxide catalyst materials (Figure 1.1).[7] However, for Pt-based catalysts these yields can be obtained at lower

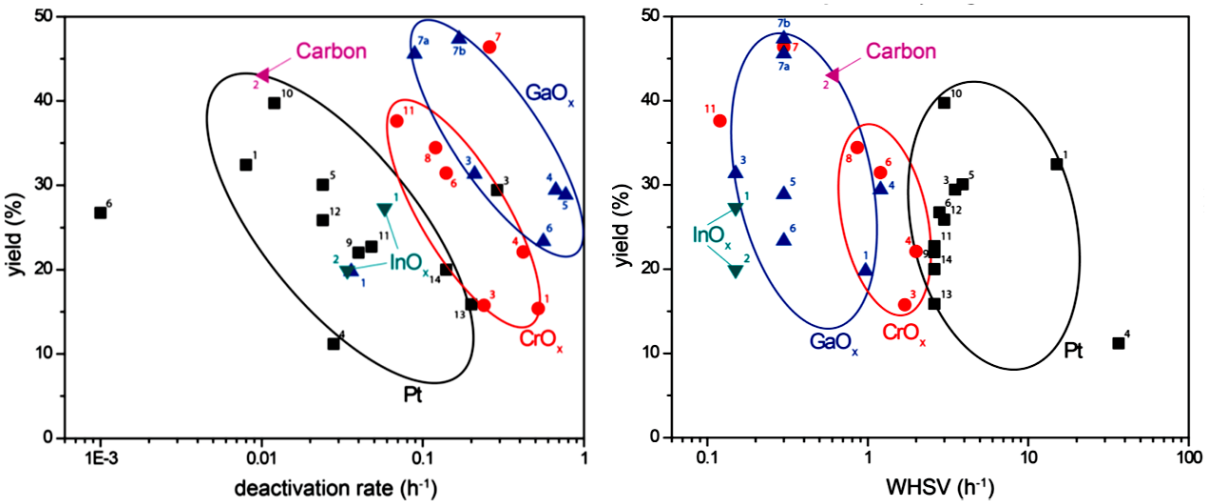

Figure 1.1: Propylene yield of different types of catalysts during non-oxidative dehydrogenation of propane versus (left) deactivation rate and (right) space velocity (WHSV).[7]

space-times (Figure 1.1). Indeed, an estimation of the average specific activity of Pt-based catalysts compared to CrO_x- and GaO_x-based catalysts shows that Pt has a turnover frequency which is 4 orders of magnitude higher than Cr- and Ga-based oxide catalysts (~ 3 x 10^{-1} s^{-1} versus ~ 8 x 10^{-5} s^{-1}).[7] Besides this higher activity of Pt-based catalysts, their deactivation rate is significantly lower compared to metal oxide dehydrogenation catalysts (Figure 1.1). In summary, Pt-based dehydrogenation catalysts behave far superiorly compared to their metal oxide counterparts: Pt-based catalysts deactivate relatively slow during dehydrogenation and exhibit significantly higher activities compared to metal oxide dehydrogenation catalysts.

1.3 Pt-based dehydrogenation catalyst design

Selective alkane dehydrogenation requires the catalyst to exhibit high activity towards C-H bond cleavage and low activity for C-C bond scission. Amongst the noble metals, Pt shows these properties in a superior way compared to others.[7] Within the group of high-performing Pt-based dehydrogenation catalysts, the olefin selectivity is determined by the extent to which side reactions are allowed. These side reactions consist of hydrogenolysis, catalytic cracking and isomerization.[15] Hydrogenolysis takes place at the Pt cluster surface and is believed to be the major cause of catalyst deactivation by coke formation.[17-21] Catalytic

cracking and isomerization are catalyzed by support Brønsted acid sites.[15] Fortunately, these selectivity losses can be (partially) suppressed by means of intelligent catalyst design.

As Brønsted acid sites are not required for dehydrogenation itself and only promote side reactions, the olefin selectivity can be increased by excluding supports which contain considerable Brønsted acidity. Besides the necessity of having a large specific surface area, the support needs to be hydrothermally stable during reaction and regeneration cycles around 650 °C. In addition, a strong interaction between Pt clusters and the support is desired since strong Pt-O-M_s bonds (M_s = support metal) prevent rapid Pt nanoparticle sintering, avoiding a quick loss in activity (see below).

It is generally accepted that Pt-catalyzed side reactions (hydrogenolysis) are structure sensitive, while dehydrogenation itself is structure insensitive.[18-21] Despite intense research, a general consensus on the mechanisms influencing the kinetics of the side reactions is lacking up to date. However, it is evident that well-dispersed Pt nanoparticles are aimed for during catalyst synthesis, since the latter particles provide a higher number of exposed Pt sites during dehydrogenation reaction.

A valuable means to further improve alkene selectivity and catalyst stability is offered by the addition of promoter elements, such as Sn, Ga, In.[22-24] These post-transition metals not only modify the Pt phase but also the support material.[7] For example, the addition of Sn promoters in widely studied Pt-Sn catalysts suppresses hydrogenolysis, neutralizes support acid sites, minimizes nanoparticle sintering and promotes the migration of coke species from the cluster surface to the support. Such coke migration prevents the accumulation of coke on the Pt-Sn cluster surface and consecutive site blockage during reaction.

Alloying of Pt with a promoter element M (M = Sn, In, Ga) is inducing both geometric and electronic changes in the properties of the active Pt phase. Up to date, the exact effect on the catalyst performance of these geometric and electronic changes is however not fully understood, although significant insights have been obtained. For the geometric effect

one can invoke the 'ensemble-effect' to clarify the improved dehydrogenation selectivity. Pt-M alloyed nanoparticles have decreased Pt ensemble sizes owing to the presence of promoter elements M at the Pt-M cluster surface. Alkane dehydrogenation is a structure insensitive reaction, implying that this reaction can occur on large as well as small ensembles of Pt – even on single Pt atoms. Alkane dehydrogenation on the Pt-M alloyed nanoparticle surface is therefore still taking place. In contrast, undesired side reactions are suppressed on Pt-M alloys, as these are structure sensitive and require larger ensembles of Pt. Indeed, Olsbye et al.[25] and Nagaraja et al.[26] have suggested that the decreased density of Pt-rich domains on Pt-M alloyed clusters is the underlying cause for the improved catalyst performance.

Pt-M alloying of Pt with a promoter M also induces changes in the electronic structure of Pt, thereby altering its adsorptive and catalytic properties. Adsorption microcalorimetry and DFT studies reveal two general conclusions which clarify the macroscopic changes in the catalytic behavior of Pt-Sn nanoparticles relative to pure Pt clusters.[27-32] Firstly, Sn promotion reduces the propane dehydrogenation reaction rate due to an increase in the energy barrier for dissociative adsorption of propane (Figure 1.2). Secondly, Sn promotion weakens the adsorption of ethylene on the Pt surface and suppresses the formation of propylidyne ($H_3C\text{-}CH_2\text{-}C{\equiv}Pt$), an important precursor of coke. The weakened propylene adsorption can be understood by the fact that bond formation between Pt and Sn results in electron transfer from the promoting element towards the Pt 5d band. This increases the 5d electron density of Pt and reduces its electronegativity, leading to weakened adsorption and the suppression of further reaction with ethylene.[33] Ideally, the degree of Pt promotion should be equilibrated to find the optimal balance between a decrease in dehydrogenation activity and an increase in alkene selectivity.

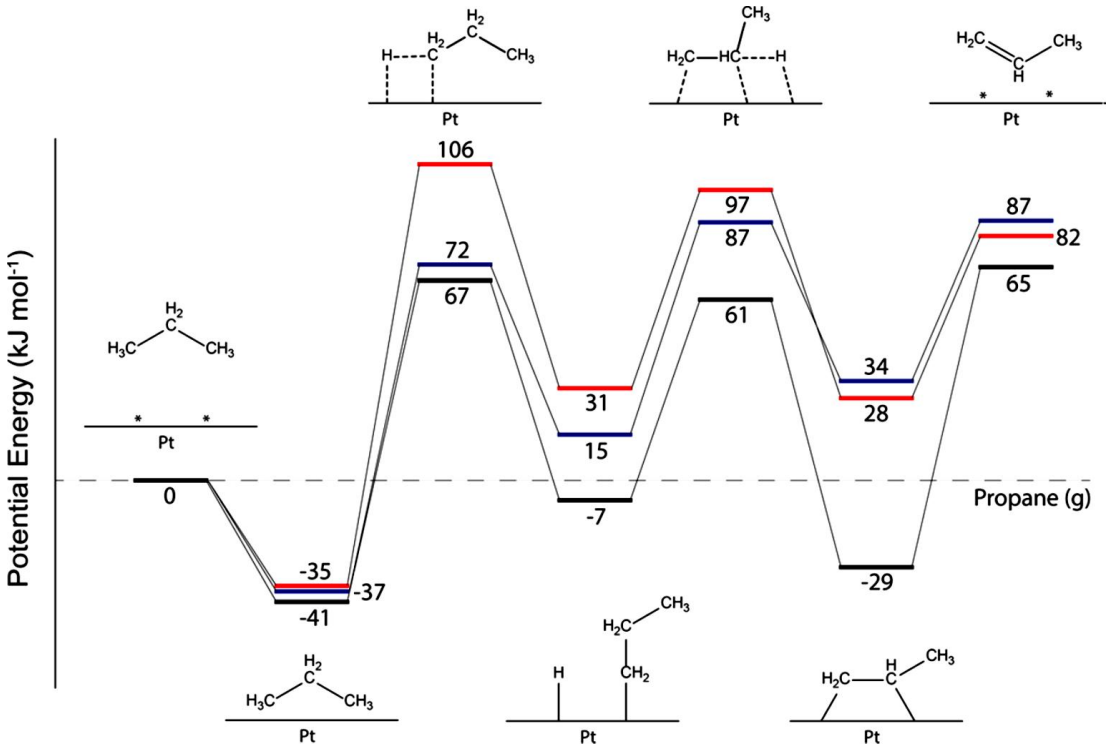

Figure 1.2: Energy diagrams during propane dehydrogenation to propylene on Pt (111) (black), Pt_3Sn (111) (blue), and Pt_2Sn (111) (red) surfaces, obtained by DFT calculations. The intermediates are shown together with their corresponding energies.[27]

1.4 Scope and research objectives

In the current economic climate, increasingly efficient and durable dehydrogenation catalysts are required for the on-purpose production of high-purity propylene from propane (Section 1.1). Pt-based catalysts have shown to perform superiorly during propane and isobutane dehydrogenation compared to metal oxide-based catalysts, the latter showing lower dehydrogenation activities and more rapid deactivation (Section 1.2). More particularly, well-dispersed Pt-Sn/In/Ga/Ge alloyed nanoparticles supported on non-acidic, hydrothermally stable and high surface area supports are the most promising materials to catalyze tomorrow's dehydrogenation processes in chemical industry (Section 1.3). In this work, two recently developed synthesis strategies for the formation of Pt-In and Pt-Ga dehydrogenation catalysts are explored and investigated, as they provide specific advantages over other, conventional methodologies.

1.4.1 **Layered Double Hydroxide (LDH) derived catalysts**

In industry as well as academia, deposition-precipitation and incipient wetness impregnation (WI) are amongst the two most frequently used preparation methods for supported metal catalysts. However, these methods display significant drawbacks which often result in rapidly deactivating and non-optimized catalysts.[34, 35] For example, obtaining well-dispersed and uniformly (size-)distributed (bi)metal nanoparticles with good thermal stability is not trivial, especially at higher metal loadings. An inhomogeneous distribution of metal precursor on the support surface after impregnation and weak precursor-support and metal-support interactions respectively hamper proper catalyst preparation and accelerate catalyst deactivation.

Layered double hydroxides (LDHs) or hydrotalcites (HTs) offer a valuable solution for the design and synthesis of catalysts with dispersed (bi)metallic nanoparticles, having a uniform size distribution and high stability.[34] To synthesize these catalysts, first, divalent M^{2+} (e.g., Mg^{2+}) and trivalent M^{3+} metal cations (e.g., Ga^{3+}) assemble into the layered LDH structure during a single step co-precipitation (M^{2+}/M^{3+} ~ 3, Section 2.1.1). During subsequent calcination and reduction of these basic materials, reducible metal cations migrate and form (bi)metal clusters on the remaining non-reducible mixed metal oxide (MMO) support.

This LDH-based catalyst synthesis strategy provides a multitude of advantages which are not offered by conventional synthesis methodologies.[34, 35] First, the number of synthesis steps can be drastically reduced, ultimately leading to a single step process where all components are incorporated during one-pot synthesis. Such one-pot procedure also allows the preparation process to be easily scalable, and therefore attractive for industrial use. Second, by incorporating the appropriate fractions of reducible metal cationic species into the LDH precursor, the (bi)metallic nanoparticle size (and composition) can be tuned to yield optimal performance. Third, intelligent selection of suitable non-reducible metal species allows for fine-tuning of the support properties, e.g. improve hydrothermal stability, surface

area. Such tailoring of the support material can also prevent rapid nanoparticle sintering – and concomitant deactivation – by increasing the interaction between the (bi)metal clusters and the support. Fourth, the homogeneous distribution of reducible active metal cations in the LDH structure ensures highly-dispersed uniformly sized nanoparticles to be formed all over the surface of the activated catalyst.

In this work, one end goal is to achieve and understand the one-pot synthesis and formation of Pt-M (M = Ga or In) alloyed nanoparticles on Mg(Pt)(M)(Al)O_x MMO supports after calcination and reduction of Pt and M incorporated Mg,Al,Pt,M-LDH precursors. As an intermediate step between one-pot synthesis and conventional wet impregnation of both Pt and M precursors on Mg(Al)O_x, the formation of Pt-M/Mg(M)(Al)O_x dehydrogenation catalysts is studied during calcination and reduction, starting from wet impregnated $Pt(acac)_2$ on Mg(M)(Al)O_x mixed oxides.

The specific choice of the constituent element types contained within these dehydrogenation catalysts can be justified as follows. MgO-type materials offer hydrothermal stability during reaction and regeneration cycling.[36, 37] In addition, MgO is non-acidic and therefore suppresses side reactions such as catalytic cracking and isomerization.[7] Al-based oxides are more acidic though strongly increase the specific surface area of the support and show hydrothermal stability. To balance between Al-induced high surface area and acidic properties, therefore, the Mg/Al atomic ratio was fixed around 3.[34, 35] In addition, an atomic ratio around 3 is also necessary for obtaining LDH structured materials. Evidently, Pt-In and Pt-Ga alloyed nanoparticles promote effective dehydrogenation.[22-24] Sn was not utilized as a promoter element as it is not trivial to incorporate it in the LDH-structure.

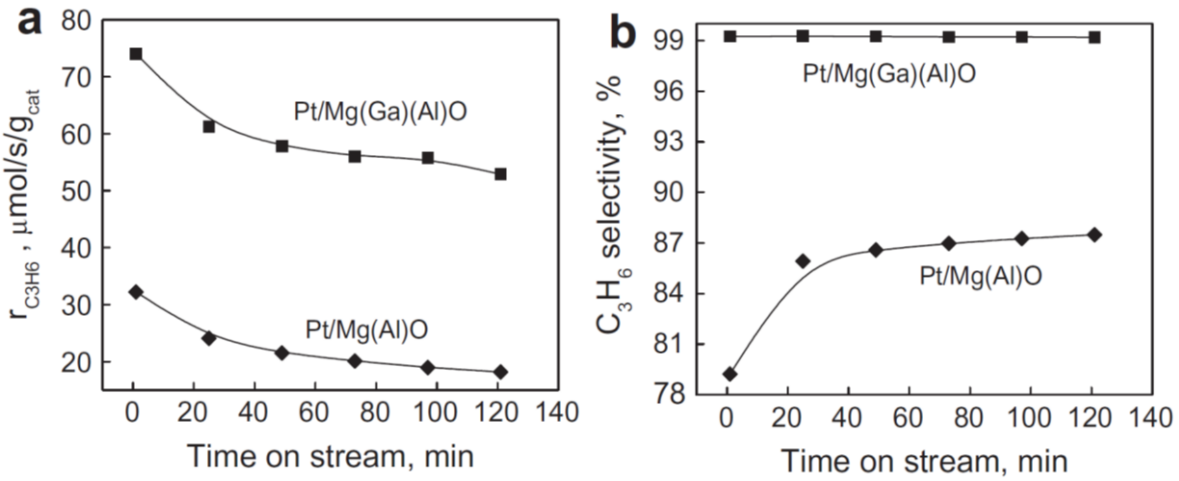

Figure 1.3. Comparison of Pt-Ga/Mg(Ga)(Al)O_x (labeled as 'Pt/Mg(Ga)(Al)O', Ga/Pt = 2.86) and Pt/Mg(Al)O_x catalyst performance: (a) activity and (b) propylene selectivity during propane dehydrogenation (600 °C, 20 vol% C_3H_8, H_2/C_3H_8 = 1.25, 60 ml/min).[23]

Besides the above listed advantages of LDH-based synthesis, these Pt-Ga catalysts exhibit superior performance compared to bimetallic Pt-Ga catalysts for which both Pt and Ga are wet impregnated.[23] In addition, the activities and alkene selectivities of Pt-Ga/Mg(Ga)(Al)O_x catalysts are significantly higher than for monometallic Pt/Mg(Al)O_x (Figure 1.3).[23]

1.4.2 Atomic Layer Deposition (ALD) derived catalysts

Atomic layer deposition utilizes sequential self-saturating reactions between gaseous molecules and a solid surface to grow thin films in a layer-by-layer fashion.[38, 39] An ALD process typically consists of alternating precursor (A) and reactant gas (B) pulses, i.e. cyclic AB-type exposures which allow to deposit material with atomic layer precision in a conformal way. However, the deposition of metals – in contrast to metal oxides – on oxide supports generally results in metal island growth due to the low reactivity between the metal precursor and the oxide surface. This generates a multitude of opportunities for the atomic scale tailoring of supported nanoparticle catalysts.

In contrast to the formation of LDH-derived catalysts, the method of ALD is a rather expensive and time-consuming process due to the low sticking probability of the precursor

molecules (low growth rates). However, ALD offers the strong advantage of exhibiting superior control over the morphology of the deposited bimetal phase – here Pt(-In) – in general.[40, 41] For example, first, the nanoparticle size of the deposited clusters can be controlled down to the (sub-)monolayer level by varying the number of deposition cycles. ALD thereby allows atomically precise tailoring of the nanoparticle size. Second, depending on the length of the precursor pulse period or the temperature of deposition, the number of clusters grown per m^2 of support surface can be varied in a controlled way. In the long run, the catalyst loading can thus be increased, while keeping the size and morphology of the deposited nanoparticles constant. Third, the possibility of depositing bimetallic nanoparticles by ALD opens a multitude of opportunities for tailoring the cluster composition and morphology. Depending on the implemented ALD procedure, e.g. ABABAB or AAABBB (A = Pt, B = M), a quasi-unlimited number of combinations can be made which permits full control over the deposited bimetallic phase, ranging from fully mixed to core-shell cluster types, respectively.

In spite of these advantages, the fundamental understanding of important atomic scale processes occurring during ALD – including atomic surface migration, Ostwald ripening – is still lacking up to date. To fully exploit the advantages that ALD-based catalyst synthesis can provide, a detailed understanding of these processes is necessary. Therefore, in this work, we aim to increase the understanding of the mechanistic events, ongoing during Pt ALD, by developing a novel methodology which exploits detailed information on the nanoparticle properties. Another goal concerns the fabrication of ALD-derived bimetallic Pt-In nanoalloys with control over the alloy composition. A proof-of-principle study is aimed for which explores the compositional flexibility provided by ALD-based deposition of Pt-In bimetallic nanostructures.

In order to provide a model support for the fundamental study of pure Pt ALD, a spin-coated 180 nm thick mesoporous SiO_2 film is selected, supported on a flat non-porous Si wafer. In addition, a novel Pt ALD process is employed, i.e. $MeCpPtMe_3/O_3$, to provide full

temperature flexibility during deposition (100 – 300 °C). For the proof-of-principle study on Pt-In bimetallics, analogous concepts are used as for the formation of LDH-derived Pt-based catalysts: (1) the gradual insertion of support In into the Pt fcc structure during reduction of Pt/In_2O_3 – as for $Pt/Mg(In)(Al)O_x$ – and (2) direct Pt-In alloying during reduction of Pt-containing $In(Pt)O_x$ layers – as for $Mg(Pt)(In)(Al)O_x$. Depending on the thickness of the In_2O_3 films in Pt/In_2O_3 ALD-derived samples, different Pt-In alloys can be expected.

To acquire deeper understanding of the formation of Pt-M nanocatalysts, both via ALD- or LDH-derived synthesis, proper characterization tools should be available to detail the structure and physicochemical properties of the active (noble) metal phase. X-ray absorption spectroscopy (XAS) and X-ray fluorescence (XRF) are particularly well-suited to fulfill this task as they display a number of strong advantages: they (1) can be applied *in situ*, (2) are element specific, (3) provide simultaneous Å-scale structural information on the local environment around the X-ray absorber as well as electronic information on the absorber, and (4) they do not require long range order.[41] The use of these X-ray spectroscopies in the field of ALD is scarce to date. However, novel combined *in situ* XRF-XAS methodologies are to be developed to extract more detailed and fundamental information during ALD deposition. The area of catalysis is more familiar with the application of XAS. However, the direct discrimination of the elemental nature of the X-ray absorber's neighbors remains a bottleneck up to date. In combination with the above-mentioned goals, the further development of these X-ray spectroscopic techniques is aimed for in order to improve the characterization during of LDH- and ALD-based catalyst formation.

LDH- and ALD-based synthesis methods are quite different approaches for catalyst synthesis, each of them exhibiting specific drawbacks and advantages. However, both methods ultimately yield supported Pt-M alloyed nanocatalysts, the formation of which depends on the same set of reactions, e.g. H-dissociation, In_2O_3 reduction, Pt-In bond formation, and atomic transport mechanisms, e.g. Pt, H, In surface migration. For the sake of

fundamental understanding, this work aims to unravel the intricate interplay between these atomic scale reactions and transport mechanisms, eventually yielding Pt-M nanoparticles. Deeper knowledge on the atomic scale behavior of these catalytic systems should smoothen the pathway towards the controlled design and tailored fabrication of tomorrow's high-performance catalysts. Lastly, it should be mentioned that results presented in this work are not only valid for Pt-based dehydrogenation catalysts in particular, but also for Pt- or even metal-based catalysts in general.

1.5 Outline

This work contains nine chapters: this introduction, a materials and methods chapter, six result chapters and a chapter with general conclusions on the performed research. The result chapters consist of two major parts: (Part 1) LDH-based and (Part 2) ALD-based catalyst synthesis and formation, ranging from chapter 3 – 6 and chapter 7 – 8, respectively.

Chapter 2 starts with an explanation of the synthesis protocol used for the formation of LDH-derived bimetallic Pt-M catalysts. Thereafter, a general overview is given of an ALD process. After introducing these synthesis/deposition protocols, the technique of XAS is described in more detail.

Chapter 3 exemplifies the capabilities and drawbacks of wavelet transformation (WT) during XAS analysis to discriminate in the elemental nature of the X-ray absorber's neighbors. Starting from $Pt(acac)_2$/$Mg(In)(Al)O_x$, WT XAS is shown to provide first-hand insights in the formation of Pt-In/$Mg(In)(Al)O_x$ catalysts (1 wt% Pt).

Chapter 4 concerns a more detailed study of the formation of Pt-Ga/$Mg(Ga)(Al)O_x$ catalysts, in which both conventional and WT XAS are used as characterization tools. After wet impregnation of a $Pt(acac)_2$-toluene solution on the Ga-incorporated $Mg(Ga)(Al)O_x$ support, the transformations of the Pt(-Ga) phase during calcination and H_2 reduction are discussed.

Chapter 5 discusses the role of hydrogen during Pt-Ga/Mg(Ga)(Al)O_x catalysts formation, starting from pure Pt clusters on Ga-incorporated Mg(Ga)(Al)O_x supports. During H_2 reduction to 650 °C, mechanisms such as H spill over, the mobility of H and its reductive ability are investigated by using Pt-Ga alloy formation as a probe reaction.

Chapter 6 presents a one-pot synthesis method for obtaining efficient bimetallic Pt-based catalysts as derived from LDHs. The study proposes an evolutional picture of the synthesized material upon one-pot synthesis, and after calcination and reduction treatment to 650 °C.

Chapter 7 contains a detailed study of the initial stages of the $MeCpPtMe_3/O_3$ ALD process. State-of-the-art EXAFS modeling in combination with XRF measurements allows to exploit the Pt nanoparticle morphological properties in the course of the ALD process. By applying this *in situ* XRF-XAS methodology, insights are obtained on mechanisms such as nucleation and coalescence.

Chapter 8 is a proof-of-concept study which details the mechanisms of Pt-In alloying during H_2 reduction of ALD-derived Pt/In_2O_3 and In(Pt)O_x nanocomposites. The results show that the composition of Pt-In alloys can be controlled by varying the In_2O_3 layer thickness for Pt/In_2O_3 material configurations.

Chapter 9 summarizes and unifies the conclusions obtained throughout the different chapters. In addition, suggestions are made for future research.

Additional information is given in **Appendices A-E**.

This PhD thesis comprises a collection of journal papers published in the course of this PhD period (Chapters 3 – 7). Chapter 8 in the onset for future research on the topic of bimetal ALD, and the presented results will be included in a manuscript that will be submitted in the near future.

1.6 References

(1) Advanced MTO: Breakthrough Technology for the Profitable Production of Light Olefins, http://www.wraconferences.com/sites/default/files/day%202%201130%20petchemRick%20Kempf.pdf

(2) Budavari, S.; O'Neil, M.; Smith, A.; Heckelman, P.; Obenchain, J. In The Merck Index, 12th ed.; Budavari, S., Ed.; Merck & Co.: NJ, 1996; 1348−1349.

(3) McCoy, M.; Reisch, M.; Tullo, A. H.; Short, P. L.; Tremblay, J.-F. Chem. Eng. News 2006, 84, 59.

(4) Ethylene Uses and Market Data, http://www.icis.com/Articles/2007/11/05/9075777/ethylene-uses-and-market-data.html.

(5) Market Study: Propylene (UC-1705), http://www.ceresana.com/en/market-studies/chemicals/propylene/

(6) Nexant. Industry Report - Independent Market Report on the Global and Indonesian Petrochemicals Industry, http://www.chandraasri.com/UserFiles/201105151926340.NexantIndustryReport2011.pdf

(7) Sattler, J. J. H. B.; Ruiz-Martinez, J.; Santillan-Jimenez, E.; Weckhuysen, B. M. *Chem. Rev.* **2014**, *114*, 10613-10653.

(8) Tullo, A. H. *Chem. Eng. News* **2012**, *90*, 10.

(9) McFarland, E. *Science* **2012**, *338*, 340.

(10) Torres Galvis, H. M.; de Jong, K. P. *ACS Catal.* **2013**, *3*, 2130.

(11) Stocker, M. *Micr. Meso. Mater.* **1999**, *29*, 3.

(12) Bullin, K.; Krouskop, P. Composition Variety Complicates Processing Plans for US Shale Gas, http://www.bre.com/portals/0/technicalarticles/KeithBullin-CompositionVariety_USShaleGas.pdf

(13) Chemical Composition of Natural Gas, http://www.uniongas.com/about-us/about-natural-gas/Chemical-Composition-of-Natural-Gas#L

(14) Schut, J. H. How Shale Gas Is Changing Propylene, http://plasticsengineeringblog.com/2013/02/20/how-shale-gas-is-changingpropylene/

(15) Bhasin, M. M.; McCain, J. H.; Vora, B. V.; Imai, T.; Pujadó, P. R. *Appl. Catal.-A* **2001**, *221*, 397.

(16) UOP Oleflex process for light olefin production, http://pet-oil.blogspot.nl/2012/10/uop-oleflex-process-for-light-olefin.html

(17) Redekop, E. A.; Galvita, V. V.; Poelman, H.; Bliznuk, V.; Detavernier, C.; Marin, G. B. *ACS Catal.* **2014**, *4*, 1812–1824.69-72

(18) Rioux, R. M.; Song, H.; Hoefelmeyer, J. D.; Yang, P.; Somorjai, G. A. *J. Phys. Chem. B* **2005**, *109*, 2192.

(19) Song, H.; Rioux, R. M.; Hoefelmeyer, J. D.; Komor, R.; Niesz, K.; Grass, M.; Yang, P.; Somorjai, G. A. *J. Am. Chem. Soc.* **2006**, *128*, 3027.

(20) Santhosh Kumar, M.; Chen, D.; Walmsley, J. C.; Holmen, A. *Catal. Commun.* **2008**, *20*, 747.

(21) Yang, M.-L.; Zhu, Y.-A.; Fan, C.; Sui, Z.-J.; Chen, D.; Zhou, X.-G. *Phys. Chem. Chem. Phys.* **2011**, *13*, 3257.

(22) Galvita, V. V.; Siddiqi, G.; Sun, P. P.; Bell, A. T. *J. Catal.* **2010**, *271*, 209-219.

(23) Siddiqi, G.; Sun, P. P.; Galvita, V. V.; Bell, A. T. *J. Catal.* **2010**, *274*, 200-206.

(24) Sun, P. P.; Siddiqi, G.; Vining, W. C.; Chi, M. F.; Bell, A. T. *J. Catal.* **2011**, *282*, 165-174.

(25) Virnovskaia, A.; Morandi, S.; Rytter, E.; Ghiotti, G.; Olsbye, U. *J. Phys. Chem. C* **2007**, *111*, 14732.

(26) Nagaraja, B. M.; Shin, C.-H.; Jung, K.-D. *Appl. Catal.-A* **2013**, *467*, 211.

(27) Yang, M.; Zhu, Y.; Zhou, X.; Sui, Z.; Chen, D. *ACS Catal.* **2012**, *2*, 1247.

(28) Cortright, R. D.; Dumesic, J. A. *J. Catal.* **1995**, *157*, 576.

(29) Natal-Santiago, M. A.; Podkolzin, S. G.; Cortright, R. D.;Dumesic, J. A. *Catal. Lett.* **1997**, *45*, 155.

(30) Shen, J.; Hill, J. M.; Watwe, R. M.; Spiewak, B. E.; Dumesic, J. A. J. *Phys. Chem. B* **1999**, *103*, 3923.

(31) Nykänen, L.; Honkala, K. *J. Phys. Chem. C* **2011**, *115*, 9578.

(32) Gao, J.; Zhao, H.; Yang, X.; Koel, B. E.; Podkolzin, S. G. *Angew. Chem. Int. Ed.* **2014**, *53*, 3641.

(33) Siri, G. J.; Ramallo-López, J. M.; Casella, M. L.; Fierro, J. L. G.; Requejo, F. G.; Ferretti, O. A. *Appl. Catal.-A* **2005**, *278*, 239.

(34) Fan, G.; Li, F.; Evans, D. G.; Duan, X. *Chem. Soc. Rev.* **2014**, *43*, 7040-7066.

(35) He, S.; An, Z.; Wei, M.; Evans, D. G.; Duan, X. *Chem. Comm.* **2013**, *49*, 5912-5920.

(36) Akporiaye, D.; Jensen, S. F.; Olsbye, U.; Rohr, F.; Rytter, E.; Ronnekleiv, M.; Spjelkavik, A. I. *Ind. Eng. Chem. Res.* **2001**, *40*, 4741–4748.

(37) Virnovskaia, A. Jørgensen, S. Hafizovic, J. Prytz, Ø. Kleimenov, E. Hävecker, M. Bluhm, H. Knop-Gericke, A. Schlögl, R. Olsbye, U. *Surf. Sci.* **2007**, *601*, 30–43.

(38) George, S. M. *Chem. Rev.* **2010,** *110*, 111–131.

(39) Detavernier, C.; Dendooven, J.; Sree, S. P.; Ludwig, K. F.; Martens, J. A. *Chem. Soc. Rev.* **2011**, *40*, 5242-5253.

(40) Lu, J.; Low, K.-B.; Lei, Y.; Libera, J. A.; Nicholls, A.; Stair, P. C.; Elam, J. W. *Nat. Commun.* **2013**, *5*, 3264.

(41) O'Neill, B. J.; Jackson, D. H. K.; Lee, J.; Canlas, C.; Stair, P. C.; Marshall, C. L.; Elam, J. W.; Kuech, T. F.; Dumesic, J. A.; Huber, G. W. *ACS Catal.* **2015**, *5*, 1804−1825.

Chapter 2. Materials and methods

In this chapter, the two catalyst synthesis methods used for this work, being LDH- and ALD-based catalyst synthesis, are further elaborated. Subsequently, the basic principles of X-ray absorption spectroscopy (XAS) theory and data analysis are explained.

2.1 Materials

2.1.1 LDH-based catalyst synthesis

Layered double hydroxides (LDHs) or hydrotalcite-like anionic clays (HTs) are a broad class of functional materials which originate from the natural mineral hydrotalcite ($Mg_6Al_2CO_3(OH)_{16}{\cdot}4(H_2O)$).[1] The name 'hydrotalcite' is derived from its similarities to the layered 'talc' structure and its high water content ('hydro'). Besides the natural occurrence of hydrotalcite minerals, HTs or LDHs are produced synthetically by co-precipitation of M^{2+} and M^{3+} metal cations into layered $[M_{1-a}{}^{2+}M_a{}^{3+}(OH)_2]^{a+}[A^{n-}]_{a/n}{}^{a-}.mH_2O$ structures (see experimental sections of coming chapters for more details).[2, 3] These crystalline materials consist of stacked cationic 2D $[M_{1-a}{}^{2+}M_a{}^{3+}(OH)_2]^{a+}$ sheets with charge-compensating anions $[A^{n-}]_{a/n}{}^{a-}$ and water in the interlayer galleries (Figure 2.1).[2] The fraction of trivalent metal cations can range from a = 0.2 to 0.5. Within these 2D sheets, $M^{2/3+}(OH)_6$ octahedrons are joined in a layered configuration by interconnection of the octahedron edges. This sheet structure is often called brucite-like due to its resemblance to the mineral $Mg(OH)_2$. The anionic species ($CO_3{}^{2-}$, OH^-) in the interlayer galleries are weakly bound to the cationic brucite-type $[M_{1-a}{}^{2+}M_a{}^{3+}(OH)_2]^{a+}$ sheets, making these materials suitable for anion-exchange

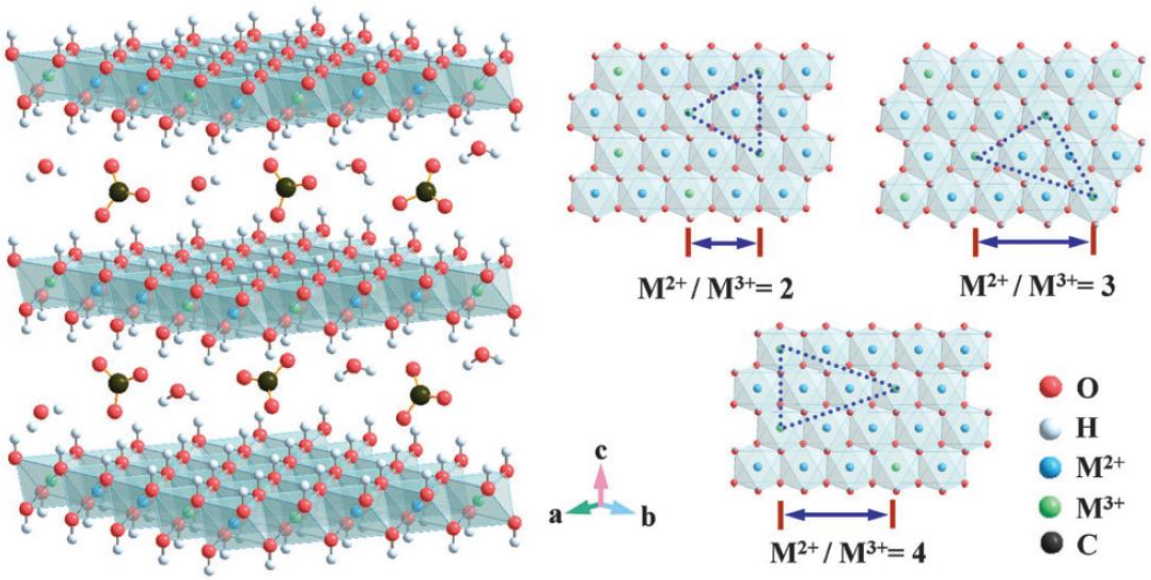

Figure 2.1: ideal LDH structure with different M^{2+}/M^{3+} ratios. 2D sheets of connected octahedrons are visualized. In between the 2D sheets, carbonates and water are present.[2]

reactions.[2] The layered structure of HTs has been the source of inspiration to denote these materials as layered double hydroxides or LDHs.

LDH materials are often used as precursor for more functionalized materials, such as supported metal catalysts. Several treatments can be performed on precipitated LDHs in order to generate high-performing catalysts: intercalation of anionic species, calcination and subsequent rehydration or reduction, exfoliation, etc..[2, 3] In this work, special emphasis is put on calcination and reduction treatment of LDH precursors as a means to synthesize well-dispersed supported bimetallic Pt-based nanoparticles.

Calcination treatment of LDH precursors can yield a variety of mixed metal oxides (MMOs) by controlled thermal decomposition of the layered hydrotalcite structure. For example, Bellotto et al. showed that Mg,Al-LDH calcination yields disordered spinel-type $Mg(Al)O_x$ mixed oxides, which contain octahedral Mg^{2+} and tetrahedral Al^{3+} cations (Figure 2.2).[4] After low temperature dehydration of Mg,Al-LDH, Al^{3+} cations rearrange from octahedral to tetrahedral sites by migrating from the 2D Mg,Al-hydroxide layers to the interlayer galleries (Figure 2.2.b). Around 400 °C, the interlayer anions decompose and complete dehydroxylation of the material is observed. This results in a collapse of the layers to form a 3D MgO-type structure consisting of a regular oxygen cubic closed packed network

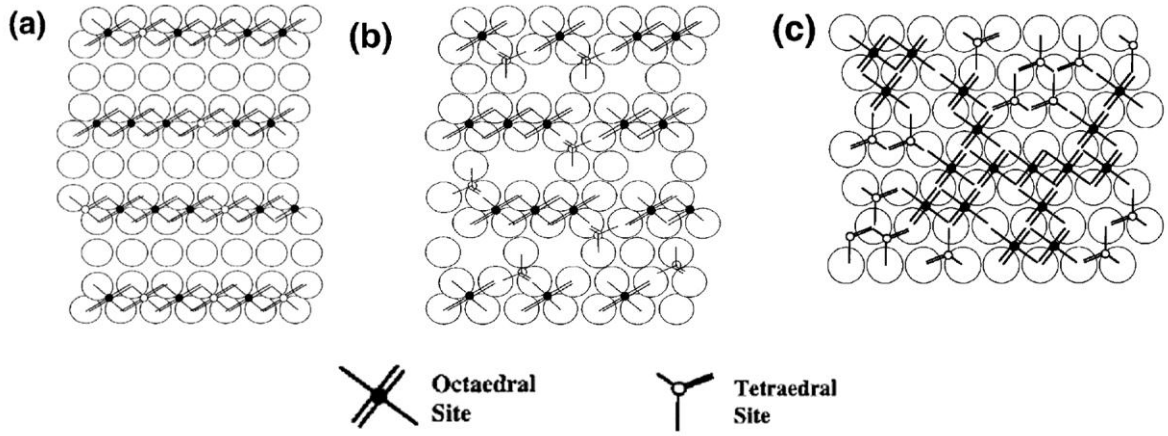

Figure 2.2: Structural model for (a) initial LDHs consisting of 2D sheets, (b) the dehydrated state, and (c) the disordered 3D network.

with a disordered distribution of Mg^{2+}/Al^{3+} cation at the interstices (Figure 2.2.c). As exemplified by the calcination of Mg,Al-LDHs, this topotactic transformation leads to the formation of MMOs owing to the uniform distribution of metal cations in the original LDH structure. The resulting MMOs can be considered as a metal oxide solid solution of the originally precipitated metal cations.[2, 4]

In order to obtain (bi)metal nanoparticles on MMO-based supports, reducible metal cations should be incorporated or deposited at some point of the catalyst formation process. During the last step of catalyst formation, namely H_2 reduction, these reducible metal cations will migrate and form clusters on the MMO support. In this work, different strategies are explored and investigated to obtain bimetallic Pt-M nanoparticles on Mg,Al-based MMOs (M = In, Ga):

Strategy A. Double impregnation

(1) Co-precipitation → Mg,Al-LDH synthesis;

(2) calcination → $Mg(Al)O_x$ MMOs;

(3) $Pt(acac)_2$ impregnation → $Pt(acac)_2/Mg(Al)O_x$;

(4) calcination → $Pt/Mg(Al)O_x$;

(5) M impregnation → $M/Pt/Mg(Al)O_x$;

(6) calcination → $M/Pt/Mg(Al)O_x$;

(7) H_2 reduction → $Pt\text{-}M/Mg(Al)O_x$.

Strategy B. Incorporation and impregnation

(1) Co-precipitation → Mg,Al,M-LDH synthesis;

(2) calcination → Mg(M)(Al)O_x MMOs;

(3) Pt(acac)$_2$ impregnation → Pt(acac)$_2$/Mg(M)(Al)O_x;

(4) calcination → Pt/Mg(M)(Al)O_x;

(5) H_2 reduction → Pt-M/Mg(M)(Al)O_x.

Strategy C. Doubly incorporation

(1) Co-precipitation → Mg,Al,Pt,M-LDH synthesis;

(2) calcination → Mg(Pt)(M)(Al)O_x MMOs;

(3) H_2 reduction → Pt-M/Mg(Pt)(M)(Al)O_x.

Strategy A is quite standard and therefore serves as a reference. Strategy B and C involve a reduced number of formation steps, making these protocols more cost efficient. In addition, it has been shown before that the performance of Pt-M/Mg(M)(Al)O_x catalysts (Strategy B) is better as compared to Pt-M/Mg(Al)O_x catalysts (Strategy A).[5] In order to explore the potential of these simplified LDH-based protocols, Strategies B (Chapters 3, 4, 5) and C (Chapter 6) are studied in this work.

2.1.2 **ALD-based catalyst synthesis**

In Figure 2.3, the principle of ALD is illustrated by the layer-by-layer deposition of Al_2O_3, a standard ALD process.[6] Initially, a hydroxylated SiO_2 surface is exposed to trimethylaluminium vapor (TMA, top left). The surface OH groups form active sites for reaction with the methyl groups of the TMA precursor. The TMA molecules react with these surface sites and chemisorb on the surface until all available OH sites are consumed. Thereafter, no further reaction takes place since the support surface is saturated (top right). Subsequently, the reaction chamber is purged with inert or evacuated to remove all remaining TMA precursor molecules and reaction products. These two parts, i.e. TMA reaction and

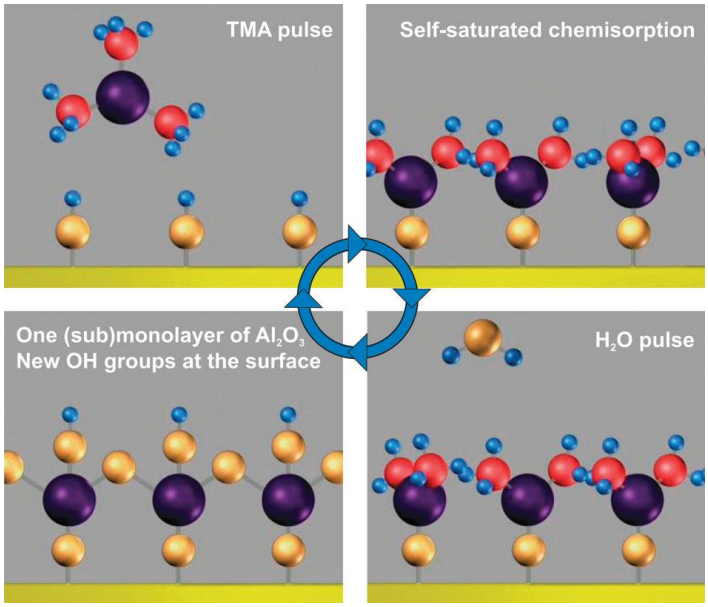

Figure 2.3: Principle of ALD illustrated with Al_2O_3 process using TMA and water (blue = H, red = C, violet = Al, yellow = O).[6]

pumping/purging, constitute the first half-cycle. In the next half-cycle, water vapor – the so-called reactant gas pulse – is injected in the ALD chamber, which hydrolyses the remaining methyl groups of the chemisorbed TMA molecules (bottom right). This terminates the deposited Al_2O_3 atomic layer with OH groups, creating novel reaction sites for the next TMA pulse in the coming ALD cycle (bottom left). The protocol can be repeated several times until the desired layer thickness is obtained.

In practice, the ideal representation of the ALD process in Figure 2.3 is difficult to achieve. For example, steric hindrance between precursor molecules can limit the surface site accessibility, resulting in only sub-monolayer quantities being deposited each cycle.[6] Site blockage by additional reactions between the ligands of chemisorbed precursor molecules and the surface can also cause sub-monolayer growth per cycle.[7, 8] Such non-idealities occur during the vast majority of the ALD processes – including Pt ALD. Another non-ideality, which is manifestly present during Pt ALD, concerns the limited reactivity between the Pt precursor and oxide support surfaces as compared to Pt surfaces.[8] Indeed, whereas on a Pt surface Pt ALD growth takes off instantaneously, metal oxide surfaces such as SiO_2, show a delay in growth due to difficult nucleation behavior. As mentioned in the introduction, this

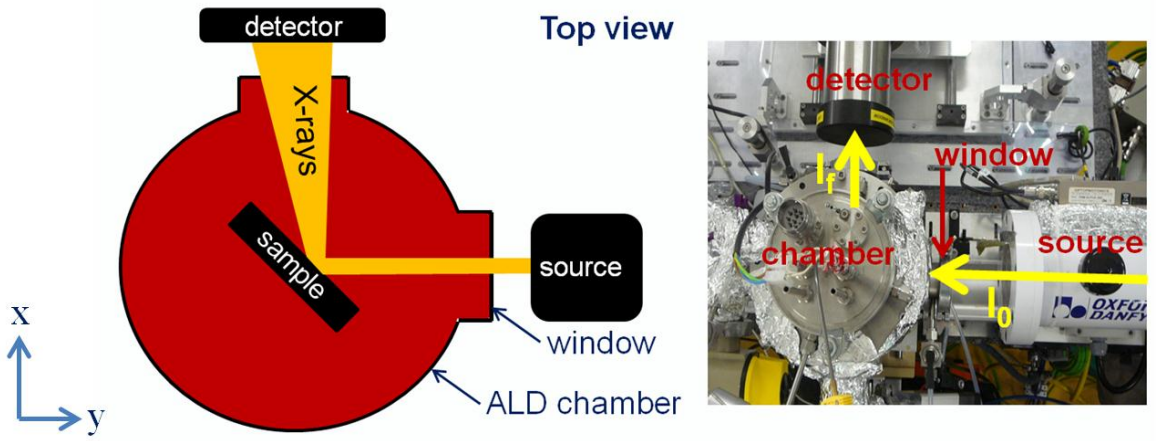

Figure 2.4: (left) schematic and (right) real top view of the ALD setup mounted at the SAMBA beamline. The incoming X-ray beam I_0 and the emerging fluorescent radiation I_f are indicated, as well as the windows, sample, chamber and detector.

yields opportunities for the deposition of Pt nanoparticles with sub-monolayer size control, and is the process under study in this work.[8-15]

In view of studying the nucleation behaviour of Pt particles on metal oxide surfaces in the first stages of ALD, a dedicated chamber for *in situ* combined ALD-XRF-XAS was developed by the CoCooN (Conformal Coating of Nanomaterials) research group at Ghent University. Figure 2.4 provides a top view of this ALD setup installed at the synchrotron beam line SAMBA of the SOLEIL synchrotron. This figure only intends to give a conceptual image of the ALD setup and the *in situ* XRF-XAS measurement mode at the synchrotron beam line (the full ALD procedure is described in detail in Chapter 7). During the Pt ALD process, the chamber is (1) filled by $MeCpPtMe_3$ precursor, (2) pumped, (3) filled with O_3 reactant gas and (4) evacuated again during a single cycle. *In situ* XRF and XAS measurements are performed in fluorescence mode (see Section 2.2.2). The incoming X-ray beam and emerging fluorescent radiation are indicated by their intensity I_0 and I_f. The sample is positioned inside the X-ray beam and is rotated 5° around the z-axis (here the z-axis comes out of the page) in order to maximize the X-ray fluorescence yield.

2.2 X-ray absorption spectroscopy

Since the discovery of X-rays by Wilhelm Conrad Röntgen in 1895, X-rays have become an indispensable tool for studying the structure of matter.[16] The past decades, both the theoretical understanding as well as the experimental possibilities have grown rapidly, making X-ray science a field of research in strong progress.[17] In the coming sections, the phenomenon of X-ray Absorption Spectroscopy (XAS) is explained and XAS data analysis is described.

2.2.1 X-ray interaction with matter

In general, X-rays interact with matter in two different ways.[18] First, X-rays can be absorbed by atomic electrons which are subsequently expelled from their core-level to unoccupied electron states above the Fermi level. The unoccupied states can be either valence orbitals (bound-bound transition) or the continuum (bound-unbound transition). If the core-electron is excited to the continuum, the excess photon energy is transferred to the so-called photoelectron as kinetic energy. This photoelectric effect was first explained by Albert Einstein ten years after the discovery of X-rays, for which he was rewarded with the Nobel prize in physics in 1921.[19] The second type of interaction is X-ray scattering, in which the original direction of the incident X-rays is altered upon collision with matter. This scattering process can occur with (Compton scattering) or without energy loss (Rayleigh scattering).

As depicted in Figure 2.5.a, the probability of X-ray absorption (~ cross-section) in the X-ray regime is orders of magnitude higher compared to the probabilities of Rayleigh and Compton scattering, implying that X-ray absorption is the dominant process for Pt atoms in this energy range.[20] In contrast to the continuous evolution of the scattering cross-sections, the X-ray absorption cross-section shows multiple discontinuities. These sudden jumps are termed edges and originate from X-ray absorption at different core-electron levels. At (above) the edge energy, the X-ray energy equals (exceeds) the energy difference between the initial and final electron states. When the X-ray energy is below the edge energy, no photoelectric

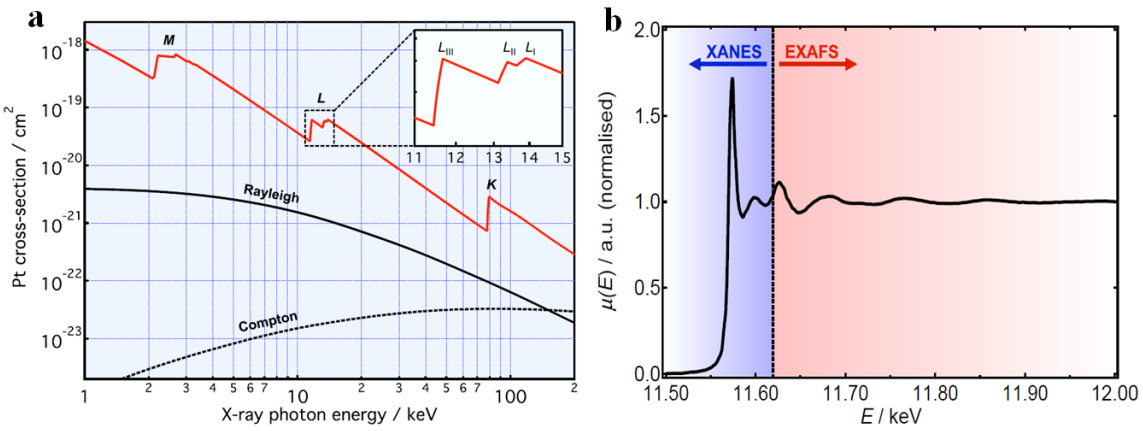

Figure 2.5: (a) Pt X-ray scattering (black) and X-ray absorption (solid, red) cross-section as a function of the X-ray photon energy. The inset shows the L_I, L_{II} and L_{III} edges ~ 12 keV; (b) Pt L_{III} edge XAS spectrum consisting of XANES and EXAFS regions.[20]

excitation and X-ray absorption can occur. The gradual increasing of the X-ray energy from below to above the edge energy therefore results in the observed sharply rising edge features.

The described edges are the basis of X-ray absorption spectroscopy (XAS).[18, 21, 22] A XAS spectrum is typically recorded by scanning over energies (E) below, around and above the edge energy (E_0). In essence, the X-ray absorption coefficient displays modulations which are superimposed on a non-oscillatory background. The background can be thought of as the absorption signal of an isolated atom which does not have neighbors in the near environment, and is therefore named 'atomic background'.[21, 22] In the presence of neighboring atoms, modulations arise from scattering of the excited photoelectron by these surrounding atoms and subsequent signal interference. The modulations contain detailed information on the atomic structure as well as on the electronic properties of the materials.[21] Two parts are distinguished in a XAS spectrum (Figure 2.5.b): the X-ray absorption near edge structure (XANES, $E - E_0 \leq 50$ eV) and extended X-ray absorption fine structure (EXAFS, $E - E_0 \geq 50$ eV) region.[22] XANES and EXAFS signals contain different types of information, namely electronic and structural respectively, and will be elaborated in the subsequent sections in more detail.

X-ray absorption spectroscopy has a number of strong advantages compared to other spectroscopies.[21] In contrast to other techniques, XAS provides both electronic and structural

information in a single experiment. Owing to the deep penetration of high energy X-rays (or hard X-rays), gas phase molecules do not induce strong X-ray absorption, allowing for *in situ* and *operando* experiments. The latter remains difficult during for example X-ray photoelectron spectroscopy (XPS) experiments, where electrons are being measured. In contrast to X-ray diffraction (XRD), no long range structural order is required to perform XAS experiments. This makes XAS a technique which can be applied to a broad range of systems, ranging from liquids to solids and catalysts. Furthermore, XAS is an atom specific technique, since the structural and electronic properties of each atomic type can be probed at its characteristic edge. The possibility of probing the structural and electronic properties of disordered nanomaterials at once under *in situ* conditions makes XAS the ideal technique to monitor the formation processes of catalysts.

2.2.2 XAS measurements and data reduction

The degree of X-ray absorption by matter can be quantified by means of the linear absorption coefficient μ. The attenuation of the intensity I_t of a light beam – here X-rays – through an infinitesimally thin slab of material (thickness dx) at a distance x from the sample surface is described by:

$$dI_t = -I_t(x)\mu dx$$

Upon integration over x the Lambert-Beer law is obtained, in which I_0 represents the incoming intensity:[23]

$$I_t(x) = I_0 e^{-\mu x}$$

Through recombination and by applying natural logarithms at both sides, the expression for the linear absorption coefficient for transmission experiments is found:

$$\mu = \frac{\ln\left(\frac{I_0}{I_t}\right)}{x}$$

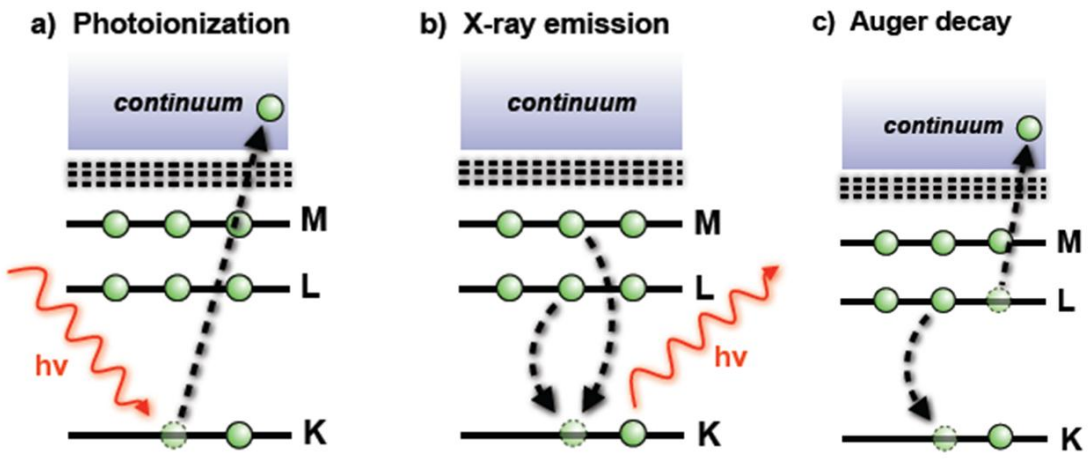

Figure 2.6: (a) the process of X-ray absorption through photo-ionization; and two de-excitation processes: (b) X-ray emission yielding fluorescent X-rays and (c) Auger decay yielding Auger electrons.[20]

The absorption coefficient, commonly represented as the total absorption μx, is thus proportional to $\ln(I_0/I_t)$.

The most preferred experimental configuration for recording an X-ray absorption spectrum is transmission mode. During transmission experiments, an optimal S/N ratio is obtained when $\mu x = 2.5$ (20) above the edge and/or the edge step $\Delta\mu(E)x = 1$.[24] In order to reach these criteria, the sample thickness x can be adjusted, and/or the sample can be diluted (e.g. by weakly-absorbing BN) while fixing the sample thickness. The sample has to be as uniform as possible and should not contain pinholes, as the latter is dramatic for the signal quality. The grain size of the catalyst powder is preferably small (75 – 100 μm), which can be achieved by sieving.

In addition to photoelectric absorption, two de-excitation processes allow for the measurement of the X-ray absorption in an indirect way (Figure 2.6). After X-ray absorption and excitation of the core-electron, a core-hole is created. The atom is then in an excited state and will relax by filling the core-hole with electrons from higher energy levels. The transition from high to low energy level is accompanied by an energy release in the form of fluorescent X-rays or by the emission of an Auger electron.[18, 20, 22] The former is dominant in the hard X-ray regime (> 2 keV), while the latter prevails at lower X-ray energies (< 2 keV). The detection of these X-rays or Auger electrons provides valuable alternatives for situations

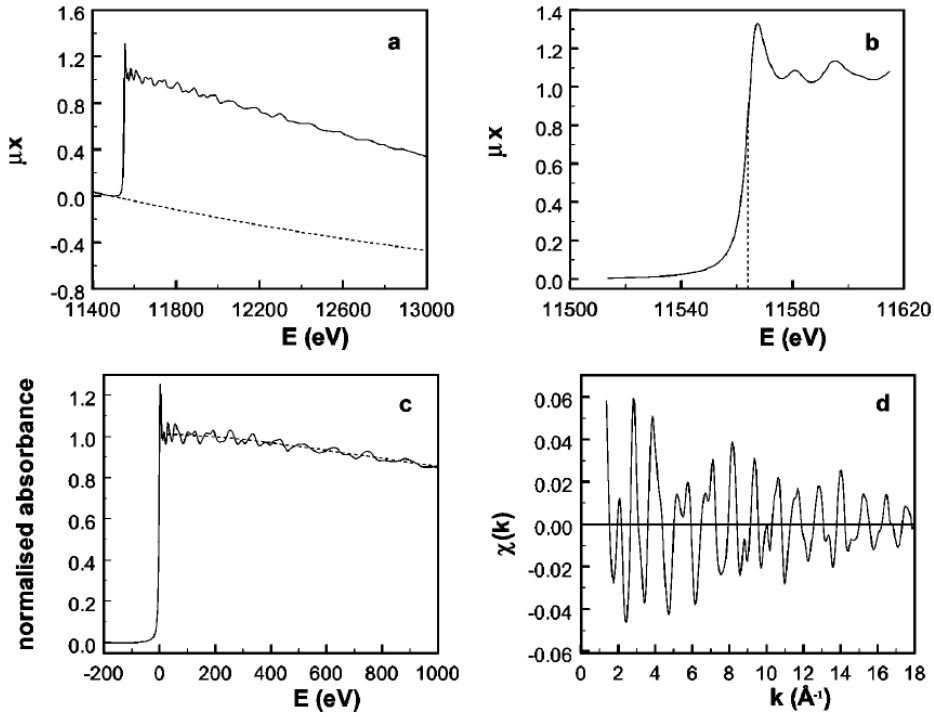

Figure 2.7: different steps of XAS data processing: (a) pre-edge background subtraction, (b) edge energy determination, (c) post-edge background removal and normalization, (d) isolation of the EXAFS signal and transformation to k-space.[21]

where the sample properties do not allow transmission measurements. The absorption coefficient is then – in contrast to transmission measurements – proportional to the fluorescence and electron yields I_f and I_e, respectively. During fluorescence measurements, the photon detector is directed perpendicular to the incoming X-ray beam – if possible – to minimize the detection of scattering peaks. Auger electrons should be measured *in vacuo*, making Auger detection unsuitable for performing *in situ* XAS experiments.

XAS spectra are typically recorded from a few hundred eV below the absorption edge up to 1000 eV above. After obtaining the absorption signal, data reduction is performed to ultimately yield XANES spectra and the EXAFS signal. According to Koningsberger et al. this should be done in five consecutive steps (Figure 2.7):[21]

1. *Pre-edge background subtraction*: a Victoreen $(V(E) = C_0 + C_1/E + C_2/E^2)$ is fitted through the pre-edge region, extrapolated and subtracted from the whole absorption spectrum $\mu(E)$.

2. *Edge energy E_0 determination*: the first maximum of the first derivative of the absorption spectrum is defined as the edge energy E_0.
3. *Fitting the atomic background μ_0*: a cubic spline function is fitted to the absorption signal in the range above the edge energy E_0. By means of a smoothing factor, the background is optimized and is chosen not to remove any oscillations of the data signal.
4. *Edge step normalization*: the total absorption signal $\mu(E)$ is divided by the value of $\mu_0(E_0 + 50)$, namely the atomic background around 50 eV above the edge energy E_0. This generates the normalized absorption spectrum.
5. *Isolation of the EXAFS signal $\chi(k)$*: the atomic background μ_0 is subtracted from the normalized absorption spectrum and subsequently the resulting $(\mu - \mu_0)$ is divided by the same atomic background, yielding $(\mu - \mu_0)/\mu_0 = \chi(E)$. Finally, the E-space EXAFS signal is transformed to k-space ($k = \sqrt{8\pi^2 m_e(E - E_0)/h^2}$), eventually resulting in the k-space EXAFS signal $\chi(k)$.

2.2.3 X-ray absorption near edge structure (XANES)

The rising edge in the absorption spectrum originates from bound-bound transitions from the core-electron level to electron orbitals above the Fermi level. According to the dipole selection rule, the orbital quantum number l can only change by $\Delta l = \pm 1$ during electron transitions (l = 1, 2, 3 for s, p and d electrons, respectively).[22, 26] Within this general picture, for example, Pt 2p electrons can undergo transitions to 5d states at Pt L edges.[21]

The intensity of the rising edge feature – called the white line intensity – is proportional to the number of transitions taking place. In turn, the number of transitions is proportional to the density of unoccupied final electron states (Pauli principle).[25] According to the Pauli exclusion principle, two electrons cannot be in the same quantum state. For this reason, the excitation of a core-electron to a filled orbital is forbidden, which decreases the

probability of such transition. When however the final state orbital is empty (high density of unoccupied states), core-electron transitions can occur. This gives rise to a high number of X-ray absorption events which yields strong white line intensities. If the final state is the valence band, the XANES white line is a sensitive tool for probing the density of unoccupied states and therefore the atom's oxidation state.[22, 26] For the particular case of Pt, the L_{III} edge XANES white line intensity monitors $2p_{3/2} \rightarrow 5d_{5/2}$ transitions and is known to exhibit linear proportionality with the Pt oxidation state.

As mentioned before, s → d transitions are forbidden according to the dipole selection rule. However, p-d hybridization of the X-ray absorber's orbitals through binding with other atoms can make s → d transitions partially allowed.[22, 26] This and other types of hybridization give rise to pre-edge peaks which yield information on the local geometry around the X-ray absorber. These pre-edge peaks are very sensitive to changes in the local environment around the absorber, as perturbed atomic configurations can change the hybridization and therefore inhibit partially allowed transitions.[27]

Besides white line and pre-edge features, the edge energy E_0 itself can serve as a tool for compound identification. Indeed, the position of the edge will shift to higher/lower values as a result of electron donation/acceptance, making it a useful probe for monitoring e.g. alloy formation or oxidation. Finally, the oscillations shortly above the edge are caused by multiple scattering (MS) of the photoelectron with the absorber's neighbors.[27] Since photoelectron scattering processes are the basis for EXAFS oscillations, MS will be discussed in the next section.

2.2.4 Extended X-ray absorption fine structure (EXAFS)

EXAFS phenomenon and equation

The EXAFS oscillations originate from a complex interplay between several quantum phenomena: photoelectric effect, wave-nature of electrons, scattering and

interference.[21] The linear absorption coefficient μ(E) is proportional to the transition probability of the photoelectric event. According to Fermi's Golden Rule, this transition probability is proportional to $|\langle\psi_f|\hat{e}\cdot\mathbf{r}|\psi_i\rangle|^2$, namely a squared transition matrix element (dipole approximation).[18, 22] Herein, $\hat{e}$ is the electric field polarization vector of the photon, while **r** corresponds to the coordinate vector of the electron. Together, $\hat{e}\cdot\mathbf{r}$ acts as an electric dipole operator on the initial $|\psi_i\rangle$ and final $|\psi_f\rangle$ electron wave functions. The initial core-electron state $|\psi_i\rangle$ is independent of the atomic environment around the X-ray absorbing atom, as electrons at higher energy levels shield the deeper lying core-electron. For this reason, the final electron state $|\psi_f\rangle$ is the most important factor, inducing the oscillations in the X-ray absorption coefficient.

In the EXAFS regime, core-electrons are excited to the continuum (bound-unbound transition) through photo-ionization of the X-ray absorber. From a quantum-mechanical point of view, the excited photoelectron behaves as a spherical wave which propagates radially outward of the emitting X-ray absorber. The excess X-ray energy, which is not consumed for expelling the core-electron, is transformed into kinetic energy of the generated propagating electron wave. The De Broglie wavelength λ_{el} of this electron wave is therefore a function of the X-ray energy hν (E_0 = edge energy, $E_{kin} = h\nu - E_0 = p^2/2m_e$, $\lambda_{el}(\nu) = h/p(\nu)$). The outgoing photoelectron is subsequently scattered by the X-ray absorber's neighbors, yielding electron waves, which are backscattered towards the original X-ray absorbing position. The final electron state $|\psi_f\rangle$ therefore consists of a superposition of the outgoing and backscattered electron waves, which interfere depending on the X-ray energy.[18, 22] As the photoelectron path length is constant during a XAS measurement, alternating constructive and destructive interference occurs upon increase of the X-ray energy, yielding the oscillations as fine structure above the absorption edge.[21] The amplitude and frequency of these modulations depends on the elemental type, number and disorder of the absorber's neighbors as well as on the interatomic distances between scatterer-absorber pairs.[21, 22]

The X-ray absorption coefficient of a free atom $\mu_0(E)$ does not exhibit an oscillatory fine structure $\chi(E)$ because of the absence of backscattered electron waves and its concomitant interference effects. For this reason, the atomic background can be used as a (hypothetical) background signal for extracting the fine structural modulations $\chi(E)$ from the original absorption signal $\mu(E)$: $\mu(E) = \mu_0(E)(1 + \chi(E))$.[21] As discussed before, the EXAFS signal is typically represented in 'k-space' as a function of the photoelectron wavenumber k instead of in the X-ray energy 'E-space' ($k = 2\pi/\lambda_{el}$, $k = \sqrt{8\pi^2 m_e(E - E_0)/h^2}$, $E = h\nu$). The total $\chi(E)$ signal is a superposition of all the separate backscattered photoelectron path contributions. These paths can be either single scattering (SS) or multiple scattering (MS) paths. Multiple scattering paths are dominant at low k-values ($k < 3$ Å^{-1}) – in the so-called 'XANES multiple scattering region' – and involve more than one neighboring scattering atom, e.g. two for double scattering.[21, 22] Single scattering paths are always located in higher k-regions ($k > 3$ Å^{-1}) and involve only backscattering by a single X-ray absorber neighbor.

Several theories have been reported to describe the phenomenon of EXAFS in a quantitative way. In the most simplistic description, the actual spherical electron wave is approximated by a plane-wave to reduce the mathematical complexity.[28] This plane wave approximation was originally only applicable for single scattering paths ($k > 3$ Å^{-1}) but was reformulated later by Rehr et al. to also correctly describe multiple scattering paths (by incorporating $F_j^{eff}(k)$ instead of $f_j(k)$, see below).[29] According to this widely used – reformulated – plane wave description, the EXAFS signal $\chi(k)$ is the sum over all contributions $\chi_j(k)$, i.e. photoelectron scattering paths j:[30]

$$\chi(k) = \sum_{j=1}^{path} \chi_j(k) = \sum_{j=1}^{path} A_j(k) \cdot \sin \Phi_j(k)$$

$$= \sum_{j=1}^{path} \frac{S_0^2}{kR_j^2} \cdot N_j F_j^{eff}(k) \cdot \sin\left(2kR_j + \delta_j(k)\right) \cdot e^{-2\sigma_j^2 k^2} e^{-2R_j/\lambda(k)}$$

The latter equation is called the EXAFS equation. Each EXAFS contribution, originating from different photoelectron scattering paths around the absorber, consists of an amplitude part $A_j(k)$ and a sine function $\sin \Phi_j(k)$, both describing the actual oscillatory evolution of the EXAFS fine structure. The more elaborated version of the EXAFS equation contains several factors:[21]

1. S_0^2 is the amplitude reduction factor, which accounts for the energy loss of the photoelectron caused by many-body effects (shake-up/shake-off).
2. R_j represents the photoelectron half-path length of path j and equals to the average interatomic distance between the scatterer and the X-ray absorber for SS paths.
3. N_j is the number of equivalent scattering paths j, and represents the coordination number for SS paths.
4. $F_j^{eff}(k)$ is the effective photoelectron backscattering amplitude function of the scatterers in path j.
5. $\delta_j(k)$ is the phase factor which accounts for the effect of the absorber and scatterer atomic potentials.
6. σ_j^2 is the squared Debye-Waller (DW) bond length disorder factor, which corresponds to the average squared deviation in interatomic absorber-scatterer bond length relative to the average interatomic distance R_j, i.e. $\langle (r_j - R_j)^2 \rangle$, for SS paths.
7. $\lambda(k)$ is the energy dependent mean-free path distance of the photoelectron and accounts for the finite lifetime of the excited state.

The strength of photoelectron backscattering by scatterers in path j – and thereby the signal amplitude of $\chi_j(k)$ – is proportional to N_j and the effective backscattering amplitude $F_j^{eff}(k)$. In contrast to the latter two factors, S_0^2 and $1/kR_j^2$ as well as the exponentials $e^{-2\sigma_j^2 k^2}$ and $e^{-2R_j/\lambda(k)}$ dampen the amplified sine oscillations generated by the product $N_j F_j^{eff}(k) \cdot \sin\left(2kR_j + \delta_j(k)\right)$. Since $\chi_j(k) \sim 1/R_j^2$, the contributions of the higher materials shells around the X-ray absorber are increasingly dampened with increasing absorber-scatterer interatomic distance. From the $\sin\left(2kR_j + \delta_j(k)\right)$ function in the EXAFS equation, it is clear

that with increasing half-path length R_j the frequency of the sine functions in k-space increases. Sine contributions which have short wavelengths therefore originate from higher shells, i.e. further away from the X-ray absorber, and vice versa.

The above described EXAFS equation assumes a Gaussian distribution of the absorber-scatterer bond lengths around the average value of R_j. In this case, such symmetric pair distribution function is the result of the oscillation of atoms in a harmonic potential. This approximation yields acceptable structural parameters (R_j, N_j, σ_j) after EXAFS modeling. Generally, the data quality and range do not allow for more detailed modeling (see below), making the assumption of symmetric pair distribution functions mandatory. However, sometimes asymmetric pair distribution functions should be used – when data quality allows – for more detailed structural studies. For example, thermal expansion can only be studied when anharmonic potentials are considered.[31] Likewise, for nanocatalysts, more anharmonicity is expected for surface atoms compared to bulk.[32] For this reason, a third cumulant $\sigma^{(3)} = \langle (r_j - R_j)^3 \rangle$ can be included in the argument of the sine function, yielding $\sin(2kR_j + \delta_j(k) - 4/3\,\sigma^{(3)}k^3)$. The third cumulant quantifies the skewness of the pair distribution function and is therefore a measure for the asymmetry in the interatomic absorber-scatterer bond length. The implementation of the third cumulant yields more correct estimations for R_j, since a non-zero value for $\sigma^{(3)}$ corrects the perturbed value of R_j under the original assumption of harmonic potentials. The full mathematical derivation of the EXAFS equation which includes the third cumulant is not the focus of this work and can be found elsewhere.[32]

The origin of the EXAFS oscillations can be found in the backscattering of photoelectrons by the X-ray absorber's neighbors. As denoted before, the function which quantifies the intensity of photoelectron backscattering is the effective backscattering amplitude $F_j^{eff}(k)$. Scattering is a resonant process, implying that photoelectron backscattering occurs when the kinetic energy of the photoelectron equals the kinetic energy of the bound electrons in the neighbor's orbitals.[21] This suggests that the amplitude of photoelectron backscattering function $F_j^{eff}(k)$ depends on the electronic structure of the

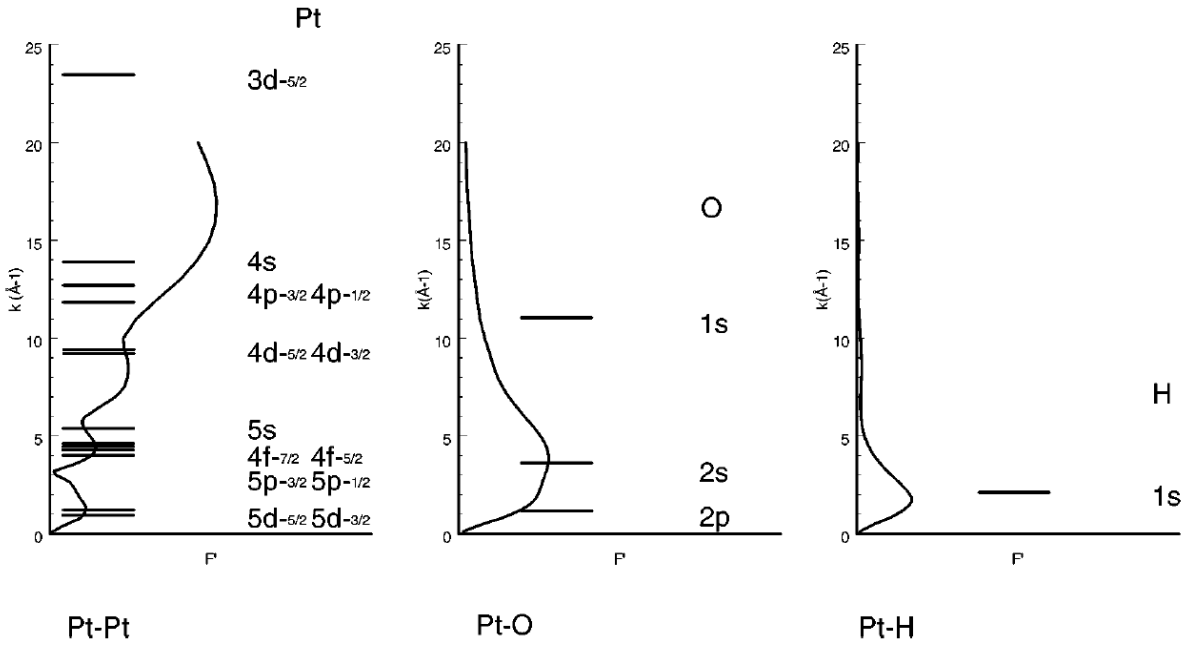

Figure 2.8: Pt-Pt, Pt-O and Pt-H backscattering amplitudes as a function of k in the EXAFS region. $E_{binding}$ is converted to k-space according to the relation $\mathbf{k} = \sqrt{\mathbf{8\pi^2 m_e (E_{binding})/h^2}}$.[21]

neighboring atoms, and is therefore element specific. Indeed, in Figure 2.8 the backscattering amplitude functions of Pt-H, Pt-O and Pt-Pt are shown together with the orbital energies of some bound electrons for the respective atoms.[21] The backscattering amplitude is high when the orbital energy equals the photoelectron energy (here in units of k), confirming the resonant and element specific nature of the backscattering functions.

As a consequence of their electronic structure, light elements (H, O) generally backscatter photoelectrons at lower photoelectron energies – in 'lower k-regions' –compared to heavy elements (such as Pt). For this reason, the k-space location of the EXAFS oscillations contains information on the nature of the atomic species which surround the X-ray absorber. The efficient exploitation of this information is of crucial importance for understanding processes which involve multiple types of elements, such as catalyst formation processes. As described below, wavelet transformed XAS is a tool to directly visualize both the nature and the location of the X-ray absorber's neighbors.

Fourier- and wavelet transformed XAS analysis

In 1971, Sayers et al. evidenced that Fourier transformation of the original k-space EXAFS signal with respect to k yields a radial structure function around the X-ray absorber in R-space.[33] The spectral analysis performed by Fourier transformation therefore elegantly provides access to the structural parameters of interest (R_j, N_j, σ_j). Fourier transformation of the k-space EXAFS signal is defined by:[21]

$$\chi(R) = \frac{1}{\sqrt{2\pi}} \int_{k_{min}}^{k_{max}} k^z \chi(k) e^{i2kR} dk$$

The k-space EXAFS signal can be weighted by k^z (z = 1, 2, 3) in order to better distinguish between light (low k-values) and heavy (high k-values) scatterers. The resulting $\chi(R)$ signal is a complex function, the modulus of which corresponds to the radial distribution function around the X-ray absorber. However, without phase correction the k-weighted Fourier transformed EXAFS magnitude/modulus $|\chi(R)|$ displays the shells of the X-ray absorber's neighbors circa 0.2 to 0.5 Å below their actual values owing to the energy dependence of the phase factor $\delta_j(k)$ in the EXAFS signal.[21]

In Figure 2.9.a and Figure 2.9.b, two hypothetical EXAFS signals are displayed in k-space.[34] Signal 1 consists of two contributions at different k-space locations which are superimposed to yield a single signal. Signal 2 contains the same contributions but the latter are now located in the same k-space region. Superposition of the two signal contributions therefore leads to interference. After Fourier transformation of signal 1 and 2, identical Fourier transformed EXAFS moduli are obtained in R-space (Figure 2.9.c). This exemplifies that the k-space information on the nature of the atomic species causing the R-space peaks cannot be directly retrieved from the Fourier transformed EXAFS modulus.[34-39] Evidently, the real and imaginary Fourier transformed EXAFS signals contain information on the k-space location yielding the R-space peaks, but their analysis is often complex and used by experts only.

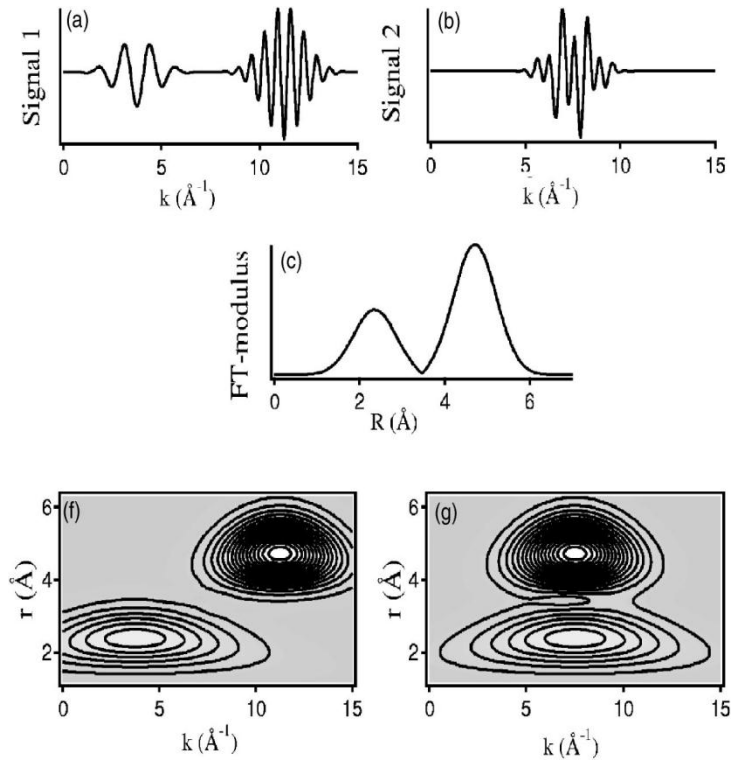

Figure 2.9: (a, b) two k-space EXAFS model signals, (c) FT EXAFS modulus displaying the same profile for (a) and (b), (f) WT XAS modulus of Signal 1, (g) WT XAS modulus of Signal 2.

A more accessible analysis method which can exploit both k- as well as R-space information simultaneously is wavelet transformed XAS. Instead of using an infinite sine-type function (e^{i2kR}) as in Fourier transformation, finite wave packets – wavelets – are used for wavelet transformation. Wavelets are square integrable functions and have a specific location in k-space. For the latter reason, their k-space location can be altered in addition to their frequency, yielding simultaneous k- and R-space resolution when the wavelet sweeps over k-space. Indeed, the k-space location of each R-space EXAFS peak can be directly resolved in the wavelet transformed XAS contour plots of Figure 2.9.f and Figure 2.9.g.[34] Mathematically, wavelet transformation of the k-space $\chi(k)$ signal is defined as follows:[34]

$$\chi(c,d) = \frac{1}{c}\int_{k_{min}}^{k_{max}} k^z \chi(k)\overline{\psi}\left(\frac{k-c}{d}\right) dk$$

Herein, $\overline{\psi}$ denotes the complex conjugate of the so-called mother wavelet ψ. The parameter c shifts the wavelet over k-space, while the scale parameter d changes the oscillatory frequency of the wavelet.[40] The latter two operations respectively yield k- and R-space resolution in

wavelet transformed XAS space, yielding multi-resolution. The wavelet-type used in this work is the complex continuous Cauchy wavelet, which can be described as follows:[36]

$$\psi(k) = \left(\frac{i}{k + i}\right)^{n_c+1}$$

with i the imaginary number ($\sqrt{-1}$) and n_c the Cauchy order ($n_c > 1$). Upon reduction of the Cauchy order n_c, the wavelet width decreases. Narrow (wide) wavelets provide more (less) k-space resolution, but less (more) R-space resolution. Decreasing the Cauchy order therefore increases k-space resolution at the expense of R-space resolution. The balance between the required k- and R-space resolution – Δk and ΔR respectively – should be maintained, and is described mathematically by a constraint analogous to the Heisenberg inequality: $\Delta k \cdot \Delta R \geq ¼$. Further details on Cauchy wavelet transformation can be found elsewhere.[36]

EXAFS modeling

The ultimate goal of EXAFS analysis is to obtain quantitative structural information. More precisely, numerical estimates of the coordination numbers N_j, interatomic distances R_j and Debye-Waller disorder factors σ_j can be generated by modeling the EXAFS equation to the experimental EXAFS signal. The EXAFS equation contains several parameters, namely E_0, R_j, N_j, σ_j, S_0, $F_j^{eff}(k)$, $\delta_j(k)$ and $\lambda(k)$. The edge energy E_0 is contained within the k-variable as $k = \sqrt{8\pi^2 m_e(E - E_0)/h^2}$. The first five parameters are estimated by minimization of the objective function during EXAFS modeling (see below). The three k-dependent parameters ($F_j^{eff}(k)$, $\delta_j(k)$, $\lambda(k)$) are obtained independently prior to modeling either by experimental extraction from reference materials, or by theoretical ab initio computation. Over the past years, the ab initio FEFF code (from $F_j^{eff}(k)$ ~ Feff) has made major steps forward and now allows to exclude the need for experimentally obtained k-dependent parameters.[41-43]

EXAFS data modeling can be performed in k-space, R-space as well as in inverse Fourier transformed or Fourier filtered q-space. R-space is preferred above k-space and q-

space EXAFS modeling. Modeling in k-space is only advisable when the full R-range is selected for modeling, while q-space EXAFS modeling suffers from truncation effects, which accompany the inverse Fourier transformation of the R-space signal portion. Another difficulty for q-space EXAFS modeling is overlapping shells in R-space, making shell-by-shell inverse Fourier transformation difficult and q-space EXAFS modeling erroneous.

Prior to R-space EXAFS modeling, the k-space signal is prepared to yield the highest possible signal quality in R-space. First, the original k-space signal is multiplied by a rectangular windowing function to select the data which are kept for further analysis. The low k-region ($k < 3$ Å^{-1}) is eliminated since it contains XANES contributions. In addition, the windowing function cuts the noisy high k-region signal portion of the k-space EXAFS signal. Truncation by a purely rectangular shaped windowing function will yield truncation ripples in the R-space signal. For this reason, smoothly edged windowing functions are used to prevent such truncation ripples. In addition to signal windowing, an optimal k-weight for the k-space EXAFS signal should be selected such that the signal amplitude is concentrated in the middle of the windowing function and is dampened at the window edges.

Once Fourier transformation is performed, a structural model should be selected to fit the experimental R-space EXAFS signal $|\chi(R)|$. In the vast majority of cases, this is not an evident task because of the presence of two or more interfering shells at similar R-space locations. These interference effects might not be directly separable: two overlapping contributions can for example give rise to a sharp minimum in the middle of a $|\chi(R)|$ peak, creating two apparently separated peaks at differing radial distances (Figure 2.10.a). When the situation is further complicated by the presence of more single and multiple scattering shells, model selection based on visual inspection of the $|\chi(R)|$ signal becomes very challenging. Inverse Fourier transformation of the R-space signal is not always helpful since the apparent $|\chi(R)|$ peaks do not always correspond to true material shells. Selection of the proper R-range for inverse Fourier transformation is therefore a difficult task. However, wavelet transformed XAS can provide the way out for selecting the correct EXAFS model. By systematically

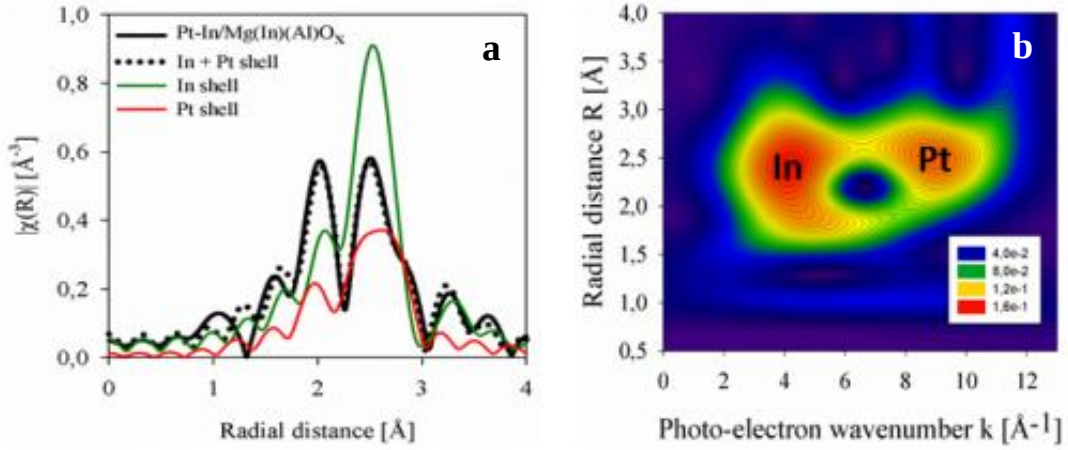

Figure 2.10: (a) FT EXAFS modulus (black, full) displaying double peak feature due to overlapping In (green) and Pt (red) shells, (b) WT XAS contour plot which separates both In and Pt in a simple way. The gained knowledge from WT XAS allows for modeling the FT EXAFS signal in a successful way (black, dotted) in (a).

providing simultaneous k- and R-space resolution, different shell contributions can be easily separated in k- and R-space (Figure 2.10.b). Evidently, this triggers more rapid selection of a structural model as the different types of elements as well as their location can be obtained from one single contour plot.

Once model selection is established, the k-dependent parameters discussed above can be calculated from first principles by using the FEFF code, incorporated as part of the Artemis software, which is included in the IFEFFIT package.[41-43] In the FEFF routine, all possible photoelectron backscattering paths are calculated based on an input structure supplied as a list of (x,y,z)-coordinates around the X-ray absorber. Subsequently, the most intense paths are selected for inclusion in the EXAFS model based on their overall amplitude to the EXAFS signal.[41] For each selected photoelectron backscattering path, the backscattering amplitude function, phase shift and photoelectron mean-free path are then calculated.[30]

During R-space EXAFS modeling, the IFEFFIT program fits the structural model to the experimental EXAFS signal by minimizing the so-called chi-squared objective function:[42-43]

$$\chi^2 = \frac{N_{idp}}{N_{pts}\epsilon^2}\sum_{i=1}^{N_{pts}}\left[\mathrm{Re}\left(\chi_e(R_i) - \chi_t(R_i)\right)^2 + \mathrm{Im}\left(\chi_e(R_i) - \chi_t(R_i)\right)^2\right]$$

where N_{pts} is the number of data points used for data fitting, ϵ is the measurement uncertainty, and $\chi_e(R_i)$ and $\chi_t(R_i)$ are the complex Fourier transformed experimental and theoretical $\chi(k)$ signals, respectively. It should be noted that this chi-squared objective function χ^2 should not be confused with the EXAFS fine structure $\chi(E)$, $\chi(k)$ or $\chi(R)$. ϵ is calculated based on the average Fourier transformed EXAFS signal between R = 15 – 25 Å. At these radial distances, no significant signal is expected above noise level. For this reason, ϵ is used as quantification of the measurement uncertainty. N_{idp} represents the number of independent points and is a measure for the information content of the data. This number can be calculated based on the principles of information theory:[44]

$$N_{idp} = \frac{2\Delta k \Delta R}{\pi} + 1$$

in which Δk and ΔR are the employed k- and R-space fitting ranges, respectively. It is shown – by using Bayesian methods – that the true information content of an EXAFS signal is $2/3 \cdot N_{idp}$ or less.[45] The number of fitting parameters should therefore ideally remain below this limit. In practice, N_{idp} amounts to ~ 8 – 10, implying that the number of photoelectron scattering paths should remain low, as each path can potentially require 4 or more fitting parameters (E_0, R_j, N_j, σ_j, S_0). For this reason, the total number of parameters used during EXAFS modeling is reduced by relating different parameters in a physically acceptable way. For example, in some cases the $\boldsymbol{m}$ half-path length parameters R_j (j = 1 – $\boldsymbol{m}$) can be replaced by a single isotropic expansion coefficient α by using the following formulation: $R_j = \alpha \cdot R_{eff}$, in which R_{eff} is the (known) half-path length in the EXAFS model. Evidently, other assumptions can also be made in order to reduce the number of implemented fitting parameters.

In addition to the chi-squared function χ^2, IFEFFIT also provides a related statistical parameter being reduced chi-square $\chi_\nu^2 = \chi^2/\boldsymbol{\nu}$, in which $\boldsymbol{\nu} = N_{idp} - N_{par}$, and N_{par} is the number of parameters used during the fit.[43, 46] This reduced chi-square is more suitable for model discrimination within the same data set as it includes the number of parameters of the

EXAFS model. A lower χ_ν^2 value for Model 1 relative to Model 2 implies that the fit significantly improves when Model 1 is used, independent of the number of used parameters. In theory, a good fit should yield χ_ν^2-values around 1 if ϵ is a random fluctuation. In practice, the obtained χ_ν^2-values are much higher, namely from 10 to 100's.[43] The reason for these high values can be found in the poor theoretical description of the experimental EXAFS signal by the FEFF code, as well as the nature of ϵ which is a poor estimate for the measurement uncertainty.

χ^2 and χ_ν^2 chi-squared values are only suited for comparison between different fits. Based on their absolute value it is difficult to distinguish between truly bad fits, large theoretical errors or noisy data. For this reason, a more absolute measure for the goodness of fit is provided by the R-factor:[46]

$$\mathrm{R-factor} = \frac{\sum_{i=1}^{N_{pts}} \left[\mathrm{Re}\left(\chi_e(R_i) - \chi_t(R_i)\right)^2 + \mathrm{Im}\left(\chi_e(R_i) - \chi_t(R_i)\right)^2\right]}{\sum_{i=1}^{N_{pts}} \left[\mathrm{Re}\left(\chi_e(R_i)\right)^2 + \mathrm{Im}\left(\chi_e(R_i)\right)^2\right]}$$

representing the fractional sum of squared residuals of misfit. Good fits are common to have R-factors below 0.02 and χ_ν^2 above 10.[46]

The structural parameters estimated during EXAFS modeling are often strongly correlated because some parameters affect the Fourier transformed EXAFS signal in a similar way. For example, a decrease in S_0 results in an overall decrease of the $|\chi(R)|$ signal amplitude, which can equally originate from decreasing coordination numbers N_j or increasing Debye-Waller factors σ_j. For this reason, N_j, σ_j and S_0 have high binary correlation coefficients during EXAFS modeling. The same is true for R_j and E_0. Ideally, the binary correlation coefficients of all parameters should be below 0.85 to yield meaningful estimates. More literature on the calculation of the binary correlation coefficients and the parameter uncertainties in IFEFFIT can be found elsewhere.[46]

After modeling the experimental Fourier transformed EXAFS signal, the structural parameters N_j, σ_j and R_j are obtained. Based on the near neighbor coordination numbers N_j,

calculations can be performed to obtain the shape and size of nanoparticles.[47-49] The first and second nearest coordination number N_1 and N_2 are good probes for the cluster size and are rather independent of the cluster shape. In contrast, the higher shell coordination numbers are a tool to capture the shape of the nanoparticles.[49] In Chapter 7, the topic of N_j-based cluster size and shape determination of Pt particles is discussed in great detail. It should be noted that such detailed characterization is complex and requires extreme caution.

Besides X-ray absorption spectroscopy, other conventional catalyst characterization techniques are used on a basic level to complement the XAS results: X-ray diffraction (XRD), transmission electron microscopy (TEM), temporal analysis of products (TAP), nitrogen physisorption and inductively coupled plasma atomic emission spectrometry (ICP-AES). More information on XRD and TEM can be found in 'Spectroscopy in Catalysis: An Introduction' (Chapter 6.2 (XRD) and Chapter 7.2.1 (TEM)).[50] A clear explanation of N_2 physisorption and ICP-AES is available in 'Handbook of Heterogeneous Catalysis' Chapter 3.[51] Furthermore, an insightful overview of TAP is given in reference 52. In general, details on the experiments can be found in the experimental sections of the subsequent chapters and in the appendices.

2.3 References

(1) Sels, B. F.; De Vos, D. E.; Jacobs, P. A. *Catal. Rev.* **2001**, *43*, 443.

(2) Fan, G.; Li, F.; Evans, D. G.; Duan, X. *Chem. Soc. Rev.* **2014**, *43*, 7040.

(3) He, S.; An, Z.; Wei, M.; Evans, D. G.; Duan, X. *Chem. Comm.* **2013**, *49*, 5912.

(4) Bellotto, M.; Rebours, B.; Clause, O.; Lynch, J.; Bazin, D.; Elkaïm, E. *J. Phys. Chem.* **1996**, *100*, 8535.

(5) Siddiqi, G.; Sun, P. P.; Galvita, V. V.; Bell, A. T. *J. Catal.* **2010**, *274*, 200.

(6) Detavernier, C.; Dendooven, J.; Sree, S. P.; Ludwig, K. F.; Martens, J. A. *Chem. Soc. Rev.* **2011**, *40*, 5242.

(7) Mackus, A. J. M.; Leick, N.; Baker, L.; Kessels, W. M. M. *Chem. Mater.* **2012**, *24*, 1752.

(8) Mackus, A. J. M.; Verheijen, M. A.; Leick, N.; Bol, A. A.; Kessels, W. M. M. *Chem. Mater*. **2013**, *25*, 1905.

(9) George, S. M. *Chem. Rev*. **2010,** *110*, 111.

(10) Baker, L.; Cavanagh, A. S.; Seghete, D.; George, S. M.; Mackus, A. J. M.; Kessels, W. M. M.; Liu, Z. Y.; Wagner, F. T. *J. Appl. Phys.* **2011**, *109*, 084333.

(11) Lee, H. B. R.; Bent, S. F. *Chem. Mat.* **2012**, *24*, 279.

(12) Lee, H. B. R.; Mullings, M. N.; Jiang, X. R.; Clemens, B. M.; Bent, S. F. *Chem. Mat.* **2012**, *24*, 4051.

(13) Enterkin, J. A.; Setthapun, W.; Elam, J. W.; Christensen, S. T.; Rabuffetti, F. A.; Marks, L. D.; Stair, P. C.; Poeppelmeier, K. R.; Marshall, C. L. *ACS Catal.* **2011**, *1*, 629.

(14) Li, J. H.; Liang, X. H.; King, D. M.; Jiang, Y. B.; Weimer, A. W. *Appl. Catal. B-Environ.* **2010**, *97*, 220.

(15) King, J. S.; Wittstock, A.; Biener, J.; Kucheyev, S. O.; Wang, Y. M.; Baumann, T. F.; Giri, S. K.; Hamza, A. V.; Baeumer, M.; Bent, S. F. *Nano Lett.* **2008**, *8*, 2405.

(16) Röntgen, W. C. *Nature* **1896**, *53*, 274.

(17) Beale, A. M.; Jacques, S. D. M.; Weckhuysen, B. M. *Chem. Soc. Rev.* **2010**, *39*, 4656.

(18) Als-Nielsen, J.; McMorrow, D. *Elements of modern X-ray physics* **2001**, John Wiley & Sons, Ltd.

(19) Einstein, A. *Ann. Phys-Berlin* **1905**, *17*, 132.

(20) Van Der Veen, R. M. *Ultrafast X-ray and Optical Spectroscopy of Binuclear Molecular Complexes.* **2010**, Thèse EPFL, 4905.

(21) Koningsberger, D. C.; Mojet, B. L.; van Dorssen, G. E.; Ramaker, D. E. *Top. Catal.* **2000**, *10*, 143.

(22) Koningsberger, D. C.; Prins, R. *X-ray absorption: principles, applications, techniques of EXAFS, SEXAFS, and XANES.* **1988**, Wiley-Interscience.

(23) Beer, A. *Ann. Phys-Berlin* **1852**, *162*, 78.

(24) Bunker, G. *Introduction to XAFS: A Practical Guide to X-ray Absorption Fine Structure Spectroscopy.* **2010**, Cambridge University Press.

(25) Basdevant, J.-L.; Dalibard, J. *Quantum Mechanics.* **2005**, Springer.

(26) de Groot, F. M. F. J. Phys.: Conference Series 2009, 190, 012004.

(27) Ankudinov, A. L.; Ravel, B.; Rehr, J. J.; Conradson, S. D. *Phys Rev. B* **1998**, *58*, 7565.

(28) Lee, P. A.; Pendry, J. B. *Phys. Rev. B* **1975**, *11*, 2795.

(29) Rehr, J. J.; Albers, R. C. *Phys. Rev. B* **1990**, *41*, 8139.

(30) Rehr, J. J.; Albers, R. C. *Rev. Mod. Phys.* **2000**, *72*, 621.

(31) Frenkel, A. I.; Rehr, J. J. *Phys. Rev. B* **1993**, *48*, 585.

(32) Bus, E.; Miller, J. T.; Kropf, J. A.; Prins, R.; van Bokhoven, J. A. *Phys. Chem. Chem. Phys.* **2006**, *8*, 3248.

(33) Sayers, D. E.; Stern, E. A.; Lytle, F. W. *Phys. Rev. Lett.* **1971**, *27*, 1204.

(34) Funke, H.; Scheinost, A. C.; Chukalina, M. *Phys. Rev. B* **2005**, *71*, 094110.

(35) Antoniak, C. *Beilstein J. Nanotechnol.* **2011**, *2*, 237.

(36) Munoz, M.; Argoul, P.; Farges, F. *Am. Mineral.* **2003**, *88*, 694.

(37) Munoz, M.; Farges, F.; Argoul, P. *Phys. Scr.* **2005**, *T115*, 221.

(38) Chukalina, M. V.; Dubrovskii, Y. V.; Funke, H. *Low Temp. Phys.* **2004**, *30*, 930.

(39) Funke, H.; Chukalina, M.; Rossberg, A. *Phys. Scr.* **2005**, *T115*, 232.

(40) Le, T.-P.; Argoul, P. *J. Sound Vap.* **2004**, *277*, 73.

(41) Zabinsky, S. I.; Rehr, J. J.; Ankudinov, A.; Albers, R. C.; Eller, M. *J. Phys. Rev. B* **1995**, *52*, 2995.

(42) Newville, M. *J. Synchrotron Radiat.* **2001**, *8*, 322.

(43) Ravel, B. *EXAFS Analysis with FEFF and FEFFIT; Part 2: Commentary.* http://cars9.uchicago.edu/~ravel/course/notes.pdf

(44) Brillouin, L. Science and information theory. **2004**, Dover Phoenix Editions.

(45) Krappe, H. J.; Rossner, H. H. *J. Synchrotron Radiat.* **1999**, *6*, 302.

(46) Newville, M. *FEFFIT - Using FEFF to model XAFS data.* **1998**.

(47) Frenkel, A. I.; Hills, C. W., Nuzzo, R. G. *J. Phys. Chem. B* **2001**, *105*, 51.

(48) Frenkel, A. I. *J. Synchrotron Rad.* **1999**, *6*, 293.

(49) Jentys, A. *Phys. Chem. Chem. Phys.* **1999**, *1*, 4059.

(50) Niemantsverdriet, J. W. *Spectroscopy in Catalysis: An Introduction.* **2007**, Wiley-VCH.

(51) Ertl, G.; Knözinger, H.; Weitkamp, J. *Handbook of Heterogeneous Catalysis: Characterization of Solid Catalysts.* **2008**, Wiley-VCH.

(52) Gleaves, J. T.; Yablonsky, G.; Zheng, X.; Fushimi, R.; Mills, P. L. *J. Mol. Catal. A-Chem.* **2010**, *315*, 108.

Chapter 3. Advanced elemental characterization during Pt-In catalyst formation by wavelet transformed X-ray absorption spectroscopy

Abstract

Complementary to conventional X-ray absorption near edge structure (XANES) and Fourier transformed (FT) extended X-ray absorption fine structure (EXAFS) analysis, the systematic application of wavelet transformed (WT) XAS is shown to disclose the physicochemical mechanisms governing Pt-In catalyst formation. The simultaneous k- and R-space resolution of the WT XAS signal allows for the efficient allocation of the elemental nature to each R-space peak. Because of its elemental discrimination capacity, the technique delivers structural models which can subsequently serve as an input for quantitative FT EXAFS modeling. The advantages and limitations of applying WT XAS are demonstrated (1) before and (2) after calcination to 650 °C of a $Pt(acac)_2$ impregnated $Mg(In)(Al)O_x$ support, and (3) after subsequent H_2 reduction to 650 °C. Combined XANES, FT and WT XAS analysis shows that the acac ligands of the Pt precursor decompose during calcination, leading to atomically dispersed Pt^{4+} cations on the $Mg(In)(Al)O_x$ support. H_2 reduction treatment eventually results in the formation of 1.5 nm Pt-In alloyed nanoparticles. Wide-spread use and systematic application of wavelet-based XAS can potentially reveal in greater details the intricate mechanisms involved in catalysis, chemistry and related fields.

3.1 Introduction

In natural sciences, the atomic structure around X-ray absorbing atoms has become an indispensable source of information for fundamental as well as applied research. Since the pioneering work of Röntgen on the discovery of X-rays, continuously advancing spectroscopies have revolutionized chemistry[1-3], materials science[4-7] and biology[8, 9]. In catalysis, for example, novel X-ray absorption spectroscopic (XAS) techniques – XMT, µ-XAFS, QXAS – enable structure-performance relationships to be scrutinized in hitherto unavailable details through increased spatio-temporal resolution.[10, 11] Concurrently, novel mathematical methods for *a posteriori* data treatment are being developed, allowing for intelligent information filtering and modeling of measured signals.[12] In fact, these more powerful analysis methods may be as valuable for disclosing nanoscale information as increasingly advanced spectroscopies.

Fourier transformation (FT) of the extended X-ray absorption fine structure (EXAFS) signal is a classic example of such mathematical manipulation, which yields direct structural information on the X-ray absorber's neighbours.[13] During FT EXAFS modeling, parameters such as coordination numbers, interatomic distances and bond length disorders are estimated. However, direct determination of the elemental nature of the absorber's neighbors is not straightforward, requiring dedicated analysis methods for chemical nature allocation. In the past, Koningsberger et al. made major contributions in the development of these methods, which include EXAFS modeling with different k-weightings for detecting low Z scatterers, the observation of asymmetries in imaginary phase- and amplitude-corrected Fourier transforms and difference file technique combined with backward Fourier transformation.[13]

Although these dedicated methods have been proven effective and triggered tremendous scientific progress, their application is labor intensive and typically reserved for the expert user. In contrast, wavelet-based XAS analysis is a dedicated method developed for unraveling both the elemental nature and spatial location of the neighbors surrounding the X-

ray absorber.[14-15] Readily performed wavelet transformation (WT) of the XAS signal yields a 3D image, showing the k-region from which single FT R-space peaks originate. Elemental discrimination and spatial localization can be established from a single WT plot because the k-region can be correlated with the nature of the chemical elements – light (heavy) elements generally backscattering in low (high) k-regions .

To date, the use of WT XAS is limited to a handful of studies[14-18], certainly in the field of catalysis, and is far from being applied systematically. In recent work of Filez et al., the physicochemical mechanisms which govern the formation of Pt-Ga bimetallic catalysts were elucidated.[19] Complementary to conventional XAS analysis, WT XAS served as a tool to gain deeper insight into the process of Pt-Ga catalyst formation.

The current work emphasizes the advantages and limitations of systematically applying WT XAS itself, using the formation process of Pt-In bimetallic catalysts as a case study. As exemplified below, this catalyst material is ideally suited to demonstrate the technical advantages of using WT XAS above conventional XAS, thereby facilitating the elucidation of phenomena playing a role during the formation of Pt-In alloyed catalysts.

The starting material of catalyst synthesis is a Mg,Al-based layered double hydroxide (LDH) with In incorporated into its framework. It belongs to a family of materials which gained increased attention as versatile non-acidic supports with unique properties, such as a tunable electric conductivity[20] and their ability to serve as nanoscale delivery sources for promoting elements in catalysis[21] and therapeutic agents in pharmaceuticals[22]. Calcination of LDH at 650 °C causes the original layered structure to collapse, resulting in the formation of $Mg(In)(Al)O_x$ mixed oxides. This support oxide is then impregnated with a $Pt(acac)_2$-toluene solution and dried at 110 °C. After high temperature oxidation and consecutive H_2 reduction, Pt-In alloyed nanoparticles are formed on the surface of $Mg(In)(Al)O_x$. The resulting Pt-In catalyst has shown superior performance and stability during alkane dehydrogenation, an industrially important process certainly in view of the novel shale gas reserves.[23] Notwithstanding its significant potential for future applications, multiple answers to

fundamental questions remain (partially) unanswered: (i) the structure and stability of the Pt precursor bound to the support surface, (ii) the Pt-support interaction and Pt phase morphology after calcination, e.g. plate- or cluster-like, and (iii) the mechanism of Pt alloying and the final alloy composition, influencing the cluster surface composition and reactivity. The answers to these questions are crucial not only from a fundamental point of view, but are also necessary for further catalyst optimization. This study addresses these mechanistic questions on the formation of LDH-based Pt-In catalysts, while illustrating the advantages of systematic application of wavelet-based XAS.

3.2 Experimental

3.2.1 Material synthesis

The $Mg(In)(Al)O_x$ support material was produced by the co-precipitation method described by Sun et al..[24] First, an aqueous solution (250 mL) of $Mg(NO_3)_2.6H_2O$ (29 g, Sigma-Aldrich, 98 – 102%), $Al(NO_3)_3.9H_2O$ (4.2 g, Sigma-Aldrich, 98.5%) and $In(NO_3)_3.xH_2O$ (0.07 g, Sigma-Aldrich, 99.99%) was mixed with an aqueous solution (250 mL) of Na_2CO_3 (0.6 g, EMD Chemicals Inc., 99.5%) and NaOH (6 g, Fisher Scientific, 98.3%). After 24h of room temperature aging, the precipitated support material was filtered, washed with deionized water until pH 7, and dried at 110 °C. The resulting material was then calcined in air for 3h at 650 °C, leading to a $Mg(In)(Al)O_x$ mixed oxide.

Second, the Pt precursor was deposited on the $Mg(In)(Al)O_x$ support by incipient wet impregnation. For this purpose, a toluene (1.5 mL, Sigma-Aldrich, 99.9%) solution of $Pt(acetylacetonate)_2$ precursor (0.021 g, Sigma-Aldrich, 99.99%) was added to the powder support. Subsequently, toluene was evaporated by heating the sample up to 110 °C. The

resulting wet impregnated powder served as starting point for the experiments performed for this work.

3.2.2 Material characterization

ICP-AES. Inductively coupled plasma atomic emission spectrometry (ICP-AES) (Ultima, Jobin Yvon Emission Horiba Group) was used to determine the bulk chemical composition of the calcined sample. 50 mg of sample was dissolved by adding 2 mL of aqua regia (1:3 ≡ HNO_3:HCl) and 0.5 mL HF. After 3h at room temperature, 0.5 g H_3BO_3 (99.99%) was added and mixed with bidistilled water until a total volume of 125 mL was reached. The calcined sample contained ~ 1 wt% Pt, 36 wt% Mg, 8 wt% Al, 2 wt% In.

TEM. Structural analysis was performed by transmission electron microscopy (TEM). Samples were prepared by immersion of a lacey carbon film on a nickel support grid into the catalyst powder, after which the excess powder was shaken off. The remaining particles, sticking to the carbon film, were examined in scanning transmission dark field (STEM-DF) mode. A JEOL JEM2200FSCs-corrected microscope was used, operated at 200 kV and equipped with Schottky-type FEG, EDX JEOL JED-2300D and JEOL in column omega filter.

XAS. *In situ* XAS experiments were performed at the Pt L_{III} edge (11564 eV) at the DUBBLE beam line[25, 26] of the 6 GeV European Synchrotron Radiation Facility (ESRF, Grenoble, current 160 – 200 mA). The as prepared material was inserted into a 2 mm quartz capillary and fixed by quartz wool plugs. The capillary was connected to gas feed lines through swagelok® fittings and mounted below a gas blower (FMB Oxford). The DUBBLE gas flow system was utilized to regulate the gas flows through the capillary.[27] The optics alignment and energy referencing was performed using a Pt foil. XAS measurements (± 45 min/spectrum) were recorded in transmission mode.

During calcination, $Pt(acac)_2$ impregnated on $Mg(In)(Al)O_x$ was heated in 20% O_2/He (50 NmL/min) to 650 °C. After 20 minutes of dwelling time at 650 °C, the material was quenched to room temperature to record XAS spectra. Subsequently, the flow was switched to 5% H_2/He (50 NmL/min) followed by temperature programmed reduction to 650 °C. Once the temperature of 650 °C was reached, 20 more minutes of H_2/He reduction were performed at 650 °C. The reduced sample was then cooled down to room temperature to measure XAS.

XAS data analysis. Data analysis was performed using the Demeter 0.9.13 package (Athena and Artemis).[28] Background subtraction, normalization, $\chi(k)$ isolation and Fourier transformation were accomplished by using the methodology of Koningsberger et al..[13]

The Pt-C, Pt-O, Pt-Mg, Pt-Al, Pt-In and Pt-Pt phase shifts and backscattering amplitude functions were calculated with the FEFF 6.0 code.[29] In order to estimate the implemented structural parameters, the Levenberg-Marquardt algorithm was applied for non-linear least-squares minimization of the objective function. This minimization was carried out with the IFEFFIT software[28] through multiple shell fitting in R-space using multiple k-weightings.

A Cauchy wavelet of order 50 was used to wavelet transform the k^2-weighted EXAFS signals. The HAMA Fortran code[30] allowed for calculation of these wavelet transformed XAS signals. All XAS plots, including Fourier and wavelet transformed, are represented without phase correction. Therefore, the radial distances observed in the EXAFS plots are ~ 0.4 – 0.5 Å below their actual value.

3.3 Results and discussion

$Pt(acac)_2$ wet impregnated $Mg(In)(Al)O_x$. XAS measurements are performed during different stages of catalyst formation. Figure 3.1.a depicts a XANES spectrum of $Pt(acac)_2$ impregnated on $Mg(In)(Al)O_x$ and dried at 110 °C. The white line intensity at the Pt

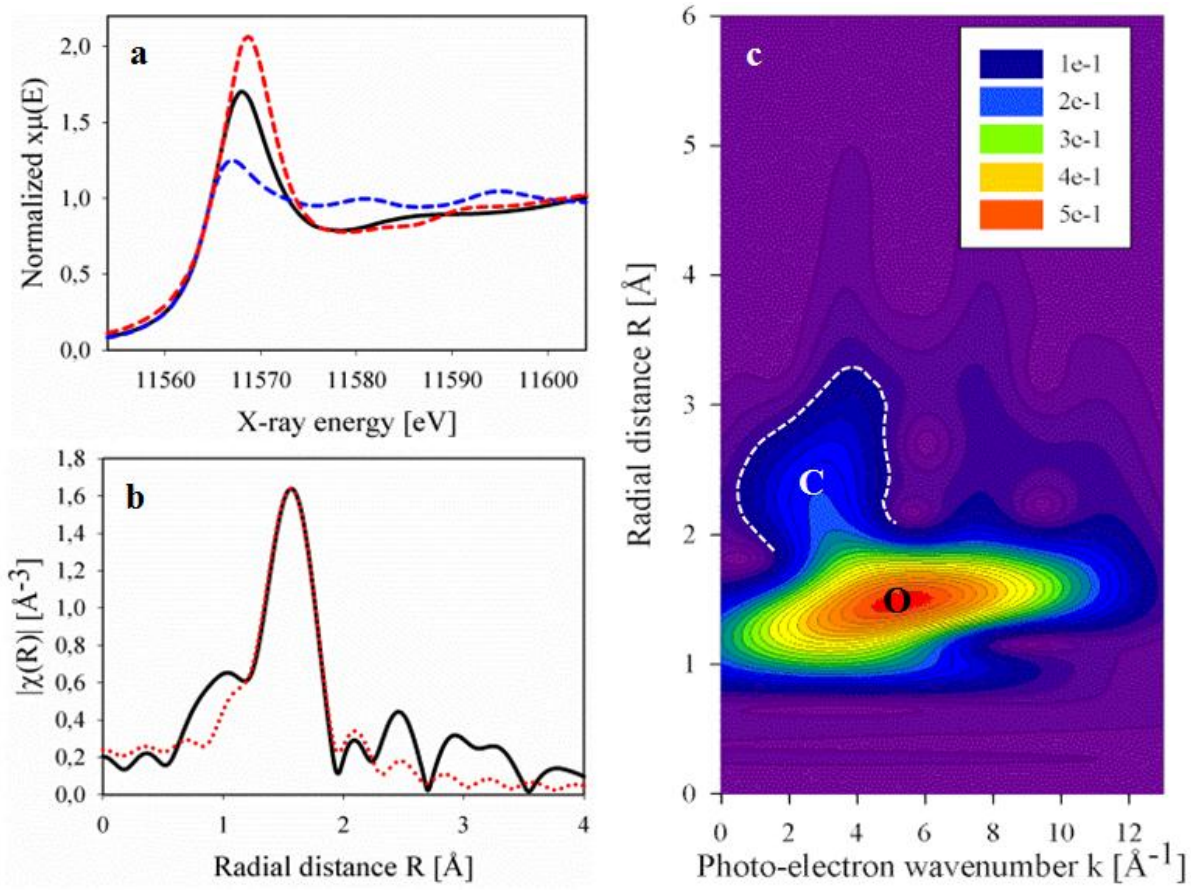

Figure 3.1: Pt L_{III} edge (a) XANES spectra of $Pt(acac)_2$ wet impregnated on $Mg(In)(Al)O_x$ (——), metallic Pt (- - -) and PtO_2 (- - -). (b) k^2-weighted Fourier transformed EXAFS magnitude of $Pt(acac)_2$ wet impregnated on $Mg(In)(Al)O_x$ (——) and O shell model fit (·····) (R = 0.004). (c) Wavelet transformed XAS signal of $Pt(acac)_2$ wet impregnated on $Mg(In)(Al)O_x$. Oxygen (O) and carbon peaks (C, white dashed line) are indicated. All FT and WT signals in this study are non-phase corrected.

L_{III} edge, i.e. the surface area below the intense edge peak (~ 11570 eV), is proportional to the Pt oxidation state.[31] Compared to bulk Pt and PtO_2 reference signals, the experimental signal of the $Pt(acac)_2$ impregnated $Mg(In)(Al)O_x$ has an intermediate white line intensity. The corresponding average oxidation state of Pt amounts to ~ 2+, being in-between Pt^0 (Pt) and Pt^{4+} (PtO_2). First shell modeling of the Fourier transformed (FT) EXAFS signal yields a fourfold Pt-O coordination configured in a highly ordered structure around Pt (Figure 3.1.b – dotted line, Appendix A.1: Table A-1). XANES and FT EXAFS both are in accord with the presence of full $Pt(acac)_2$ molecules, in which Pt^{2+} cations have a fourfold O coordination in a highly ordered planar geometry ($H_7C_5O_2$-Pt-$O_2C_5H_7$). However, a definitive proof of this structural assignment requires additional information about higher coordination shells to

confirm that $Pt(acac)_2$ does not undergo decomposition upon impregnation and drying at 110 °C.

Detailed FT EXAFS modeling of the higher shells around Pt is not straightforward, in contrast to a readily established first shell fit (Figure 3.1.b). Hydrocarbons residing in the acac ligands increase the number of possible higher shell EXAFS contributions and decrease the feasibility of FT EXAFS modeling, as the number of used parameters that can be meaningfully estimated is limited. Consequently, higher shell EXAFS modeling (here R > 2 Å) is often challenging and time expensive. By invoking wavelet transformed XAS, first hand insight into the nature and location of the atomic species in the local environment around Pt can be gained with relative ease.

The application of wavelet transformed XAS requires a basic understanding of the methodology. During Fourier transformation, infinite sine functions with varying wavelength are used to transform the EXAFS signal from k-space [$Å^{-1}$] to R-space [Å]. This yields a radial structure function – the R-space EXAFS magnitude – which correlates with the radial distribution function around the absorber.[13] The same structural information can be retrieved by wavelet transformed XAS analysis. For this purpose, wave packets with finite k-range – wavelets – are systematically altered in their wavelength. In contrast to the infinite sine functions used for Fourier transformation, the k-space wavelet position is also altered during wavelet transformation.[16] This additional degree of freedom provides k-space resolution for each R-space value, which allows to retrieve from which k-region each R-space peak originates. As this k-region depends on the nature of the absorber's neighbors, the allocation of an elemental type to each separate R-space peak is made possible by wavelet transformed XAS. Such elemental information remains concealed during standard FT EXAFS analysis since no k-space resolution is then provided.

Equipped with the methodology of wavelet transformation, XAS data can now be interpreted in a more meaningful way. Figure 3.1.c displays a 2D contour plot of the wavelet transformed XAS magnitude of $Pt(acac)_2$ impregnated on $Mg(In)(Al)O_x$. The vertical axis

represents the radial distance R around Pt and is identical to the horizontal axis is Figure 3.1.b. The horizontal axis in Figure 3.1.c shows the photoelectron wavenumber k which provides k-space resolution for each R-space value. An intense peak is detected at R ~ 1.5 Å and k ~ 5 $Å^{-1}$, characteristic for O, as also evidenced by FT EXAFS modeling. In addition, a foothill of this intense O peak is observed between R ~ 2 – 3 Å at lower k-values. This low k-range contribution can be correlated to the occurrence of C species around Pt inside $Pt(acac)_2$, causing Pt-O-C-Pt double scattering EXAFS contributions. Such double scattering contributions occur at low k-values[13], making it a signature for the presence of acac ligands around Pt.

In combination, the acac ligands detected by WT XAS and a fourfold Pt-O coordination with low bond length disorder obtained from FT EXAFS strongly suggest that $Pt(acac)_2$ precursor molecules are present. This implies that the adsorbed $Pt(acac)_2$ molecules remain intact during toluene evaporation at 110 °C. This is in line with a study of Womes et al.,[32] in which the stability and decomposition of $Pt(acac)_2$ molecules on Al_2O_3 surfaces was investigated by conventional XAS. Based on visual inspection of k-space EXAFS oscillations, the evolution of $Pt(acac)_2$ under different conditions was qualitatively evaluated based on complex and time consuming interpretations. This classic analysis method, typically reserved for expert users, can be circumvented by applying more time efficient and readily established WT XAS, as illustrated above.

O_2/He oxidation to 650 °C. Calcination of $Pt(acac)_2/Mg(In)(Al)O_x$ up to 650 °C significantly alters the material's state (Figure 3.2). The XANES white line of calcined $Pt(acac)_2/Mg(In)(Al)O_x$ has an intensity similar to PtO_2 (Figure 3.2.a). This implies that the Pt phase is completely oxidized to a Pt^{4+} oxidation state during calcination. The XANES oscillations at higher energies also show similarities to the PtO_2 XANES profile. Moreover, the FT EXAFS magnitude of calcined $Pt(acac)_2/Mg(In)(Al)O_x$ resembles the profile of the PtO_2 reference (Appendix A.2: Figure A-3). These observations suggest that the Pt phase is PtO_2-like after calcination to 650 °C. However, modeling the EXAFS profile of calcined

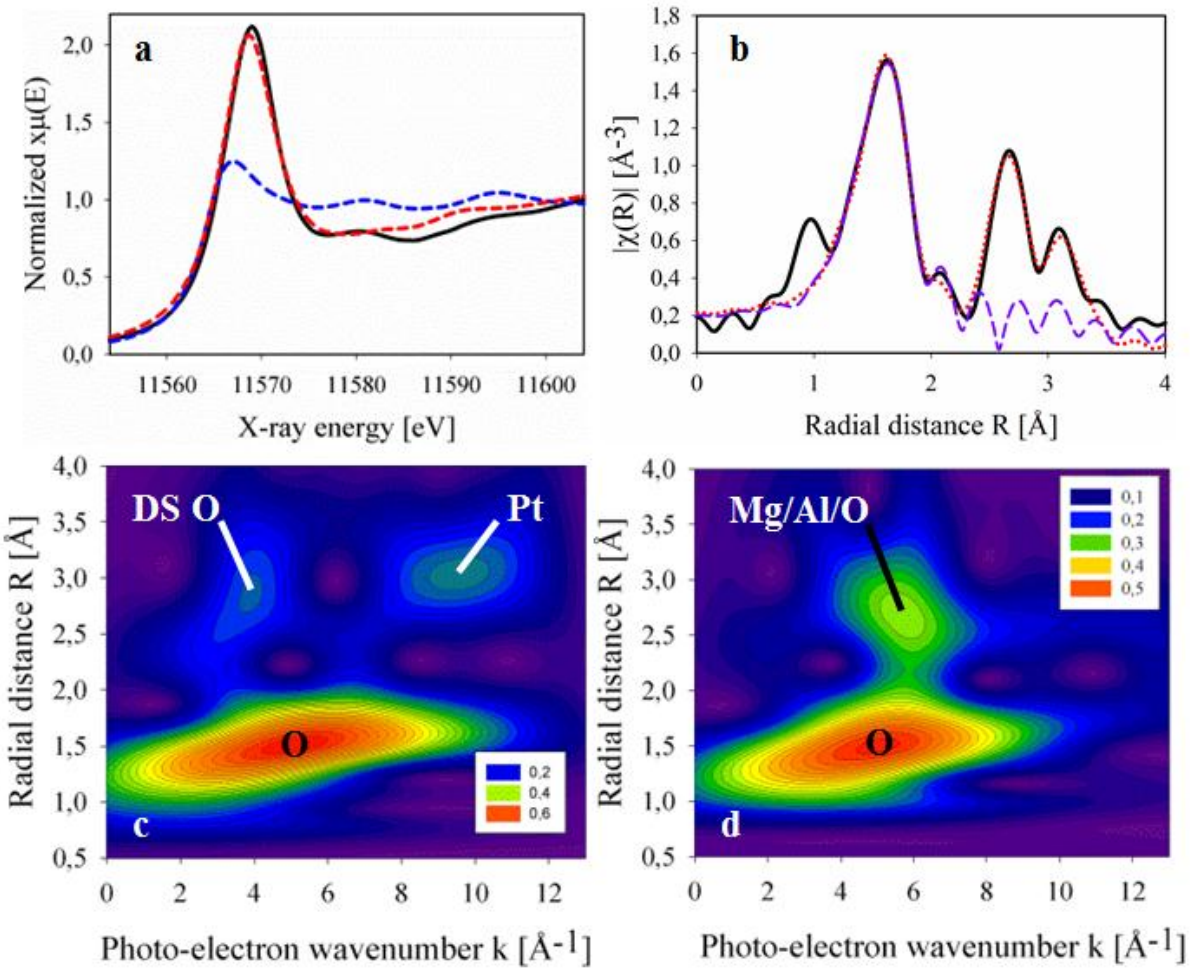

Figure 3.2: Pt L_{III} edge (a) XANES spectra of calcined $Pt(acac)_2/Mg(In)(Al)O_x$ to 650 °C (——), metallic Pt (- - -) and PtO_2 (- - -) references. (b) k^2-weighted Fourier transformed EXAFS magnitude of calcined $Pt(acac)_2/Mg(In)(Al)O_x$ to 650 °C (——), PtO_2 model fit (– – –) (R = 0.318) and Pt-**O** + Pt-O-**Mg** + Pt-O-Mg-**O** shell model fit (·····) (R = 0.010). Wavelet transformed XAS signal of (c) PtO_2 reference and (d) $Pt(acac)_2/Mg(In)(Al)O_x$ calcined to 650 °C. O, Mg and Pt peaks are indicated.

$Pt(acac)_2/Mg(In)(Al)O_x$ using a PtO_2 structure fails (Figure 3.2.b – dashed line). Although this model yields good convergence for the first Pt-O shell (R = 1 – 2 Å), it cannot describe the experimental signal in the higher R-region. Employing conventional XAS analysis – XANES and FT EXAFS – thus leads to an incomplete understanding of the nanoscale structure of the Pt phase after calcination.

The application of WT XAS to the spectra of a PtO_2 reference and calcined $Pt(acac)_2/Mg(In)(Al)O_x$ produces the 2D contour plots in Figures 2.c and 2.d, respectively. The WT XAS signal of the PtO_2 reference shows multiple peaks. An O peak is observed at R ~ 1.5 Å and k ~ 5 $Å^{-1}$ which was also present for $Pt(acac)_2/Mg(In)(Al)O_x$ before calcination

(Figure 3.1.c). In higher R-regions (R ~ 3 Å), two distinct peaks are observed at k ~ 3 – 4 $Å^{-1}$ and k ~ 8 – 10 $Å^{-1}$. These peaks originate primarily from Pt-O-O-Pt double scattering contributions and Pt-Pt bonds, respectively.

The WT XAS signal of calcined $Pt(acac)_2/Mg(In)(Al)O_x$ also shows an O peak at R ~ 1.5 Å (Figure 3.2.d). But in contrast to the PtO_2 reference, a single peak around R ~ 2.6 Å is observed at similar k-values compared to the O peak. Since Mg, Al and O atoms give rise to WT peaks at similar k-values (Appendix A.3: Figure A-4), it is very likely that the peak at R ~ 2.6 Å originates from Mg and Al support metal cations. As the abundance of In in the $Mg(In)(Al)O_x$ support is small compared to the fractions of Mg and Al (36 wt% Mg, 8 wt% Al, 2 wt% In), the In contribution to the WT XAS signal is presumably not detectable.

Four additional remarks are worth mentioning. First, third shell O atoms (Pt-O-Mg-**O**) could also contribute to the WT peak at R ~ 2.6 Å in addition to Mg and Al, since O also leads to a WT peak in the same k-region. Second, the foothill to the O peak between R ~ 2 – 3 Å present before calcination of $Pt(acac)_2/Mg(In)(Al)O_x$ (Figure 3.1.c) is no longer observed after calcination to 650 °C (Figure 3.2.d). Third, no Pt nor PtO_2 clusters are formed during calcination. This is evidenced by the absence of Pt peaks which are expected to appear between k ~ 8 – 10 $Å^{-1}$ (e.g. Figure 3.2.c). Fourth, it should be noted that WT XAS is not capable of discriminating between Mg, Al and O, as these elements generate a k-space signal in the same k-region. However, this limitation of WT XAS also applies to conventional FT EXAFS analysis as it is inherent to XAS technique as a whole.

The structural information extracted by WT analysis of the XAS spectra can now serve as input for quantitative structural modeling of the FT EXAFS signal of the calcined $Pt(acac)_2/Mg(In)(Al)O_x$. For this purpose, three different contributions are implemented: (i) a first neighbor Pt-**O** shell, (ii) a second neighbor Pt-O-**Mg** shell, and (iii) a third neighbor Pt-O-Mg-**O** shell. This structural model yields excellent convergence with the experimental signal (Figure 3.2.b – dotted line, Appendix A.1: Table A-2, Figure A-1). Hence, WT XAS

analysis facilitates the search for an appropriate structural model suitable for FT EXAFS modeling.

As mentioned before, the foothill of the O peak (R ~ 2 – 3 Å, k ~ 3 $Å^{-1}$) disappears upon calcination of $Pt(acac)_2/Mg(In)(Al)O_x$ to 650 °C. This suggests that the acac ligands of the Pt precursor decompose upon calcination. As evidenced by XANES, this decomposition is accompanied by the full oxidation of Pt^{2+} cations into Pt^{4+}. Combined WT and FT XAS analysis shows that these oxidized Pt^{4+} species are atomically dispersed and remain in close contact with the $Mg(In)(Al)O_x$ support. No significant Pt or PtO_2 cluster formation is observed in the course of high temperature calcination. In a recent study of Filez et al.,[19] Pt cluster formation is observed after a 135 min calcination treatment at 650 °C for 5 wt% $Pt(acac)_2/Mg(Ga)(Al)O_x$. Consequently, the absence of Pt cluster formation for the current material can be attributed to a combined effect of strong Pt-metal oxide support interaction (basic MgO support), low density of atomically dispersed Pt species on the $Mg(In)(Al)O_x$ support (1 wt% Pt) and the relatively short calcination period (20 min).

H_2/He reduction to 650 °C. During the next step of catalyst formation, the calcined $Pt(acac)_2/Mg(In)(Al)O_x$ – now labeled as $Pt/Mg(In)(Al)O_x$ – is subjected to a 5% H_2/He flow during temperature programmed heating up to 650 °C. After reaching 650 °C, the sample is cooled down to room temperature in 5% H_2/He to record good quality XAS scans. The resulting XANES spectrum (Figure 3.3.a) displays a considerable decrease in the Pt L_{III} white line intensity after compared to before reduction (Figure 3.2.a). After reduction, the white line lies below the one of a metallic Pt reference. In addition, a significant edge shift to higher photon energies is observed compared to metallic Pt. Both features are characteristic for alloying of Pt with a promoting element such as In, Ga, Au, etc.[33] During Pt-In alloying, In donates electrons to Pt since the electronegativity of In (1.78 eV) is lower compared to the one of Pt (2.28 eV). This results in the stabilization of Pt-In bonds and gives rise to Pt-In alloying during reduction, being reflected in the white line features of the Pt L_{III} edge XANES spectra.

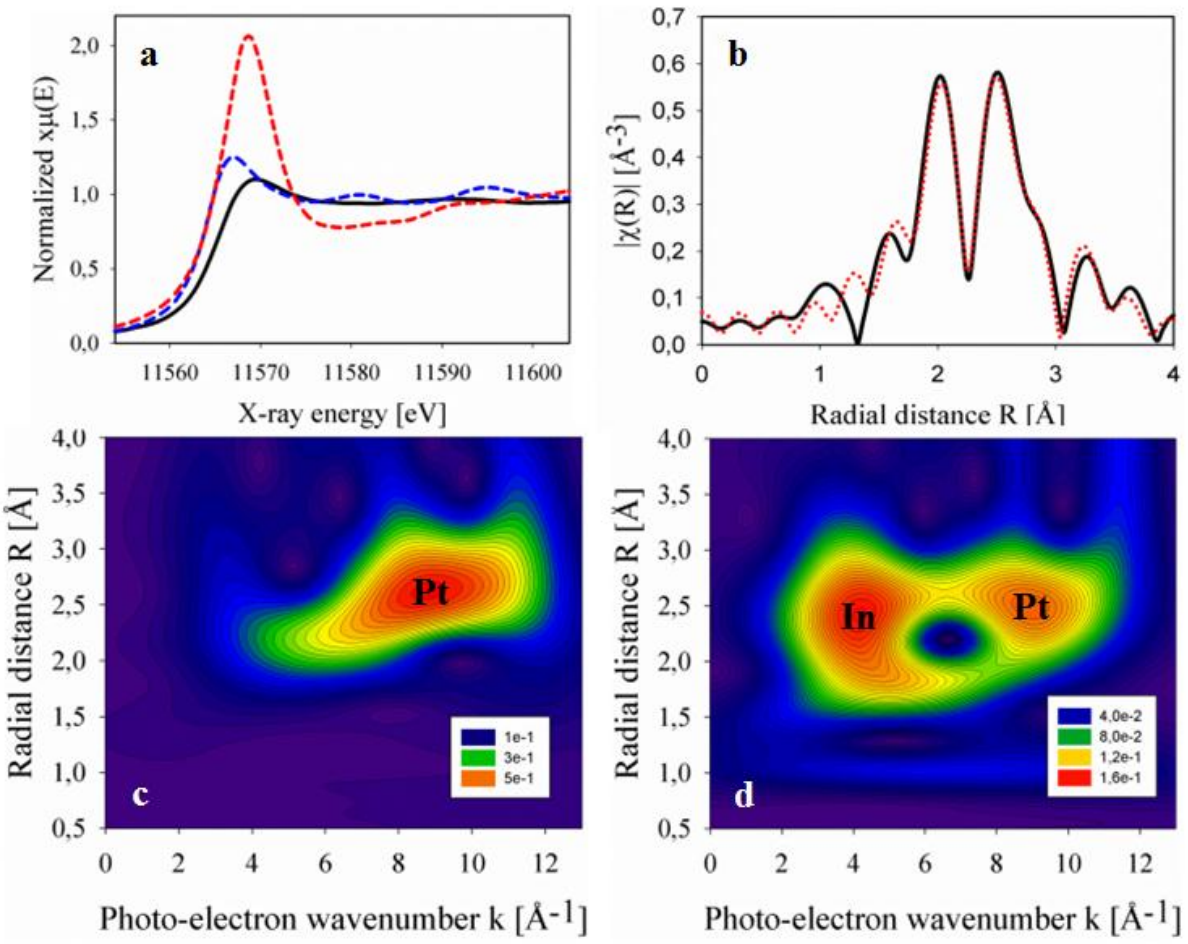

Figure 3.3: Pt L_{III} edge (a) XANES spectra of reduced Pt/Mg(In)(Al)O_x to 650 °C (——), metallic Pt (- - -) and PtO_2 (- - -) references. (b) k²-weighted Fourier transformed EXAFS magnitude of reduced Pt/Mg(In)(Al)O_x to 650 °C (——) and Pt-In + Pt-Pt shell model fit (·····) (R = 0.019). Wavelet transformed XAS signal of (c) Pt reference and (d) reduced Pt/Mg(In)(Al)O_x to 650 °C. In and Pt peaks are indicated.

The FT EXAFS magnitude of 650 °C reduced Pt/Mg(In)(Al)O_x is depicted in Figure 3.3.b. Two intense peaks are observed, namely at R ~ 2 Å and R ~ 2.6 Å. It should be noted that no Pt-O contribution is detected, since then a FT peak at R ~ 1.5 Å would be observable. Since XANES indicates that Pt and In are alloyed after reduction to 650 °C, both In and Pt are expected to be present as nearest neighbors around Pt. However, as the Pt-In and Pt-Pt bond lengths are similar, i.e. R ~ 2.68 Å and R ~ 2.78 Å respectively, the double peak is not expected and presents another challenge for the WT analysis.

In Figure 3.3.c and 3.3.d the WT XAS contour plots of a Pt reference and the reduced Pt/Mg(In)(Al)O_x sample are shown. The WT XAS magnitude of the metallic Pt reference shows a single peak with maximum around R ~ 2.6 Å and k ~ 8 – 10 $Å^{-1}$. In

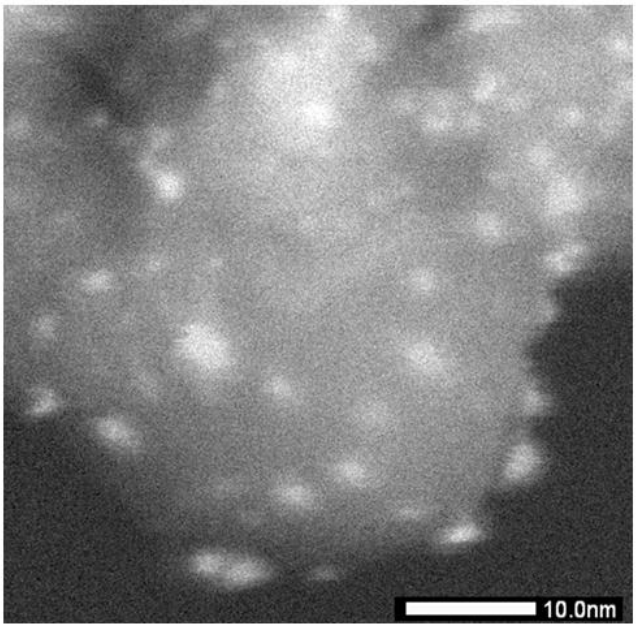

Figure 3.4: STEM-DF image of the Pt-In alloyed nanoparticles on the Mg(In)(Al)O_x support.

contrast, two intense WT XAS peaks are observed for Pt/Mg(In)(Al)O_x reduced up to 650 °C. The peak at k ~ 8 – 10 $Å^{-1}$ originates majorly from the presence of Pt atoms surrounding the Pt absorber. In addition, the second peak at k ~ 4 $Å^{-1}$ stems from In neighbors around Pt (Appendix A.3: Figure A-4). Both Pt and In WT peaks are located at similar R-values, implying that Pt-In and Pt-Pt bond lengths are similar, as expected. The superposition of the In and Pt contributions in the original k-space EXAFS signal therefore results in interference yielding a double peak feature in FT EXAFS (Figure 3.3.b, Appendix A.1: Figure A.2). WT XAS resolves the elemental nature of this non-physical FT double-peak feature in an elegant way.

Based on this WT XAS result, FT EXAFS modeling with a Pt-In + Pt-Pt shell model indeed leads to agreement between model and experimental signal of the alloyed Pt-In/Mg(In)(Al)O_x catalyst (Figure 3.3.b – dotted line, Appendix A.1: Table A-3). The estimated Pt-Pt and Pt-In coordination numbers respectively amount to N_{Pt-Pt} = 2.4 ± 0.8 and N_{Pt-In} = 4.4 ± 0.7. The total Pt coordination number, namely N_{Pt-Pt} + N_{Pt-In} = 6.8 ± 1.5, corresponds to a cluster size of 1.5 nm when hemispherical nanoparticle shapes are assumed.[34] This average size is in correspondence with TEM measurements (Figure 3.4).

These results show that the atomically dispersed Pt^{4+} species at the $Mg(In)(Al)O_x$ support surface – present after calcination – undergo considerable changes during reduction. On the one hand, H_2 treatment up to 650 °C increases the mobility of Pt species, leading to enhanced surface migration, so that Pt transport over the $Mg(In)(Al)O_x$ support results in Pt cluster formation. In addition, In atoms from the support are mobilized and alloy with Pt to form 1.5 nm Pt-In alloyed nanoparticles.

3.4 Conclusions

Wavelet transformed (WT) XAS is a powerful tool for boosting the reconstruction of the X-ray absorber's local environment. By providing simultaneous k- and R-space resolution, WT XAS allows for both elemental discrimination and spatial localization of the atomic neighbors surrounding the X-ray absorber. The advantages and limitations of wavelet-based XAS analysis are illustrated throughout this study. First, the application of WT XAS can circumvent time consuming and complex analysis procedures applied during conventional EXAFS analysis. Second, the exploitation of the elemental nature of the X-ray absorber's neighbors by WT XAS facilitates the development of a structural model, subsequently employed for quantitative Fourier transformed (FT) EXAFS modeling. Third, the absence or presence of specific atomic species can be unambiguously claimed based on visual inspection of the WT XAS magnitude, the latter being difficult when using FT EXAFS. Fourth, FT peaks in R-space not corresponding to physical neighbors – originating from k-space interference – can be characterized by WT XAS analysis with relative ease. A drawback of WT XAS concerns its limited capability of distinguishing atomic species with similar masses, such as Mg, Al, O. However, this limitation is intrinsic to the technique of XAS itself and will also be present during FT EXAFS analysis. Finally, up to date, no quantitative WT XAS modeling routine has been developed to evaluate the structural model derived from qualitative analysis and estimate its structural parameters.

Used in combination with XANES and FT EXAFS analysis, WT XAS advances the retrieval of mechanistic insights into the formation of LDH-based Pt-In catalysts. After wet impregnation of a $Pt(acac)_2$-toluene solution on a LDH-derived $Mg(In)(Al)O_x$ mixed oxide support, $Pt(acac)_2$ is adsorbed on the support while the precursor structure remains intact. Calcination to 650 °C leads to precursor decomposition and Pt oxidation, resulting into atomically dispersed Pt^{4+} species residing at the $Mg(In)(Al)O_x$ support surface. Subsequent H_2 reduction treatment to 650 °C results in Pt cluster formation, accompanied by the migration of In from the $Mg(In)(Al)O_x$ support towards these Pt clusters. This leads to the formation of Pt-In alloyed nanoparticles. Our findings are relevant not only for research on bimetallic and LDH-based catalysts, but also for a wider range of XAS applications across multiple disciplines in which mechanistic investigations with different atomic species are performed.

3.5 References

(1) Pollock, C. J.; Grubel, K., Holland, P. L.; DeBeer, S. *J. Am. Chem. Soc.* **2013**, *135*, 11803.

(2) Sarangi, R.; Yang, L.; Winikoff, S. G.; Gagliardi, L.; Cramer, C. J.; Tolman, W. B.; Solomon, E. I. *J. Am. Chem. Soc.* **2011**, *133*, 17180.

(3) Hatzistavros, V. S.; Kallithrakas-Kontos, N. G. *Anal. Chem.* **2011**, *83*, 3386.

(4) Friebel, D.; Viswanathan, V.; Miller, D. J.; Anniyev, T.; Ogasawara, H.; Larsen, A. H.; O'Grady, C. P.; Norskov, J. K.; Nilsson, A. *J. Am. Chem. Soc.* **2012**, *134*, 9664.

(5) Buurmans, I. L. C.; Weckhuysen, B. M. *Nat. Chem.* **2012**, *4*, 873.

(6) Beale, A. M.; Jacques, S. D. M.; Weckhuysen, B. M. *Chem. Soc. Rev.* **2010**, *39*, 4656.

(7) Filez, M.; Poelman, H.; Ramachandran, R. K.; Dendooven, J.; Devloo-Casier, K.; Fonda, E.; Detavernier, C.; Marin, G. B. *Catal. Today* **2014**, *229*, 2.

(8) Goldsmith, R. H.; Moerner, W. E. *Nat. Chem.* **2010**, *2*, 179.

(9) Fears, K. P. *Anal. Chem.* **2014**, *86*, 8526.

(10) Gonzalez-Jimenez, I. D.; Cats, K.; Davidian, T.; Ruitenbeek, M.; Meirer, F.; Liu, Y.; Nelson, J.; Andrews, J. C.; Pianetta, P.; de Groot, F. M. F.; Weckhuysen, B. M. *Angew. Chem. Int. Ed.* **2012**, *124*, 12152.

(11) Singh, J.; Alayon, E. M. C.; Tromp, M.; Safonova, O. V.; Glatzel, P.; Nachtegaal, M.; Frahm, R.; van Bokhoven, J. A. *Angew. Chem. Int. Ed.* **2008**, *47*, 9260.

(12) König, C. F. J.; van Bokhoven, J. A.; Schildhauer, T. J.; Nachtegaal, M. *J. Phys. Chem. C* **2012**, *116*, 19857.

(13) Koningsberger, D. C.; Mojet, B. L.; van Dorssen, G. E.; Ramaker, D. E. *Top. Catal.* **2000**, *10*, 143.

(14) Munoz, M.; Farges, F.; Argoul, P. *Phys. Scr.* **2005**, *T115*, 221.

(15) Funke, H.; Scheinost, A. C.; Chukalina, M. *Phys. Rev. B*, **2005**, *71*, 094110.

(16) Antoniak, C. *Beilstein J. Nanotechnol.* **2011,** *2*, 237.

(17) Munoz, M.; Argoul, P.; Farges, F. *Am. Mineral.* **2003,** *88*, 694.

(18) Chukalina, M. V.; Dubrovskii, Y. V.; Funke, H. *Low Temp. Phys.* **2004,** *30*, 930.

(19) Filez, M.; Redekop, E. A.; Poelman, H.; Galvita, V. V.; Ramachandran, R. K.; Dendooven, J.; Detavernier, C.; Marin, G. B. *Chem. Mater.* **2014**, *26*, 5936.

(20) Long, X.; Xiao, S.; Wang, Z.; Zheng, X.; Yang, S. *Chem. Comm.* **2014**, DOI: 10.1039/C4CC08856E.

(21) Redekop, E. A.; Galvita, V. V.; Poelman, H.; Bliznuk, V.; Detavernier, C.; Marin, G. B. *ACS Catal.* **2014**, *4*, 1812.

(22) Chakraborty, J.; Roychowdhury, S.; Sengupta, S.; Ghosh, S. *Mater. Sci. Eng. C* **2013**, *33*, 2168.

(23) Sattler, J. J. H. B.; Ruiz-Martinez, J.; Santillan-Jimenez, E.; Weckhuysen, B. M. *Chem. Rev.* **2014**, *114*, 10613.

(24) Sun, P. P.; Siddiqi, G.; Chi, M. F.; Bell, A. T. *J. Catal.* **2010,** *274*, 192.

(25) Beale, A. M.; van der Eerden, A. M. J.; Jacques, S. D. M.; Leynaud, O.; O'Brien, M. G.; Meneau, F.; Nikitenko, S.; Bras, W.; Weckhuysen, B. M. *J. Am. Chem. Soc.* **2006,** *128*, 12386.

(26) Nikitenko, S.; Beale, A. M.; van der Eerden, A. M. J.; Jacques, S. D. M.; Leynaud, O.; O'Brien, M. G.; Detollenaere, D.; Kaptein, R.; Weckhuysen, B. M.; Bras, W. *J. Synchrotron Rad.* **2008,** *15*, 632.

(27) Martis, V.; Beale, A. M.; Detollenaere, D.; Banerjee, D.; Moroni, M.; Gosselin, F.; Bras, W. *J. Synchrotron Rad.* **2014,** *21*, 462.

(28) Ravel, B.; Newville, M. *J. Synchrotron Rad.* **2005,** *12*, 537.

(29) Rehr, J. J.; Deleon, J. M.; Zabinsky, S. I.; Albers, R. C. *J. Am. Chem. Soc.* **1991,** *113*, 5135.

(30) Funke, H.; Chukalina, M. Wavelet Transform for EXAFS: http://www.esrf.eu/UsersAndScience/Experiments/CRG/BM20/Software/Wavelets

(31) Yoshida, H.; Nonoyama, S.; Yazawa, Y.; Hattori, T. *Phys. Scr.* **2005**, *T115*, 813.

(32) Womes, M.; Lynch, J.; Bazin D.; Le Peltier, F.; Morin, S.; Didillon, B. *Catal. Lett.* **2003**, *85*, 25.

(33) Bus, E.; van Bokhoven, J. A. *J. Phys. Chem. C* **2007**, *111*, 9761.

(34) Frenkel, A. I.; Hills, C. W.; Nuzzo, R. G. *J. Phys. Chem. B* **2001**, *105*, 12689.

Chapter 4. Unraveling the formation of Pt-Ga alloyed nanoparticles on calcined Ga-modified hydrotalcites by *in situ* XAS

Abstract

The chemical transformations taking place during the formation of catalytic Pt-Ga alloyed nanoparticles supported on calcined Ga-modified hydrotalcite $Mg(Ga)(Al)O_x$ are investigated. The starting point is a $Pt(acac)_2$ precursor impregnated onto a $Mg(Ga)(Al)O_x$ support. An oxidative treatment first yields Pt nanoparticles, while subsequent reduction efficiently delivers Ga from the support framework to Pt, forming Pt-Ga alloyed clusters. Different steps are discerned in this process based on *in situ* XAS analysis. During oxidative heating to 350°C, the initially adsorbed $Pt(acac)_2$ precursor molecules decompose and form atomically dispersed Pt^{4+} species with five/six fold oxygen coordination. A fraction of the formed Pt-O bonds consists of strong anchoring points between Pt^{4+} species and support oxygen, decreasing the Pt mobility induced by the basic support. Further calcination to 650°C leads to scission of these Pt-O support bonds, allowing more mobile Pt species to form 3 – 11 atom Pt fcc nanoparticles with oxidized external surface. These subnanometer clusters are proposed to be bound to the $Mg(Ga)(Al)O_x$ support by extended 2.5 Å Pt^0-$(OH)^-$ induced dipole-ion interfacial bonds. Cooling down and subsequent heating in H_2 up to 450°C causes sintering and reduction of these nanoparticles. In the course of this reduction, the proposed 2.5 Å Pt^0-$(OH)^-$ interfacial bonds are replaced by common 2.0 Å Pt-O bonds. Further heating in H_2 to 650°C causes reduction of framework Ga, allowing Ga transport from the support to the Pt clusters to form 1.5 nm Pt-Ga alloyed nanoparticles. This activated Pt-Ga/$Mg(Ga)(Al)O_x$ catalyst is subjected to one O_2/H_2 redox cycle at 650 °C to mimick the catalyst regeneration procedure. The redox cycle induces an alloy restructuring, leading to a decrease in the degree of Pt-Ga alloying. Wavelet transformed XAS – complemented by XANES and EXAFS – is shown to be a key tool to disclose the mechanistic details occurring during Pt-Ga formation.

4.1 Introduction

The rational design of functional materials, such as heterogeneous catalysts, aims at manipulating the material's structure by steering the solid-phase chemistry in order to achieve the desired properties and improve material's performance.[1-6] An in-depth understanding of materials chemistry is therefore crucial for the development of better catalysts and enabling the chemical industry to shift from non-selective thermal to selective catalytic processes. Alloying of metal catalysts with promoter elements presents a particularly relevant example of better catalyst design through manipulation of materials chemistry. Even moderate gains in catalytic performance of industrial metal catalysts can result in significant improvements of economics and environmental impact of large scale hydrocarbon processing.

At present, ethene, propene and butene, the building blocks of many products in chemical industry, are mainly produced via steam cracking of oil fractions. This non-selective high temperature process is energy intensive and is accompanied by significant methane and coke formation. In contrast, catalytic dehydrogenation of light alkanes offers an attractive alternative for alkene production, since the catalyst can be tuned to be selective and durable[7-9] and stoichiometric amounts of H_2 are produced. Hydrogen is a valuable product in itself and is widely used for hydrocracking and heteroatom removal.[7, 10]

Bimetallic Pt-Ga nanoparticles supported on a calcined hydrotalcite, i.e. Pt-Ga/Mg(Al)O_x, have shown to be efficient dehydrogenation catalysts.[11] Upon introduction of Ga into Pt nanoparticles, the degree of coke formation decreases during reaction. In part this is due to the basic nature of the Mg(Al)O_x support, which prevents rapid coke formation during reaction and stabilizes the Pt-Ga clusters.[9, 12] However, Pt-Ga interactions seem to play the leading role in coking prevention. Also, an alkene product selectivity close to 100% is observed on these catalysts in addition to an increased activity.

Recently, a novel method to efficiently produce Pt-Ga bimetallic catalysts has been developed.[11, 13] For this purpose, Ga is first incorporated into the hydrotalcite framework. This

Ga-modified hydrotalcite is then calcined, resulting in a mixed oxide $Mg(Ga)(Al)O_x$ support upon which Pt precursor is impregnated. Subsequent reduction yields Pt-Ga nanoparticles composed of Pt clusters formed at the support surface and Ga from the support framework.[14] The final bimetallic Pt-Ga/$Mg(Ga)(Al)O_x$ catalyst shows superior activity, selectivity and durability compared to conventionally co-impregnated Pt-Ga/$Mg(Al)O_x$ catalysts. Similar methodologies have been developed to synthesize intermetallic Pd-Ga nanoparticles by (partially) incorporating Pd and Ga into the hydrotalcite framework.[15-17]

The different steps in the formation process of these functional materials determine the final state of the active Pt-Ga alloy, and therefore its catalytic performance. Although the performance of the bimetallic Pt-Ga/$Mg(Ga)(Al)O_x$ catalyst has been studied previously[11], the evolution of the Pt phase during catalyst formation has not been investigated in detail. This motivates the main objective of the present study to gain a deeper understanding of the evolution of this Pt phase in order to guide further catalyst optimization efforts.

In situ X-ray absorption spectroscopy (XAS) is well suited for the study of chemical transformations occurring between Pt precursor impregnation and Pt-Ga alloy formation for the following reasons: (1) no long range order is required, making it ideal to study nanoparticles, (2) the technique can be applied *in situ* and (3) its atom specificity yields first hand insights into the local environment of Pt.[18] X-ray absorption near edge structure (XANES) and extended X-ray absorption fine structure (EXAFS) techniques yield respectively average electronic and structural information at the angstrom level.[18, 19] However, throughout the Pt-Ga/$Mg(Ga)(Al)O_x$ formation process several atomic species can be located around Pt (C, O, Pt, Ga, etc.).[20] Discrimination and localization of the atomic species surrounding Pt is challenging using conventional XANES and Fourier transformed EXAFS. Here, this issue is addressed by using wavelet transformed XAS analysis providing simultaneous k- and R-range resolution.[21-25] This technique elucidates the nature of the atomic species corresponding to different R-space peaks and yields more complete structural information which cannot be obtained directly by conventional XANES and EXAFS analysis

alone. In this study, wavelet transformed XAS is shown to be an essential tool to decode the mechanistic details occurring during bimetallic nanoparticle formation processes.

4.2 Experimental

4.2.1 Material synthesis

The $Mg(Ga)(Al)O_x$ support material was produced by the co-precipitation method described by Sun et al.[13]. First, an aqueous solution of $Mg(NO_3)_2.6H_2O$ (Sigma-Aldrich, 98 – 102%), $Al(NO_3)_3.9H_2O$ (Sigma-Aldrich, 98.5%) and $Ga(NO_3)_3.xH_2O$ (Sigma-Aldrich, 99.99%) was mixed with an aqueous solution of Na_2CO_3 (EMD Chemicals Inc., 99.5%) and NaOH (Fisher Scientific, 98.3%). After 24h of room temperature aging, the precipitated support material was filtered and dried at 110 °C. The resulting Ga-incorporated hydrotalcite-like material (HT-Ga) was then calcined in air for 3h at 650 °C, leading to a mixed oxide ($Mg(Ga)(Al)O_x$, Section 4.4.1). For comparison, uncalcined hydrotalcite (HT) and 650 °C calcined hydrotalcite ($Mg(Al)O_x$), both without Ga, were also synthesized.

Second, the Pt precursor was deposited on the $Mg(Ga)(Al)O_x$ support by incipient wet impregnation. For this purpose, a toluene (Sigma-Aldrich, 99.9%) solution of $Pt(acac)_2$ precursor (Sigma-Aldrich, 99.99%) was added to the powder support. Subsequently, toluene was evaporated by heating the sample up to 110 °C. The samples obtained during these synthesis steps are designated as follows: HT, HT-Ga, $Mg(Al)O_x$, $Mg(Ga)(Al)O_x$ and $Pt(acac)_2$ wet impregnated $Mg(Ga)(Al)O_x$. The latter served as starting point for the *in situ* XAS experiments during the bimetallic Pt-Ga formation process and will be called ‘as prepared material’ in the remainder of this paper.

4.2.2 **Material characterization**

Inductively coupled plasma atomic emission spectrometry (ICP-AES) (IRIS Advantage system, Thermo Jarrell Ash) was used to determine the bulk chemical composition of the as prepared material. The sample was mineralized by peroxide fusion. The aimed-for loadings of the as prepared material were 5 wt% Pt, Ga/Pt ~ 2.8, Mg/(Ga + Al) ~ 2.5 and Al/Ga ~ 8.2. The resulting concentrations measured by ICP-AES were 4.35 wt% Pt, 32.4 wt% Mg, 4.21 wt% Ga and 14.3 wt% Al. Therefore, the atomic ratios Ga/Pt, Mg/(Ga + Al), Al/Ga were ~ 2.5, 2 and 8 respectively. The overall Mg:Al:Ga ratio of the metals present in the $Mg(Ga)(Al)O_x$ support was 100:44:6.

Structural analysis was carried out by means of transmission electron microscopy (TEM). Specimens were prepared by immersion of a lacey carbon film on a nickel support grid into the catalyst powder, followed by shaking off the excess powder. Particles sticking to the carbon film were investigated in scanning transmission dark field (STEM-DF) mode. A JEOL JEM2200FSCs-corrected microscope was used, operated at 200 kV and equipped with Schottky-type FEG, EDX JEOL JED-2300D and JEOL incolumn omega filter.

N_2 physisorption at -196 °C was utilized to determine the BET specific surface area using a Gemini V (Micromeritics) set-up. BET values with their 95 % confidence intervals were obtained by regression of the experimental data in the range $0.05<p/p^0<0.30$ with the linear BET equation.

Crystallographic phase analysis of the materials was performed using a Siemens Diffractometer Kristalloflex D5000, with Cu Kα radiation (λ = 0.154 nm). The powder patterns were collected in a 2θ range from 5° to 90° with a step of 0.02° and 30 s counting time at each angle.

4.2.3 X-ray Adsorption Spectroscopy (XAS)

Measurement details. *In situ* XAS measurements were performed at the Pt L_{III} edge (11564 eV) at the DUBBLE beam line[26, 27] of the 6 GeV European Synchrotron Radiation Facility (ESRF) in Grenoble (France) with uniform filling mode (current between 200 and 160 mA). The as prepared material was first sieved, resulting in a 60 – 100 µm grain fraction. This fraction was then diluted with 20 % BN powder to optimize the XAS signal quality. The resulting mixture was loaded into a quartz capillary with 2 mm diameter, wall thickness of 0.01 mm and length of 60 mm (Hilgenberg). This packed capillary was connected to gas feed lines through swagelok® fittings and mounted below a gas blower (FMB Oxford). Gas flows (50 NmL/min) were delivered using the DUBBLE gas rig system.[28] The optics alignment and energy referencing was performed using a Pt foil. XAS scans (± 45 min/EXAFS, ± 5 min/XANES) were taken in transmission mode.

Pt-Ga nanoparticle formation protocol. The formation process, schematically shown in Figure 4.1.1, consists of two parts: (i) temperature programmed oxidation (blue) followed by (ii) temperature programmed reduction (red), both up to 650 °C. First, an oxidative treatment (50 NmL/min of 20% O_2/He) was applied to the as prepared material during stepwise heating (5 °C/min) from room temperature up to 650 °C. Isothermal plateaus were set at room temperature, 350 °C and 650 °C to record XAS scans. Subsequently, the calcined sample was cooled down to 250 °C, where another XAS measurement was performed. The flow was then changed to He (50 NmL/min of 100% He) to flush the lines, and subsequently switched to H_2/He (50 NmL/min of 5% H_2/He) with temperature ramp to 650 °C (5 °C/min). At 350 °C, 450 °C and 650 °C, the temperature ramp was put to hold to record XAS. These isothermal periods each took around 1.5 – 2.25 h.

Data treatment. XAS data reduction and analysis were executed with Athena and Artemis, part of the Demeter 0.9.13 software package.[29] Background subtraction, normalization, $\chi(k)$ isolation and Fourier transformation were performed using the methodology of Koningsberger et al..[18]

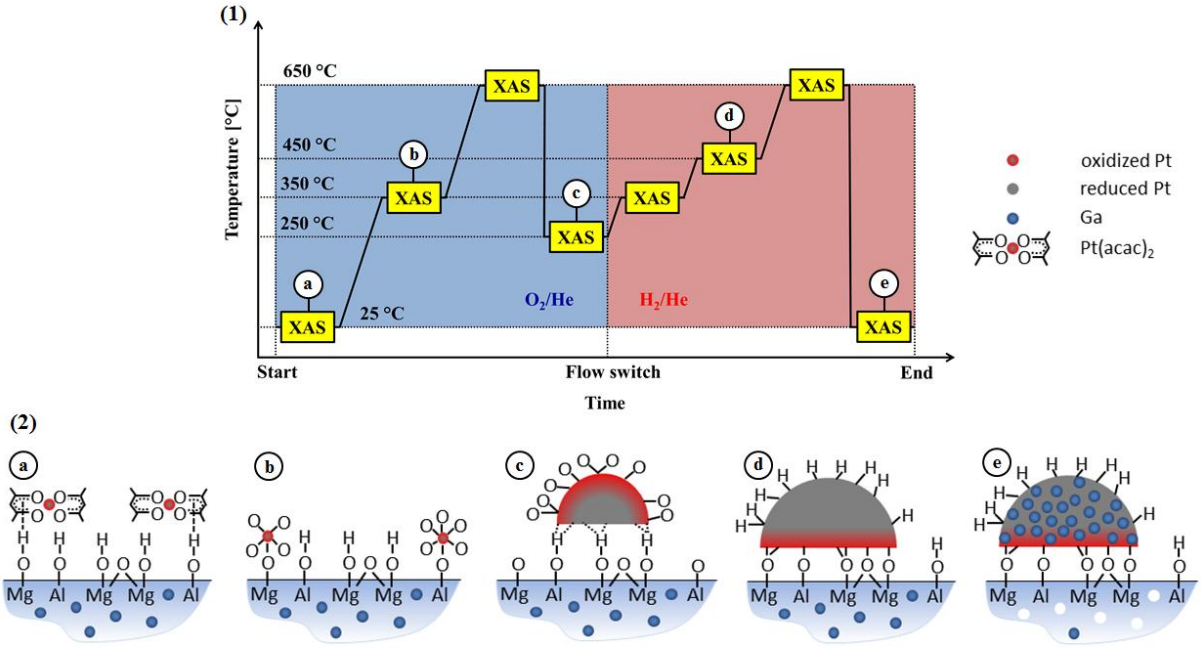

Figure 4.1: (1) process conditions during the formation of Pt-Ga alloyed nanoparticles on $Mg(Ga)(Al)O_x$ support. The temperatures, gas environments and XAS measurements are indicated; (2) schematic representation of the Pt-Ga nanoparticle formation process: (a) $Pt(acac)_2$ molecules adsorbed on $Mg(Ga)(Al)O_x$ support surface after wet impregnation of a $Pt(acac)_2$-toluene solution and consecutive 110 °C drying treatment; (b) fully oxidized five/six fold oxygen coordinated Pt species, atomically dispersed on $Mg(Ga)(Al)O_x$ support surface after oxidation treatment up to 350 °C; (c) Pt cluster formation by Pt-O bond scission during calcination up to 650 °C. The platinum-oxygen bonds at the cluster-support interface have extended bond length (Pt-O_l, ~ 2.5 Å) compared to the Pt-O bonds at the cluster external surface (Pt-O, ~ 2 Å); (d) 450 °C reduction causes sintering of the Pt clusters and the removal of the prolonged Pt-O_l interfacial bonds; (e) 650 °C H_2 reduction results in the transport of Ga support atoms towards the Pt clusters, yielding Pt-Ga alloyed nanoparticles.

The FEFF 6.0 code[30] was used to calculate the phase shifts and backscattering amplitude functions of Pt-C, Pt-O, Pt-Mg, Pt-Al, Pt-Ga and Pt-Pt. The Levenberg-Marquardt algorithm was applied for non-linear least-squares minimization of the objective function in order to estimate the implemented structural parameters. This minimization was carried out by IFEFFIT software[29] through multiple shell fitting in R-space using multiple k-weightings. The R-factor, used to evaluate the agreement between model and experiment, is defined as the ratio of the sum of squared residuals between model and experimental signal relative to the sum of the squared experimental signal. An amplitude reduction factor S_0^2 of 0.85 ± 0.04 was obtained from the fit to the Pt foil reference signal with bulk Pt fcc structure. This value was retained for further Pt L_{III} edge EXAFS modeling of the signals measured during the Pt-Ga formation. The errors reported for the estimated parameters are 66% uncertainty limits.

A Cauchy wavelet of order 200 was used to perform the wavelet transformation of the experimental k²-weighted EXAFS signals (Appendix B.1), unless stated differently. The HAMA Fortran code[31] allowed calculation of the wavelet transformed XAS signals. All EXAFS plots, including Fourier and wavelet transformed, are represented without phase correction. Therefore, the radial distances observed in the EXAFS plots are ~ 0.4 – 0.5 Å below their actual value.

4.3 Wavelet transformed XAS analysis

An X-ray absorption spectrum consists of two parts: (1) the XANES region located around the edge position E_0 ($\leq$ 30 – 50 eV above E_0) and (2) the EXAFS region containing weak oscillatory features situated well above the edge ($\geq$ 30 – 50 eV above E_0). These oscillations contain precise structural information about the local atomic structure around the X-ray absorbing atom.[19] Subjecting these EXAFS oscillations to Fourier transformation facilitates visualization of the coordination numbers, interatomic distances and bond length disorders of the atoms surrounding the absorber.[18] The Fourier transformed EXAFS magnitude is represented as a function of the radial distance R[Å] from the X-ray absorber (R-space). The EXAFS signal is commonly shown as a function of the photoelectron wavenumber k[$Å^{-1}$] (~ $(E - E_0)^{1/2}$, k-space).

Generally, neighbors of the absorber with different atomic masses backscatter the X-ray excited photoelectron in different k-regions within k-space.[18] As a result, the k-space EXAFS signal contains information on the nature of the atomic species. In contrast, the Fourier transformed magnitude in R-space is only sensitive to the k-space signal frequency, but independent of its location in k-space.[20] Therefore, the nature of the atomic species cannot be retrieved based on the Fourier transformed magnitude alone.[32] In addition, decomposing the k-space signal to obtain the separate R-space contributions is a complicated matter. A simultaneous k- and R-space resolution is therefore highly desirable to localize (R-space) and

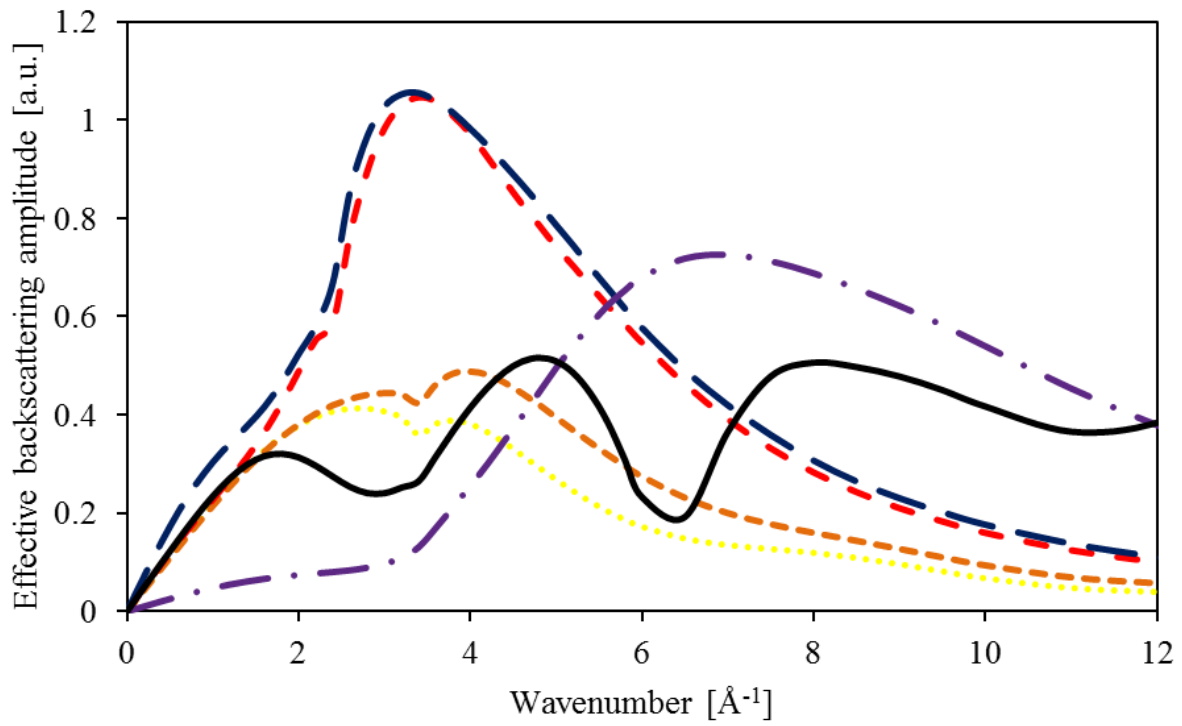

Figure 4.2: effective photoelectron backscattering amplitude functions of C ( ), O ( ), Mg ( ), Al ( ), Ga ( ) and Pt ( ) versus photoelectron wavenumber k.

discriminate (k-space) between atomic species. This is essential when diverse atomic species occur as neighbors within a sample, e.g. during bimetallic nanoparticle formation processes.

Simultaneous k- and R-space resolution can be achieved by performing wavelet transformed XAS analysis. Upon Fourier transformation, infinite periodic sine functions are used to transform the k-space EXAFS signal. The sine function frequency is then a variable which introduces the R-space resolution. Wavelets are square-integrable functions with a zero overall integral.[33] In contrast to the infinite periodic sine function, a wavelet should be considered as a wave packet with finite range. As a result, wavelets have a specific location in k-space which, after wavelet transformation, results in k-space resolution in addition to the R-space resolution.[32] As mentioned before, the simultaneous k- and R-space resolution allows for a proper localization and identification of the atomic species. Wavelet transformed XAS analysis will therefore be used to complement more conventional XANES and Fourier transformed EXAFS analysis in this study.

In Figure 4.2, the effective backscattering functions of C, O, Mg, Al, Ga and Pt are shown. These functions describe the degree of photoelectron backscattering by the neighbors (C, O, Mg, Al, Ga, Pt) of the absorber (Pt) for different photoelectron wavenumbers k. The backscattering functions can be considered as a qualitative fingerprint of the k-region in which a neighbor contributes to the k-space EXAFS signal. Therefore, the following conclusions can be drawn based on Figure 4.2: (i) C, O, Mg and Al backscatter in the same k-region of the EXAFS signal since their backscattering functions are conformal, (ii) Ga backscatters at higher k-range than C, O, Mg and Al and (iii) the Pt backscattering contribution in the EXAFS signal is present in a relatively broad k-range and will dominate at the high k-values. These conclusions are in line with a more general trend of heavier atomic species backscattering in higher k-regions of the EXAFS signal.[20] In Appendix B.2, a more thorough analysis shows that the k-region of backscattering is indeed proportional to the atomic mass (k-region of O < Ga < Pt, since $A_O = 16 < A_{Ga} = 70 < A_{Pt} = 195$), which is observed in both the k-space EXAFS signal and the peak maximum of its wavelet transformed signal.

4.4 Results and discussion

4.4.1 Pre-characterization

Analysis of the XRD patterns of the uncalcined HT and HT-Ga samples reveals that (00*l*) diffractions are present, typical for hydrotalcite[34, 35] (Appendix B.3 - Figure A-10.a-b). This implies that Ga insertion into hydrotalcite preserves its lamellar structure. After 650 °C calcination of the HT and HT-Ga samples, strong MgO peaks are detected in XRD (Appendix B.3 - Figure A-10.c-d). The latter is characteristic for the collapse of the lamellar hydrotalcite structure.[36] In addition, a decreased lattice parameter is obtained for the $Mg(Ga)(Al)O_x$ and

$Mg(Al)O_x$ samples compared to periclase MgO (Table A-4). This suggests that lattice contraction is occurring owing to the incorporation of Al^{3+} and Ga^{3+} into the MgO lattice.[36] The resulting Mg-Ga-Al-O mixed oxide support material is therefore termed as $Mg(Ga)(Al)O_x$, as mentioned before. The presence of other nanostructures or amorphous phases cannot be excluded by XRD analysis alone. However, TEM experiments reveal that the mixed oxide $Mg(Ga)(Al)O_x$ periclase structure is the major phase present. A thorough XRD analysis is provided in Appendix B.3.

Before starting execution of the Pt-Ga nanoparticle formation process with the $Pt(acac)_2$ wet impregnated $Mg(Ga)(Al)O_x$, a XAS scan is recorded at room temperature at the Pt L_{III} edge. The resulting XANES spectrum and the reference spectra of bulk metallic Pt and PtO_2 are shown in Figure 4.3.a. The white line (WL) intensity, i.e. the area below the first maximum at the edge, of the as prepared material is intermediate to the ones of Pt and PtO_2. The Pt L_{III} WL intensity is known to be linearly proportional to the Pt oxidation state.[37] Application of this linear relationship yields an average Pt oxidation state of 2.4+, approaching the 2+ state of $Pt(acac)_2$. It should be noted that oxidation state calculations should be done with care, since coordination, ligands and cluster size can perturb the white line region.

In Figure 4.3.b, the experimental k^2-weighted Fourier transformed EXAFS signal is shown in R-space. $Pt(acac)_2$ is used as a structure to model this experimental signal, yielding good correspondence between theoretical and experimental signal (Figure 4.3.b, R-factor = 0.014). The R-space peak around 1.6 Å (phase uncorrected) corresponds to the first oxygen shell around Pt. A fourfold Pt-O coordination (Table 4.1, O_2 – 25 °C) is obtained by EXAFS modeling, in full agreement with the oxygen coordination around Pt atoms in the $Pt(acac)_2$ structure ($H_7C_5O_2$-Pt-$O_2C_5H_7$). The Debye-Waller factor amounts to 1.5×10^{-3} Å². This rather low value indicates a high degree of structural order of the oxygen atoms around the Pt atom, characteristic for the planar configuration of the $Pt(acac)_2$ molecule. Womes et al.[38] found similar values for the oxygen coordination number and Debye-Waller factor before

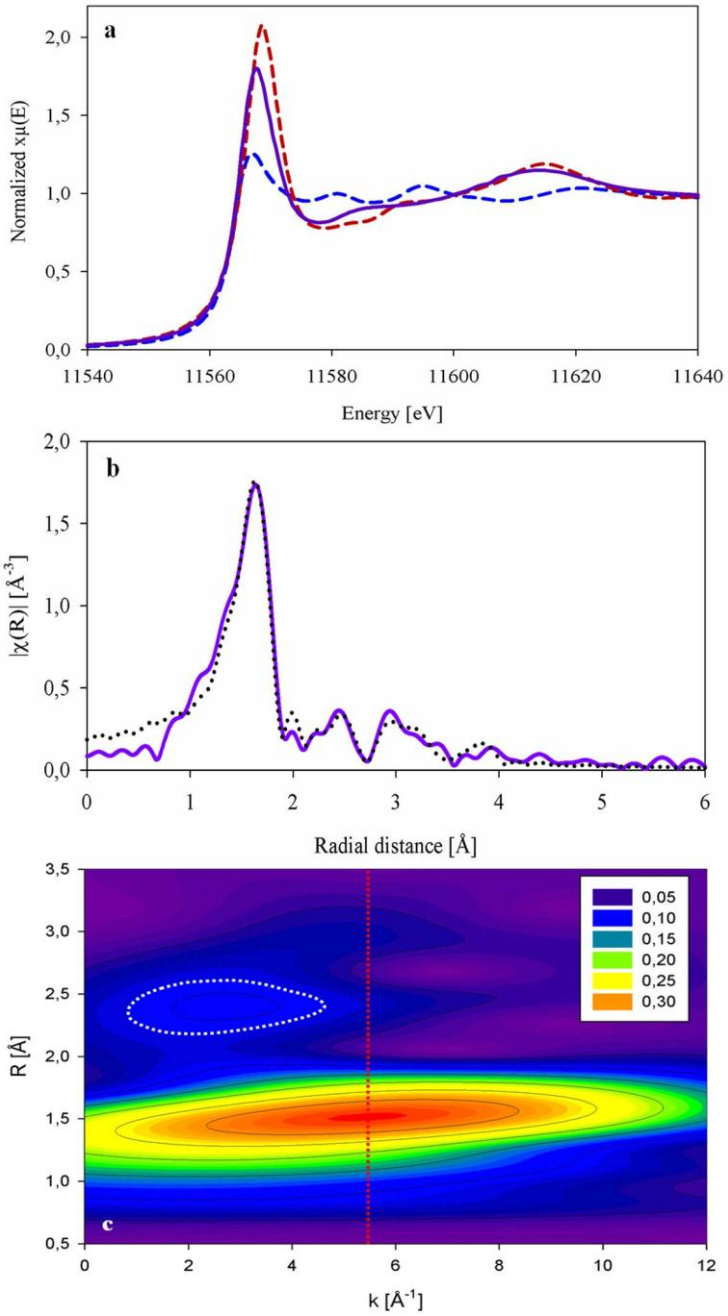

Figure 4.3: XAS at 25 °C in O_2/He. (a) XANES spectra of the as prepared material (——), Pt (– – –) and PtO_2 (– – –) references; (b) Fourier transformed k²-weighted EXAFS signal of as prepared material (——) and model fit (·····) using $Pt(acac)_2$ model (R-factor = 0.014); (c) wavelet transformed XAS signal of Pt/Mg(Ga)(Al)O_x. The red dashed line shows that the peak around R ~ 1.5 Å is in a higher k-region than the one at 2.4 Å, the latter indicated by the white dashed line.

decomposition of $Pt(acac)_2$ molecules. The higher shells mainly originate from carbon atoms present at higher radial distances around Pt in the $Pt(acac)_2$ structure. The structural parameters obtained for these higher shell contributions are in line with the expectations for the $Pt(acac)_2$ structure (not shown in Table 4.1).

In Figure 4.3.c, the wavelet transformed EXAFS signal at room temperature is represented in a 2D contour plot. On the vertical axis, the radial distance R from the Pt absorber is shown. A simultaneous k-space resolution is shown for each R-space value on the horizontal axis. Therefore, the k-region of photoelectron backscattering of the R-space peaks can be retrieved. As mentioned before, this region of backscattering varies for different atomic species, especially when their atomic masses differ significantly (Figure 4.2). In this way, wavelet transformed XAS facilitates the assignment of atomic species to R-space peaks.

An intense peak is present around R = 1.5 Å with maximum k-region of backscattering around 5.5 $Å^{-1}$. This region of backscattering can be identified as originating from O (Appendix B.2), in line with the Fourier transformed EXAFS results. A second less intense peak is seen around R = 2.4 Å (white dashed line). The k-value of maximum backscattering is much lower compared to the oxygen peak, namely around k = 3 $Å^{-1}$. This low k-space peak can be linked to the presence of C atoms in the higher shells around Pt leading to multiple scattering photoelectron paths. Three photoelectron scattering paths within $Pt(acac)_2$ contribute significantly to the Fourier transformed EXAFS signal within the R-range of 2 – 3 Å: two single scattering Pt-C-Pt paths (~ 2.4 and 2.7 Å in phase uncorrected space) and one obtuse triangular Pt-O-C-Pt double scattering path (~ 2.6 Å in phase uncorrected space). The single scattering Pt-C-Pt paths are expected to have a similar photoelectron backscattering region in k-space as Pt-O-Pt (Figure 4.2), since C and O atomic masses are similar. However, it is known that multiple scattering paths contribute in the XANES region at low k-values, i.e. $0 < k < 3$.[18, 22, 39] The double scattering Pt-O-C-Pt path therefore lies at the origin of the backscattering peak at low k-value around R = 2.5 Å. Hence, the low k-range multiple scattering peak is a signature of the acac ligands around Pt in the as prepared material.

These results show that (i) the $Pt(acac)_2$ molecules are deposited successfully on the $Mg(Ga)(Al)O_x$ support and (ii) do not decompose significantly after toluene evaporation at 110 °C – the last synthesis step to produce the as prepared material – since the precursor

structure remains intact. Therefore, the interaction between the $Pt(acac)_2$ molecules and the $Mg(Ga)(Al)O_x$ support surface is not sufficiently strong to break up the precursor ligands.[38, 40]

The subtle increase of the Pt oxidation state from 2+ to 2.4+ can possibly be explained by a mechanism suggested by Kenvin et al.[40] for physisorbed $Pt(acac)_2$ molecules on hydroxylated silica surfaces. In the latter case, hydrogen bonds between OH groups of the surface and the oxygen atoms of the acac ligands or the π-electron system of the chelate ring are formed. This interaction is likely to induce the withdrawal of electron density from Pt towards the acac ligands. Therefore, the Pt density of unoccupied 5d states increases, leading to an increased WL intensity, which manifests itself as a higher value for the Pt oxidation state. The increased value for the Pt oxidation state in this study is therefore possibly caused by the interaction between the $Pt(acac)_2$ molecule and the $Mg(Ga)(Al)O_x$ support surface (Figure 4.1.a). However, precursor chemisorption on the support surface cannot be excluded.

4.4.2 Oxidative heating from room temperature up to 350 °C

During the calcination of the sample up to 350 °C, the XANES WL intensity (Figure 4.4.a) strongly increases compared to the one at room temperature (Figure 4.3.a). An average Pt oxidation state of ~ 4+ is obtained at 350 °C, showing a complete oxidation of the Pt phase. In addition, the XANES spectrum becomes more PtO_2-like, although small features in the multiple scattering region perturb full correspondence with the bulk PtO_2 reference spectrum.

In R-space (Figure 4.4.b), the Fourier transformed k^2-weighted EXAFS signal exhibits peak features similar to the bulk PtO_2 signal, although with lower peak intensities. Both XANES and Fourier transformed EXAFS observations suggest a PtO_2-like structure.

A first shell fit of the nearest neighboring peak around ~ 1.6 Å (~ Pt-O) yields good correspondence to the data using a single O shell model (Figure 4.4.b, R-factor = 0.005). The oxygen coordination number increases from 4 before to 5.3 after the 350 °C calcination (Table 4.1, O_2 – 25 °C and 350 °C). In addition, a strongly increased Debye-Waller disorder

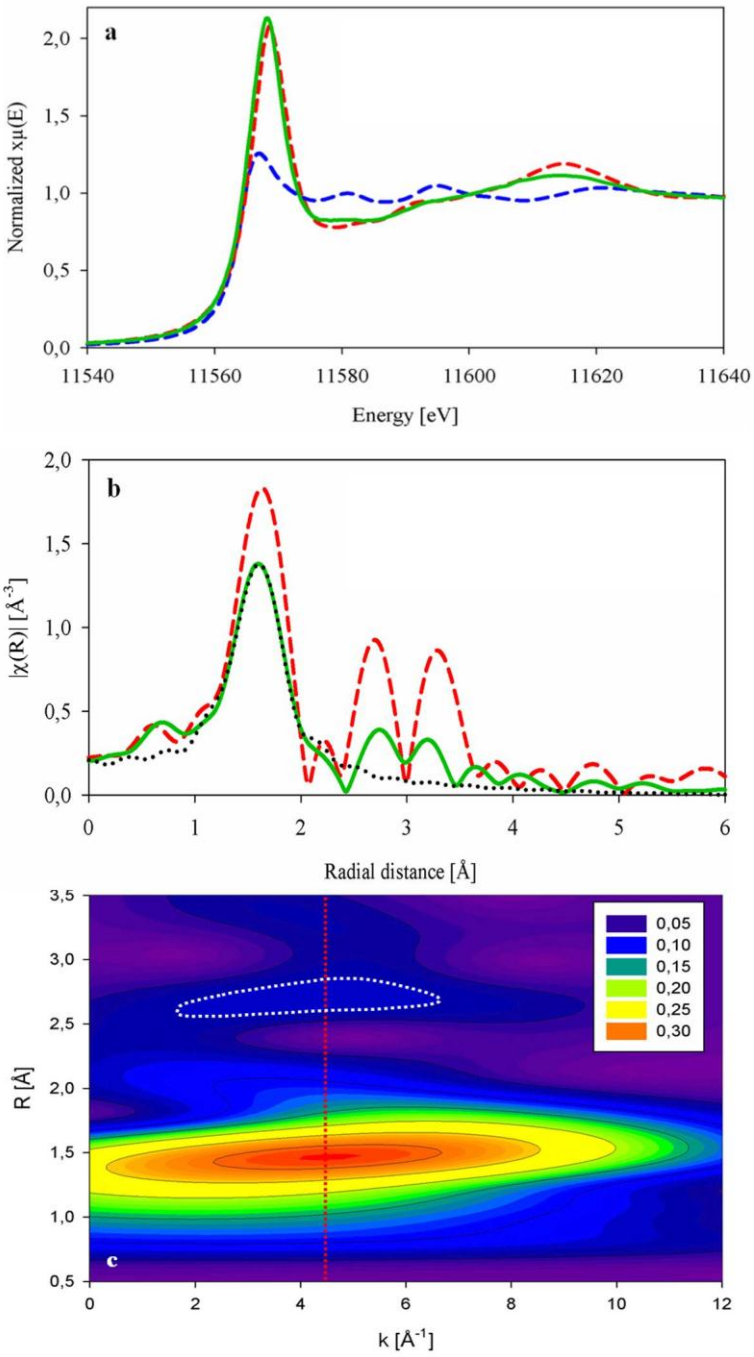

Figure 4.4: XAS at 350 °C calcination in O_2/He. (a) XANES spectra of Pt/Mg(Ga)(Al)O_x (——), Pt (– – –) and PtO_2 (– – –) references; (b) Fourier transformed k²-weighted EXAFS signal of Pt/Mg(Ga)(Al)O_x (——), PtO_2 (– – –) reference and model fit (·····) with single O shell (R-factor = 0.005); (c) wavelet transformed XAS signal of Pt/Mg(Ga)(Al)O_x. The peak at R ~ 1.5 Å occurs in the same k-region (red dashed line) as the one ~ 2.7 Å (white dashed circle).

factor is obtained: from 1.5 × 10^{-3} Å² at room temperature to 6.6 × 10^{-3} Å² after oxidative heating to 350 °C. Further attempts to model the higher shells around Pt with the full PtO_2 structure failed. This is not surprising since PtO_2 is unstable during heating.[41]

At this point, the actual nature of the atoms in the higher shells around Pt is unknown. A PtO_2 structure is inappropriate to model the higher shells of the experimental EXAFS signal. In addition, the shapes of the R-space EXAFS profiles at 25 °C and 350 °C do not differ significantly. It therefore remains challenging to unambiguously assign the nature and location of atomic species in the higher shells using conventional XANES and EXAFS methodology. Wavelet transformation of the EXAFS signal can resolve this issue by discriminating and localizing the atomic species present.

The wavelet transformed EXAFS contour plot of the material after calcination at 350 °C is shown in Figure 4.4.c. Similar to the as prepared material (Figure 4.3.c), the intense oxygen peak around R = 1.5 Å remains present. Its peak maximum is situated at somewhat lower k-value compared to before calcination, namely 4.5 versus 5.5 $Å^{-1}$ at room temperature (Figure 4.3.c). This is explained by the temperature increase, which causes the wavelet transformed peaks to shift to lower k-region (Appendix B.2). The weak peak around k = 3 $Å^{-1}$ before calcination (white dashed line, Figure 4.3.c, R = 2.4 Å) has shifted to higher k-value after calcination up to 350 °C (white dashed line, Figure 4.4.c, R = 2.7 Å). Moreover, the maxima of the O peak at R = 1.5 Å and the peak at 2.7 Å have evolved to the same k-value.

The peak around R = 2.7 Å is expected to originate from Mg, Al and O, i.e. the support material. As mentioned in Section 4.3, these elements have quasi-conformal backscattering functions (Figure 4.2) due to their similar atomic masses (A_O = 16, A_{Mg} = 24, A_{Al} = 27). Therefore, the peak maxima in the wavelet transformed signal occur in the same k-region as O. In addition, the disappearance of the peak at R = 2.4 Å in the low k-region (k = 3 $Å^{-1}$) implies that Pt-O-C-Pt double scattering does not occur anymore after the 350 °C calcination. Further, no high k-range peaks are present in the 2 – 3 Å range of the contour plot in Figure 4.4.c. Therefore, no Pt is present in the neighborhood of the Pt absorber since Pt has a non-negligible backscattering amplitude in the higher k-range (Figure 4.2, Appendix B.2).

The above findings from XANES WL analysis, EXAFS modeling and wavelet transformed XAS lead to the following conclusions regarding the first step of Pt-Ga

nanoparticle formation. During oxidative heating, the adsorbed $Pt(acac)_2$ molecules decompose through oxidation of the acac ligands. At 350 °C, Pt atoms are fully oxidized (4+) and have a five/six fold oxygen coordination (N_{Pt-O} = 5.3). A fraction of these 2.0 Å Pt-O bonds consists of bonds between the Pt cation and support oxygen, whereas the remainder fraction involves bonds of Pt with chemisorbed oxygen (Figure 4.1.b). Pt resides as atomically dispersed species at the $Mg(Ga)(Al)O_x$ support surface which do not cluster at 350 °C (no high k-range Pt peaks in Figure 4.4.c). Finally, no PtO_2 bulk is formed, since in that case a Pt peak should also be present at higher k-ranges.

4.4.3 **Oxidative heating from 350 °C to 650 °C and cooling down to 250 °C**

After oxidative heating to 350 °C, the sample is further calcined up to 650 °C at which temperature a XAS scan is recorded. Subsequently, the material is cooled down to 250 °C in O_2/He (Figure 4.1.1) to record another isothermal XAS measurement.

In Figure 4.5.a, the XANES spectra at both 650 °C and 250 °C are shown together with the bulk PtO_2 and metallic fcc Pt references. Two features are worth mentioning. First, the full XANES spectra at 650 °C and 250 °C are identical, both in their WL intensity and the multiple scattering region. The latter region is known to be very sensitive to structural changes.[42-44] It can therefore be safely assumed that no changes occur around Pt during cooling down. Second, the oxidation state after calcination amounts to ~ 2.4+, i.e. $Pt^{2.4+}$ at 650 °C and 250 °C, and is equal to the one of the $Pt(acac)_2/Mg(Ga)(Al)O_x$ as prepared material (Figure 4.3.a). In contrast, major differences are observed in their respective multiple scattering regions. Before calcination, the multiple scattering region of $Pt(acac)_2/Mg(Ga)(Al)O_x$ is PtO_2-like. After the 650 °C calcination, metallic Pt-like oscillations are visible in the XANES multiple scattering region. This strongly indicates that important structural changes occur during calcination between 350 °C and 650 °C, namely metallic fcc Pt phase formation.

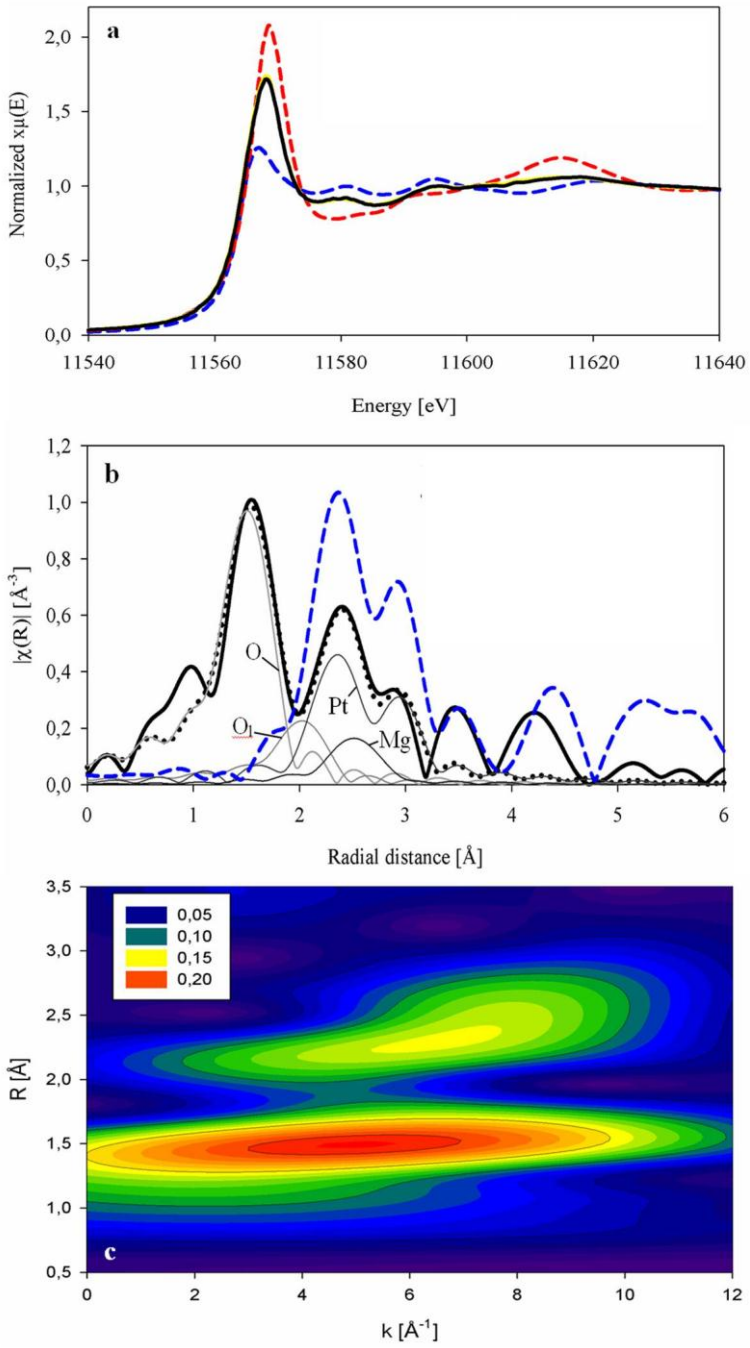

Figure 4.5: (a) XANES spectra of Pt/Mg(Ga)(Al)O_x at 650 °C (——) and cooled down to 250 °C (——) in O_2/He, Pt (– – –) and PtO_2 (– – –) references; (b) Fourier transformed k²-weighted EXAFS signal of Pt/Mg(Ga)(Al)O_x at 250 °C in O_2/He (——), four shell model (Pt-O, Pt-O_l, Pt-Pt, Pt-Mg) fit to data (·····) and its separate shell contributions as indicated, Pt reference (– – –); (c) wavelet transformed XAS signal at 250 250 °C in O_2/He.

The k²-weighted Fourier transformed EXAFS magnitude after calcination and cooling down to 250 °C is plotted in Figure 4.5.b. This EXAFS profile is representative for both structures of the Pt phase at 650 °C and 250 °C, since their XANES spectra are identical. In addition to this EXAFS profile, the reference signal of metallic fcc Pt is shown in R-space.

Two contributions can be distinguished in the experimental R-space signal: (i) a Pt-O first nearest neighbour shell around 1.6 Å and (ii) a metallic fcc Pt profile beyond 2 Å (both phase uncorrected).

Initially, one Pt-O ~ 2.0 Å and Pt-Pt shell ~ 2.75 Å are used in an attempt to model these contributions of the R-space signal. Some correspondence between model and experimental signal is obtained (R-factor = 0.052). However, adding a second – longer – oxygen shell Pt-O_l ~ 2.5 Å and a Pt-Mg shell ~ 2.95 Å leads to further improvement of the correspondence between fit and data (R-factor = 0.015). O_l and Mg represent support oxygen and magnesium respectively. Note that the Pt-Mg shell captures both Al and Mg contributions originating from the Mg(Ga)(Al)O_x support since both Al and Mg have identical backscattering functions (Figure 4.2). Application of an F-test[45] for model discrimination yields a 69.3% confidence in the four shell model (Pt-O, Pt-O_l, Pt-Pt, Pt-Mg), implying a significant improvement. The R-space fit of this model to the experimental EXAFS signal is represented in Figure 4.5.b, showing the four different shell contributions. The modeling results are presented in Table 4.1 (O_2 – 250 °C). It should be noted that for the sake of robustness and statistical significance of parameter estimation, only one Debye-Waller factor is considered for all four shells (Pt-O, Pt-O_l, Pt-Pt, Pt-Mg). Therefore, the estimate obtained for this disorder factor can only approximate the true values of Debye-Waller factors of the separate shells.

The wavelet transformed EXAFS signal of the material after 650 °C calcination and cooling down to 250 °C is plotted in Figure 4.5.c. The oxygen peak is present at R ~ 1.5 Å. After 650 °C calcination, another intense peak appears between R = 2 – 3 Å with its peak maximum situated at higher k-values (k ~ 7 $Å^{-1}$) compared to the O peak (Figure 4.5.c). This peak can be assigned to a Pt contribution ($A_{Pt} > A_O$ and therefore k-region Pt > O, Appendix B.2). As in the Fourier transformed EXAFS signal, the Pt peak dominates the Pt-O_l and Pt-Mg/Al contributions. This largely hinders a proper detection of the support species by visual inspection of the wavelet/Fourier transformed EXAFS signals.

As mentioned before, at 350 °C, atomically dispersed Pt species are anchored to the support by bonds between Pt and support oxygen. During high temperature treatment up to 650 °C, these Pt-O support bonds are expected to break due to increased thermal disorder.[46] Lytle et al.[46] and Nagai et al.[47] suggested that such Pt-O support bond scission leads to more mobile Pt, in turn leading to agglomeration/sintering. The latter results in the appearance of Pt-Pt bonds after calcination up to 650 °C in the Fourier and wavelet transformed EXAFS signals (Figure 4.5.b-c). Therefore, the increase (decrease) in Pt-Pt (Pt-O) coordination during 650 °C calcination evidences the agglomeration of atomically dispersed Pt species into Pt clusters (Table 4.1, O_2 – 350 °C, O_2 – 250 °C).

Judging by the low Pt-Pt coordination (N_{Pt-Pt} = 3.4 ± 1.4, Table 4.1, O_2 – 250 °C), these clusters have sub-nanometer dimensions and contain 3 – 11 Pt atoms.[48] Simulations have shown that the Pt-Pt fourth shell coordination number approaches 0 for sub-nanometer (hemi-)spherical nanoparticles.[48, 49] This is in full agreement with the Fourier transformed EXAFS signal at 250 °C (Figure 4.5.b) in which no significant Pt-Pt fourth shell amplitude can be observed between 5 and 6 Å. However, the absence of this Pt-Pt fourth shell amplitude can also be ascribed to badly crystallized nanoparticles. Also, the presence of a metallic fcc Pt EXAFS profile in Figure 4.5.b ensures that the Pt clusters are fcc packed.

The fundamental reason for the formation of these small sub-nanometer Pt clusters can be addressed by considering the basicity of the Mg(Ga)(Al)O_x support material. Nagai et al.[47] and Yoshida et al.[50] reported that the support basicity can be correlated to the Pt-O-M bond strength (M = support metal). More basic supports, e.g. (earth) alkali oxides, display a stronger Pt-O-M interaction which promotes the increased stabilization of Pt within the Pt-O-M support bond. A stronger Pt-O-M bond (partially) inhibits migration of Pt species over the support surface eventually leading to the formation of smaller clusters, if any are formed.

The support basicity is expected to decrease with increasing Sanderson electronegativity. MgO is known to have a low Sanderson electronegativity of 2.19[51], implying that it is a strong basic support forming strong Pt-O-Mg bonds. In contrast, the

higher electronegativities of Al_2O_3 and Ga_2O_3, being 2.70 and 3.10 respectively[51], should result in a decreased basicity of the $Mg(Ga)(Al)O_x$ support compared to MgO. Di Cosimo et al.[52-54] indeed showed that the density and strength of the basic surface sites on $Mg(Al)O_x$ supports decreased with increasing Al concentration. However, since the abundance of Mg in the support is predominant compared to the amounts of Al and Ga, the latter two only somewhat weaken the strong support basicity originating from MgO. The overall strong basicity exerted by $Mg(Ga)(Al)O_x$ could therefore cause a strong Pt-support interaction. During 650 °C calcination, the thermally induced Pt-O-M bond scission is then (partially) hindered. This leads to the formation of smaller sub-nanometer Pt clusters compared to Pt clusters on more acidic supports, e.g. Pt/γ-Al_2O_3.[55, 56]

When sub-nanometer Pt clusters are formed, a relatively high fraction of the Pt atoms are bound to the support, allowing the detection of the support in the local environment of Pt. Indeed, the presence of longer Pt-O_l and Pt-Mg/Al bonds in addition to Pt-Pt and Pt-O bonds is suggested by EXAFS modeling after cluster formation during calcination (Table 4.1, O_2 – 250 °C). It is therefore hypothesized that Pt atoms at the nanoparticle-support interface interact with the support by making longer Pt-O_l (~ 2.5 Å) and Pt-Mg/Al (~ 2.95 Å) interfacial bonds. In contrast to strong ion-ion Pt-O bonds, Pt-O_l bonds reported here most likely originate from weaker induced dipole-ion interactions between metallic Pt^0 and $(OH)^-$ surface groups.[57] The presence of H in between support oxygen and Pt atoms at the interface leads to the observation of longer Pt-O_l bonds compared to common Pt-O bonds. These extended Pt-O_l bonds were previously reported after low temperature reduction (< 350 °C)[58], vacuum treatment on MgO supports[59] and under NO + O_2 environment[60]. In addition, the Pt-O_l bond formation was confirmed by theoretical calculations for small Pt clusters on hydroxylated γ-Al_2O_3.[61, 62]

After 650 °C calcination, the results indicate that sub-nanometer sized fcc Pt clusters are anchored to the $Mg(Ga)(Al)O_x$ support surface through 2.5 Å Pt^0-O_l interfacial bonds. However, these Pt clusters are partially oxidized as indicated by the intermediate $Pt^{2.4+}$

oxidation state (XANES) and the Pt-O shell contribution (EXAFS). The cluster core is metallic fcc Pt and Pt atoms at the cluster-support interface are expected to be metallic Pt^0 too. Therefore, oxidized Pt atoms should be situated at the cluster exterior surface and bind chemisorbed oxygen (Figure 4.1.c). This results in a Pt-O contribution in the EXAFS signal at 250 °C (Figure 4.5.b, Table 4.1, O_2 – 250 °C).

4.4.4 Stepwise reductive heating from 250 °C to 450 °C

After the XAS measurement at 250 °C, the flow is switched from O_2/He to H_2/He. Thereafter, the calcined sample is heated from 250 °C to 350 °C and subsequently up to 450 °C. Isothermal XAS scans are recorded at 350 °C and 450 °C.

The XANES spectra at 250 °C in O_2/He and 350 °C and 450 °C in H_2/He are compared in Figure 4.6.a. A gradual decrease in the WL intensity is observed during stepwise reductive heating in H_2/He. The average Pt oxidation state decreases from $Pt^{2.4+}$ (250 °C) to $Pt^{0.4+}$ (450 °C), showing that reduction takes place. In addition, a gradual evolution of the multiple scattering region towards the XANES profile of the metallic Pt state is observed.

The Fourier transformed EXAFS magnitudes at 250 °C in O_2/He and 350 °C and 450 °C in H_2/He are shown in Figure 4.6.c. Although the temperature increase during reduction has a considerable impact on the Fourier transformed signals, the same peaks remain present in these signals. This suggests that the Pt cluster structure largely persists during reduction.

The Fourier transformed EXAFS signal at 450 °C in H_2/He is modeled by using a single Pt-O (~ 2 Å) and Pt-Pt (~ 2.75 Å) shell. In contrast to the Fourier transformed EXAFS signal at 250 °C, good agreement between this two shell model (Pt-O, Pt-Pt) and the experimental signal is obtained (Figure 4.6.c, R-factor = 0.016). The low R-factor indicates that a further increase of the model complexity, i.e. inclusion of Pt-O_l and Pt-Mg shells, is unnecessary. Equivalently, Pt-O_l and Pt-Mg do not contribute significantly to the EXAFS signal at 450 °C.

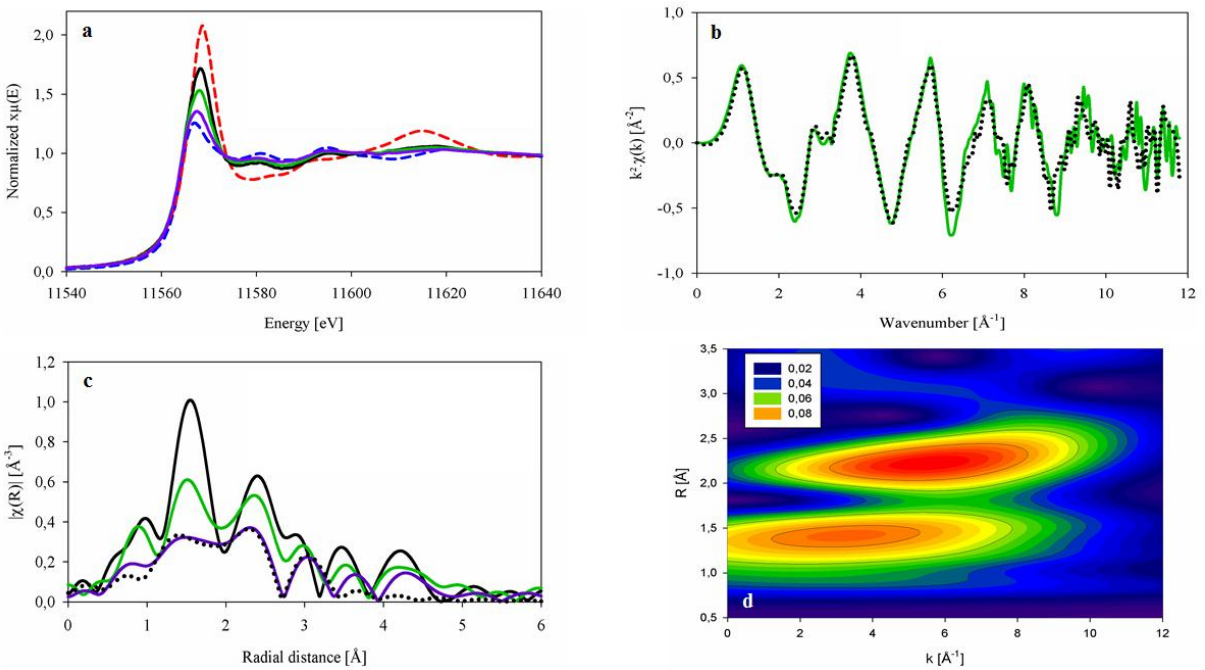

Figure 4.6: (a) XANES spectra of Pt/Mg(Ga)(Al)O_x at 250 °C in O_2/He (——), 350 °C (——) and 450 °C (——) in H_2/He, Pt (– – –) and PtO_2 (– – –) references; (b) k²-weighted EXAFS signal of Pt/Mg(Ga)(Al)O_x at 350 °C in H_2/He (——) and the linear combination fitting (LCF) result (·····) using the EXAFS signals of Pt/Mg(Ga)(Al)O_x at 250 °C and 450 °C; (c) Fourier transformed k²-weighted EXAFS signal of Pt/Mg(Ga)(Al)O_x at 250 °C in O_2/He (——), 350 °C (——) and 450 °C (——) in H_2/He, O + Pt shell model fit (·····); (d) wavelet transformed XAS signal of Pt/Mg(Ga)(Al)O_x at 450 °C in H_2/He.

The wavelet transformed EXAFS signal recorded in H_2/He at 450 °C is shown in Figure 4.6.d. Similar O (R = 1.5 Å) and Pt (R = 2 – 3 Å) peaks are present as compared to the signal after calcination at 250 °C in O_2/He (Figure 4.5.c). During reduction from 250 °C to 450 °C, only their relative intensities alter: the O peak loses intensity compared to the Pt peak. These findings reconfirm that reduction of the oxidized part of the Pt phase is taking place.

Modeling the signal recorded at 350 °C in H_2/He using the two or four shell model did not yield good convergence. However, linear combination fitting (LCF) of this 350 °C XAS signal by using the spectra at 250 °C and 450 °C, yields excellent correspondence both in the XANES and EXAFS region (Figure 4.6.b, $\chi(k)_{350\,°C} \approx 0.5 \times \chi(k)_{250\,°C} + 0.5 \times \chi(k)_{450\,°C}$). This indicates that the Pt state at 350 °C is intermediate to the ones at 250 °C and 450 °C.

During H_2 reduction up to 450 °C, the prolonged Pt-O_l cluster-support interfacial bonds disappear and are replaced by (common) shorter Pt-O bonds, probably changing the cluster-support interaction. This evolution is in correspondence with other studies[49, 57, 63]

showing that Pt-O_l bonds disappear above 350 °C in H_2 environment. At 450 °C, therefore, platinum-oxygen bonds at the cluster-support interface cannot be distinguished from Pt-O bonds at the cluster exterior surface.

The increase in the Pt-Pt coordination number N_{Pt-Pt} during reduction from 250 °C to 450 °C (Table 4.1, O_2 – 250 °C, H_2 – 450 °C) implies that additional nanoparticle sintering is occurring (Figure 4.1.d). The Pt cluster shape does not change significantly during sintering since the R-space EXAFS signal shape remains largely unchanged during reduction to 450 °C (Figure 4.6.c). Pt dispersion decreases upon sintering, resulting in a decrease in the fraction of exposed Pt atoms. Therefore, the decrease in Pt-O bonds (Table 4.1: O_2 – 250 °C, H_2 – 450 °C) and Pt oxidation state (Figure 4.6.a, WL decrease) originates from (i) nanoparticle sintering and/or (ii) oxygen removal at the cluster exterior surface through H_2 reduction. In general, the reduction of the Pt phase is corroborated through the decrease in N_{Pt-O} to N_{Pt-Pt} ratio, evolving from N_{Pt-O}/N_{Pt-Pt} ~ 0.8 at 250 °C to 0.2 after 450 °C H_2 reduction. It should be noted that the increased Debye-Waller factor during reduction is caused by increased thermal disorder at elevated temperatures.

In comparison to other studies[55, 64], a difficult reduction of Pt is noticed. Nagai et al.[55] observed a more deep reduction of Pt clusters for catalysts with different supports at similar reduction conditions. In addition, Grunwaldt et al.[64] generally obtained a close to complete reduction of Pd for Pd/Al_2O_3 catalysts after a room temperature 5% H_2/He reduction treatment. The small Pt cluster size can be thought of as a possible cause for the difficult reduction. Small clusters have relatively high fractions of cluster-support interface Pt atoms. At 450°C in H_2/He, these atoms are expected to be oxidized owing to the strong Mg(Ga)(Al)O_x support interaction. This will lead to a higher average oxidation state for small clusters compared to larger ones.

4.4.5 **Reductive heating from 450 °C to 650 °C**

As a last step in the Pt-Ga formation process, an additional H_2/He treatment on Pt/Mg(Ga)(Al)O_x is applied from 450 °C up to 650 °C. At 650 °C, the XAS data quality only permits the application of the XANES spectra. In Figure 4.7.a, both the XANES spectra at 450 °C and 650 °C are shown in addition to the bulk Pt and PtO_2 references. From 450 °C to 650 °C, the WL peak height decreases and the edge energy shifts to higher energies.

Giedigkeit et al.[65] and Hsu et al.[66] obtained similar XANES spectra for $PtGa_2$ alloys. Bus et al.[67] simulated the Pt L_{III} edge XANES spectra during PtAu alloying. They concluded that interatomic charge transfer from Au to Pt resulted in a positive shift in the edge energy and a decreased WL intensity. Hence, in the present study, the shift in edge energy and the decreased WL intensity at 650 °C could be assigned to charge transfer from Ga to Pt. This charge transfer is likely to occur since the electronegativity of Ga (1.81 eV) is below that of Pt (2.28 eV). The electron transfer then leads to the stabilization of a bimetallic Pt-Ga bond, resulting in Pt-Ga alloying.

Since obtaining good EXAFS data quality at 650 °C is very challenging, a spectrum of the activated Pt-Ga alloyed catalyst is recorded at room temperature after cooling down from 650 °C in H_2/He. In Figure 4.7.b, the resulting k^2-weighted Fourier transformed EXAFS signal is represented. Compared to the measurement at 450 °C (Figure 4.6.c), the Pt-O and Pt-Pt shells are replaced by a single shell at intermediate position of ~ 2.1 Å (~ 2.5 – 2.6 Å in phase corrected space) (Figure 4.7.b). As the characteristic Pt-Ga bond length is ~ 2.50 Å[68], this peak position suggests that Pt-Ga bonds (partially) replace the original Pt-O and Pt-Pt bonds observed during reduction up to 450 °C.

For unambiguous evidence of the presence of Ga in the local environment of Pt, wavelet transformed analysis is applied to the EXAFS spectrum after 650 °C reduction. For proper comparison, the latter analysis is also applied to an additional room temperature EXAFS measurement recorded after the 450 °C reduction, i.e. before alloying. In Figure 4.7.c and Figure 4.7.d, the wavelet transformed XAS signals (Cauchy order = 200) are shown both

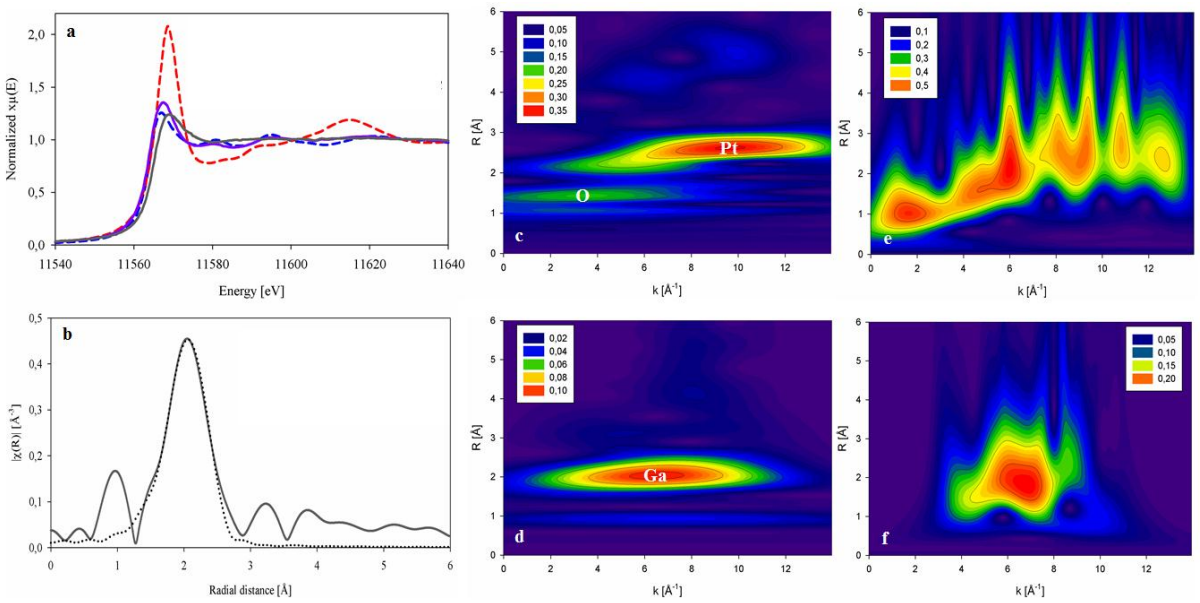

Figure 4.7: (a) XANES spectra of (pre-)catalyst at 450 °C (——) and 650 °C (——) in H_2/He, Pt (– – –) and PtO_2 (– – –) references; (b) Fourier transformed k²-weighted EXAFS signal of final catalyst at room temperature after cooling down from 650 °C in H_2/He (——), model fit (·····) using single Ga shell (R-factor = 0.018); wavelet transformed XAS signal of Pt/Mg(Ga)(Al)O_x at room temperature after 450 °C reduction in H_2/He, (c) Cauchy order 200, (e) Cauchy order 5; wavelet transformed XAS signal at room temperature after 650 °C reduction in H_2/He, (d) Cauchy order 200, (f) Cauchy order 5.

after 450 °C and 650 °C H_2/He reduction respectively. After the 450 °C reduction, both O (~ R = 1.5 Å, k = 4 $Å^{-1}$) and Pt (~ R = 2.7 Å, k = 10 $Å^{-1}$) contributions are present. In contrast, after the 650 °C reduction, O and Pt peaks disappear and one Ga peak (~ R = 2 Å, k = 6 – 7 $Å^{-1}$) emerges. The intermediate atomic mass of Ga (A_{Ga} = 70) compared to O (A_O = 16) and Pt (A_{Pt} = 195) causes the Ga peak to appear at k-values intermediate to O and Pt (Appendix B.2). As elaborated in Appendix B.2, the peak maxima of O and Pt (Figure 4.7.c) occur at different k-values compared to the ones after reduction at 450°C (Figure 4.6.d) due to the difference in measurement temperatures.

The presence of Ga can be evidenced more clearly by decreasing the Cauchy order (Appendix B.1) and thereby increasing the k-space resolution of the wavelet transformed XAS signal. In Figure 4.7.e and Figure 4.7.f, the wavelet transformed XAS signals with Cauchy order 5 after 450 °C and 650 °C H_2/He reduction are shown, respectively. With this value of the Cauchy order, the k-space resolution improves significantly at the expense of the R-space resolution. This permits a more detailed investigation of the backscattering region of the neighbouring atoms around Pt. The intense high k-range Pt peak after 450 °C reduction (~

R = 2.7 Å, k = 10 $Å^{-1}$, Figure 4.7.c) participates in photoelectron backscattering events over the entire investigated k-range (Figure 4.7.e). In contrast, the Ga peak after 650 °C reduction (~ R = 2 Å, k = 6 – 7 $Å^{-1}$, Figure 4.7.d & f) exhibits a localized backscattering region with maximum peak intensity around 6 – 7 $Å^{-1}$. This fully agrees with the backscattering function evolution of Pt and Ga shown in Figure 4.2: Ga exhibits a monomodal backscattering function while a multimodal evolution is seen for Pt.

Consistent with Redekop et al.[14], these results show that Pt-Ga alloying occurs during reductive heating between 450 °C and 650 °C. Modeling of the Fourier transformed EXAFS signal after 650 °C H_2/He reduction yields a good fit (R-factor = 0.018, Figure 4.7.b, Table 4.1) using a single scattering Pt-Ga shell, i.e. without Pt-Pt contributions. The Pt-Ga coordination number $N_{Pt\text{-}Ga}$ obtained is 5.5 ± 1.3 whereas the Pt-Ga interatomic distance $R_{Pt\text{-}Ga}$ is around 2.5 Å, the latter in agreement with other studies[68].

Two reasons could underlie the increased Debye-Waller disorder factor $\sigma^2_{Pt\text{-}Ga}$. First, the Pt-Ga alloyed cluster structure can be somewhat distorted by the migration of Ga atoms into the original Pt cluster during the Pt-Ga alloying process. In this case, Ga atoms substitute fcc Pt positions to form a Pt-Ga substitutional alloy. Second, Pt and Ga form an intermetallic Pt_xGa_y compound, resulting in a more complex structure. The increased structural complexity could cause a significant spread of the Pt-Ga bond distances around the central Pt-Ga bond distance (~ 2.5 Å). This spread could result in a broader peak in the Fourier transformed EXAFS signal, leading to an increased Debye-Waller disorder factor $\sigma^2_{Pt\text{-}Ga}$. The variation of ΔE_0 in the course of the full Pt-Ga formation process, i.e. from 11.8 eV to -6.7 eV, likely originates from the use of different theoretical models to describe the experimental data.

The above findings suggest that a H_2/He treatment between 450 °C and 650 °C leads to reduction of Ga species incorporated in the support framework. These reduced species migrate towards the Pt clusters to alloy and form bimetallic Pt-Ga clusters. Hence, the 650 °C reductive treatment results in the formation of alloyed Pt-Ga nanoparticles supported on $Mg(Ga)(Al)O_x$ (Figure 4.1.e).

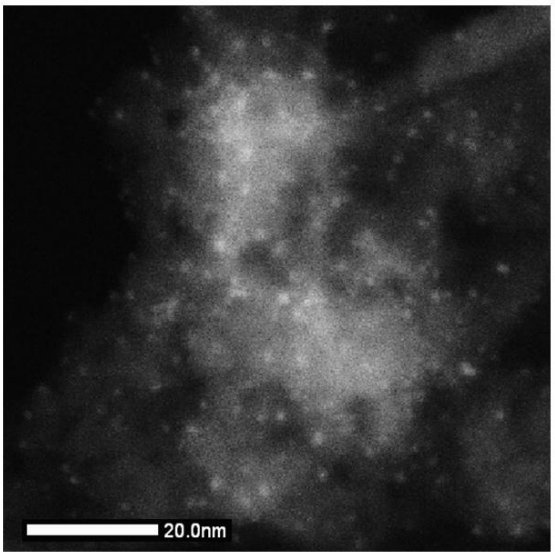

Figure 4.8: STEM-DF image of the Pt-Ga alloyed nanoparticles on the Mg(Ga)(Al)O_x support.

STEM-DF measurements are performed on this Pt-Ga alloyed material. The TEM image in Figure 4.8 reveals that the Mg(Ga)(Al)O_x support surface is densely populated by ~ 1.5 nm Pt-Ga clusters. Assuming hemispherical clusters, the Pt-Ga coordination number N_{Pt-Ga} (Table 4.1) corresponds to the average cluster size of 1.5 nm[48], confirming TEM results.

As detailed in Appendix B.3, XRD analysis does not reveal additional insights into the catalyst formation process, since particle sizes are too small to yield X-ray diffraction patterns. The latter confirms the importance of performing *in situ* XAS during the Pt-Ga formation process. BET measurements on the material after $Pt(acac)_2$ wet impregnation on Mg(Ga)(Al)O_x, 650 °C calcination and 650 °C reduction, yield a specific surface area of 107.7 m²/g, 87.1 m²/g and 104.7 m²/g respectively.

4.4.6 O_2/H_2 redox cycling at 650 °C

As mentioned in the introduction, the ultimate role of Pt-Ga alloyed nanoparticles supported by calcined Ga-incorporated hydrotalcite Mg(Ga)(Al)O_x is to serve as dehydrogenation catalyst.[11, 14] During alkane dehydrogenation, side reactions lead to coke formation after considerable reaction times even on promoted Pt catalysts.[14] Coke deposition eventually results in active site blockage, preventing further reaction. Coke burn off through

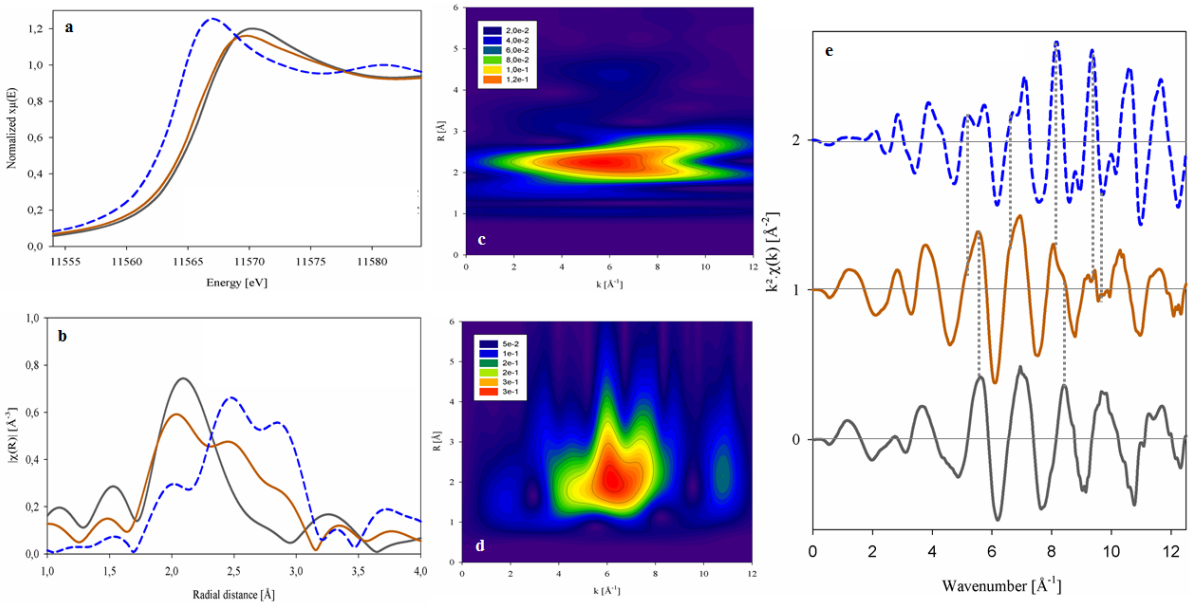

Figure 4.9: (a) XANES, (b) Fourier transformed EXAFS magnitudes and (e) k-space EXAFS signals of the Pt-Ga/Mg(Ga)(Al)O_x catalyst before (———, H_2/He 650°C) and after one redox cycle (———, O_2/H_2 650°C) and the Pt reference (– – –); the grey dashed lines show which features of the metallic Pt and Pt-Ga/Mg(Ga)(Al)O_x signal are present in the one after one redox cycle; wavelet transformed XAS after a O_2/H_2 redox cycle with Cauchy order (c) 200 and (d) 5.

oxygen treatment at high temperatures is therefore necessary to regenerate the Pt-Ga active nanoparticles, allowing further reaction. Alternating oxidative (O_2) and reductive (C_3H_8 or H_2) treatments, referred to as redox cycling, are therefore common practice. To mimic the phase changes occurring after one full redox cycle, one O_2/He and H_2/He pulse are applied at 650 °C to compare the Pt-Ga alloyed nanoparticle structure before and after this redox cycle.

Results presented in Figure 4.9 indicate that Pt-Ga alloy structure changes upon application of one redox cycle. Based on Figure 4.9.b, the Fourier transformed EXAFS signal after one redox cycle suggests a significant Pt contribution (~ 2 – 3 Å) in addition to the Ga peak around 2 Å. In Figure 4.9.e, the k-space EXAFS signals after the first 650 °C reduction, after the redox cycle and the metallic fcc Pt foil are compared. The spectrum measured after one redox cycle largely appears as a combination of the metallic Pt signal (majorly Pt) and the signal after the first 650 °C reduction (majorly Ga). This confirms that besides Ga neighbors, Pt atoms also reside in the local environment of Pt. These findings are also suggested by wavelet transformed XAS since lobes are present at higher k-values after the redox cycle (Figure 4.9.c, Cauchy order 200) compared to before the redox cycle, i.e. after

650 °C reduction (Figure 4.7.d, Cauchy order 200). An increase in k-space resolution results in the appearance of a subtle peak around 11 $Å^{-1}$ likely originating from Pt (Figure 4.9.d, Cauchy order 5). When compared to Figure 4.7.f (Cauchy order 5), the high k-range peak is absent after the first 650 °C reduction, i.e. before the redox cycle. Finally, the XANES white line intensity decreases while the edge position shifts to lower energies. This corresponds to a decrease in Pt-Ga alloying according to Sun et al.[10]. Such decreased alloying after one redox cycle is caused by the appearance of Pt atoms besides Ga in the first shell around Pt, preventing Pt to alloy to the same degree as before the redox cycle at 650 °C.

These results suggest that during redox cycling, the structure of Pt-Ga alloyed nanoparticles changes compared to their initial state after activation through 650 °C reduction. This is in correspondence with recent work of Redekop et al.[14] in which structural changes were also observed during initial redox cycling experiments. Therefore, the initial Pt-Ga alloyed nanoparticles behave dynamically during redox cycling, signifying that the Pt-Ga alloy structure is in continuous change in the course of reaction. The occurring structural changes might influence the catalytic performance during dehydrogenation owing to the structure-performance relationship. A more detailed investigation of this topic in out the scope of this study and will be reported elsewhere.

Table 4.1: estimates of the structural parameters obtained by EXAFS modeling of the recorded signals: the coordination number N_{Pt-X} [-], energy origin correction ΔE_0 [eV], interatomic distance R_{Pt-X} [Å] and Debye-Waller disorder factor σ^2_{Pt-X} [10^{-3} × Å²] (X = O, O_l, Pt, Mg, Ga). In addition, the structural models used to fit the data and the modelling range in k- and R-space are given.

	O_2 – 25 °C	O_2 – 350 °C		O_2 – 250 °C	H_2 – 450 °C		H_2 – 650 °C*
N_{Pt-O}	4.0 ± 0.5	5.3 ± 0.4	N_{Pt-O}	2.7 ± 0.5	1.3 ± 0.2	N_{Pt-Ga}	5.5 ± 1.3
ΔE_0	11.8 ± 1.7	12.3 ± 1.0	N_{Pt-Ol}	1.2 ± 0.7	-	ΔE_0	-6.7 ± 2.8
R_{Pt-O}	1.98 ± 0.02	2.01 ± 0.01	N_{Pt-Pt}	3.4 ± 1.5	5.6 ± 1.3	R_{Pt-Ga}	2.50 ± 0.02
σ^2_{Pt-O}	1.5 ± 2.0	6.6 ± 1.3	N_{Pt-Mg}	1.0 ± 0.9	-	σ^2_{Pt-Ga}	16.6 ± 2.4
			ΔE_0	7.6 ± 2.9	8.1 ± 1.3		
			R_{Pt-O}	1.97 ± 0.02	1.98 ± 0.02		
			R_{Pt-Ol}	2.51 ± 0.02	-		
			R_{Pt-Pt}	2.77 ± 0.02	2.76 ± 0.02		
			R_{Pt-Mg}	2.95 ± 0.07	-		
			σ^2_{Pt-X}	3.7 ± 2.8	9.5 ± 3.1		
Model	$Pt(acac)_2$	Pt-O		Pt-O + Pt-Pt + $Pt-O_l$ + Pt-Mg	Pt-O + Pt-Pt		Pt-Ga
k-range ($Å^{-1}$)	3.0 – 16.5	3.0 – 11.8		2.0 – 9.9	2.0 – 8.4		3.3 – 10.9
R-range (Å)	1.2 – 3.6	1.1 – 2.1		1.2 – 3.2	1.2 – 3.2		1.3 – 2.9

*The EXAFS modeling is performed on a room temperature measurement after cooling down from 650 °C in H_2.

4.5 Conclusions

The formation process of Mg(Ga)(Al)O_x supported Pt-Ga alloyed nanoparticles is monitored using *in situ* XAS experiments. A combined XAS analysis was applied: XANES white line analysis to obtain the Pt oxidation state, Fourier transformed EXAFS to yield structural information, as well as wavelet transformed XAS analysis. The latter can identify the nature and location of the atomic species present around Pt based on simultaneous k- and R-space resolution. The combination of wavelet transformed XAS with conventional XANES and Fourier transformed EXAFS analysis proved essential to unravel the mechanistic details occurring during Pt-Ga formation. Wavelet transformed XAS has the potential to replace or strengthen more complex state-of-the-art methodologies for determining the nature and location of atomic species around the absorber during processes in catalysis, including catalyst formation, bimetallic alloying, etc..

Upon incipient wet impregnation of the $Pt(acac)_2$ precursor on a Mg(Ga)(Al)O_x mixed oxide support, the precursor adsorbs at the support surface without significant chemical acac ligand decomposition. The precursor-support interaction is not strong enough to induce direct precursor decomposition. Oxidative heating to 350 °C leads to the oxidation and decomposition of the acac ligands resulting in atomically dispersed Pt^{4+} species with five/six fold oxygen coordination residing at the Mg(Ga)(Al)O_x support surface.

Upon further calcination to 650 °C, these atomically dispersed Pt species undergo thermal Pt-O support bond scission, though possibly counteracted by the basic nature of the Mg(Ga)(Al)O_x support. This leads to more mobile atomically dispersed Pt species which cluster through migration at high temperatures, resulting in 3 – 11 atom Pt nanoparticles with fcc packing and oxidized external surface. These sub-nanometer clusters are proposed to be bound to the support by extended 2.5 Å Pt-O_l cluster-support interfacial bonds replacing the 2.0 Å Pt-O support bonds at 350 °C. These Pt-O_l bonds are suggested to originate from a

(weak) induced dipole-ion interfacial interaction between Pt atoms at the cluster interface and hydroxyl groups at the support surface, i.e. Pt^0-$(OH)^-$ bonds. After cooling down and switching to H_2/He, stepwise heating to 450 °C induces nanoparticle sintering and reduction. In the course of this reduction, the extended interfacial cluster-support bonds are substituted by common 2.0 Å Pt-O bonds.

A final temperature increase from 450 °C to 650 °C in H_2/He reduces Ga incorporated into the Mg(Ga)(Al)O_x framework, allowing migration of Ga atoms towards the reduced Pt clusters. This results in Pt-Ga alloying as evidenced by the shifted white line (XANES) and first shell position (EXAFS) as well as Ga neighbors around Pt in wavelet transformed XAS. Therefore, H_2 reduction to 650 °C eventually results in the activation of the alloyed Pt-Ga/Mg(Ga)(Al)O_x dehydrogenation catalyst. It should be noted that this activated catalyst undergoes Pt-Ga alloy restructuring after one O_2/H_2 redox cycle at 650 °C, the latter being common practice to regenerate the catalyst. The decreased degree of Pt-Ga alloying after one redox cycle demonstrates the dynamic behavior of the active Pt-Ga phase during the catalyst lifetime.

4.6 References

(1) Kockrick, E.; Borchardt, L.; Schrage, C.; Gaudillere, C.; Ziegler, C.; Freudenberg, T.; Farrusseng, D.; Eychmuller, A.; Kaskel, S. *Chem. Mater.* **2011**, *23*, 57.

(2) Knecht, M. R.; Weir, M. G.; Myers, V. S.; Pyrz, W. D.; Ye, H. C.; Petkov, V.; Buttrey, D. J.; Frenkel, A. I.; Crooks, R. M. *Chem. Mater.* **2008**, *20*, 5218.

(3) Hull, R. V.; Li, L.; Xing, Y. C.; Chusuei, C. C. *Chem. Mater.* **2006**, *18*, 1780.

(4) Bonnemann, H.; Waldofner, N.; Haubold, H. G.; Vad, T. *Chem. Mater.* **2002**, *14*, 1115.

(5) Mackus, A. J. M.; Verheijen, M. A.; Leick, N.; Bol, A. A.; Kessels, W. M. M. *Chem. Mater.* **2013**, *25*, 1905.

(6) Weber, M. J.; Mackus, A. J. M.; Verheijen, M. A.; van der Marel, C.; Kessels, W. M. M. *Chem. Mater.* **2012**, *24*, 2973.

(7) Galvita, V.; Siddiqi, G.; Sun, P. P.; Bell, A. T. *J. Catal.* **2010**, *271*, 209.

(8) Jablonski, E. L.; Castro, A. A.; Scelza, O. A.; de Miguel, S. R. *Appl. Catal., A* **1999**, *183*, 189.

(9) de Miguel, S. R.; Jablonski, E. L.; Castro, A. A.; Scelza, O. A. *J. Chem. Technol. Biotechnol.* **2000**, *75*, 596.

(10) Sun, P. P.; Siddiqi, G.; Vining, W. C.; Chi, M. F.; Bell, A. T. *J. Catal.* **2011**, *282*, 165.

(11) Siddiqi, G.; Sun, P. P.; Galvita, V.; Bell, A. T. *J. Catal.* **2010**, *274*, 200.

(12) Akporiaye, D.; Jensen, S. F.; Olsbye, U.; Rohr, F.; Rytter, E.; Ronnekleiv, M.; Spjelkavik, A. I. *Ind. Eng. Chem. Res.* **2001**, *40*, 4741.

(13) Sun, P. P.; Siddiqi, G.; Chi, M. F.; Bell, A. T. *J. Catal.* **2010**, *274*, 192.

(14) Redekop, E. A.; Galvita, V. V.; Poelman, H.; Vitaliy, B.; Detavernier, C.; Marin, G. B. *ACS Catal.* **2014**, *4*, 1812.

(15) Ota, A.; Krohnert, J.; Weinberg, G.; Kasatkin, I.; Kunkes, E. L.; Ferri, D.; Girgsdies, F.; Hamilton, N.; Armbruster, M.; Schlogl, R.; Behrens, M. *ACS Catal.* **2014**, *4*, 2048.

(16) Ota, A.; Kunkes, E. L.; Kasatkin, I.; Groppo, E.; Ferri, D.; Poceiro, B.; Yerga, R. M. N.; Behrens, M. *J. Catal.* **2012**, *293*, 27.

(17) Ota, A.; Armbruster, M.; Behrens, M.; Rosenthal, D.; Friedrich, M.; Kasatkin, I.; Girgsdies, F.; Zhang, W.; Wagner, R.; Schlogl, R. *J. Phys. Chem. C* **2011**, *115*, 1368.

(18) Koningsberger, D. C.; Mojet, B. L.; van Dorssen, G. E.; Ramaker, D. E. *Top. Catal.* **2000**, *10*, 143.

(19) Sayers, D. E.; Stern, E. A.; Lytle, F. W. *Phys. Rev. Lett.* **1971**, *27*, 1204.

(20) Antoniak, C. *Beilstein J. Nanotechnol.* **2011**, *2*, 237.

(21) Munoz, M.; Argoul, P.; Farges, F. *Am. Mineral.* **2003**, *88*, 694.

(22) Munoz, M.; Farges, F.; Argoul, P. *Phys. Scr.* **2005**, *T115*, 221.

(23) Chukalina, M. V.; Dubrovskii, Y. V.; Funke, H. *Low Temp. Phys.* **2004**, *30*, 930.

(24) Funke, H.; Chukalina, M.; Rossberg, A. *Phys. Scr.* **2005**, *T115*, 232.

(25) Funke, H.; Chukalina, M.; Scheinost, A. C. *Mathematical Methods and Computational Techniques in Research and Education;* World Scientific and Engineering Acad. and Soc.: Athens, Greece, **2007**, 117.

(26) Beale, A. M.; van der Eerden, A. M. J.; Jacques, S. D. M.; Leynaud, O.; O'Brien, M. G.; Meneau, F.; Nikitenko, S.; Bras, W.; Weckhuysen, B. M. *JACS* **2006**, *128*, 12386.

(27) Nikitenko, S.; Beale, A. M.; van der Eerden, A. M. J.; Jacques, S. D. M.; Leynaud, O.; O'Brien, M. G.; Detollenaere, D.; Kaptein, R.; Weckhuysen, B. M.; Bras, W. *J. Synchrotron Rad.* **2008**, *15*, 632.

(28) Martis, V.; Beale, A. M.; Detollenaere, D.; Banerjee, D.; Moroni, M.; Gosselin, F.; Bras, W. *J. Synchrotron Rad.* **2014**, *21*, 462.

(29) Ravel, B.; Newville, M. *J. Synchrotron Rad.* **2005**, *12*, 537.

(30) Rehr, J. J.; Deleon, J. M.; Zabinsky, S. I.; Albers, R. C. *J. Am. Chem. Soc.* **1991**, *113*, 5135.

(31) Funke, H.; Chukalina, M. Wavelet Transform for EXAFS: http://www.esrf.eu/UsersAndScience/Experiments/CRG/BM20/Software/Wavelets

(32) Antoniak, C.; Spasova, M.; Trunova, A.; Fauth, K.; Wilhelm, F.; Rogalev, A.; Minar, J.; Ebert, H.; Farle, M.; Wende, H. *J. Phys.: Condens. Matter* **2009**, *21*, 336002.

(33) Funke, H.; Scheinost, A. C.; Chukalina, M. *Phys. Rev. B* **2005**, *71*, 094110.

(34) Bellotto, M.; Rebours, B.; Clause, O.; Lynch, J.; Bazin, D.; Elkaim, E. *J. Phys. Chem.* **1996**, *100*, 8535.

(35) Bellotto, M.; Rebours, B.; Clause, O.; Lynch, J.; Bazin, D.; Elkaim, E. *J. Phys. Chem.* **1996**, *100*, 8527.

(36) Valente, J. S.; Rodriguez-Gattorno, G.; Valle-Orta, M.; Torres-Garcia, E. *Mater. Chem. Phys.* **2012**, *133*, 621.

(37) Yoshida, H.; Nonoyama, S.; Yazawa, Y.; Hattori, T. *Phys. Scr.* **2005**, *T115*, 813.

(38) Womes, M.; Lynch, J.; Bazin, D.; Le Peltier, F.; Morin, S.; Didillon, B. *Catal. Lett.* **2003**, *85*, 25.

(39) Zabinsky, S. I.; Rehr, J. J.; Ankudinov, A.; Albers, R. C.; Eller, M. J. *Phys. Rev. B* **1995**, *52*, 2995.

(40) Kenvin, J. C.; White, M. G.; Mitchell, M. B. *Langmuir* **1991**, *7*, 1198.

(41) Ono, L. K.; Croy, J. R.; Heinrich, H.; Cuenya, B. R. *J. Phys. Chem. C* **2011**, *115*, 16856.

(42) Rehr, J. J.; Albers, R. C. *Rev. Mod. Phys.* **2000**, *72*, 621.

(43) Zhang, P.; Sham, T. K. *Appl. Phys. Lett.* **2002**, *81*, 736.

(44) Sun, S. H.; Zhang, G. X.; Gauquelin, N.; Chen, N.; Zhou, J. G.; Yang, S. L.; Chen, W. F.; Meng, X. B.; Geng, D. S.; Banis, M. N.; Li, R. Y.; Ye, S. Y.; Knights, S.; Botton, G. A.; Sham, T. K.; Sun, X. L. *Scientific Reports* **2013**, *3*.

(45) Bacchi, A.; Lamzin, V.S.; Wilson, K.S. *Acta Crystallogr., Sect. D: Biol. Crystallogr.* **1996**, *52*, 641.

(46) Lytle, F.W.; Greegor, R.B.; Marques, E.C.; Sandstrom, D.R.; Via, G.H.; Sinfelt, J.H. *J. Catal.* **1985**, *95*, 546.

(47) Nagai, Y.; Hirabayashi, T.; Dohmae, K.; Takagi, N.; Minami, T.; Shinjoh, H.; Matsumoto, S. *J. Catal.* **2006**, *242*, 103.

(48) Frenkel, A. I.; Hills, C. W.; Nuzzo, R. G. *J. Phys. Chem. B* **2001**, *105*, 12689.

(49) Vaarkamp, M.; Miller, J.T.; Modica, F.S.; Koningsberger, D.C. *J. Catal.* **1996**, *163*, 294.

(50) Yoshida, H.; Nonoyama, S.; Yazawa, Y.; Hattori, T. *Catal. Today* **2010**, *153*, 156.

(51) Cardonamartinez, N.; Dumesic, J. A. *J. Catal.* **1991,** *127*, 706.

(52) Di Cosimo, J. I.; Diez, V. K.; Apesteguia, C. R. *Appl. Clay Sci.* **1998,** *13*, 433.

(53) Di Cosimo, J. I.; Diez, V. K.; Xu, M.; Iglesia, E.; Apesteguia, C. R. *J. Catal.* **1998,** *178*, 499.

(54) Diez, V. K.; Apesteguia, C. R.; Di Cosimo, J. I. *J. Catal.* **2003,** *215*, 220.

(55) Nagai, Y.; Dohmae, K.; Teramura, K.; Tanaka, T.; Guilera, G.; Kato, K.; Nomura, M.; Shinjoh, H.; Matsumoto, S. *Catal. Today* **2009,** *145*, 279.

(56) Yoshida, H.; Yazawa, Y.; Hattori, T. *Catal. Today* **2003,** *87*, 19.

(57) Koningsberger, D.C.; Gates, B.C. *Catal. Lett.* **1992**, *14*, 271.

(58) Koningsberger, D.C.; Sayers, D.E. *Solid State Ionics* **1985**, *16*, 23.

(59) Chang, J.R.; Koningsberger, D.C.; Gates, B.C. *J. Am. Chem. Soc.* **1992**, *114*, 6460.

(60) Lira, E.; Merte, L.R.; Behafarid, F.; Ono, L.K.; Zhang, L.; Cuenya, B.R. *ACS Catal.* **2014**, *4*, 1875.

(61) Mager-Maury, C.; Bonnard, G.; Chizallet, C.; Sautet, P.; Raybaud, P. *ChemCatChem* **2011**, *3*, 200.

(62) Hu, C.H.; Chizallet, C.; Mager-Maury, C.; Corral-Valero, M.; Sautet, P.; Toulhoat, H.; Raybaud, P. *J. Catal.* **2010**, *274*, 99.

(63) Vaarkamp, M.; Modica, F.S.; Miller, J.T.; Koningsberger, D.C. *J. Catal.* **1993**, *144*, 611.

(64) Grunwaldt, J. D.; Kimmerle, B.; Hannemann, S.; Baiker, A.; Boye, P.; Schroer, C. G. *J. Mater. Chem.*, **2007**, ***17***, 2603.

(65) Giedigkeit, R.; Hu, Z.; Grin, Y. XANES study on the intermetallic compounds PdGa and PtGa, two representatives of the FeSi structure: http://hasyweb.desy.de/science/annual_reports/2002_report/part1/contrib/41/6974.pdf

(66) Hsu, L. S.; Guo, G. Y.; Denlinger, J. D.; Allen, J. W. *Phys. Rev. B* **2001**, *63*, 15, 155105.

(67) Bus, E.; van Bokhoven, J. A. *J. Phys. Chem. C* **2007**, *111*, 9761.

(68) Chao, K. J.; Wei, A. C.; Wu, H. C.; Lee, J. F. *Microporous Mesoporous Mater.* **2000**, *35-6*, 413.

Chapter 5. The role of hydrogen during Pt-Ga nanocatalyst formation

Abstract

Hydrogen plays an essential role during the assembly of tailored catalytic materials, and serves as key ingredient in multifarious chemical reactions promoted by these catalysts. Despite intensive debate for several decades, the existence and nature of hydrogen-involved mechanisms – such as hydrogen spill over, surface migration – have not been unambiguously proven and elucidated up to date. Here, Pt-Ga alloy formation is used as a probe reaction to study the behavior and atomic transport of H and Ga, starting from Pt nanoparticles on hydrotalcite-derived $Mg(Ga)(Al)O_x$ supports. *In situ* XANES spectroscopy, time-resolved TAP kinetic experiments, HAADF-STEM imaging and EDX mapping are combined to probe Pt, Ga and H in a series of H_2 reduction experiments up to 650 °C. $Mg(Ga)(Al)O_x$ by itself dissociates hydrogen, but these dissociated hydrogen species do not induce significant reduction of Ga^{3+} cations in the support. Only in the presence of Pt, partial reduction of Ga^{3+} into $Ga^{\delta+}$ is observed, suggesting that Pt and $Mg(Ga)(Al)O_x$ deliver different forms of dissociated hydrogen which exhibit a non-equal reductive ability. This partial reduction of Ga^{3+} is made possible by Pt-dissociated H species which spill over onto non-reducible $Mg(Al)O_x$ or partially reducible $Mg(Ga)(Al)O_x$ and undergo long range transport over the support surface. Moderately mobile $Ga^{\delta+}O_x$ migrates towards Pt clusters, where $Ga^{\delta+}$ is only fully reduced to Ga^0 on condition of immediate stabilization inside Pt-Ga alloyed nanoparticles.

5.1 Introduction

Supported metallic nanoparticles[1-5] are widely employed in energy storage, catalysis, and environmental management. Currently, multiple methods are being developed for atomic tailoring of these nanostructured materials with unprecedented precision. Examples include atomic layer deposition (ALD)[6,7] and shape-controlled synthesis[8], techniques which offer an ever-increasing control of the nanoparticle morphology and thereby yield superior functional properties. However, these methods are often prohibitively expensive for production in industrially relevant quantities. Instead, commercial manufacturing of nanostructured materials typically relies on bulk synthesis methods such as deposition-precipitation and incipient wetness impregnation, which are based on the thermodynamically or kinetically controlled ordering of elements within the material[9].

In recent years, a family of materials derived from bulk synthesized layered double hydroxides (LDHs) has emerged as versatile catalysts[10-13], electrocatalyts[14], photocatalysts[15], chemical storage materials[16], and drug delivery agents[17]. To produce mono- or bimetallic heterogeneous catalysts, multiple metal ions are first incorporated into the framework of a LDH precursor during a scalable and inexpensive synthesis procedure[18]. The LDH structure is then collapsed by high-temperature oxidation (calcination), forming a thermally stable non-reducible metal oxide support which contains and exposes reducible isolated metal ions or very small oxidized metal clusters. Upon subsequent high-temperature H_2 reduction, the incorporated metal ions reduce and assemble into well-dispersed (multi-)metallic nanoparticles on the support surface. Alternatively, active metals may be deposited onto the LDH-derived supports via conventional impregnation techniques, as in the well-described Pt-Sn/Mg(Al)O_x system[19-22]. Since many applications for LDH-derived materials have already emerged, with more expected to come, deeper insight into their chemistry is highly desirable.

The collapse of the LDH structure during calcination treatment is typically accompanied by complex processes, including the removal of CO_2, H_2O and residual organic

ligands, that have been extensively characterized[23,24]. However, the mechanisms and driving forces acting during H_2 reduction[25] and leading to the formation of high-performing multi-metallic nanoparticles are not well-established. These formation mechanisms involve highly concerted actions of convoluted atomic scale processes including the migration of metal atoms and ions, reactions of hydrogen, alloying and phase transitions. In fact, these events determine the catalytic properties of the resulting nanostructured catalyst under operating conditions, as they induce subtle changes in the distribution of constituent elements at the catalytic surface. For this reason, the facile *in situ* formation of these specific active sites should be investigated in order to rationally design synthesis and pre-treatment protocols and better predict the precise *operando* catalyst nanostructure and performance.

Hydrogen spill over (H spill over) is an important mechanism in catalysis which may control the reduction behavior and catalytic activity of LDH-derived metallic catalysts. Several studies have invoked H spill over to explain the enhancement of cation reduction from the calcined LDH framework by the presence of other metals on the surface, which serve as hydrogen activators[26,27]. However, unambiguous evidence of the spill over phenomenon in LDH-derived materials is lacking, and H spill over onto non-reducible supports such as MgO is still a matter of intense debate[28-30]. It is unclear to what degree the observations attributed to spill over can be explained by the mobility of H_2-dissociating metal species over the support surface, since the spatial range of metal mobility in these materials has not been systematically characterized. Im et al. constructed a sophisticated model catalyst featuring Pt nanoparticles embedded deeply within an aluminosilicate matrix[31]. The absence of extra-framework Pt in their catalyst system was confirmed by chemisorption measurements, and the only molecule small enough to diffuse towards Pt was H_2. Using this model catalyst with guaranteed absence of metal transport, hydrogenation reactions at the zeolite external surface involving only the hydrogen spilled over from embedded Pt and migrated to the surface could be studied. Such model systems are, however, rare and not available for LDH-derived supports.

Here, both the migration of metal atoms and the involvement of H spill over are examined during the formation of highly active and selective Pt-Ga/Mg(Ga)(Al)O_x dehydrogenation catalysts from calcined Mg,Ga,Al-LDH precursors (Mg(Ga)(Al)O_x) decorated with Pt nanoparticles. In addition to the significant industrial relevance of Pt-Ga catalysts in general[32, 33], these specific materials present a convenient fundamental model system for studying H spill over and nano-alloying in catalysis. Recently, a comprehensive characterization of these catalysts as well as their Pt-In and Pt-Sn analogs has been performed by our group[22,34-40] and others[19-21,41]. The reduction of framework Ga^{3+} is a highly-activated process, characterized by much higher transition temperatures than the reduction of other reducible metal ions such as Cu and Ni[42] or Pd and Zn[26] in LDH-derived frameworks. Consequently, Pt deposited on a Mg(Ga)(Al)O_x support provides a sensitive model for examining the processes that could lower the activation energy for Ga^{3+} reduction, such as Ga migration towards Pt or H spill over.

5.2 Experimental

5.2.1 Catalyst synthesis

Mg(Al)O_x and Mg(Ga)(Al)O_x supports were synthesized by employing the co-precipitation routine reported by Sun et al.[34]. For the production of Mg(Al)O_x, an aqueous solution of $Mg(NO_3)_2.6H_2O$ (Sigma-Aldrich, 98 – 102%) and $Al(NO_3)_3.9H_2O$ (Sigma-Aldrich, 98.5%) was mixed with an aqueous solution of Na_2CO_3 (EMD Chemicals Inc., 99.5%) and NaOH (Fisher Scientific, 98.3%). For the synthesis of Mg(Ga)(Al)O_x, $Ga(NO_3)_3.xH_2O$ (Sigma-Aldrich, 99.99%) was added to the aqueous solution in addition to the components listed for the production of Mg(Al)O_x. After room temperature aging during 24h, the precipitated support material was filtered, washed with deionized water until pH 7,

and dried at 110 °C. The resulting hydrotalcite-like material (pure Mg,Al-HT and Ga-incorporated Mg,Ga,Al-HT) was then calcined in air for 4h at 650 °C, leading to a mixed oxide ($Mg(Al)O_x$ and $Mg(Ga)(Al)O_x$).

Pt deposition on these supports consisted of incipient wet impregnation of a toluene (Sigma-Aldrich, 99.9%) - $Pt(acac)_2$ (Sigma-Aldrich, 99.99%) solution on $Mg(Al)O_x$ and $Mg(Ga)(Al)O_x$. Next, toluene was evaporated by heating the material at 110 °C. A calcination treatment to 650 °C in air was performed in order to decompose the precursor ligands and allow Pt nanoparticle formation on the support surface, labeled as '$Pt/Mg(Al)O_x$' and '$Pt/Mg(Ga)(Al)O_x$'.

5.2.2 Catalyst characterization

XANES. *In situ* XAS measurements were executed at the Pt L_{III} edge (11564 eV) using the DUBBLE beam line[43] of the ESRF synchrotron (6 GeV, current 160 – 200 mA, Grenoble - France). The prepared material was introduced into a 2 mm quartz capillary and fixed with quartz wool plugs. This capillary was then connected to gas lines by swagelok® fittings and subsequently mounted below the gas blower (FMB Oxford). The DUBBLE gas rig system was employed to regulate the gas flows through the capillary.[44] Optics alignment and energy referencing was performed using a Pt foil and Ge reference. XANES measurements (± 5 min/spectrum) were recorded in transmission mode. XAS data analysis was executed by using the Demeter 0.9.13 software package.[45] Background subtraction and subsequent normalization were performed by employing the methodology of Koningsberger et al.[46].

HAADF-STEM imaging and EDX mapping. HAADF-STEM imaging and EDX mapping were carried out on a FEI Tecnai Osiris microscope, equipped with a "Super-X" four quadrant EDX detector for EDX mapping, operated at 200 kV acceleration voltage.

Temporal Analysis of Products (TAP) experiments. Each sample was loaded into the TAP microreactor as a thin zone located between two larger, inert zones. The tip of the internal thermocouple was placed inside the sample zone. The sample was first reduced for 20 minutes in a flow of H_2 at 650 °C and then evacuated for 20 minute to the background pressure of 10^{-7} torr. After evacuation, a series of H_2/He (1:1) pulses was introduced into the microreactor by firing a magnetically-driven pulse-valve (feed pressure 2.2 bar, driving voltage 18V). Pulse width was kept at 90 μs. The exit-flow rate was monitored every millisecond with a calibrated Extrel QMS. Further experimental characteristics and the TAP data analysis procedure are respectively listed (Appendix C.1: Table A-5) and described in Appendix C.1.

5.3 Results and discussion

To obtain evidence of the spill over phenomena and to simultaneously determine how far Ga species travel within the support during catalyst formation, *in situ* XAS measurements at both the Pt L_{III} and Ga K edges (Figure 5.1) were performed during a temperature-programmed reduction treatment (H_2 TPR over 25 – 650 °C, 0.2 °C/s, 5% H_2/He) for the following four materials: (i) the actual bimetallic Pt/Mg(Ga)(Al)O_x catalyst, (ii) the parent Pt-free support material Mg(Ga)(Al)O_x, (iii) a Ga-free monometallic Pt/Mg(Al)O_x catalyst with comparable Pt content, and (iv) a physical mixture of the Pt-free support Mg(Ga)(Al)O_x and the Ga-free catalyst Pt/Mg(Al)O_x, i.e. (iv) = (ii) + (iii). All materials were calcined for 4 hours in air at 650 °C prior to the TPR procedure. The details of XAS measurements and data analysis can be found in the Experimental section.

During TPR, the XANES spectra at the Pt L_{III} edge of the Pt/Mg(Ga)(Al)O_x catalyst exhibit two characteristic trends (Figure 5.1.f): the white line intensity decreases and the edge shifts to higher energies[36,39-40]. The white line intensity decreases due to Pt reduction, as confirmed by the reduction of Ga-free Pt/Mg(Al)O_x reference (Figure 5.1.d), while the edge

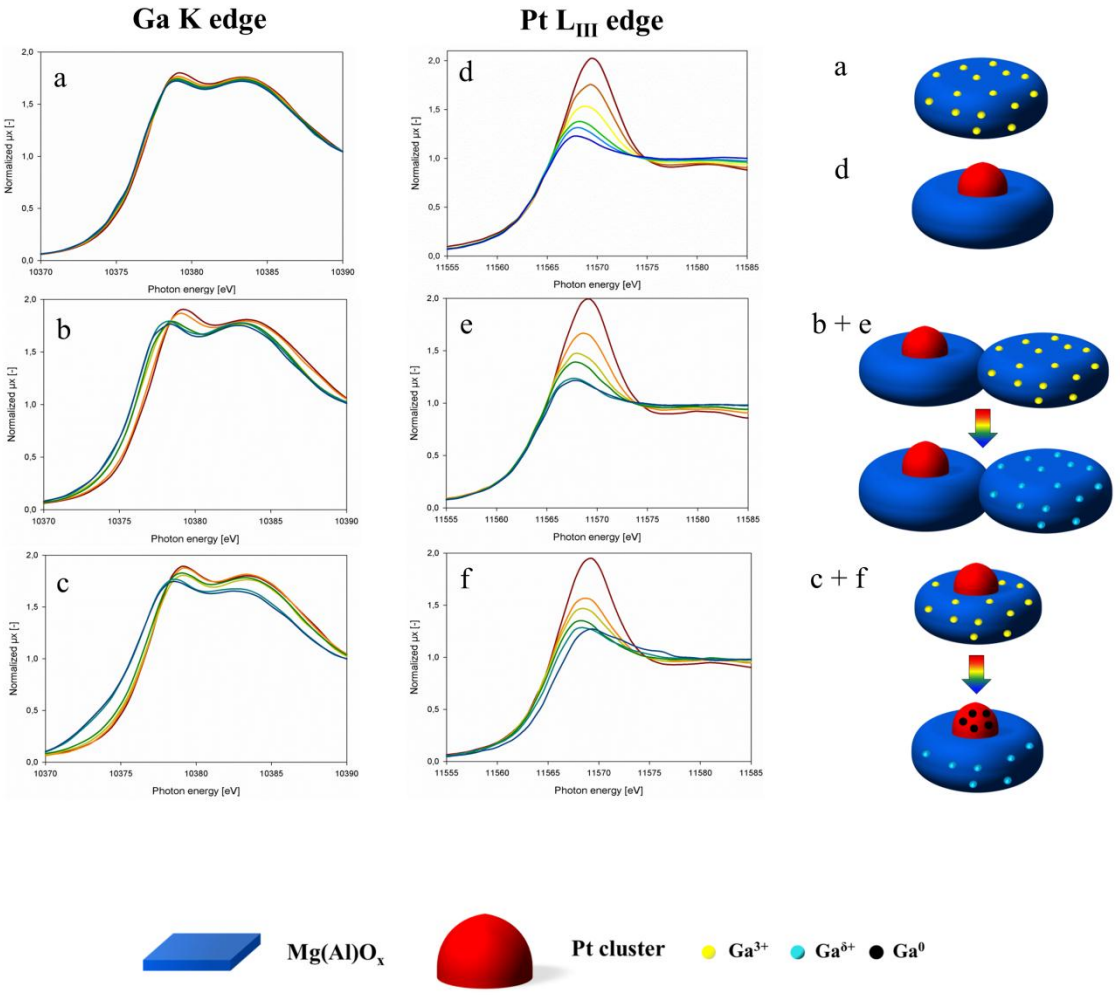

Figure 5.1: Ga K edge XANES spectra recorded during H_2/He TPR to 650 °C of (a) Mg(Ga)(Al)O_x, (b) physical mixture of Pt/Mg(Al)O_x + Mg(Ga)(Al)O_x and (c) Pt/Mg(Ga)(Al)O_x; Pt L_{III} edge XANES spectra recorded during H_2/He TPR to 650 °C of (d) Pt/Mg(Al)O_x, (e) physical mixture of Pt/Mg(Al)O_x + Mg(Ga)(Al)O_x and (f) Pt/Mg(Ga)(Al)O_x. During TPR, the recorded spectra evolve from red (start) towards blue (end). All plots are provided with a representation of the materials before and after reduction.

shifts due to Pt-Ga alloying[39]. Hsu et al.[47] and Giedigkeit et al.[48] observed a similar Pt L_{III} edge shift for $PtGa_2$ alloys. Bus and van Bokhoven[49] reported that electron donation from Au to Pt during PtAu alloying results in a positive edge shift at the Pt L_{III} edge. Since Ga is less electronegative than Pt (Ga: 1.81 eV, Pt: 2.28 eV), charge transfer from Ga to Pt is likely to occur, leading to the observed edge shift. This electron transfer results in stabilization of Pt-Ga bonds and Pt-Ga alloying, as observed after TPR of Pt/Mg(Ga)(Al)O_x (Figure 5.1.f).

The complementary Ga K edge XANES spectra also exhibit decreasing white line intensity due to Ga reduction during TPR (Figure 5.1.c). Moreover, a significant shoulder

develops below 10375 eV due to the formation of metallic Ga^0, in agreement with a reported negative Ga K edge shift of ~5 eV observed when Ga_2O_3 is reduced to metallic Ga[50]. In the present case, Ga^0 most probably resides within alloyed Pt-Ga nanoparticles. To differentiate between the different steps involved in the process of Ga reduction and alloying within these materials, Pt and Ga XANES spectra obtained during the actual catalyst formation were compared to those obtained during the reduction of the Pt-free $Mg(Ga)(Al)O_x$ support (ii) and the physical mixture (iv).

During TPR, the Ga K edge XANES spectra of bare $Mg(Ga)(Al)O_x$ support reveals insignificant changes, implying that negligible Ga reduction occurs below 650 °C on the time scale of the experiment (Figure 5.1.a). In contrast, the Ga K edge XANES spectra acquired during the H_2 TPR of the physical mixture, i.e. $Pt/Mg(Al)O_x$ + $Mg(Ga)(Al)O_x$, undergo significant changes indicative of partial Ga^{3+} reduction (Figure 5.1.b). Namely, the edge shifts to lower energies and the white line decreases. Hence, the reduction of Ga is promoted in the presence of Pt even when Pt and Ga are located on separate grains. Despite clear signs of Ga reduction within the physical mixture, the shoulder is not observed in the Ga K pre-edge (Figure 5.1.b), suggesting that no or a negligible amount of Ga^0 is formed.

The white line of the Pt L_{III} XANES edge also decreases during the reduction of the physical mixture (Figure 5.1.e), in a similar way to the Ga-free $Pt/Mg(Al)O_x$ reference material and the bimetallic $Pt/Mg(Ga)(Al)O_x$ catalyst. However, the edge does not shift to higher energies, unlike in the case of the bimetallic catalyst. It can be concluded that both Pt and Ga within the physical mixture are reduced without undergoing the long range transport which could lead to alloying. In combination with XANES results for the bimetallic $Pt/Mg(Ga)(Al)O_x$ catalyst, this observation indicates that the semi-mobile $Ga^{\delta+}$ species on the support are capable of further reduction into Ga^0 at 650 °C, but only if the Ga^0 can be immediately stabilized through formation of an alloy with nearby Pt. It should be noted that contrary to the Ga^{3+} species embedded within the $Mg(Ga)(Al)O_x$ framework, partial reduction of Ga^{3+} in neither bulk[38] nor nano-dispersed[33] Ga_2O_3 into the $Ga^{\delta+}$ species occurs.

The enhancement of Ga reduction by the presence of spatially-remote Pt can be explained by the spill over of dissociated hydrogen from Pt clusters onto the $Mg(Al)O_x$ support surface. The spilled over H migrates between the physically mixed grains of $Mg(Al)O_x$ and $Mg(Ga)(Al)O_x$ and then reduces Ga^{3+} species. This mechanism of long range transport of spilled over hydrogen must also be involved in Ga reduction and subsequent Pt-Ga cluster formation on Pt-Ga/$Mg(Ga)(Al)O_x$ catalysts. However, conflicting reports on the occurrence of hydrogen spill over necessitate additional consideration before unambiguously concluding that hydrogen spill over explains these XAS results.

In a recent critical review[28] of possible mechanisms of hydrogen transport over the surfaces of catalysts and functional materials, Prins defined spill over as "the transport of a species, adsorbed or formed on a surface, to another surface, which does not adsorb or form this species under the same conditions". It is generally accepted that H_2 dissociatively chemisorbs on Pt surfaces, making Pt cluster surfaces H-rich. The fact that Ga does not reduce in $Mg(Ga)(Al)O_x$ in the absence of Pt suggests that the surface of Ga-incorporated support is rather H-poor (see below), but Ga reduction does take place in the presence of Pt within the same physical mixture. This necessitates a long range net transport of dissociated H from the H-rich Pt cluster surfaces towards H-poor $Mg(Al)O_x$, followed by its migration towards $Mg(Ga)(Al)O_x$ to reduce Ga. Such net H-transport from Pt to $Mg(Al)O_x$ indicates H spill over at the boundary between Pt clusters and the non-reducible $Mg(Al)O_x$ support.

Prins points out that spill over onto non-reducible supports is energetically unfavorable and therefore slow or unlikely[28]. Other mechanisms have been suggested to explain the apparent H spill over effect. In the present context, these alternatives include the migration of hydrogen-dissociating Pt species[51, 52] over the support surface towards Ga^{3+}, the migration of Ga^{3+} towards Pt, and hydrocarbon contamination of the catalyst[28]. The former two possibilities are inconsistent with high angle annular dark field scanning transmission electron microscopy (HAADF-STEM) imaging and energy dispersive X-ray (EDX) mapping experiments performed on the physical mixture of Pt/$Mg(Al)O_x$ and $Mg(Ga)(Al)O_x$. Figure

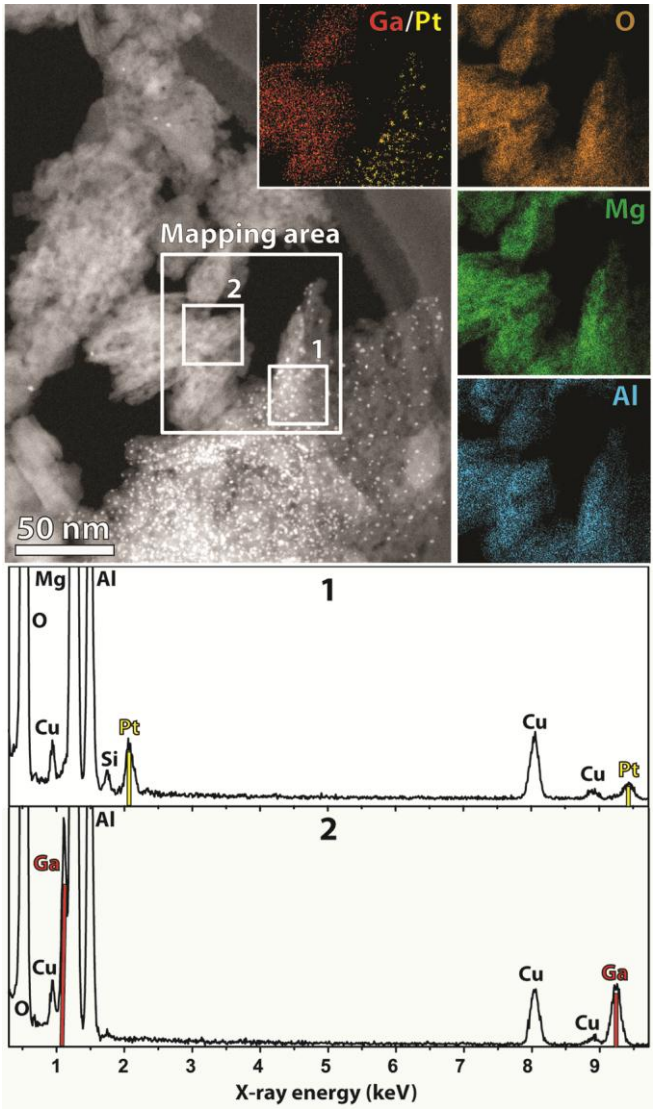

Figure 5.2: HAADF-STEM image, EDX maps and EDX spectra of the physical mixture, i.e. Pt/Mg(Al)O_x + Mg(Ga)(Al)O_x, after H_2/He TPR to 650 °C. The white rectangle in the HAADF-STEM image indicates the region mapped by STEM-EDX. EDX maps for Ga, Pt, O, Mg and Al are inset. Extracted EDX spectra from regions 1 and 2 indicated in the HAADF-STEM image are plotted below. The red lines indicate the positions of the main peaks for Ga (L at 1.099 keV & K_α at 9.242 keV) and the yellow lines indicate the positions of the main peaks for Pt (M_α at 2.050 keV & L_α at 9.435 keV)

5.2 shows a HAADF-STEM (Z-contrast) image of two distinct, spatially separated Mg(Ga)(Al)O_x and Pt/Mg(Al)O_x grains after TPR treatment to 650 °C. The inset EDX elemental maps clearly show a Ga-rich but Pt-poor Mg(Ga)(Al)O_x grain next to a Pt-rich but Ga-poor Pt/Mg(Al)O_x grain. Based on the extracted EDX spectra, no Pt (Ga) is detected on Mg(Ga)(Al)O_x (Pt/Mg(Al)O_x) after TPR to 650 °C. This evidences that neither Pt nor Ga species migrate towards other grains to induce Ga reduction during TPR treatment. Hydrocarbon contamination that could account for the apparent H-transport can also be

excluded, since all samples were calcined for 4 hours at 650 °C. High temperature calcination burns off all carbonaceous species remaining after $Pt(acac)_2$ precursor impregnation, and no hydrocarbons were used during the experiments. It should be noted that the Somorjai group[30] recently suggested the occurrence of H spill over from Pt across non-reducible SiO_2 support to Co during CO_2 methanation.

To substantiate the involvement of H spill over, the interaction of H_2 with the $Mg(Al)O_x$, $Mg(Ga)(Al)O_x$, and $Pt/Mg(Al)O_x$ materials at 650 °C was characterized using Temporal Analysis of Products (TAP) pulse-response experiments[53,54] (see Section 5.2.2 and Appendix C.1). Each material was first reduced for 20 minutes in a flow of H_2 at 650 °C and then, after a 20 minute evacuation to the background pressure of 10^{-5} Pa, was subjected to a series of very small (10^{-8} mol) and short pulses of a 1:1 H_2/He mixture. The flow rates of H_2 and He exiting from the reactor were measured with a calibrated QMS with millisecond time resolution. Quantitative observations of H_2 behavior in heterogeneous media of catalytic materials often face experimental challenges due to the exceptional mobility and light mass of H atoms and H_2 molecules. In the state-of-the-art TAP-3 instrument employed in this study, H_2 transport through the catalyst bed and within the catalytic particles could be very accurately quantified (time-resolved and high S/N ratio) based on the transport of an internal inert standard, in this case He.

The exit-flow rates of H_2 pulsed at 650 °C over different materials are reported in Figure 5.3.a. The scaled abscissa of the plot in Figure 5.3.a represents dimensionless time, which is defined as $\tau = tD/\varepsilon L_{cat} L_{in2}$, where t (s) is real time, D (m^2/s) is an effective diffusion coefficient, ε is bed porosity (-), L_{cat} (m) and L_{in2} (m) are the lengths of the catalyst zone and the inert zone downstream of the catalyst zone, respectively. The ordinate of the plot represents the exit-flow rate divided by the amount of admitted molecules. Such scaling of the experimental curves takes into account all transport- and geometry-related variations between different experiments and allows one to focus only on the chemistry-related effects. The curves were scaled according to the pulse intensities and the time axis was scaled according to

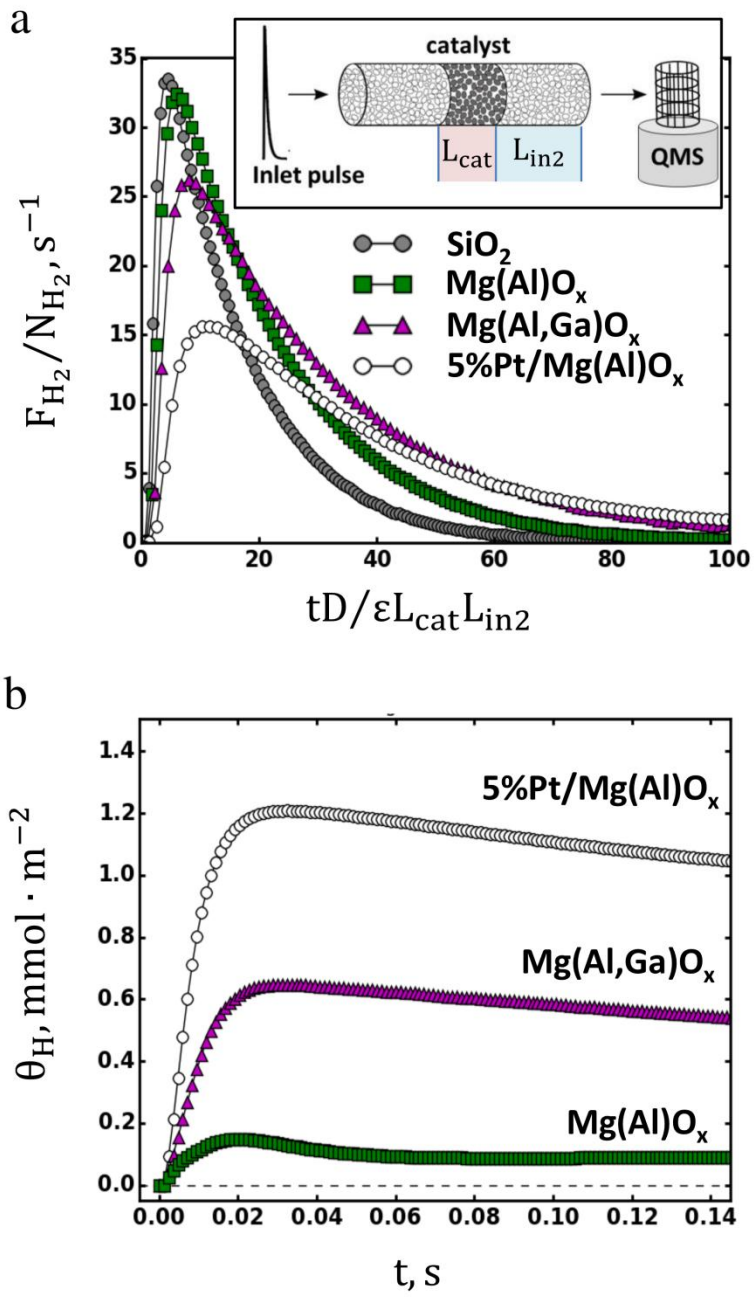

Figure 5.3: TAP pulse-response experiments at 650 °C; (a) H_2 exit-flow rates in 1/s normalized by the injected amount N_{H2} as a function of dimensionless time normalized by the effective diffusivity D in m^2/s, the bed porosity ε, the catalyst length L_{cat} in m, and the length of the second inert zone L_{in2} in m. The curves are compared for different materials: SiO_2 (●), $Mg(Al)O_x$ (■), $Mg(Ga)(Al)O_x$ (▲), and $Pt/Mg(Al)O_x$ (○). The inset conceptually depicts a TAP experiment; (b) H-uptakes in mmol/m^2 of BET surface area on different materials versus time.

the effective bed-scale diffusion coefficients in order to account for all except chemistry-related variations between different experiments. The hydrogen response over a bed of inert SiO_2 particles represents the diffusion-only process in the absence of chemical interactions. In experiments with the actual materials investigated in this study, the same SiO_2 particles were

used to pack the two inert zones upstream and downstream of the catalytic sample. As evident from Figure 5.3.a, the other three curves increasingly deviate from the SiO_2 curve in the following order $Mg(Al)O_x$ < $Mg(Ga)(Al)O_x$ < $Pt/Mg(Al)O_x$, suggesting that all three materials adsorb hydrogen at 650 °C. The peak value decreases and shifts to the right, while the tail rises. This behavior is indicative of the increasing life-time of reversibly dissociated H_2 on the catalyst surface. Other factors which could account for the increased delay of hydrogen response include side reactions leading to additional products and additional transport limitations, e.g. due to intra-particle pore diffusion. However, these factors are excluded since (1) no other products evolved from the catalyst and (2) the simultaneously recorded He response conformed to Knudsen diffusion through the bed with no pore diffusion.

Based on the exit-flow rates, the instantaneous surface coverage of hydrogen on the catalyst (mol_H/m^2_{cat}) was evaluated under the assumption of dissociative chemisorption (H_2 + 2* = 2H), but with no additional kinetic assumptions[52] (see Figure 5.3.b). On all materials, H-coverage achieves a peak value within the first 0.02-0.03 s of the experiment and then very slowly decreases due to desorption. The Pt-free $Mg(Al)O_x$ support clearly dissociated H_2 by itself, in agreement with multiple studies evidencing either homolytic or heterolytic H_2 dissociation on defective MgO surfaces[56,57]. A much more substantial coverage is developed on the $Mg(Ga)(Al)O_x$ support. The latter observation is consistent with the intrinsic hydrogen dissociation[58] and alkane dehydrogenation[59] activity of Ga oxide, the inclusions of which may be present within the mixed oxide framework of $Mg(Ga)(Al)O_x$. It is also plausible that isolated Ga sites are responsible for H_2 dissociation or that the presence of Ga sites significantly increases the concentration of H_2-dissociating defects of MgO. As expected, the coverage on the Pt-containing catalyst was an order of magnitude higher than on the Pt-free $Mg(Al)O_x$ support and at least twice higher than on $Mg(Ga)(Al)O_x$.

Considering all presented findings, we conclude that the reduction and alloying of Pt and Ga during the formation of $Pt\text{-}Ga/Mg(Ga)(Al)O_x$ catalysts is mediated primarily by H-

species which are dissociatively chemisorbed on Pt nanoparticles and spilled over onto the support. Although the LDH-derived supports are capable of dissociating hydrogen by themselves, the combined *in situ* XAS and TAP experiments suggest that not all H-species on the support surface contribute equally to the reduction of Ga^{3+}. TAP experiments demonstrate a significant life-time of H on the $Mg(Ga)(Al)O_x$ surface, but *in situ* XANES data reveal that Ga reduction on Pt-free materials is insignificant at 650 °C. It can, therefore, be argued that Ga reduction is kinetically hindered by the limited ability of the support to form a reduction-capable H-species. Only in the presence of Pt does the population of such species on the support surface increase and accelerate Ga reduction. While the diverse speciation of hydrogen on defective MgO[57] and Ga_2O_3 surfaces is well documented[58], the exact nature of H-species primarily responsible for Ga reduction in the samples investigated remains an open question requiring further studies. However, one could hypothesize that Pt-dissociated hydrogen species are capable of migrating through the support lattice, thereby partially reducing the majority of the framework-incorporated bulk Ga^{3+} species into $Ga^{\delta+}$ and resulting in the average decrease of the Ga K edge XANES white line during H_2 TPR (Figure 5.1.b). In contrast, the mobility of $Mg(Ga)(Al)O_x$-dissociated hydrogen could be restricted to migration on the support surface only, resulting in the partial reduction of Ga^{3+} cations at the support surface and leading to the negligible changes in XANES spectra during H_2 TPR of pure $Mg(Ga)(Al)O_x$ (Figure 5.1.a).

The range of metal migration during the reduction process also plays an important role in the bimetallic catalyst formation. As evidenced by XANES and TEM results for the physical mixture, partially reduced $Ga^{\delta+}$ species possess limited mobility at 650 °C and cannot be further reduced into Ga^0 in the absence of nearby Pt. Complementary experiments at 750 °C demonstrated that Pt-Ga alloying does occur when the mobility of partially reduced $Ga^{\delta+}$ species is increased at higher temperatures (see Appendix C.2). In the bimetallic catalysts investigated, an energy gain from alloying with vicinal Pt allows $Ga^{\delta+}$ to overcome the activation barrier towards Ga^0 at 650 °C. For this reason, the H_2 reduction process of

framework incorporated Ga^{3+} cations which eventually alloy with Pt during the formation of Pt-Ga/Mg(Ga)(Al)O_x catalysts consists of three consecutive steps: (1) partial reduction of Ga^{3+} into $Ga^{\delta+}$ by Pt-dissociated hydrogen, (2) support surface migration of partially reduced, moderately mobile $Ga^{\delta+}$ species towards Pt clusters, followed by (3) complete reduction of $Ga^{\delta+}$ to metallic Ga^0 on the condition of simultaneous stabilization of Ga^0 in a Pt-Ga alloy.

5.4 Conclusions

Novel mechanistic details were elucidated for H spill over, metal reduction, and metal mobility involved in the formation of bimetallic Pt-Ga catalysts on LDH-derived supports. Non-equal reductive ability of different forms of dissociated H_2 was suggested, motivating further research and more detailed characterization of surface-bound hydrogen species on the surfaces of mixed oxides. These results suggest that hydrogen spill over from catalytic metal nanoparticles onto non-reducible supports may play a decisive role not only in the catalytic reactions themselves, but also in shaping the "working state" of the catalyst during the pretreatment. These results boost the opportunity to influence the formation and reactivity of catalysts supported on non-reducible oxides derived from LDHs by taking advantage of the H spill over and its consecutive migration.

5.5 References

(1) Gates, B. C. *Chem. Rev.* **1995**, *95*, 511–522.

(2) Kweskin, S. J.; Rioux, R. M.; Song, H.; Komvopoulos, K.; Yang, P.; Somorjai, G. A. *ACS Catal.* **2012**, *2*, 2377–2386.

(3) Kondratenko, V. A.; Berger-Karin, C.; Kondratenko, E. V. *ACS Catal.* **2014**, *4*, 3136–3144.

(4) Yu, W.; Porosoff, M. D.; Chen, J. G. *Chem. Rev.* **2012**, 112, 5780–5817.

(5) Zhang, L.; Henkelman, G. *ACS Catal.* **2015**, *5*, 655–660.

(6) Feng, H.; Libera, J. A.; Stair, P. C.; Miller, J. T.; Elam, J. W. *ACS Catal.* **2011**, *1*, 665–673.

(7) O'Neill, B. J.; Jackson, D. H. K.; Lee, J.; Canlas, C.; Stair, P. C.; Marshall, C. L.; Elam, J. W.; Kuech, T. F.; Dumesic, J. A.; Huber, G. W. *ACS Catal.* **2015**, *5*, 1804−1825.

(8) Xia, Y.; Xiong, Y.; Lim, B.; Skrabalak, S. E. *Angew. Chem. Int. Ed.* **2009**, *48*, 60–103.

(9) Satterfield, C. N. *Heterogeneous Catalysis in Industrial Practice*; Mcgraw-Hill: New York, **1991**.

(10) Basile, F.; Basini, L.; Fornasari, G.; Gazzano, M.; Trifirò, F.; Vaccari, *Chem. Commun.* **1996**, 2435–2436.

(11) Sels, B. F.; De Vos, D. E.; Jacobs, P. A. *Cat. Rev.* **2001**, 43, 443–488.

(12) Xu, Z. P.; Zhang, J.; Adebajo, M. O.; Zhang, H.; Zhou, C. *Appl. Clay Sci.* **2011**, *53*, 139–150.

(13) He, L.; Huang, Y.; Wang, A.; Wang, X.; Chen, X.; Delgado, J. J.; Zhang, T. *Angew. Chem. Int. Ed.* **2012**, *51*, 6191–6194.

(14) Ballarin, B.; Seeber, R.; Tonelli, D.; Vaccari, A. *J. Electroanal. Chem.* **1999**, *463*, 123–127.

(15) Xiao, Q.; Liu, Z.; Bo, A.; Zavahir, S.; Sarina, S.; Bottle, S.; Riches, J. D.; Zhu, H. *J. Am. Chem. Soc.* **2015**, *137*, 1956–1966.

(16) Walspurger, S.; Cobden, P. D.; Safonova, O. V.; Wu, Y.; Anthony, E. J. *Chem. Eur. J.* **2010**, *16*, 12694–12700.

(17) Aguzzi, C.; Cerezo, P.; Viseras, C.; Caramella, C. *Appl. Clay Sci.* **2007**, *36*, 22–36.

(18) Khan, A. I.; O'Hare, D. *J. Mater. Chem.* **2002**, *12*, 3191–3198.

(19) Virnovskaia, A.; Jørgensen, S.; Hafizovic, J.; Prytz, Ø.; Kleimenov, E.; Hävecker, M.; Bluhm, H.; Knop-Gericke, A.; Schlögl, R.; Olsbye, U. *Surf. Sci.* **2007**, *601*, 30–43.

(20) Virnovskaia, A.; Morandi, S.; Rytter, E.; Ghiotti, G.; Olsbye, U. *J. Phys. Chem. C* **2007**, *111*, 14732–14742.

(21) Virnovskaia, A.; Rytter, E.; Olsbye, U. *Ind. Eng. Chem. Res.* **2008**, *47*, 7167–7177.

(22) Galvita, V.; Siddiqi, G.; Sun, P.; Bell, A. T. *J. Catal.* **2010**, *271*, 209–219.

(23) Basile, F.; Fornasari, G.; Gazzano, M.; Vaccari, A. *Appl. Clay Sci.* **2000**, *16*, 185–200.

(24) Velu, S.; Suzuki, K.; Okazaki, M.; Osaki, T.; Tomura, S.; Ohashi, F. *Chem. Mat.* **1999**, *11*, 2163–2172.

(25) Ribet, S.; Tichit, D.; Coq, B.; Ducourant, B.; Morato, F. *J. Solid State Chem.* **1999**, *142*, 382–392.

(26) Ota, A.; Kunkes, E. L.; Kasatkin, I.; Groppo, E.; Ferri, D.; Poceiro, B.; Navarro Yerga, R. M.; Behrens, M. *J. Catal.* **2012**, *293*, 27–38.

(27) Kühl, S.; Tarasov, A.; Zander, S.; Kasatkin, I.; Behrens, M. *Chemistry* **2014**, *20*, 3782–3792.

(28) Prins, R. *Chem. Rev.* **2012**, *112*, 2714.

(29) Prins, R; Palfi, V.K.; Reiher, M. *J. Phys. Chem. C.* **2012**, 116, 14274-14283

(30) Beaumont, S. K.; Alayoglu, S.; Specht, C.; Kruse, N.; Somorjai, G. A. *Nano Lett.* **2014**, *14*, 4792.

(31) Im, J.; Shin, H.; Jang, H.; Kim, H.; Choi, M. *Nat Commun* **2014**, *5*, 3370.

(32) Shpiro, E. S.; Shevchenko, D. P.; Tkachenko, O. P.; Dmitriev, R. V. *Applied Catalysis A: General* **1994**, *107*, 147–164.

(33) Sattler, J. J. H. B.; Gonzalez-Jimenez, I. D.; Luo, L.; Stears, B. A.; Malek, A.; Barton, D. G.; Kilos, B. A.; Kaminsky, M. P.; Verhoeven, T. W. G. M.; Koers, E. J.; Baldus, M.; Weckhuysen, B. M. *Angew. Chem. Int. Ed.* **2014**, *53*, 9251–9256.

(34) Sun, P.; Siddiqi, G.; Chi, M.; Bell, A. T. *J. Catal.* **2010**, *274*, 192–199.

(35) Siddiqi, G.; Sun, P.; Galvita, V.; Bell, A. T. *J. Cat.* **2010**, *274*, 200–206.

(36) Sun, P.; Siddiqi, G.; Vining, W. C.; Chi, M.; Bell, A. T. *J. Cat.* **2011**, *282*, 165–174.

(37) Peng, Z.; Somodi, F.; Helveg, S.; Kisielowski, C.; Specht, P.; Bell, A. T. *J. Catal.* **2012**, *286*, 22–29.

(38) Redekop, E. A.; Galvita, V. V.; Poelman, H.; Bliznuk, V.; Detavernier, C.; Marin, G. B. *ACS Catal.* **2014**, *4*, 1812–1824.

(39) Filez, M.; Redekop, E. A.; Poelman, H.; Galvita, V. V.; Ramachandran, R. K.; Dendooven, J.; Detavernier, C.; Marin, G. B. *Chem. Mater.* **2014**, *26*, 5936–5949.

(40) Filez, M.; Redekop, E. A.; Poelman, H.; Galvita, V. V.; Marin, G. B. *Anal. Chem.* **2015**, *87*, 3520-3526.

(41) Belskaya, O. B.; Leont'eva, N. N.; Gulyaeva, T. I.; Drozdov, V. A.; Doronin, V. P.; Zaikovskii, V. I.; Likholobov, V. A. *Kinet Catal* **2011**, *52*, 761–769.

(42) Dragoi, B.; Ungureanu, A.; Chirieac, A.; Ciotonea, C.; Rudolf, C.; Royer, S.; Dumitriu, E. *Appl. Cat. A.* **2014,** DOI: 10.1016/j.apcata.2014.11.016

(43) Nikitenko, S. *et al.* Implementation of a combined SAXS/WAXS/QEXAFS set-up for time-resolved in situ experiments. *J. Synchrotron Rad.* **15**, 632 (2008).

(44) Martis, V. *et al.* A high-pressure and controlled-flow gas system for catalysis research. *J. Synchrotron Rad.* **21**, 462 (2014).

(45) Ravel, B. & Newville, M. ATHENA, ARTEMIS, HEPHAESTUS: data analysis for X-ray absorption spectroscopy using IFEFFIT. *J. Synchrotron Rad.* **12**, 537-541 (2005).

(46) Koningsberger, D. C., Mojet, B. L., van Dorssen, G. E. & Ramaker, D. E. XAFS spectroscopy; fundamental principles and data analysis. *Top.Catal.* **10**, 143 (2000).

(47) Hsu, L. S.; Guo, G. Y.; Denlinger, J. D.; Allen, J. W. *Phys. Rev. B* **2001**, *63*, 155105.

(48) Giedigkeit, R.; Hu, Z.; Grin, Y. XANES study on the intermetallic compounds PdGa and PtGa, two representatives of the FeSi structure: http://hasyweb.desy.de/science/annual_reports/2002_report/part1/contrib/41/6974.pdf.

(49) Bus, E.; van Bokhoven, J. A. *J. Phys. Chem. C* **2007**, *111*, 9761.

(50) Chao, K. J.; Wei, A. C.; Wu, H. C.; Lee, J. F. *Microporous Mesoporous Mater.* **2000**, *35*−*36*, 413.

(51) Liu, H. Y.; Chiou, W. A.; Fröhlich, G.; Sachtler, W. H. *Top. Catal.* **2000**, *10*, 49.

(52) Filez, M.; Poelman, H.; Ramachandran, R. K.; Dendooven, J.; Devloo-Casier, K.; Fonda, E.; Detavernier, C.; Marin, G. B. *Catal. Today* **2014**, *229*, 2.

(53) Gleaves, J. T.; Yablonskii, G. S.; Phanawadee, P.; Schuurman, Y. *Appl. Cat. A.* **1997**, *160*, 55–88.

(54) Gleaves, J. T.; Yablonsky, G.; Zheng, X.; Fushimi, R.; Mills, P. L. *J. Mol. Catal.* **2010**, *315*, 108–134.

(55) Yablonsky, G. S.; Constales, D.; Shekhtman, S. O.; Gleaves, J. T. *Chem. Eng. Sci.* **2007**, *62*, 6754–6767.

(56) Boudart, M.; Delbouille, A.; Derouane, E. G.; Indovina, V.; Walters, A. B. *J. Am. Chem. Soc.* **1972**, *94*, 6622–6630.

(57) Knözinger, E.; Jacob, K.-H.; Hofmann, P. *J. Chem. Soc., Faraday Trans.* **1993**, *89*, 1101–1107.

(58) Collins, S. E.; Baltanas, M.A.; Bonivardi, A. L. *Langmuir* **2005**, 21, 962-970

(59) Zheng, B.; Hua, W.; Yue, Y.; Gao, Z. *J. Catal.* **2005** 232, 143-151.

Chapter 6. One-pot synthesis of Pt-based mono- and multimetallic catalysts derived from layered double hydroxides

Abstract

There is a need for simple and scalable synthesis methods of Pt-based catalysts which also allow for tailoring the active sites. Here, we demonstrate a one-pot synthesis method for the controlled production of bimetallic Pt-In catalysts based on the single-step formation of Mg,Al,Pt,In-containing layered double hydroxides (LDHs). Besides their simple synthesis, these Pt-In catalysts exhibit superior propane dehydrogenation activity compared to their multi-step synthesized analogs. The presented material serves as a showcase for the one-pot synthesis of a broader class of LDH-derived multimetallic Pt catalysts. The compositional flexibility provided by LDH-materials can pave the way towards high-performing Pt-based catalysts with tunable physicochemical properties.

6.1 Introduction

Heterogeneous catalysts are the key enablers of multiple chemical reactions, making them essential in the vast majority of industrial chemical processes.[1-2] Amongst them, mono- and bimetallic Pt-based catalysts constitute a class of utmost importance, as they promote reactions ranging from (de)hydrogenation to and CH_4 conversion.[3] Besides their wide applicability, they function as model catalysts which have been intensely researched for decades. Nowadays, it is widely established that the size and composition of bimetallic Pt nanoparticles strongly impact the overall catalyst performance.[2, 4-5] For this reason, high precision synthesis techniques have been developed for the fabrication of tailoring Pt-based nanoparticles.[6-10] However, such techniques are typically very expensive and complex, as they involve multiple synthesis steps, and lack scalability for producing industrially relevant quantities. More simple synthesis procedures – such as wet chemical impregnation – can offer suitable alternatives, but generally lack proper control over the metal nanoparticle size and composition. As a consequence, a persuasive need has arisen for simple, cheap and scalable catalyst synthesis methods which allow for rational design of nanostructured catalysts with fine control over the active sites.

Layered double hydroxides (LDHs) have emerged as versatile and high-performing materials applicable in diverse fields, including catalysis, photochemistry and pharmaceutics.[11-15] This large family of materials consists of cationic 2D brucite-type $[M_{1-a}^{2+}M_a^{3+}(OH)_2]^{a+}$ layers, containing octahedrally OH-coordinated di- and trivalent metal cations.[16, 17] By electrostatic interaction with charge-compensating anions and water, these 2D layers self-assemble into a stacked configuration of alternating cationic brucite-type layers and anionic interlayer galleries, yielding $[M_{1-a}^{2+}M_a^{3+}(OH)_2]^{a+}[A^{n-}]_{a/n}^{a-}.mH_2O$ LDHs. These LDH materials have proven efficient as catalysts, catalyst precursors and catalyst supports. Their high compositional flexibility – by tuning the type of metal cations and/or interlayer anions – enables the fabrication of nanoarchitectures with adaptable physicochemical

properties. In addition, the uniform distribution of metal cations in the brucite-type layers yields controllable and well-dispersed (bimetallic) nanoparticles after calcination and reduction treatment. For example, some studies report on one-pot synthesized LDH-derived nanocatalysts, including supported bimetallic Cu-Zn or Pd-Ga nanoparticles, exhibiting superior performance during reaction, such as methanol synthesis and acetylene hydrogenation respectively.[18-21] Some attempts have been made to synthesize LDH-derived monometallic Pt catalysts in multiple steps.[22-24] However, to the best of our knowledge, single-step synthesis of Pt-containing LDHs as precursors for tailored (multi)metallic Pt-based catalysts has not been reported to date.

Here, we demonstrate a one-pot synthesis protocol for the production of Mg,Al,Pt,In-LDHs based on the single-batch intercalation of Pt^{4+} species in the interlayer galleries of precipitated $[(Mg)_{1-a}^{2+}(Al/In)_a^{3+}(OH)_2]^{a+}$ layers. After consecutive calcination and reduction, these LDHs yield well-dispersed Pt-In nanoparticles on $Mg(Pt)(In)(Al)O_x$ supports with superior performance during propane dehydrogenation. The presented material serves as a showcase for the cheap and scalable one-step synthesis of a broader family of Pt-containing LDHs and LDH-derived catalysts. Throughout Mg,Al,Pt,In-LDH synthesis and activation, X-ray absorption spectroscopy (XAS) and X-ray diffraction (XRD) are used to probe the short and long range structural characteristics, respectively. High-angle annular dark field scanning transmission electron microscopy (HAADF-STEM) combined with spatially resolved energy-dispersive X-ray spectroscopy (EDX) is used complementary to XAS and XRD to provide spatial resolution. This work exemplifies the intelligent design of multifunctional Pt-based catalysts based on one-pot synthesized LDH precursors.

6.2 Experimental

6.2.1 Catalyst synthesis

First, an aqueous solution (250 mL) of $Mg(NO_3)_2.6H_2O$ (29 g, Sigma-Aldrich, 98 – 102%), $Al(NO_3)_3.9H_2O$ (4.2 g, Sigma-Aldrich, 98.5%) and $In(NO_3)_3.xH_2O$ (0.07 g, Sigma-Aldrich, 99.99%) was mixed with an aqueous solution (250 mL) of Na_2CO_3 (0.6 g, EMD Chemicals Inc., 99.5%), NaOH (6 g, Fisher Scientific, 98.3%) and H_2PtCl_6 (0.05 g, Company), and was kept at pH ~ 14. After 24h of aging at room temperature, the precipitate was filtered, washed with deionized water until pH 7 was reached and dried at 110 °C, yielding the 'Mg,Al,Pt,In-LDH' sample. Subsequent calcination and H_2 reduction treatment – both for 4 hours at 650 °C – resulted in 'Mg(Pt)(In)(Al)O_x' and 'Pt-In/Mg(Pt)(In)(Al)O_x' samples.

6.2.2 Catalyst characterization

ICP-AES. Inductively coupled plasma atomic emission spectrometry (ICP-AES) (IRIS Advantage system, Thermo Jarrell Ash) was used to obtain the chemical composition of the synthesized material. To obtain the concentrations, Mg(Pt)(In)(Al)O_x was mineralized by peroxide fusion. Mg(Pt)(In)(Al)O_x contains 0.45 wt% Pt, 1.64 wt% In, 43.4 wt% Mg, and 5.8 wt% Al.

XAS. *Ex situ* XAS measurements were performed at the SuperXAS beamline of the SLS synchrotron (2.4 GeV, 400 mA, Villigen – Switzerland). In addition, *in situ* XAS measurements were executed at the DUBBLE beam line[25, 26] of the ESRF synchrotron (6 GeV, current 160 – 200 mA, Grenoble - France). At DUBBLE, 2 mm quartz capillaries were connected to gas lines by swagelok® fittings and subsequently mounted below the gas blower (FMB Oxford). The DUBBLE gas rig system was employed to regulate the gas flows through

the capillary.[25, 26] All XAS measurements were recorded in transmission mode at the Pt L_{III} edge. XAS data analysis was executed by using the Demeter 0.9.13 software package. Background subtraction and normalization were performed for extracting the XANES and EXAFS signals.

XRD. Crystallographic phase analysis of the materials was done by using a Siemens Diffractometer Kristalloflex D5000, with Cu Kα radiation (λ = 0.154 nm). The patterns were collected in a 2θ range from 5° to 90° with a step of 0.02° and 30 s counting time at each angle.

HAADF-STEM imaging and EDX mapping. HAADF-STEM imaging and EDX elemental mapping were carried out on a FEI Titan "cubed" microscope equipped with and aberration corrector and large solid angle "Super-X" EDX detector and operated at 120 kV. The convergence semi-angle used for STEM was 21 mrad, the acceptance inner semi-angle for HAADF-STEM imaging was 85 mrad.

6.3 Results and discussion

During one-pot synthesis of Mg,Al,Pt,In-LDH, an aqueous solution of $Mg(NO_3)_2.6H_2O$, $Al(NO_3)_3.9H_2O$ and $In(NO_3)_3.xH_2O$ is mixed with an aqueous solution of NaOH, Na_2CO_3 and H_2PtCl_6 (see Experimental Section). The initial NaOH-Na_2CO_3-H_2PtCl_6 solution is yellow-colored, which is characteristic of basic H_2PtCl_6-containing aqueous solutions.[27] Upon mixing the two solutions, rapid precipitation is observed due to the self-assembly of LDHs.[16, 17] After precipitation, the solution still exhibits a yellow color which strongly indicates that Pt is not as yet incorporated inside the LDH structure at this stage. However, after a few hours of aging, the yellow-colored mixture gradually evolves to a transparent solution, suggesting that Pt is being inserted inside the pre-existing Mg,Al,In-LDH precipitate, yielding Mg,Al,Pt,In-LDH.

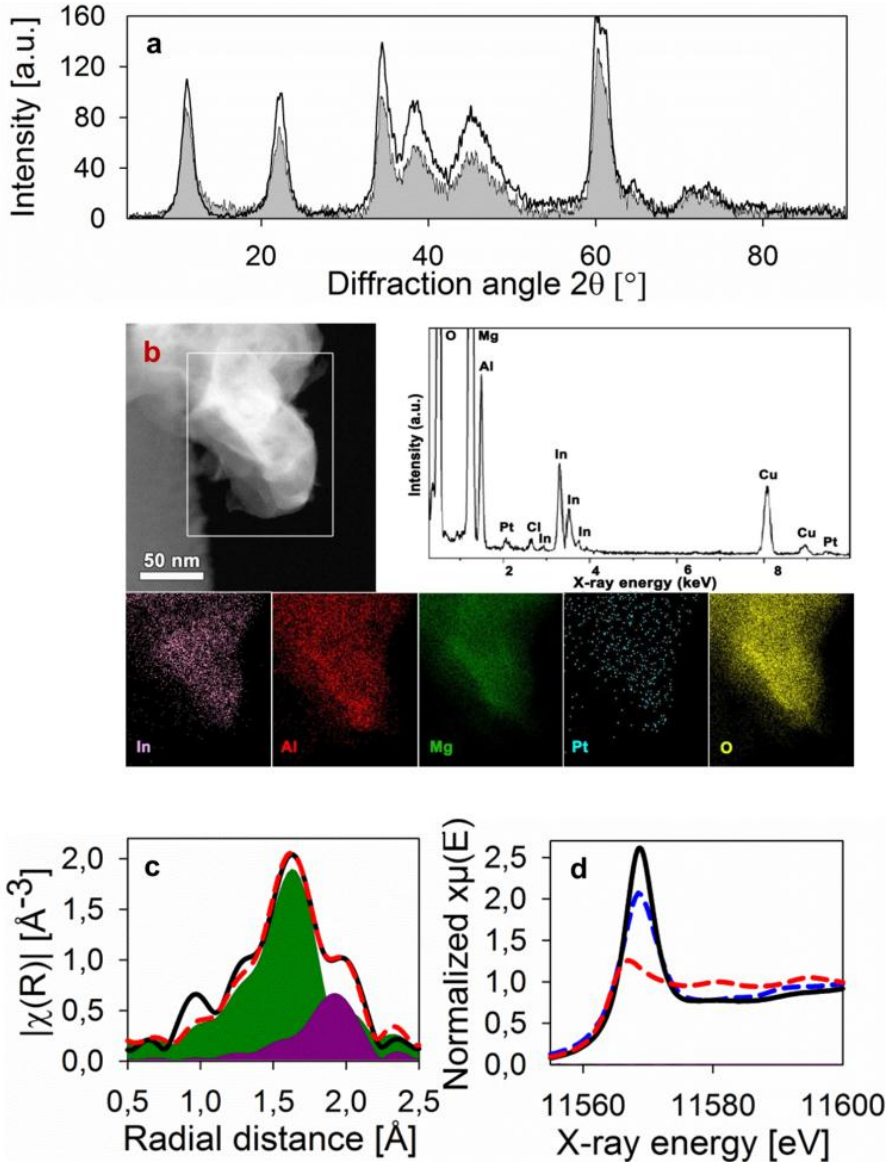

Figure 6.1: Presented data are measured on 'Mg,Al,Pt,In-LDH', i.e. the sediment obtained after co-precipitation of Mg-Al-In- and Pt-containing aqueous solutions. (a) XRD profile of Mg,Al,Pt,In-LDH (grey area) and a Mg,Al-LDH reference (solid black line); (b) HAADF-STEM overview image of a precipitate grain and the corresponding EDX chemical maps of the region marked by the white rectangle in the overview image. The summed EDX spectrum shows that Mg, Al, Pt, Cl and In are present within the precipitate; (c) Pt L_{III} edge Mg,Al,Pt,In-LDH Fourier transformed EXAFS magnitude (black solid line), Pt-O + Pt-Cl model fit (red dashed line) between R = 1.1 – 2.2 Å (R-factor = 0.005), Pt-O (green area) and Pt-Cl (purple area) contributions; (d) Pt L_{III} edge XANES spectrum of Mg,Al,Pt,In-LDH (black solid line), bulk PtO_2 (blue dashed line) and Pt (red dashed line) references.

An XRD scan of the precipitate – measured after aging, filtering, washing and drying – indeed displays typical LDH diffraction peaks (Figure 6.1.a, filled area) as compared to a Mg,Al-LDH reference (Figure 6.1.a, solid black line). In addition, the presence of Mg, Al, Pt, Cl and In inside this LDH structure is evidenced by the EDX spectrum of a separate precipitate grain (Figure 6.1.b), confirming that Mg,Al,Pt,In-LDH is formed.

The local environment and electronic state of Pt inside the LDH precipitate is monitored by Pt L_{III} EXAFS (Figure 6.1.c) and XANES (Figure 6.1.d), respectively. Modeling of the Fourier transformed (FT) EXAFS peak between R ~ 1.1 and 2.2 Å only succeeds when both Pt-O and Pt-Cl shells are included (Figure 6.1.c). Although the Pt-O contribution is dominant (N_{Pt-O} = 4.3 ± 0.3, R_{Pt-O} = 1.99 ± 0.01 Å), the Pt-Cl peak constitutes a significant part of the FT EXAFS peak shape (N_{Pt-Cl} = 1.0 ± 0.2, R_{Pt-Cl} = 2.29 ± 0.01 Å). EXAFS modeling results therefore suggest that octahedrally coordinated Pt species reside inside the LDH structure as $[PtCl_1(OH)_5]^{2-}$-type complexes (see below). XANES is consistent with these EXAFS results as the strong white line feature, which exceeds the one of bulk PtO_2, is characteristic for Cl^--OH^- ligand exchanged Pt complexes (Figure 6.1.d).[28]

After mixing of the Mg,Al,In- and Pt-containing solutions, the pH in the solution is maintained at ~ 14. At this pH and Pt precursor concentration (Experimental Section), octahedrally coordinated $[PtCl_6]^{2-}$ anions undergo rapid hydrolysis reactions yielding $[PtCl_{6-x}(H_2O)_x]^{x-2}$ species.[29] During co-precipitation of LDHs, it is known that tetravalent cations (Pt^{4+}) cannot be incorporated inside di- and trivalent (Mg^{2+}, Al^{3+}, In^{3+}) metal containing brucite-type layers.[16, 17] Moreover, the rapidly formed neutral/cationic $[PtCl_{6-x}(H_2O)_x]^{x-2}$ species do not interact with the precipitated LDH structure – in contrast to OH^- and CO_3^{2-} anions – as they cannot act as charge-compensating agents. In addition, $[PtCl_{6-x}(H_2O)_x]^{x-2}$ complexes are not compatible with the $(Mg_{1-a}^{2+}(In/Al)_a^{3+}(OH)_2)^{a+}$ brucite-layer structure due to the presence of Cl^- and H_2O^0 ligands – instead of OH^- – around Pt. This causes the Pt complexes to remain in the aqueous phase and results in a yellow-colored solution immediately after Mg,Al,In-LDH precipitation. Subsequent slower ligand exchange reactions between Cl^- or H_2O^0 and OH^- eventually result in the formation of $[PtCl_{6-x}(OH)_x]^{2-}$-type complexes (x > 3) at current conditions.[29] Hence, only after LDH assembly, these slowly formed anionic complexes undergo interaction with cationic $(Mg_{1-a}^{2+}(In/Al)_a^{3+}(OH)_2)^{a+}$ layers to neutralize the net charge of the LDH structure.[23] Such interaction leads to the intercalation

of $[PtCl_1(OH)_5]^{2-}$ complexes (XAS) inside the interlayer galleries, and results in a color change in the mixture from yellow to transparent during aging treatment.

After calcination of Mg,Al,Pt,In-LDH for 4 h at 650 °C, the XRD profile displays intense peak features around 44°, 62°, 74° and 79° (Figure 6.2.a). This is characteristic for the formation of 3D MgO-type mixed metal oxides (MMO) as a result of the collapse of the 2D lamellar LDH structure.[30, 31] The elemental EDX maps in Figure 6.2.b in combination with the Z-contrast HAADF-STEM image show rather heterogeneous distributions of Mg, Al and In cations throughout the inspected grain. Besides the typical MgO-type diffraction from the MMO and some traces of recovered LDH (memory effect), no significant XRD peaks are observed.[32] This suggests that in addition to the dominant MgO-type MMOs, some minor fractions of amorphous or nanocrystalline (mixed) metal oxide phases are formed during calcination.

Starting from binary Mg,Al-LDHs, Bellotto et al. pointed out that calcination eventually yields disordered spinel-type $Mg(Al)O_x$ mixed oxides, containing octahedral Mg^{2+} and tetrahedral Al^{3+} cations.[31] After initial dehydration of the Mg,Al-LDH structure, octahedral Al^{3+} cations rearrange by migrating from the Mg,Al-hydroxide layer to tetrahedral sites in the interlayer space. Further heating to 400 °C causes interlayer anions to decompose, and induces complete dehydroxylation of the material. This eventually leads to the formation of a 3D structure consisting of a regular oxygen cubic closed packed MgO-type network with a disordered Mg^{2+}/Al^{3+} cation distribution at the interstices. Similar to binary Mg,Al-LDHs, quaternary Mg,Al,Pt,In-LDHs are also expected to yield $Mg(Pt)(In)(Al)O_x$ MMOs – as suggested by the MgO-type diffraction reflections in XRD – in addition to a minority of XRD-insensitive amorphous/nanocrystalline (mixed) oxides (EDX).

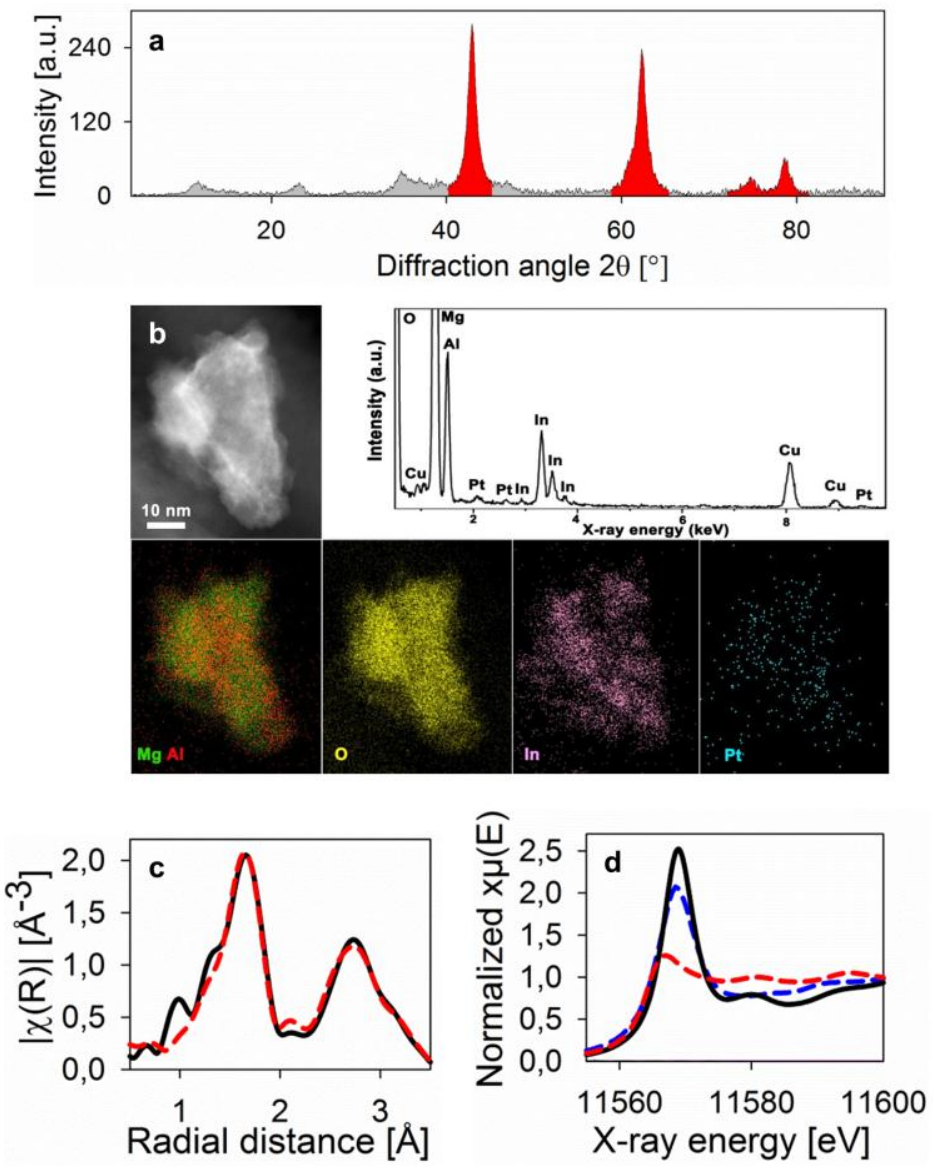

Figure 6.2: Presented data are measured on 'Mg(Pt)(In)(Al)O_x', i.e. obtained after calcination of initial Mg,Al,Pt,In-LDH. (a) XRD profile showing peak features (red areas) typical of periclase MgO. In addition, some remainders of the Mg,Al,Pt,In-LDH structure can be observed; (b) HAADF-STEM image of a Mg(Pt)(In)(Al)O_x grain and corresponding EDX elemental maps, showing that Mg, Al, Pt and In are present within the mixed metal oxide, together with a summed EDX spectrum; (c) Pt L_{III} edge Fourier transformed EXAFS magnitude of Mg(Pt)(In)(Al)O_x (black solid line) and MgO model fit (red dashed line) between R = 1.1 – 3.5 Å (R-factor = 0.012); (d) Pt L_{III} edge XANES spectrum of Mg(Pt)(In)(Al)O_x (black solid line), bulk PtO_2 (blue dashed line) and Pt (red dashed line) references.

In order to pinpoint the precise location of Pt in the calcined material, XAS measurements are used to probe its local environment as well as its electronic state. When implementing MgO as a structural model around Pt, convergence between the FT EXAFS signal of calcined Mg,Al,Pt,In-LDH and the model is obtained (Figure 6.2.c). The coordination numbers of $N_{Pt-O} = 5.4 \pm 0.4$ and $N_{Pt-Mg} = 12.6 \pm 4$ are compatible with the 6-fold

O and 12-fold Mg coordination around Mg within MgO, i.e. N_{Mg-O} = 6 and N_{Mg-Mg} = 12, respectively. In fact, the N_{Pt-Mg} coordination contains the contributions of both Mg and Al neighbors around Pt, as these two atomic species cannot be discriminated by EXAFS modeling. These EXAFS results strongly suggest that Pt is incorporated inside a Mg(Pt)(In)(Al)O_x MgO-type MMO structure. The latter finding is supported by the fact that the Pt-Mg coordination of atomically dispersed Pt atoms on MgO-type supports amounts to 4.1 ± 0.7, a significantly lower number compared to the current case.[33]

XANES (Figure 6.2.d) both complements and supports the EXAFS results. The Pt L_{III} white line height of Mg(Pt)(In)(Al)O_x exceeds the height of bulk PtO_2, demonstrating that 5d electron states of Pt atoms inside Mg(Pt)(In)(Al)O_x are more empty than in PtO_2.[34, 35] The mixed metal environment around Pt therefore induces more electron transfer from Pt towards Mg(Pt)(In)(Al)O_x as compared to pure PtO_2. The basic oxide properties exerted by the most abundant Mg^{2+} cations within Mg(Pt)(In)(Al)O_x are responsible for the strong interaction between Mg(Pt)(In)(Al)O_x and Pt.[36, 37] This leads to strong Pt oxidation and more empty 5d electron states, and results into the observed intense Pt L_{III} white line.

The possibility of Pt-incorporation inside the MMO structure after calcination implies that the original $[PtCl_1(OH)_5]^{2-}$ anions, unlike other interlayer anions, are relatively immobile and stable within the initial LDH structure. Before calcination, $[PtCl_1(OH)_5]^{2-}$ complexes are therefore suggested to have relatively strong bonds with the Mg(In)(Al)-OH groups of the layered $(Mg_{1-a}{}^{2+}(In/Al)_a{}^{3+}(OH)_2)^{a+}$ hydroxide surface. Upon calcination, initial dehydration of Mg,Al,Pt,In-LDH, In^{3+}/Al^{3+} migration to the interlayer galleries, and OH^- and $CO_3{}^{2-}$ decomposition is followed by dehydroxylation and oxidation of the metal hydroxides (metal = Mg^{2+}, Al^{3+}, In^{3+}, Pt^{4+}). As shown by XRD, HAADF-STEM and XAS, this results in the collapse of the 2D lamellar LDH structure and leads to the formation of 3D MgO-type Mg(Pt)(In)(Al)O_x MMOs plus a minority of amorphous/nanocrystalline (mixed) oxides.

The final step of catalyst activation for one-pot synthesized Mg,Al,Pt,In-LDHs consists of a H_2 TPR treatment on Mg(Pt)(In)(Al)O_x to 650 °C. *In situ* XANES spectra

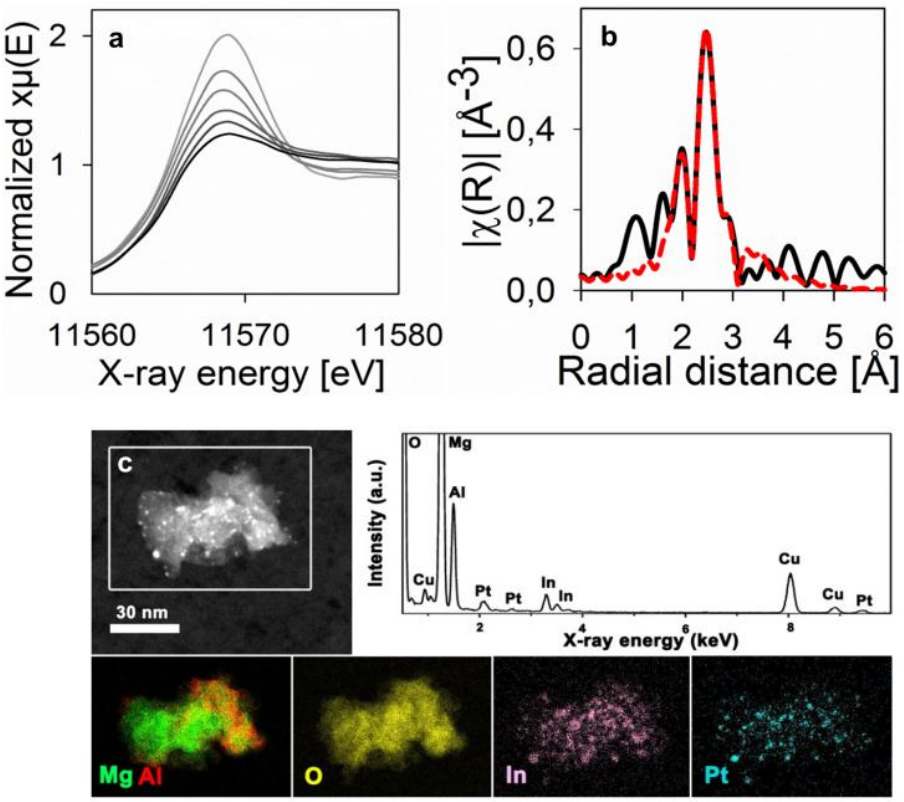

Figure 6.3: Presented data are measured on 'Pt-In/Mg(Pt)(In)(Al)O_x', i.e. obtained after H_2 TPR of Mg(Pt)(In)(Al)O_x. (a) Pt L_{III} edge XANES spectra recorded during H_2 TPR (from grey to black): white line decrease and edge shift to higher energies; (b) Fourier transformed EXAFS magnitude of Pt-In/Mg(Pt)(In)(Al)O_x (black solid line) and Pt-In + Pt-Pt model fit (red dashed line) between R = 1.8 – 3.1 Å (R-factor = 0.005); (c) HAADF-STEM image of a Pt-In/Mg(Pt)(In)(Al)O_x grain and corresponding EDX elemental maps. The summed EDX spectrum shows local concentration of both Pt and In, evidencing that Pt-In alloyed nanoparticles are formed during H_2 TPR.

recorded during this H_2 TPR display a gradual decrease of the Pt L_{III} edge white line, which is characteristic of Pt reduction (Figure 6.3.a). In addition, a significant edge shift to higher energies is observed during Pt reduction, indicating that Pt-In alloying is occurring.[33, 38] FT EXAFS modeling evidences the presence of both In and Pt neighbors around Pt, i.e. $N_{Pt\text{-}In}$ = 4.8 ± 0.4 ($R_{Pt\text{-}In}$ = 2.65 ± 0.01 Å) while $N_{Pt\text{-}Pt}$ = 2.2 ± 0.5 ($R_{Pt\text{-}Pt}$ = 2.76 ± 0.02 Å) (Figure 6.3.b), and therefore suggests the formation of Pt-In clusters. HAADF-STEM imaging confirms the formation of dispersed nanoparticles (bright dots) decorating the Mg(Pt)(In)(Al)O_x support surface (Figure 6.3.c). EDX elemental mapping shows nano-sized islands with increased Pt and In concentration, which indeed demonstrates that the clusters formed during H_2 TPR consist of Pt-In nanoalloys.

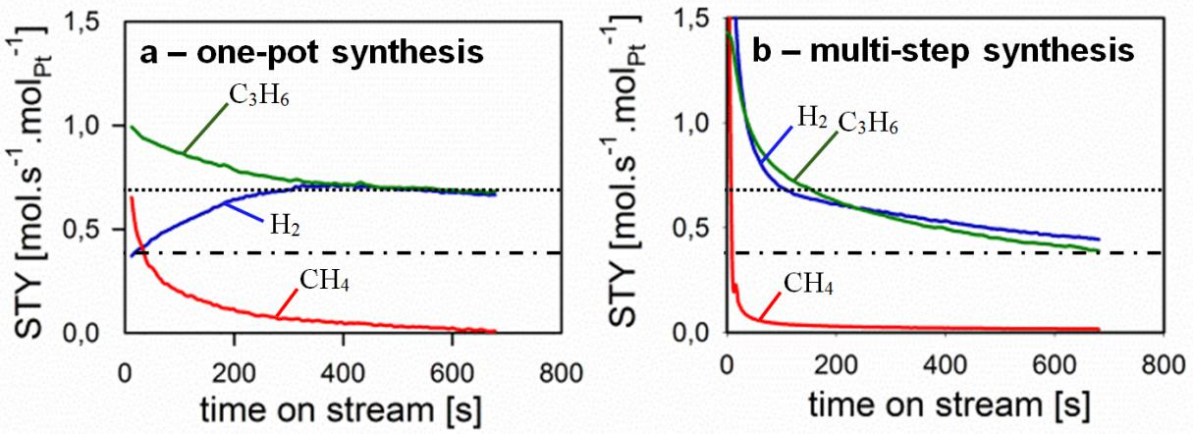

Figure 6.4: Catalytic propane dehydrogenation at 600 °C ($W_{cat}/F_{propane,0}$ = 4 $kg_{cat}\cdot s\cdot mol^{-1}$ and $P_{propane,0}$ = 5 kPa at a total pressure of 101.3 kPa): site-time yield (STY) vs. time on stream: (a) one-pot Pt-In/Mg(Pt)(In)(Al)O_x and (b) multi-step synthesized Pt-In/Mg(In)(Al)O_x.

In the course of H_2 TPR, hydrogen reduces Pt cations from the Mg(Pt)(In)(Al)O_x support (XANES, Figure 6.3.a). This causes Pt to gain mobility owing to the scission of strong Mg-O-Pt bonds. Upon temperature increase, partially reduced Pt migrates across the support and eventually forms thermodynamically stable Pt-In nanoparticles (XAS, HAADF-STEM).[39] Three mechanisms can be responsible for Pt-In alloying. Firstly, partially reduced Pt – either as migrating atoms over the support or, in a later stage, as stabilized nanoparticles – dissociates hydrogen which spills over to the Mg(Pt)(In)(Al)O_x support.[40] Subsequent long-range transport of H to In^{3+} sites results in the partial reduction of In^{3+} into $In^{\delta+}$. These moderately mobile $In^{\delta+}$ species undergo short-range transport to Pt atoms/clusters which fully reduce $In^{\delta+}$ to In^0 upon immediate stabilization inside Pt-In nano-alloys.[40] Secondly, single atoms of Pt that migrate over the support could also directly interact with In^{3+} sites and establish immediate Pt-In alloying after full reduction of In^{3+} to In^0. Thirdly, at 650 °C in H_2, a fraction of the In^{3+}-phase could reduce directly to In^0, liquefy/vaporize, undergo liquid/gas phase transport to Pt and establish Pt-In alloys.

In Figure 6.4, the one-pot synthesized Pt-In/Mg(Pt)(In)(Al)O_x catalyst performance is compared to the performance of multi-step synthesized Pt-In/Mg(In)(Al)O_x, the latter obtained through wet impregnation of Pt on Mg(In)(Al)O_x (see reference 38). The plots display the transient activity flows of C_3H_6, CH_4 and H_2 as a function of time elapsed since the introduction of a C_3H_8 step into the reactor. For all catalysts, the initial transient period is

dominated by non-selective side reactions other than propane dehydrogenation, including deep dehydrogenation (coke formation) and hydrogenolysis.[41, 42] After a few minutes, the most reactive sites are blocked by coke formation. This inhibits the occurrence of non-selective side reactions, causing the reactor outlet flow to become more rich in C_3H_6 and H_2. When comparing the stabilized steady-state activity of the two catalysts, it is clear that the one-pot synthesized Pt-In/Mg(Pt)(In)(Al)O_x exerts higher activity and similar selectivity as compared to multi-step synthesized Pt-In/Mg(In)(Al)O_x catalysts. As shown in Appendix D.1 (Figure A-14.a), one-pot synthesized Pt/Mg(Pt)(Al)O_x catalysts also exhibit some activity. However, due to the catalyst monometallic nature, initial coking leads to the blockage of the Pt active sites in Pt/Mg(Pt)(Al)O_x, yielding low activity for propylene. This emphasizes the necessity of incorporating a promoting element in the original LDH-structure, which is demonstrated here.

As can be derived from Figure 6.4.a and Figure 6.4.b, the propane dehydrogenation activity per exposed Pt site – the most expensive catalyst component – is higher for the one-pot synthesized Pt-In catalysts relative to its multi-step synthesized counterpart. These results show that the methodology of one-pot synthesis for the facile and scalable production of bimetallic Pt-based nanocatalysts is not only cost efficient during catalyst synthesis, but also during dehydrogenation reaction. More specifically, the cost of catalyst production can be drastically reduced by eliminating all-but-one synthesis steps. In addition, the propylene production cost during operation also decreases as higher yields of propylene can be obtained with the same amount of catalyst. Notably, these trends of superior dehydrogenation performance are also observed for one-pot synthesized Pt-Ga catalysts (Appendix D.1, Figure A-14.b). This demonstrates that the proposed one-pot synthesis strategy is in fact not only applicable to Pt-In/Mg(Pt)(In)(Al)O_x catalysts, but also to a broad family of Pt-based bi- or multimetallic LDH-derived catalysts.

6.4 Conclusions

A one-pot synthesis method is established for the production of tailored bimetallic Pt-based catalysts, herein exemplified by the single-step synthesis of Mg,Al,Pt,In-LDHs. Calcination of these quaternary LDHs at 650 °C results in the collapse of their 2D lamellar structure, yielding 3D Mg(Pt)(In)(Al)O_x mixed metal oxides with a MgO-type structure. Subsequent H_2 reduction treatment triggers atomic transport of reducible Pt and In cations, eventually causing well-dispersed Pt-In alloyed nanoparticles to be formed on the Mg(Pt)(In)(Al)O_x support. The one-pot synthesized Pt-In/Mg(Pt)(In)(Al)O_x catalyst exhibits superior performance during catalytic dehydrogenation of propane as compared to multi-step synthesized Pt-In catalysts. Their simple, cheap and scalable synthesis protocol as well as their high product yield make one-pot Pt-In/Mg(Pt)(In)(Al)O_x catalysts particularly attractive for industrial use. In addition, the compositional flexibility of Pt-containing LDHs allows for the rational design of the catalyst properties and fine control over the catalyst active sites. The future exploitation of this compositional flexibility could pave the way to more efficient multimetallic Pt-based catalysts.

6.5 References

(1) Schlögl, R. *Angew. Chem. Int. Ed.* **2015**, *54*, 3465-3520.

(2) Somorjai, G. A.; Park, J. Y. *Angew. Chem. Int. Ed.* **2008**, *47*, 9212-9228.

(3) Yu, W.; Porosoff, M. D.; Chen, J. G. *Chem. Rev.* **2012**, *112*, 5780-5817.

(4) Lee, H.; Nedrygoulov, I. I.; Lee, C.; Somorjai, G. A.; Park, J. Y. *Angew. Chem. Int. Ed.* **2015**, *54*, 2340-2344.

(5) Peter, M.; Flores Camacho, J. M.; Adamovski, S.; Ono, L. K.; Dostert, K.-H.; O'Brien, C. P.; Roldan Cuenya, B.; Schauermann, S.; Freund, H.-J. *Angew. Chem. Int. Ed.* **2013**, 52, 1-6.

(6) Schlögl, R. *Angew. Chem. Int. Ed.* **2004**, *43*, 1628-1637.

(7) Xia, Y. N. *Angew. Chem. Int. Ed.* **2014**, *53*, 12268-12271.

(8) Yu, T.; Kim, D. Y.; Zhang, H.; Xia, Y. *Angew. Chem. Int. Ed.* **2011**, *123*, 2825-2829.

(9) Ahmadi, T. S.; Wang, Z. L.; Green, T. C.; Henglein, A.; El-Sayed, M. A. *Science*, **1996**, *272*, 1924-1926.

(10) Guo, S.; Zhang, S.; Sun, S. *Angew. Chem. Int. Ed.* **2013**, *52*, 8526-8544.

(11) Xiao, Q.; Liu, Z.; Bo, A.; Zavahir, S.; Sarina, S.; Bottle, S.; Riches, J. D.; Zhu, H. *J. Am. Chem. Soc.* **2015**, *137*, 1956-1966.

(12) Teramura, K.; Iguchi, S.; Mizuno, Y.; Shishido, T.; Tanaka, T. *Angew. Chem. Int. Ed.* **2012**, *51*, 8008-8011.

(13) Long, X.; Li, J. K.; Xiao, S.; Yan, K. Y.; Wang, Z. L.; Chen, H. N., Yang, S. H. *Angew. Chem. Int. Ed.* **2014**, *53*, 7584-7588.

(14) Teramura, K.; Iguchi, S.; Mizuno, Y.; Shishido, T.; Tanaka, T. *Angew. Chem. Int. Ed.* **2012**, *51*, 8008-8011.

(15) Choy, J. H.; Kwak, S. Y.; Jeong, Y. J.; Park, J. S. *Angew. Chem. Int. Ed.* **2000**, *39*, 4042-4045.

(16) Fan, G.; Li, F.; Evans, D. G.; Duan, X. *Chem. Soc. Rev.* **2014**, *43*, 7040-7066.

(17) He, S.; An, Z.; Wei, M.; Evans, D. G.; Duan, X. *Chem. Comm.* **2013**, *49*, 5912-5920.

(18) Berhens, M.; Kasatkin, I.; Kühl, S.; Weinberg, G. *Chem. Mater.* **2010**, *22*, 386-397.

(19) Kühl, S.; Tarasov, A.; Zander, S.; Kasatkin, I.; Behrens, M. *Chem. – Eur. J.* **2014**, *20*, 3782-3792.

(20) Ota, A.; Kröhnert, J.; Weinberg, G.; Kasatkin, I.; Kunkes, E. L.; Ferri, D.; Girgsdies, F.; Hamilton, N.; Armbrüster, M.; Schlögl, R.; Behrens, M. *ACS Catal.* **2014**, *4*, 2048-2059.

(21) Behrens, M. *Catal. Tod.* **2015**, *246*, 46-54.

(22) Lee, J. H.; Kim, H.; Lee, Y. S.; Jung, D.-Y. *ChemCatChem* **2014**, *6*, 113-118.

(23) Belskaya, O. B.; Gulyaeva, T. I.; Leont'eva, N. N.; Zaikovskii, V. I.; Larina, T. V.; Kireeva, T. V.; Doronin, V. P.; Likholobov, V. A. *Kinet. Catal.* **2011**, *52*, 876-885.

(24) Belskaya, O. B.; Gulyaeva, T. I.; Talsi, V. P.; Kazakov, M. O.; Nizovskii, A. I.; Kalinkin, A. V.; Bukhtiyarov, V. I.; Likholobov, V. A. *Kinet. Catal.* **2014**, *55*, 786-792.

(25) Nikitenko, S.; Beale, A. M.; van der Eerden, A. M. J.; Jacques, S. D. M.; Leynaud, O.; O'Brien, M. G.; Detollenaere, D.; Kaptein, R.; Weckhuysen, B. M.; Bras, W. J. *Synchrotron Rad.* **2008**, *15*, 632-640.

(26) Martis, V.; Beale, A. M.; Detollenaere, D.; Banerjee, D.; Moroni, M.; Gosselin, F.; Bras, W. J. *Synchrotron Rad.* **2014**, *21*, 462-463.

(27) Chen, S.; Wu, Y.; Tao, S.; Cui, P.; Chu, W.; Chen, X.; Wu, Z. *J. Mol. Struct.* **2013**, *1041*, 39-43.

(28) Chen, X.; Chu, W.; Wang, L.; Wu, Z. *J. Mol. Struct.* **2009**, *920*, 40-44.

(29) Spieker, W. A.; Liu, J.; Miller, J. T.; Kropf, A. J.; Regalbuto, J. R. *Appl. Catal. A-Gen.* **2002**, *232*, 219-235.

(30) Bellotto, M.; Rebours, B.; Clause, O.; Lynch, J.; Bazin, D.; Elkaïm, E. *J. Phys. Chem.* **1996**, *100*, 8527-8534.

(31) Bellotto, M.; Rebours, B.; Clause, O.; Lynch, J.; Bazin, D.; Elkaïm, E. *J. Phys. Chem.* **1996**, *100*, 8535-8542.

(32) Rives, V. *Mater. Chem. Phys.* **2002**, *75*, 19-25.

(33) Filez, M.; Redekop, E. A.; Poelman, H.; Galvita, V. V.; Marin, G. B. *Anal. Chem.* **2015**, *87*, 3520- 3526.

(34) Filez, M.; Poelman, H.; Ramachandran, R. K.; Dendooven, J.; Devloo-Casier, K.; Fonda, E.; Detavernier, C.; Marin, G. B. *Catal. Today* **2014**, *229*, 2-13.

(35) Huebner, M.; Koziej, D.; Bauer, M.; Barsan, N.; Kvashnina, K.; Rossell, M. D.; Weimar, U.; Grunwaldt, J. D. *Angew. Chem. Int. Ed.* **2011**, *50*, 2841-2844.

(36) Nagai, Y.; Dohmae, K.; Ikeda, Y.; Takagi, N.; Tanabe, T.; Hara, N.; Guilera, G.; Pascarelli, S.; Newton, M. A.; Kuno, O.; Jiang, H.; Shinjoh, H.; Matsumoto, S. *Angew. Chem. Int. Ed.* **2008**, *47*, 9303 –9306.

(37) Nagai, Y.; Hirabayashi, T.; Dohmae, K.; Takagi, N.; Minami, T.; Shinjoh, H.; Matsumoto, S. *J. Catal.* **2006**, *242*, 103–109.

(38) Sun, P.; Siddiqi, G.; Vining, W. C., Chi, M.; Bell, A. T. *J. Catal.* **2011**, *282*, 165–174.

(39) Filez, M.; Redekop, E. A.; Poelman, H.; Galvita, V. V.; Ramachandran, R. K.; Dendooven, J.; Detavernier, C.; Marin, G. B. *Chem. Mater.* **2014**, *26*, 5936-5949.

(40) Filez, M.; Redekop, E. A.; Poelman, H.; Galvita, V. V.; Meledina, M.; Turner, S.; Van Tendeloo, G.; Bell, A. T.; Marin, G. B. *ACS Catal.* (submitted).

(41) Redekop, E. A.; Galvita, V. V.; Poelman, H.; Bliznuk, V.; Detavernier, C.; Marin, G. B. *ACS Catal.* **2014**, *4*, 1812–1824.

(42) Sattler, J. J. H. B.; Ruiz-Martinez, J.; Santillan-Jimenez, E.; Weckhuysen, B. M. *Chem. Rev.* **2014**, *114*, 10613-10653.

Chapter 7. *In situ* XAS and XRF study of nanoparticle nucleation during O_3-based Pt deposition

Abstract

X-ray absorption spectroscopy (XAS) and X-ray fluorescence (XRF) were combined *in situ* to study the ALD-based synthesis of Pt catalysts. This first time combination of synchrotron-based techniques was applied during the (methylcyclopentadienyl)trimethylplatinum/ozone deposition process executed at 150°C on a silica support. A nucleation delay indicative for nanoparticle formation was observed for Pt loadings below 1 equivalent monolayer. XAS and XRF were recorded simultaneously at different catalyst loadings in this nucleation regime. Analysis of the combined *in situ* data yielded a quantitative picture of the evolution of the diameter, shape, lattice packing and density of the deposited Pt clusters. Additionally, the degree of oxidation at the cluster surface after the ozone pulse could be monitored. At the early start of the deposition process, Pt adatoms cluster together to form stable nuclei. A strong increase in the density of nuclei is seen below 0.16 equivalent monolayers, after which coalescence gradually occurs. From 0.04 to 0.71 equivalent monolayers, Pt clusters are fcc packed and correspond best to a hemispherical (111)-truncated cuboctahedral shape. By crosslinking the XRF and XAS data, a linear increase in cluster diameter with Pt loading is observed within this range. The surface of the Pt clusters is shown to be oxidized immediately after the ozone exposure. The degree of surface oxidation remains approximately constant for clusters with a 1 – 3 nm diameter. This surface oxygen is shown to be crucial for further growth during deposition. The combined application of *in situ* XRF and XAS thus allowed for an advanced identification of the ALD-deposited Pt nanoparticles.

7.1 Introduction

Atomic layer deposition (ALD) uses sequential self-saturating reactions between gaseous precursor molecules and a solid surface to grow thin films in a layer-by-layer fashion.[1-3] The cyclic AB-type exposures make it possible to deposit material with an atomic layer precision in a conformal way.[4] However, owing to nucleation difficulties, the start of metal deposition on oxide surfaces using the ALD procedure is often characterized by very small growth rates and Volmer-Weber type island growth.[3, 5-9] This initial formation of metal nanoparticles opens the opportunity to use this deposition technique for the controlled atomic-scale design of catalysts.[10-13] Promising catalytic properties have recently been reported for Pd, Pt and Ru (bi)metallic nanoparticles grown on different supports including carbon aerogels[13], $SrTiO_3$ nanocubes[10], alumina spheres[11], and (surface-modified) silica gels[8, 12].

The most common Pt deposition process utilizes alternating exposures to (methylcyclopentadienyl)trimethylplatinum ($MeCpPtMe_3$) vapor and O_2 gas.[14, 15] During a precursor pulse in the nucleation regime, the Pt precursor may adsorb on both the oxide support surface and the existing Pt clusters. In the next O_2 pulse, oxygen burns off the remaining ligands of the newly adsorbed precursor molecules and is commonly believed to further oxidize the Pt cluster surface.[14-16] The chemisorbed oxygen atoms form anchoring points for the next arriving precursor molecules inducing combustion of the ligands. Recently, it was shown that the $MeCpPtMe_3$ precursor can also be combined with O_2 plasma[17], N_2 plasma, NH_3 plasma[18] and O_3 as a reactant[19]. The O_3 based process enables Pt deposition in a lower temperature range due to the stronger oxidizing power of O_3 compared to O_2. It is clear that oxygen plays a crucial role in both the O_2- and O_3-based Pt processes. However, the degree of oxidation of the supported Pt clusters under *in situ* conditions is not yet known in a quantitative way.

Besides knowledge on the oxidation state of the Pt clusters, a better understanding of the mechanisms occurring during nucleation is necessary for a more rational catalyst design.

In particular, the metal loading and the density and diameter of the nanoparticles are needed to reconstruct an evolutional picture of the process. Additionally, detailed structural information is required since the reactivity of Pt nanoparticles changes with both their geometry[20] and degree of oxidation[21].

In this work, information on the diameter, shape, lattice packing, density and oxidation state of the Pt clusters is acquired by applying X-ray absorption spectroscopy (XAS) and X-ray fluorescence (XRF) simultaneously under *in situ* conditions during deposition. XAS yields detailed structural and electronic information through extended X-ray absorption fine structure (EXAFS spectroscopy) and X-ray absorption near edge structure (XANES spectroscopy) respectively.[22, 23] XRF provides information on the amount of material deposited.[24] A novel setup, allowing *in situ* XAS and XRF during deposition, is used to record the Pt L_{III}-edge fluorescence signal between $MeCpPtMe_3/O_3$ cycles. An evolutional picture of the structure and oxidation state of the deposited Pt clusters is pursued during the nucleation stage. The particular method of *in situ* XRF-XAS experiments during nanoparticle deposition is, to the best of our knowledge, a first time combination. Therefore, this work is a proof-of-principle of the simultaneous *in situ* XRF-XAS application and aims to provide a stepwise procedure for the applied methodology. In addition, a structural study of the O_3-based Pt process was not yet performed before and questions concerning the degree of cluster oxidation have remained unanswered.

7.2 Experimental

7.2.1 Setup and materials

A cold-wall ALD setup was designed to study deposition processes using *in situ* XRF and *in situ* XAS at a synchrotron facility. The solid $MeCpPtMe_3$ precursor (99% Strem

Chemicals) was preserved in a stainless steel container and heated above its melting point of 30°C. This container was connected to the vacuum chamber by a 60°C heated delivery line. The precursor was pulsed to the chamber using argon as carrier gas. The sample chamber contained a heated substrate holder and evacuated double Kapton windows for X-ray transmission. A gate valve connected the chamber with a turbo pump, which was in turn backed up by a rotary pump. An OzoneLab^{TM} OL100 ozone generator was used to produce O_3 from pure O_2. The O_3 concentration obtained was 175 µg/mL.

In order to minimize particle-support interaction, SiO_2 was chosen as substrate. Rather than a flat surface, a mesoporous film of SiO_2 was used to increase the exposed surface area and hence the X-ray fluorescence signal. Thus, all Pt depositions were performed on a thin film of mesoporous silica which was supported on a flat Si wafer, i.e. SiO_2/Si. The silica film had a thickness of 188 nm, a porosity of 62% and an average pore diameter of 5 nm. A surface area ratio of ca. 30 cm² of SiO_2 substrate surface per cm² of flat Si wafer surface was obtained. This corresponds to a specific surface area of 65 m²/g SiO_2. Further details on the characteristics and synthesis of the mesoporous SiO_2 film were published elsewhere.[25]

Pt was grown at a substrate temperature of 150°C. The first deposition half-cycle consisted of controlled exposure of the substrate to the $MeCpPtMe_3$ precursor pulse at pressures up to $1.6.10^{-1}$ mbar, followed by a 50 s pump time for precursor evacuation to a pressure of ca. 2.10^{-5} mbar. Within the second half-cycle, an O_3 pulse was injected into the chamber and again followed by a 50 s pump down, both at similar pressures as for the first half-cycle. When X-ray measurements were performed *in situ*, the evacuation time after the O_3 pulse was increased (see Section 7.2.2.). No purge gas was utilized. The pulse time for the $MeCpPtMe_3$ precursor was 10 s. The gate valve connecting the chamber to the pumping system, was closed additionally for 5 s, yielding a total static exposure of 15 s. The O_3 reactant gas pulse of 5 s was followed by another 5 s of residence time in the chamber. Consequently, the static exposure acquired for O_3 was 10 s.

7.2.2 **Instrumentation and methods**

In situ XRF and *in situ* XAS measurements were performed in between Pt deposition cycles at the SAMBA beam line[26] of the 2.75 GeV SOLEIL synchrotron (Saint-Aubin, France) using a top-up electron beam of 430 mA. All experiments were recorded in fluorescence mode (Pt-Lα line) at the Pt L_{III} edge (E = 11564 eV) using a 35-element Ge detector. XRF measurements at 12 keV were performed after each deposition cycle. XANES measurements were executed every 5^{th} cycle (ca. 5 minutes/scan), whereas several EXAFS scans were taken after each 10^{th} cycle (ca. 30 minutes/scan). All measurements were recorded during the pump down period situated after the pulse of O_3 reactant gas. Background scans were obtained before the depositions started and all raw data signals measured during the deposition process were corrected for this background contribution.

The XRF counts measured during *in situ* experiments were recalculated to units of equivalent monolayers (EML) of Pt. This number of EML equals the number of atoms deposited on 1 nm² of SiO_2 support surface divided by the number of atoms necessary to form 1 monolayer of Pt on 1 nm² of Pt bulk. The latter quantity was derived theoretically by multiplying the expected thickness of 1 monolayer of Pt deposited on Pt bulk, i.e. 0.247 nm, and the number of Pt atoms residing within the volume of 1nm² (base) x 1 nm (height), i.e. 66.2 atom/(nm^3). This results in 16.4 atoms/nm². The number of Pt atoms/nm² of SiO_2 surface deposited during the synchrotron experiments was determined a posteriori by performing *ex situ* XRF measurements (Bruker Artax, Mo X-ray source, XFlash 5010 silicon drift detector) on the resulting sample. The number of XRF counts recorded for the final sample was linked with an average Pt film thickness by using an experimental relation between the XRR Pt film thickness and the number of XRF counts. The average film thickness obtained for the final sample was then transformed to the number of Pt atoms deposited/nm². By dividing the latter quantity through the number of atoms necessary to form 1 monolayer of Pt on 1 nm² of Pt bulk, the number of EML was obtained. The latter was corrected for its specific surface area.

All *ex situ* XRF measurements were recalculated to number of EML by applying the same methodology.

XAS data reduction and analysis were executed with Athena and Artemis, part of the Demeter 0.9.13 software package.[27] The pre-edge background was subtracted from the data signal. The edge energy E_0 was chosen at the maximum of the first derivative of the spectrum. The isolated atom absorption background $\mu_0(E)$ was calculated by a cubic spline fitting procedure, using the AUTOBK routine. Edge step normalization to the edge jump was performed on pre-edge background subtracted spectra, yielding the XANES signal.[22] The k^2-weighted EXAFS signal was Fourier transformed to R-space to obtain the radial distribution function.

The EXAFS signal was modeled using the extended formulation of the EXAFS function in which the third cumulant $\sigma^{(3)}$ is incorporated in the argument of the sine function.[28] The metallic Pt fcc structure with a lattice parameter of 3.92 Å was introduced as starting structural model for EXAFS fitting. In addition, Pt-O neighbors at 1.92 Å distance from the Pt absorber were implemented. The FEFF 6.0 code[29] was applied to calculate the phase shifts and backscattering amplitude functions of Pt-O and Pt-Pt contributions to the EXAFS signal. For the Pt metal structure, spherical clusters with radius 6.0 Å and maximum photoelectron path length of 6.5 Å were installed. The photoelectron paths with significant contributions to the EXAFS signal were selected and further used for modeling. The experimental spectra were modeled from R = 1.5 – 6 Å (k = 2.7 – 12.2 $Å^{-1}$). However, for the spectrum recorded at the lowest Pt loading, i.e. 0.007 EML, a restricted R-range (R = 1.5 – 3 Å, k = 2.7 – 12.2 $Å^{-1}$) is used due to its poorer data quality. The Levenberg-Marquardt algorithm was used for non-linear least-squares minimization of the objective function χ_v^2. This minimization, carried out by IFEFFIT[27], yielded estimates for the structural parameters by multiple shell fitting in R-space using multiple k-weightings. The R-factor, defined as the closeness of fit to the data[30], is used to evaluate the agreement between model and experiment. All binary correlations between the estimated parameters were below 0.85. From

the fit to the Pt foil reference signal with bulk Pt fcc structure, an amplitude reduction factor S_0^2 of 0.82 ± 0.04 was obtained. The latter value was used for further Pt L_{III} edge EXAFS modeling of the signals measured during the $MeCpPtMe_3/O_3$ deposition process onto the mesoporous SiO_2 support.

Additional *ex situ* structural analysis was carried out on the sample in the end state of the *in situ* deposition by means of transmission electron microscopy (TEM). A specimen slice was cut out of the sample in a dual beam scanning electron microscopy - focused ion beam (SEM-FIB) apparatus (FEI Nova 600 Nanolab with Sirion FEGSEM and Magnum Ion Column). After deposition of a carbon buffer and Pt protector layer for sample strength, a FIB treatment with Ga ions was applied to obtain a 100 nm slice. The thinned sample was mounted on a copper support grid and transferred to the TEM. A microscope JEOL JEM2200FS-Cs-corrected, operated at 200 kV and equipped with Schottky-type FEG, EDX JEOL JED-2300D and JEOL in-column omega filter, was used. High resolution (HR) TEM, scanning transmission bright field (STEM-BF) and energy dispersive X-ray (EDX) analysis were applied.

Crystallographic analysis was performed by means of X-ray diffraction (XRD) measurements in θ – 2θ mode using a Siemens Diffractometer Kristalloflex D5000, with Cu Kα radiation. The powder patterns were collected in a 2θ range from 15° to 60° with a step of 0.02° and 30 s counting time per angle. By fitting a Gaussian function to a diffraction peak, the crystallite diameter can be determined from the peak width via the Scherrer equation.[31]

7.3 Results and discussion

7.3.1 X-ray fluorescence measurements

Firstly, knowledge is obtained on the evolution in Pt loading of the mesoporous SiO_2 support with the number of $MeCpPtMe_3/O_3$ deposition cycles. This is done by performing *ex situ* XRF measurements on samples with 10, 30, 50, 75, 100 and 125 cycles. The XRF intensities are plotted in terms of the number of equivalent monolayers (EML) of Pt (Figure 7.1, *ex situ* XRF). Three regions can be distinguished in the XRF growth curve. During the first 30 cycles, it appears that very little material is deposited. Thereafter, a monotonic increase in growth rate is seen, implying an increased deposition rate of Pt. This growth rate evolves towards a constant value resulting in a linear growth regime starting from ± 60 cycles (1 EML). The linear growth is indicative for nanoparticle coalescence followed by film closure.[32] Because the formation of nanoparticles is of particular interest from a catalysis point of view, the focus during the *in situ* synchrotron experiments will be on the range of loadings below the onset of the linear growth regime, i.e. below 60 deposition cycles. This region corresponds to Pt loadings below 1 EML.

Although the *ex situ* XRF measurements are able to indicate the starting point of the linear growth regime, the XRF signal at low Pt loadings is less conclusive about the actual growth behavior due to its low sensitivity. This sensitivity can be improved by performing *in situ* XRF measurements at a high brilliance synchrotron facility using the same process conditions as before (Figure 7.1, *in situ* XRF, see also the inset). A subtle increase in XRF intensity is now observed from the first cycles. The latter implies that there is already growth from the beginning of the O_3-based Pt process. As the deposition evolves and the number of cycles increases, the growth rate increases monotonically during the nucleation regime in line with the *ex situ* measurements.

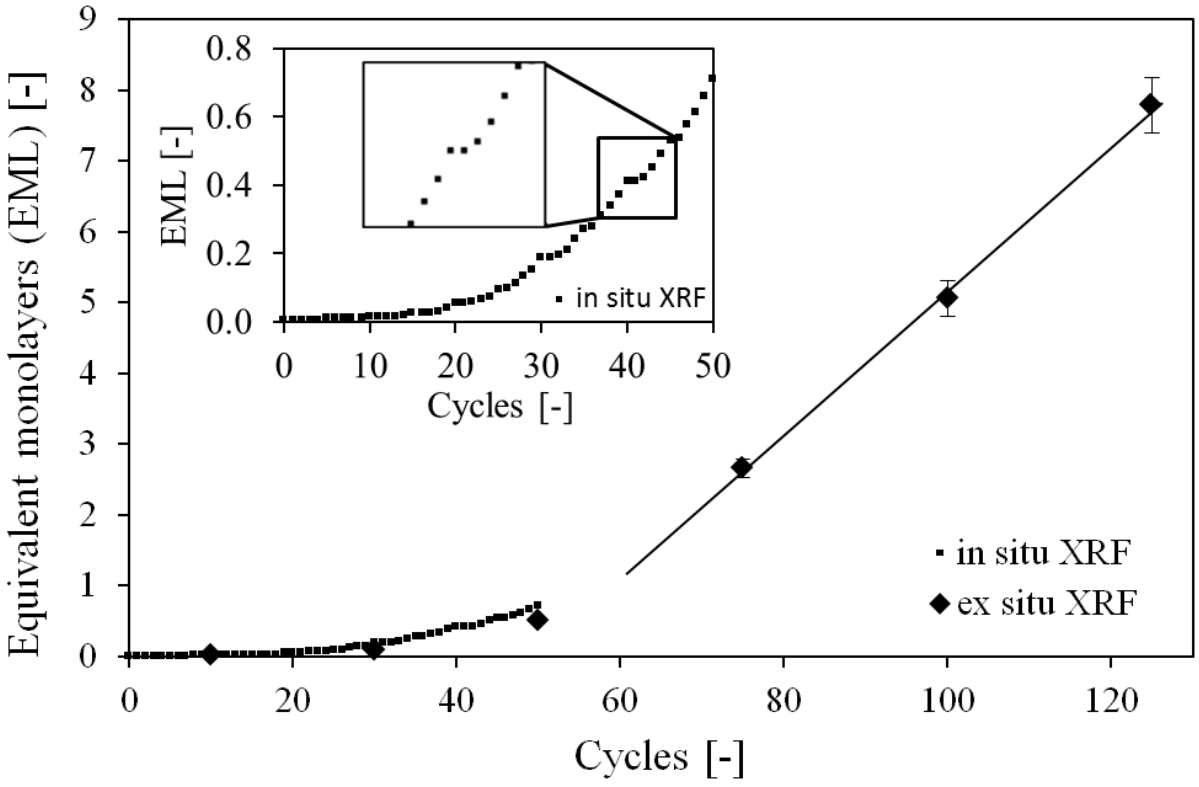

Figure 7.1: The number of equivalent monolayers (EML) of Pt deposited as a function of the number of $MeCpPtMe_3/O_3$ cycles is shown. Both *in situ* and *ex situ* XRF data are depicted. The dashed line proves the linearly of the linear growth regime above 60 cycles. In the inset, the *in situ* (synchrotron) XRF data are plotted more clearly for the first 50 cycles. An additional zoom around 40 cycles is presented within this inset.

An additional zoom is made from the *in situ* XRF data around 40 cycles in the inset of Figure 7.1. The number of EML of Pt after 40 and 41 cycles are quasi-identical. This implies that no additional Pt is deposited during the 41st $MeCpPtMe_3/O_3$ cycle. The latter is observed for each cycle following a XAS measurement. A beam influence as the underlying cause can be excluded since the same effect is observed at locations on the support that are not irradiated during the XAS measurements. In fact, the reduced growth is in agreement with an earlier study showing a decreasing growth rate of the O_3-based Pt process as a function of the pump time following the O_3 step in the deposition process.[19] During a XAS measurement the chamber is evacuated for ca. 90 min, i.e. the duration of three EXAFS scans, which is much longer than the standard pump time of 50 s between consecutive ALD cycles. Given the previous study, this difference in pump time between ALD cycles with and without

intermediate XAS measurement seems to be the underlying cause for the reduced growth rate following a XAS measurement.

7.3.2 X-ray absorption near edge structure: spontaneous reduction.

In the previous decades, numerous XANES studies have appeared on the effect of particle size, support and process conditions upon the resonance shape at the Pt edge.[33-36] It is widely known that at the Pt L_{III} edge an electronic transition occurs from the $2p_{3/2}$ core level to the $5d_{3/2}$ or $5d_{5/2}$ valence state.[37] The white line (WL) intensity, i.e. the area of the first maximum at the edge, reflects the number of transitions occurring. More electronic transitions will take place when the density of unoccupied d-electron states increases. Hence, the WL intensity is proportional to the density of unoccupied d-electron states.[38]

As indicated in the introduction, the degree of oxidation of the Pt phase is a key feature determining growth during the deposition process. However, this factor is not fully known during the deposition process and remains a question of great interest. In conventional metal oxides, ionic bonds are expected to be formed between the oxygen atoms and the metal. In the course of Pt oxidation, d-electrons could therefore participate in chemical reactions. As a result, the density of unoccupied d-electron states changes accordingly during these reactions. Therefore, probing the Pt L_{III} XANES WL intensity *in situ* can yield a deeper understanding of the chemical state of Pt during deposition.

In particular, the WL intensity at the Pt L_{III} edge is linearly proportional to the oxidation state of the Pt phase within a given cluster size range.[39, 40] In order to determine this oxidation state of the Pt phase, the WL intensity needs to be quantified and connected to the Pt^0 and Pt^{4+} states. The quantification of the WL intensity is obtained by simultaneously fitting a Gaussian and an arctangent function to the XANES WL intensity area. The WL intensity then corresponds to the area intensity of the Gaussian function. By applying this fitting procedure to both metallic Pt (Pt^0) and PtO_2 (Pt^{4+}), the WL intensities for this lowest

and highest oxidation state are obtained. By connecting these values to their respective oxidation state, the linear relationship between the WL intensity and the Pt oxidation state is established. In the following, the quantification of the WL intensity of all spectra is obtained through the simultaneous Gaussian-arctangent fitting. Once the WL intensity quantified, the oxidation state is determined by using the established WL intensity-oxidation state relationship. This WL intensity analysis is preferred to a linear combination fitting (LCF) analysis because of the direct link between the WL intensity and the Pt oxidation state. In addition, in LCF two or more separate phases are implicitly assumed to be present, which is not evidenced at this point.

Using the WL intensity methodology, the oxidation state evolution of the Pt phase is obtained as a function of the residence time of the sample in the vacuum chamber, following the O_3 step in the deposition process (Figure 7.2). Based on Yoshida et al.[39], the error bars shown for these oxidation state data are estimated to be around ± 0.1. The normalized XANES spectra utilized to calculate this oxidation state evolution are represented in the inset of Figure 7.2. After the first XANES measurement obtained immediately after the O_3 pulse, each fourth minute another scan is recorded. The arrow in the inset indicates the time evolution of the WL peak. A gradual decrease of the XANES WL intensity peak and average Pt oxidation state with time is observed for the sample with 0.52 EML. This indicates a spontaneous reduction, caused by oxygen desorption from the sample at 150°C in vacuum.[41] As explained in Section 7.3.1, an X-ray beam effect could be excluded, since the spontaneous reduction also occurs without X-ray measurements.

In Figure 7.2, two additional oxidation states measured 60 minutes after the ozone pulse are shown as horizontal lines. The two measurements are done at higher/lower Pt loadings, i.e. 0.37 EML and 0.71 EML, and represent their respective stabilized reduced oxidation states. As explained in Section 7.3.10, the stabilized oxidation state of the sample with a 0.52 EML loading will be intermediate to the former two. Hence, the major part of the spontaneous reduction takes place within the first 30 minutes after the O_3 pulse. This transient

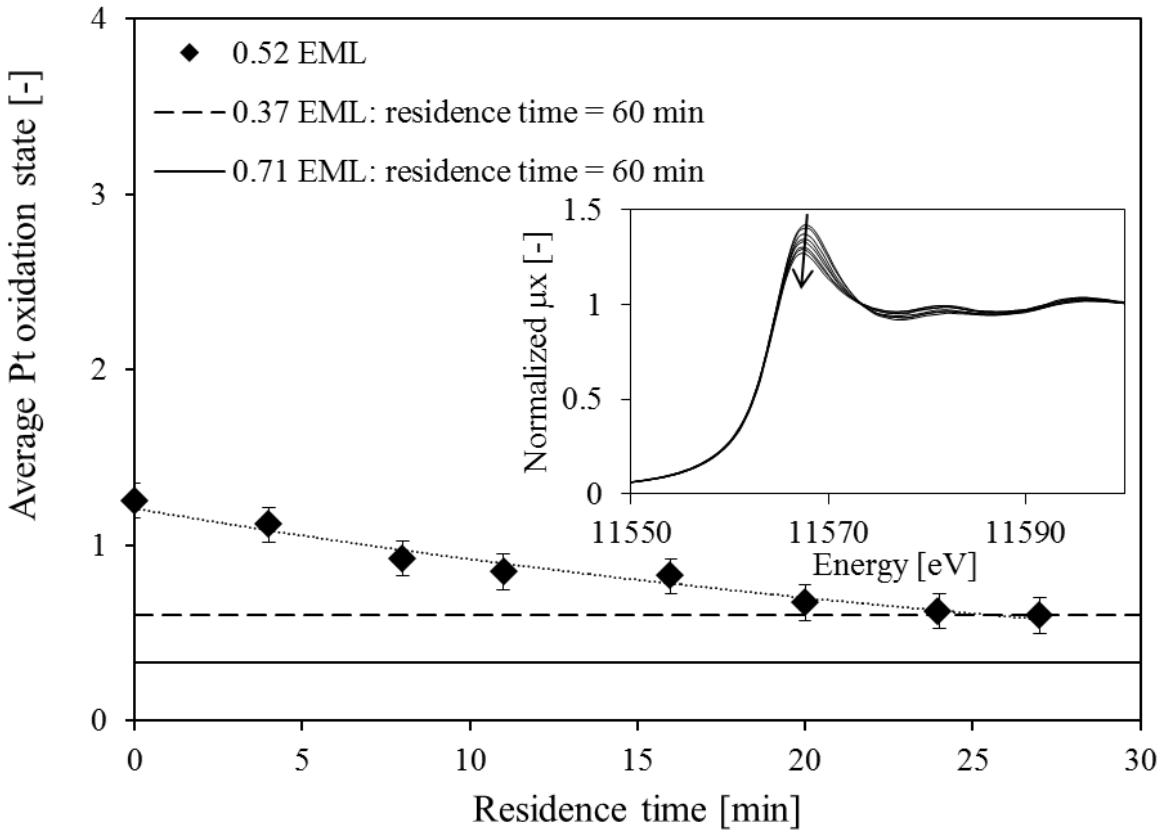

Figure 7.2: Pt oxidation state evolution as a function of the residence time of the sample in the deposition chamber following the O_3 step in the deposition process. Two additional oxidation state values at higher/lower Pt loadings are represented as horizontal lines. These two values are measured after a 60 minute evacuation in the vacuum chamber. Additionally, in the inset, the normalized XANES spectra after 0.52 EML are shown from which the corresponding values of the average Pt oxidation state are obtained.

regime covers the same timescale as the one required to record an EXAFS scan. In view of having EXAFS measured on a close to stable structure, it was chosen to perform the EXAFS measurements after a 30 min evacuation time following the O_3 pulse in the deposition process.

Some fundamental conclusions can be made concerning the event of spontaneous reduction and the reduced growth rate observed following a XAS measurement. During spontaneous reduction, originally chemisorbed oxygen desorbs from the Pt phase. After this spontaneous reduction, as illustrated in the inset of Figure 7.1, Pt deposition is disabled. Consequently, chemisorbed oxygen is essential for reaction with new precursor molecules entering the chamber during the next pulse. Equivalently, the oxygen atoms function as

anchoring points for new Pt precursors. Furthermore, the spontaneous reduction occurs to such extent that no or a negligible amount of oxygen remains at the cluster surface.

7.3.3 **Extended X-ray absorption fine structure: modeling.**

In Figure 7.3.a, the k^2-weighted EXAFS signals are represented for five different loadings below 1 EML. These spectra are recorded during the nucleation regime of the deposition process at 0.007, 0.04, 0.16, 0.37 and 0.71 EML of Pt. The data quality of the EXAFS signal at the lowest Pt loading, i.e. 0.007 EML, is low due to the very little amount of Pt deposited at this stage of deposition. The signal quality significantly improves with increasing Pt loading. Similar features, somewhat shifted to higher k-values for lower loadings, are observed from 0.04 EML on.

Figure 7.3.b represents the magnitude of the Fourier transformed k^2-weighted EXAFS signals shown in Figure 7.3.a. In addition, the metallic fcc Pt Fourier transformed signal is plotted. It is reported that the first nearest neighbor Pt-O and Pt-Pt peaks appear at about ~2 Å and ~2.8 Å respectively in the phase corrected R-space.[22] The latter distances correspond to the real interatomic distances between the respective atomic pairs and are indicated accordingly in Figure 7.3.b.

At the very beginning of the Pt deposition, i.e. 0.007 EML, a Pt-O neighbor peak is predominantly present compared to the Pt-Pt first nearest neighbor peak (Figure 7.3.b). However, with increasing Pt loading the Pt-O peak amplitude decreases significantly and the Pt-Pt first nearest neighbor peak gains intensity. Also, from 0.04 EML, a Pt fcc packing pattern can be observed, conformal to the one of the Pt fcc bulk structure. Despite the small noise contributions to the 0.04 EML k-space EXAFS signal, especially in the high k-range (0.04 EML, Figure 7.3.a), the fcc pattern is clearly discerned in R-space. This fcc packing appears to be a stable configuration from the beginning of the deposition process. This is not evident, since it is known that during the $Pt(acac)_2/O_2$-plasma deposition process at

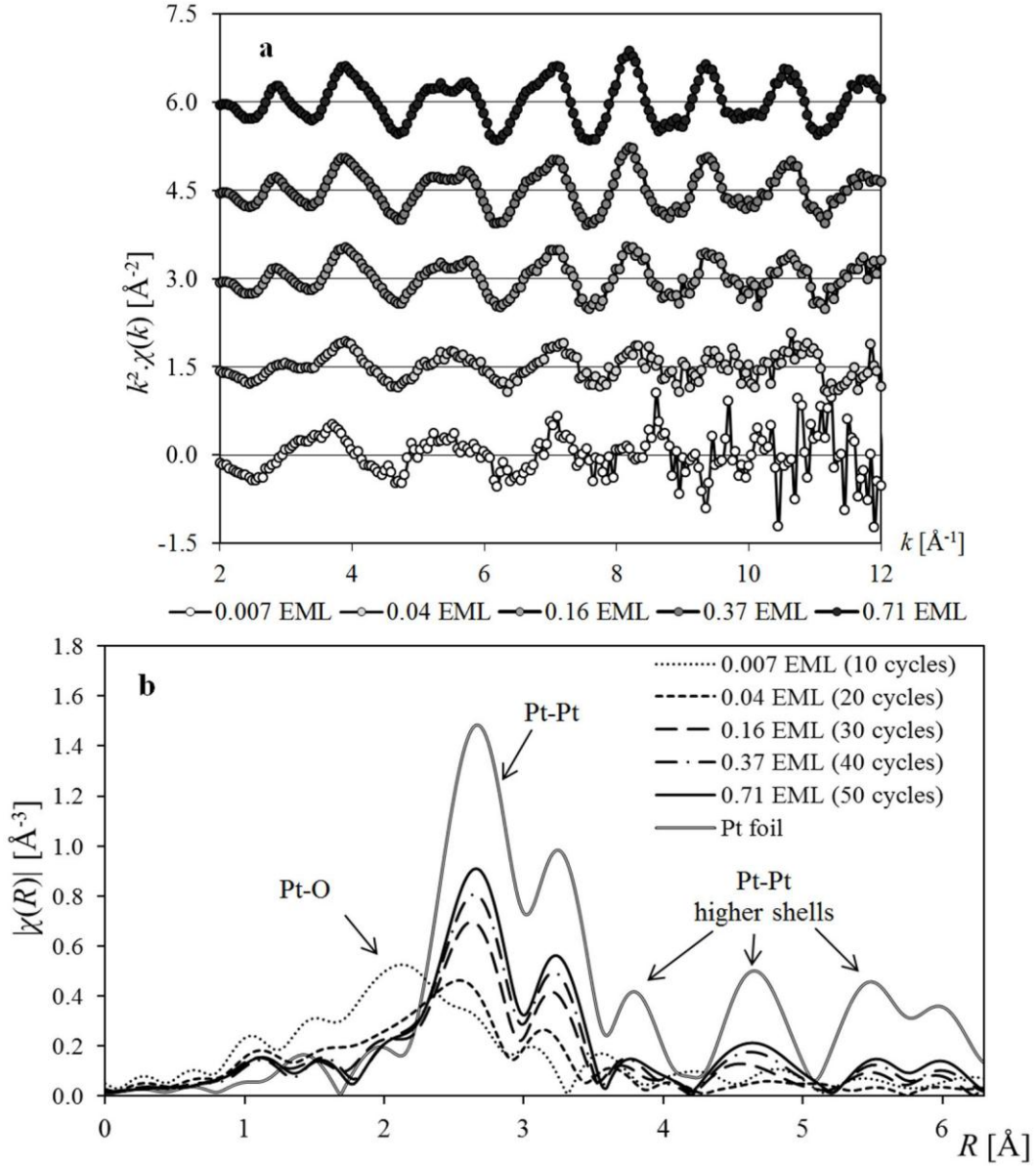

Figure 7.3: (a) the k^2-weighted EXAFS signals are shown for five different loadings below 1 EML, i.e. at 0.007, 0.04, 0.16, 0.37 and 0.71 EML. (b) Magnitudes of the Fourier transformed k^2-weighted EXAFS signals (k = 2 - 10 Å^{-1}, phase corrected) are represented for five different loadings below 1 EML. A Pt foil with metallic fcc Pt bulk structure is shown too. Around ~2 Å the Pt-O peak is expected, whereas the Pt-Pt first nearest neighbour peak appears at ~2.8 Å. Higher Pt-Pt fcc shells are indicated as well.

temperatures below 130°C, a Pt oxide phase is formed.[42] Evolving to higher Pt loadings, i.e. from 0.04 up to 0.71 EML, the Fourier transformed EXAFS signals undergo a peak amplitude increase in all near neighbor Pt-Pt fcc peaks. The latter implies that the original fcc packing perseveres to be the most stable packing within the cluster. The increased peak intensity is caused by the increased coordination indicating that Pt growth is occurring.

Based on the above findings, an EXAFS model can be constructed for further refinement. For this model, the dominant photoelectron scattering paths of the Pt fcc lattice configuration are used up to R = 6 Å. These photoelectron scattering paths are those permitting an adequate reconstruction of its bulk structure signal. In line with other reports[43], nine scattering paths are used up to R = 6 Å. These consist of four single scattering paths, i.e. the first four nearest neighbour shells, three triangular scattering paths, two collinear paths and one triple scattering path. Additionally, a Pt-O shell is added to the model to account for the predominant presence of the oxygen peak in the low R-range at 0.007 EML. This model (Pt-O + Pt fcc) is used as a starting point for modelling the 5 spectra with loadings below 1 EML from Figure 7.3.

To let the EXAFS model converge to the experimental signals, path parameters are varied to minimized the objective function.[27] Therefore, the photoelectron energy origin correction ΔE_0, the half path length R, the path degeneracy N and the Debye-Waller (DW) bond length disorder σ^2 are used as path parameters. In addition, the third cumulant $\sigma^{(3)}$ is also necessary to include in the fit.[28, 43, 44] The latter parameter is only implemented for the Pt-Pt first nearest neighbor and is a measure for the asymmetry in the pair distribution function.

The spectra from 0.04 EML up to 0.71 EML are modeled from R = 1.5 – 6 Å (k = 2.7 – 12.2 $Å^{-1}$). For these spectra, the model described above (Pt-O + Pt fcc) is used. Since the *in situ* XAS measurements are performed at increased temperatures (150°C) and little Pt is deposited (< 1 EML), some approximations have been made concerning the path parameters. The latter are defined such that its number is maximally reduced, while conserving a physically defensible model. It is assumed that ΔE_0 is the same for all scattering paths. Also, an isotropic expansion coefficient is used to estimate the Pt-Pt interatomic distances and the same DW factors are used for the second through fourth Pt-Pt single scattering paths. The latter approximation is justified since the DW factors are expected to vary little from the second Pt shell on. The Pt-Pt multiple scattering DW factors are implemented as mathematical combinations of the single scattering ones. Finally, the DW factors of the first

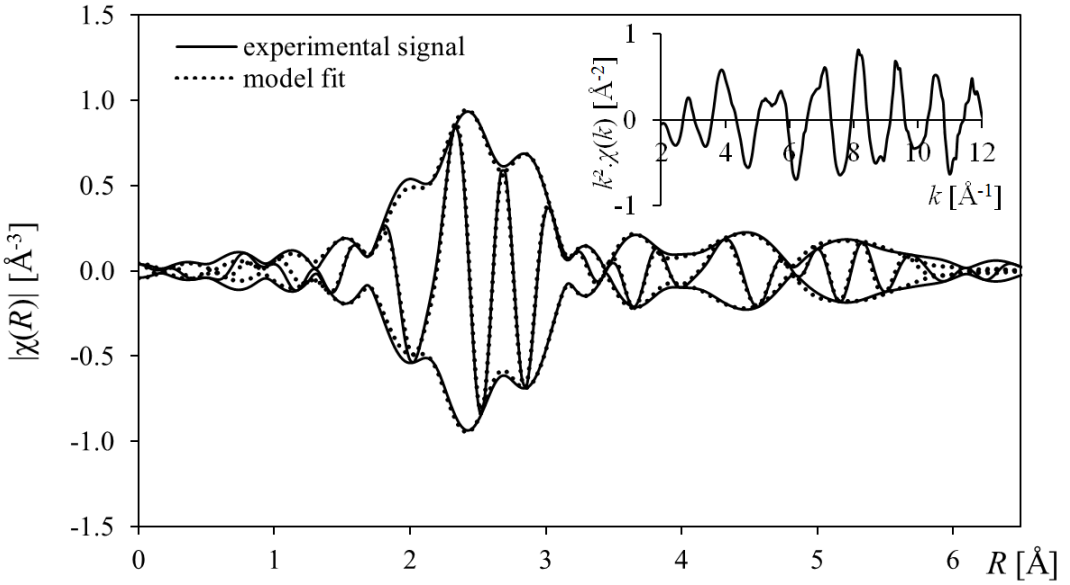

Figure 7.4: Comparison of the model fit to the experimental Fourier transformed k^2-weighted EXAFS signal at 0.71 EML (k = 2.7 - 12.2 Å^{-1}, R = 1.5 - 6 Å, R-factor = 0.008, magnitude and real part, not phase corrected). The corresponding k^2-weighted EXAFS signal $k^2.\chi(k)$ at 0.71 EML is depicted in k-space in the inset.

Pt-Pt and Pt-O shell are constrained to the same value. The oxygen contribution to the signal is very small, making a reliable estimation of a separate DW factor for oxygen challenging. In addition, this approximation does not affect the estimation of the DW factor of the Pt-Pt first shell significantly since the oxygen contribution is very small compared to the Pt contribution.

For the experimental spectrum recorded at the lowest loading of 0.007 EML, a restricted R-range (R = 1.5 – 3 Å, k = 2.7 – 12.2 Å^{-1}) is used due to its poorer data quality. In this region, only the first Pt-O and Pt-Pt shells are appropriate to model the restricted R-space signal. The DW factors of the Pt-O and Pt-Pt shells are constrained to the same value to decorrelate the Pt-Pt/O coordination number and its DW factor. This time, the latter assumption and the data quality do not allow quantitative interpretation of the estimates of the structural parameters. However, the presence of a Pt-O and Pt-Pt shell in the spectrum at 0.007 EML is evidenced since convergence between model and data is obtained.

Fitting the described models to the data yields estimates for the structural parameters. The results are tabulated in Table 7.1: (i) the Pt-O and Pt-Pt nearest neighbor coordination numbers $N_{O,NN1}$ and $N_{Pt,NNi}$ (NNi = i'th coordination shell; i = 1 – 4) respectively, (ii) the Pt-O and Pt-Pt Debye-Waller factors $\sigma^2_{O,NN1}$ and $\sigma^2_{Pt,NNi}$ respectively, (iii) the third cumulant for

the first Pt-Pt nearest neighbor $\sigma^{(3)}_{Pt,NN1}$, (iv) the Pt-O first and Pt-Pt first through fourth nearest neighbor interatomic distances $R_{O,NN1}$ and $R_{Pt,NNi}$ respectively and (v) the numbers obtained for the photoelectron energy origin correction ΔE_0. As mentioned before, the estimates for the structural parameters of the spectrum at 0.007 EML should be interpreted as indicative of the actual values rather than quantitative estimates. In contrast, the results for the other spectra are suited for quantitative use. These findings are also reflected in the R-factors shown in Table 7.1. A gradual decrease of the R-factor is observed with increasing Pt loading.

The comparison of the model fit with the k^2-weighted Fourier transformed EXAFS signal at 0.71 EML is depicted in Figure 7.4. Both the real part and the magnitude of the transformed signal are depicted. In the inset of Figure 7.4, the corresponding k^2-weighted EXAFS signal is shown in k-space. A clear correspondence between the experimental signal and the model fit is observed (R-factor = 0.008).

The previously made observations based on visual inspection of the EXAFS signals in R-space (Figure 7.3) are confirmed by the modeling results. At 0.007 EML, as mentioned before, the presence of Pt-Pt neighbors is shown, implying that Pt atoms meet already at this early stage of deposition. A Pt fcc lattice packing is not detected at this very low Pt loading. For the remaining four loadings above 0.007 EML, i.e. 0.04 – 0.71 EML, the implemented model (Pt-O + Pt fcc) is adequate to accurately describe the experimental signal. Therefore, the Pt fcc packing is the favorable stacking configuration from 0.04 EML on. Also, the total coordination in the first shell, i.e. $N_{NN1} = N_{Pt,NN1} + N_{O,NN1}$, as a function of the loading is obtained from and shown in Table 7.1. The degree of under-coordination decreases with increasing loading, implying particle growth. Lastly, the relative fraction of Pt-O neighbors compared to the fraction of Pt-Pt first nearest neighbors, i.e. $N_{O,NN1}/N_{NN1}$ and $N_{Pt,NN1}/N_{NN1}$ respectively, decreases by a factor of 10 over the investigated 0.007 – 0.71 EML range (Table 7.1). Based on *ex situ* XAS measurements, Christensen et al.[45] found a similar evolution in the Pt-O and Pt-Pt coordination numbers with progressing O_2-based Pt ALD growth on $SrTiO_3$ nanocubes.

7.3.4 **Cluster shape determination.**

It has been shown in literature that the deposition of Pt by applying the ALD procedure leads to the formation of islands.[5] However, the precise morphological and compositional evolution of these island clusters during the O_3-based Pt process has remained unanswered. Applying *in situ* XAS can help in answering these questions. In particular, EXAFS literature provides studies[43, 46-48] which can aid to reconstruct the particle shape during deposition. Simulations have shown that the nanoparticle shape can be determined most reliably in the small cluster diameter range, i.e. smaller than 3 – 5 nm.[43] In addition, the more distant shells are more adequate for sampling the particle exterior and discriminate between differently shaped clusters. EXAFS modeling can provide the experimental coordination numbers of the neighboring shells in (sub)nanometer particles (Table 7.1). By finding the best match between the latter and simulated coordination numbers for different cluster shapes, insight into the particle shape evolution during the initial stages of Pt deposition can be obtained.

A first morphological screening applies the methodology provided by Jentys et al..[48] Such screening is possible by comparing the experimentally obtained estimates for $N_{Pt,NN1}$ and $N_{Pt,NN3}/N_{Pt,NN1}$ with the theoretical values simulated for different cluster shape models. Based on this analysis, spherically shaped clusters can be excluded, whereas cubes and distorted cubes correspond best to the obtained experimental coordination numbers. Despite this acceptable result, additional refinement of the cluster morphology towards more realistic shapes is desired.

Assuming a given cluster shape model, Frenkel et al. simulated the average coordination numbers of the first few shells around Pt as a function of the cluster diameter.[43] If the four nearest neighboring shells are considered, four curves are generated as represented artificially in the inset of Figure 7.5. Subsequently, the set of experimental coordination numbers with uncertainties $\{N_{Pt,NNi} \pm \Delta N_{Pt,NNi}\}$ (NNi = i'th coordination shell with i = 1 – 4, see Table 7.1) are implemented on these simulated curves. The possible range in which $N_{Pt,NNi}$

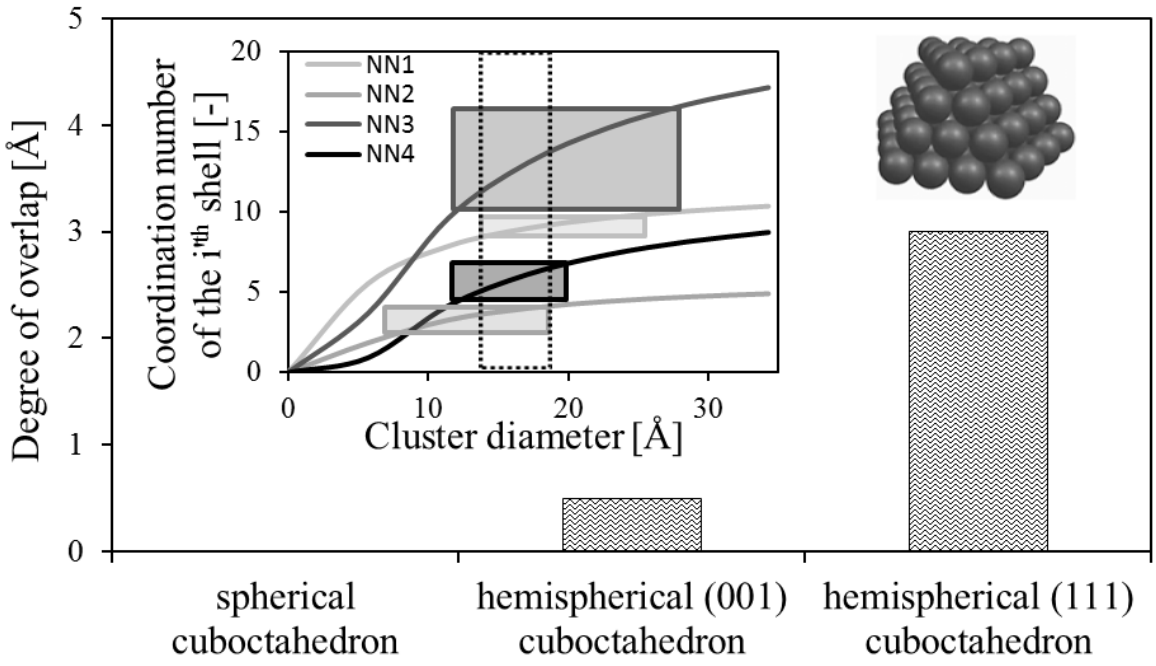

Figure 7.5: In the inset, an artifact is shown which schematically describes the procedure to compare a cluster shape model to the data (see section 3.4). The degree of overlap for the three indicated models is shown for the sample with a Pt loading of 0.71 EML. Additionally, the 3D shape of a hemispherical (111)-truncated cuboctahedral cluster is shown.

occurs, i.e. $[N_{Pt,NNi} - \Delta N_{Pt,NNi}, N_{Pt,NNi} + \Delta N_{Pt,NNi}]$, and its corresponding diameter range can be visualized by a rectangular shaped area for each i'th shell. This yields four rectangular shaped areas, as depicted in the inset of Figure 7.5. Within this plot, all true coordination numbers would lie on the same vertical line at a given cluster diameter if the actual cluster shape fully corresponds the considered cluster shape model. Consequently, there should be a large overlap between the rectangular shaped areas in the diameter dimension. The degree of overlap between these areas is therefore a measure for the agreement between the cluster shape model and the actual shape. The area of overlap is indicated by the area enclosed by the dotted lines in the inset of Figure 7.5. The degree of overlap corresponds to width of the diameter range occupied by this area of overlap.

In this study, the aim is to obtain a decent model matching close to the actual cluster shape, rather than a thorough cluster shape determination. Therefore, the described procedure is repeated for three cluster shape models[43], being (i) a spherical cuboctahedron, (ii) a hemispherical cuboctahedron truncated with a (001) basal plane and (iii) a hemispherical

cuboctahedron truncated with a (111) basal plane. The degree of overlap for these three models is shown in Figure 7.5 for the sample with a Pt loading of 0.71 EML. The cluster shape model best matching our data, i.e. presenting the largest region of overlap, is unambiguously the hemispherical (111)-truncated cuboctahedron. Similar results are obtained for all four spectra investigated, i.e. 0.04, 0.16, 0.37 and 0.71 EML. For the lowest loading of 0.007 EML this procedure is not applicable since higher coordination numbers are not obtained.

Although using Frenkel's method leads to a more detailed and realistic cluster shape, some remarks should be made. As stated in Section 7.3.2, the EXAFS spectra are measured in a stabilized state after spontaneous reduction. Clusters which are reduced, possess an increased order owing to the absence of adsorbed oxygen.[20] This facilitates the determination of the cluster structure owing to the sharpened peaks in R-space. Despite this advantageous effect, this also implies that the structure immediately after the O_3 pulse could be different from the one obtained in the stabilized state. The presence of more adsorbed oxygen could then cause rounding of these nanoparticles.[49, 50] Hence, the hemispherical (111)-truncated cuboctahedron can be considered a valid cluster shape model for the reduced state. Concerning the cluster shape after the O_3 pulse, this model is considered as a good starting point for further calculations. However, due to possible nanoparticle rounding effects more spherical Pt cluster shapes, e.g. spherical cuboctahedron, cannot be excluded.

7.3.5 **Cluster size and evolution.**

Since the cluster shape is determined, it is straightforward to determine the corresponding average particle diameters.[43] This is done for all recorded spectra for loadings from 0.04 EML, yielding the particle size evolution during the deposition process. This is depicted in Figure 7.6 as a function of the number of EML of Pt deposited. The error bars shown correspond to the width of the area of overlap between the coordination numbers (inset

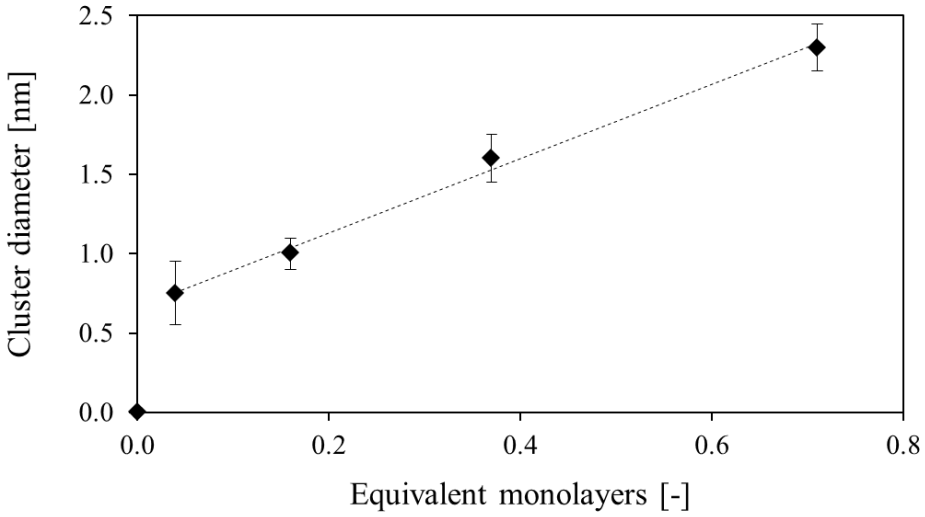

Figure 7.6: Cluster diameter evolution during the deposition process, shown as a function of the number of EML of Pt deposited. The linear curve, obtained by regression analysis from 0.04 – 0.71 EML, is shown as a dashed line.

Figure 7.5). Once the cluster shape determined, this width is a good estimate of the error on the cluster diameter. Some interesting trends can be noticed: at the very beginning of Pt deposition a strong increase in cluster diameter is seen for very low loadings, i.e. below 0.04 EML. This means that although little Pt is deposited at this stage, the atoms cluster together to form stable nuclei. Implicitly, this signifies that the combustion of the precursor ligands by O_3 takes place in an efficient way. The combustion yields PtO_x species which possess an increased diffusion coefficient compared to non-oxidized Pt adatoms.[51] This makes it possible to migrate over the surface to form stable nuclei, thus enhancing the nucleation process. Arriving at 0.04 EML, an average particle diameter of 0.75 nm is found. For loadings ranging from 0.04 up to 0.71 EML, within error bars, a linear increase in particle diameter as a function of the Pt loading is observed. At a loading of 0.71 EML, an average particle diameter of 2.3 nm is obtained.

7.3.6 **Detailed structural evolution with cluster size.**

More in-depth insight into the structural behavior of the Pt clusters during the nucleation regime is obtained by correlating the structural EXAFS parameters with cluster

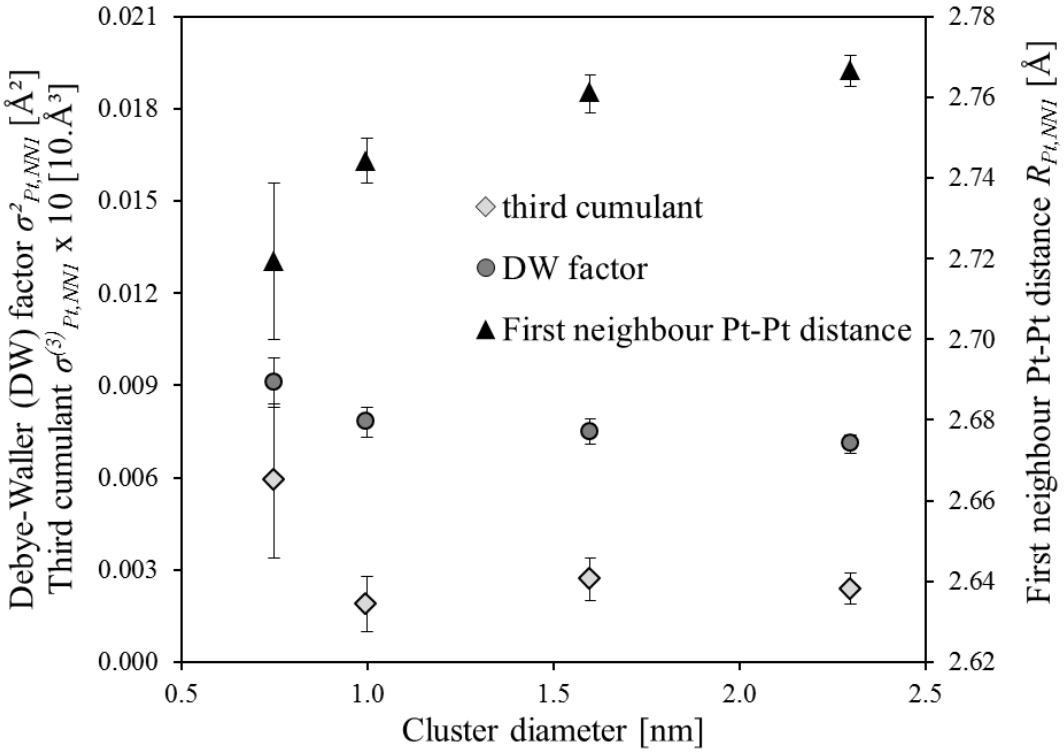

Figure 7.7: Pt-Pt first nearest neighbour Debye-Waller (DW) factor $\sigma^2_{Pt,NN1}$, third cumulant $\sigma^{(3)}_{Pt,NN1}$ and distance $R_{Pt,NN1}$ (see Table 1) as a function of the cluster diameter during the Pt deposition process. The error bars depicted correspond to the fitting errors obtained by EXAFS modelling in Artemis (IFEFFIT).

diameter. For this purpose, the evolution of the Pt-Pt first nearest neighbor Debye-Waller factor, third cumulant and interatomic distance, i.e. $\sigma^2_{Pt,NN1}$, $\sigma^{(3)}_{Pt,NN1}$ and $R_{Pt,NN1}$ respectively, with cluster size is discussed from 0.04 EML up to 0.71 EML. The estimates for the latter three quantities at 0.007 EML (Table 7.1) are not considered since these are not well-suited for quantitative use, as mentioned before.

In Figure 7.7, $\sigma^2_{Pt,NN1}$, $\sigma^{(3)}_{Pt,NN1}$ and $R_{Pt,NN1}$ are shown as a function of the cluster diameter during the Pt deposition process. A subtle but significant increase of the Pt-Pt first nearest neighbor DW factor $\sigma^2_{Pt,NN1}$ is seen with decreasing cluster diameter. This is caused by an increased fluctuation in the bond-length between two neighboring Pt atoms, leading to a broader bond-length distribution. A similar trend is detected for the third cumulant $\sigma^{(3)}_{Pt,NN1}$, although with scatter (Figure 7.7). This increasing trend with decreasing size is additionally supported by the large (qualitative) value of $\sigma^{(3)}_{Pt,NN1}$ at 0.007 EML (Table 7.1). The increased third cumulant is caused by an increased skewness in the bond-length pair distribution function with decreasing diameter.

These two trends point toward anisotropic bond-length disorder. The latter is the consequence of distortions in the ideal lattice positions at specific locations of the cluster.[43, 47] Such anisotropic disorder effects are triggered by phenomena occurring at the cluster exterior, e.g. surface relaxations, support interaction, surface adsorbates... Therefore, these will influence the structural parameters more strongly when the surface-to-bulk ratio increases, i.e. for small clusters. Consequently, the DW factor and the third cumulant have an increased value at the beginning of the deposition process.

These findings are supported by the evolution of the Pt-Pt interatomic distance $R_{Pt,NN1}$ in the first shell as a function of cluster diameter (Figure 7.7). At 0.04 EML, clusters have an average diameter of 0.75 nm with an interatomic Pt-Pt distance of 2.719 ± 0.019 Å. When the Pt loading increases and clusters grow, the Pt-Pt distance increases and evolves towards the Pt bulk value of 2.77 Å. At 0.71 EML, i.e. average cluster diameter of 2.3 nm, the Pt-Pt interatomic distance is 2.766 ± 0.004 Å. The bond-length contraction originates from the under-coordination of the surface atoms, leading to inhomogeneous strain at the cluster surface.[43, 52]

7.3.7 **Density of nuclei.**

Up to now, the lattice packing, shape, diameter and structural parameters of the clusters yielded a detailed structural characterization of the deposited Pt phase. However, in order to obtain a full evolutional picture of the deposition process, the average nanoparticle spacing on the support surface should be known as well. The latter can be quantified by the density of nuclei which is defined as the number of Pt clusters present per nm² of SiO_2 surface.

Combining EXAFS, i.e. Pt atoms per cluster, with XRF, i.e. the total number of Pt atoms deposited, and the specific surface area, yields this density of nuclei during the deposition process (Figure 7.8). An equidistant 2D spacing grid is assumed between the

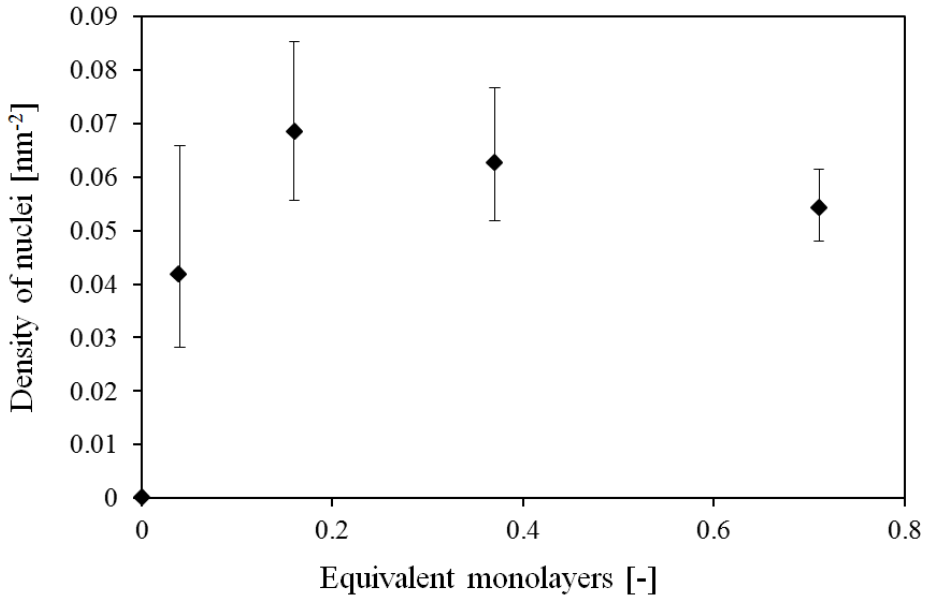

Figure 7.8: Density of nuclei as a function of the number of EML of Pt during the deposition process.

deposited clusters. The data points depicted in Figure 7.8 possess significant error bars due to error bar propagation originating from the uncertainty on the cluster size (Figure 7.6). However, two mechanisms can be distinguished. Below around 0.16 EML a sharp increase in the density of nuclei is seen. This evidences that a substantial nucleation is taking place. Focusing on the region from 0.16 EML up to 0.71 EML, the increasing trend stabilizes and slightly decreases. This behavior indicates that existing nuclei are merging together through coalescence, though this does not mean that new nuclei can't still be formed as well. The mentioned two mechanisms could aid to clarify the linear relationship between cluster diameter and Pt loading seen in Figure 7.6 (0.04 – 0.71 EML). Apparently, the balance between nanoparticle growth, new nuclei formation and coalescence leads to such linear diameter-loading relationship seen in Figure 7.6.

In Figure 7.8, the maximal density of nuclei is situated around 0.07 clusters/nm² of SiO_2 surface. At 0.71 EML, on average 5.4 Pt clusters with cluster diameter of 2.3 nm are present on a SiO_2 surface area of 10 nm x 10 nm. This corresponds to a ca. 25% surface coverage. This looks reasonable since it is known that the linear growth regime starts at about 1 EML, as evidenced by *ex situ* XRF measurements (Section 7.3.1., Figure 7.1).

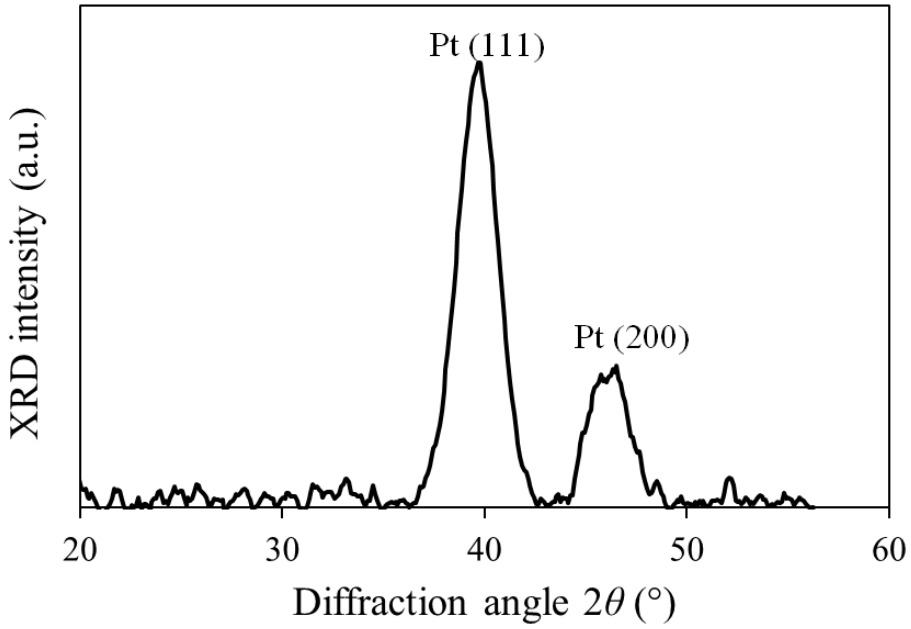

Figure 7.9: XRD scan at atmospheric conditions. Pt(111) and Pt(200) peaks are indicated. The scan originates from the resulting sample of the *in situ* synchrotron experiments, with Pt loading 0.93 EML.

7.3.8 **X-ray diffraction measurements.**

PtO_x/SiO_2 at 0.71 EML is not recovered as a separate sample during the synchrotron measurements, but rather measured as an intermediate state of Pt deposition on this sample. Therefore, the resulting sample of the *in situ* synchrotron experiments, with a 0.93 EML end loading, is used to check the crystallinity of the deposited Pt phase with XRD. The diffraction peaks found correspond to metallic fcc Pt (Figure 7.9). From the width of the peaks, the average crystallite diameter is determined to be 4 nm ± 0.2 nm. This value is larger than expected from the EXAFS analysis. Extrapolating the linear relationship in Figure 7.6 up to 0.93 EML yields an estimated average particle diameter of 2.8 nm. However, this discrepancy is not unexpected since the Scherrer equation is known to overestimate the diameter of particles below ca. 10 nm.[53]

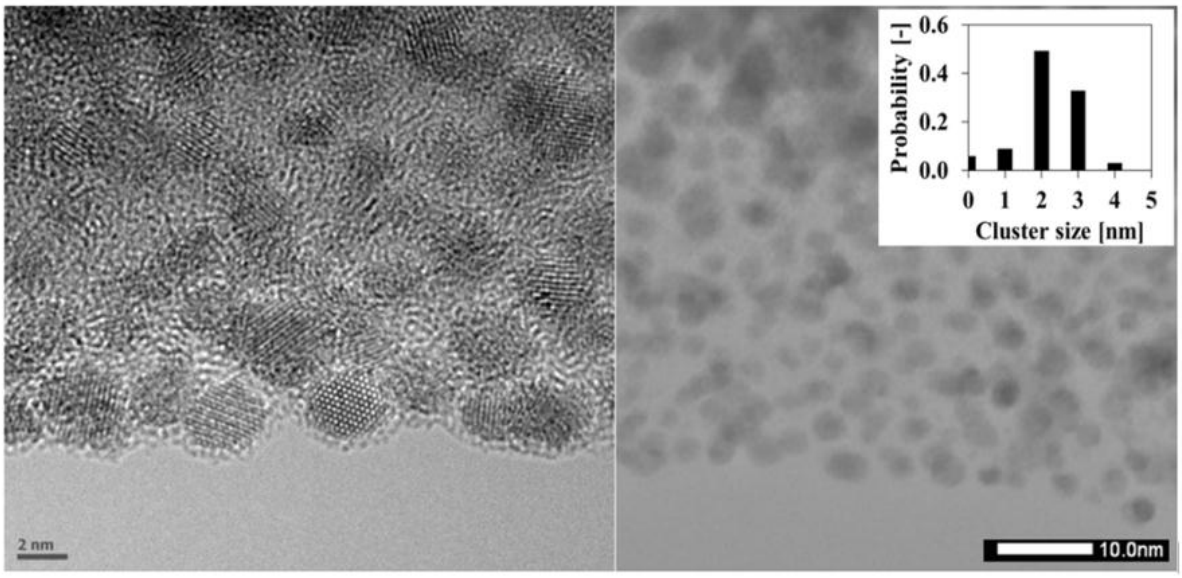

Figure 7.10: (left) HRTEM image. (right) BF STEM scan. Both images are taken at the rim of a pore hole after FIB slicing. The inset of the STEM image shows a cluster size distribution. Both images originate from the resulting sample of the *in situ* synchrotron experiments, with Pt loading 0.93 EML.

7.3.9 **(Scanning) transmission electron microscopy measurements.**

The same sample with 0.93 EML loading is also investigated with TEM. The left part of Figure 7.10 shows a HRTEM image taken at the rim of a pore hole in the mesoporous SiO_2 film. The SiO_2 matrix is amorphous, as expected.[25] The Pt clusters are visible as supported crystals packed with a high degree of order, supporting both the XRD and EXAFS results. The right part of Figure 7.10 is a STEM image of a collection of supported Pt nanoparticles, again located at the rim of a pore hole. The particle diameter distribution obtained from this image is shown in the inset. The corresponding volume averaged particle diameter of 2.8 nm is in excellent agreement with the extrapolated particle diameter from the EXAFS analysis, proving the correctness of the latter. Finally, a qualitative comparison of the density of nuclei based on Figure 7.10 and Figure 7.8 shows agreement at first glance.

XRD proves that the lattice packing is metallic fcc, even at atmospheric oxygen pressures. TEM confirms that the diameters obtained by EXAFS are correct and shows the ordered crystalline packing of the supported nanoparticles.

7.3.10 **X-ray absorption near edge structure: cluster composition.**

The following intends to improve our understanding about the degree of cluster oxidation during the deposition process. Therefore, the cluster shape model derived in Section 7.3.4 will be used as a starting point for further calculations. By appointing oxygen atoms to (a group of) Pt atoms of the cluster, e.g. interface atoms, the degree of oxidation of the cluster can be altered. Calculation of the oxidation state for each – possibly oxidized – Pt atom and averaging over all atoms present in the cluster, yields a theoretical average oxidation state. This theoretical value can be compared to the experimental one. By adapting the degree of oxidation of the model cluster, the correspondence between theory and experiment can be optimized. This opens up the possibility to elucidate the degree of oxidation of the cluster. To the best of our knowledge, this approach has never been applied before.

Before presenting the modeling results, the experimental data will be introduced first. Figure 7.11 consists of three parts. Figure 7.11.a and Figure 7.11.b show the evolution of the XANES spectra measured immediately after the O_3 pulse at different stages of the deposition process. These two figures aim to give the reader a feeling of the significance of the WL intensity variations during deposition. In addition, Figure 7.11.c shows two different experimental data series, recorded frequently at different loadings during the same deposition process. First, the WL intensity obtained from the XANES spectra immediately after the ozone pulse (Figure 7.11.a and Figure 7.11.b) is depicted. Second, the WL intensity acquired from XANES spectra recorded 1 hour after the ozone pulse is presented. The EXAFS measurements discussed in Section 7.3.3 were performed in the same stabilized catalyst state as the latter XANES spectra. The calculation method of the WL intensity is described in Section 7.3.2.. This WL intensity is plotted in a rescaled unit (vide infra). All data points mentioned are plotted as a function of the average cluster diameter during deposition. Small (large) clusters therefore correspond to low (high) Pt loadings during this deposition process (Figure 7.6). The vertical error bars in Figure 7.11.c are estimated to be around ± 0.1.[39] Based on Figure 7.6 and the determination of the errors on the particle sizes using Frenkel's

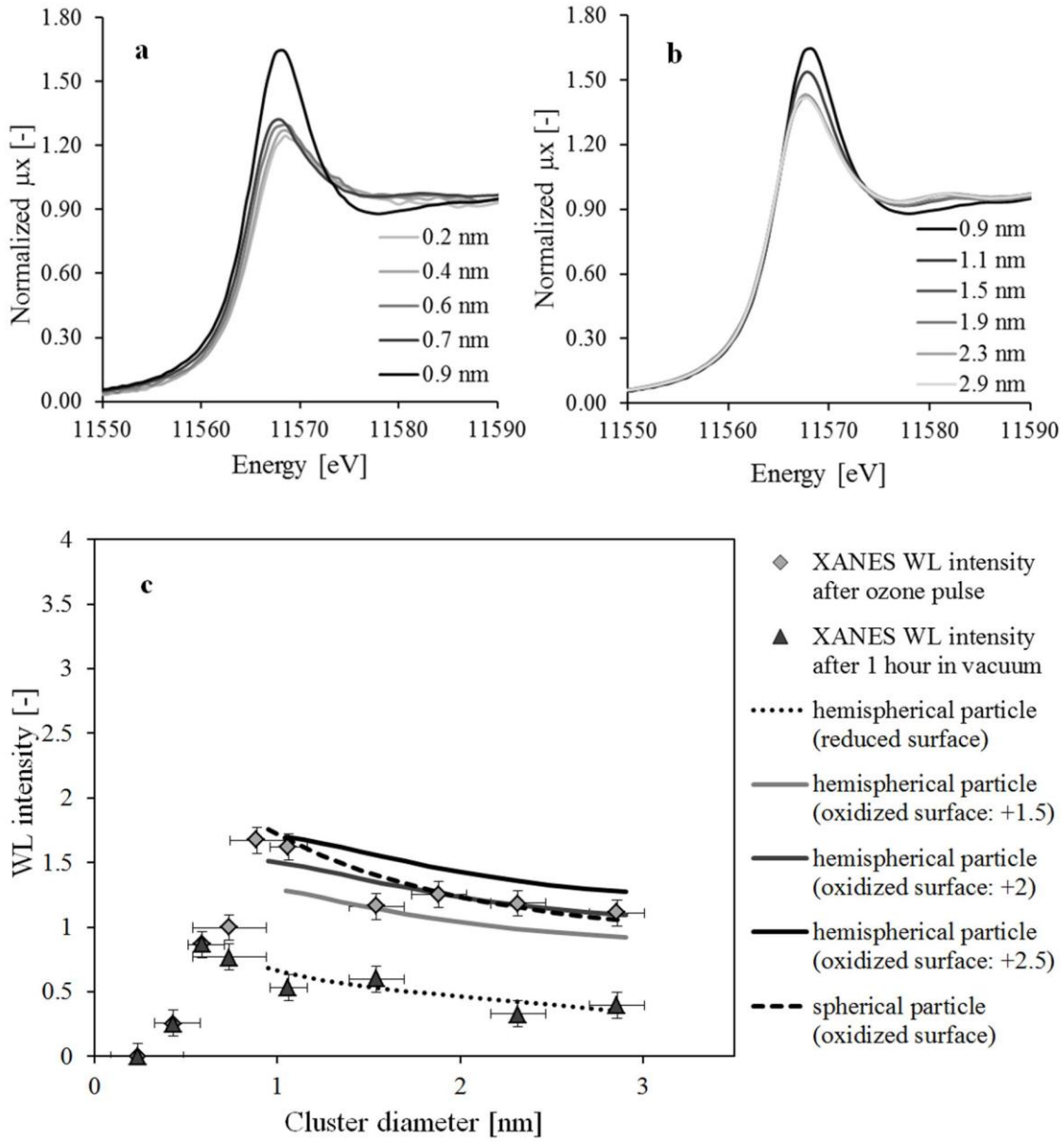

Figure 7.11: (a) Normalized XANES spectra immediately after the O_3 pulse during the deposition process for sizes ranging from 0.2 nm – 0.9 nm and (b) 0.9 nm – 2.9 nm. (c) WL intensity as a function of particle diameter during deposition. Two dataset are shown: one immediately after the ozone pulse and one after 1 hour in vacuum. These trends are modelled by different cluster models (Section 7.3.10). The resulting fits to the data series are plotted too. Finally, two additional curves are shown which possess different cluster surface oxidation states for the hemispherical cluster model. These are represented in order to give the reader a feeling on the sensitivity of the applied XANES methodology to the degree of cluster surface oxidation (Section 7.3.10).

approach (Section 7.3.5.), the horizontal error bars are obtained and implemented in Figure 7.11.c.

At the initial stages of nucleation, the WL intensity of the deposited Pt phase corresponds to the one of metallic Pt (Figure 7.11.c). When the material deposited increases and clusters grow, an increase in WL intensity is observed. Unraveling the observed trends in

the XANES WL intensity below ± 1 nm is not straightforward. General rules do not exist to predict the WL intensity[32] within this region. A combination of support effects, lattice contraction, cluster diameter and the nature of the Pt-O bond could explain the observed trends.[33, 34]

From loadings of 0.03 EML, i.e. estimated particle diameter of 0.6 nm, the WL intensity becomes dependent on the evacuation time of the chamber after the ozone pulse. From this point, the evolution of the upper and lower boundary of the WL intensity is shown in Figure 7.11.c. The upper one corresponds to the WL intensity measured immediately after the ozone pulse. In contrast, the lower one is the WL intensity of the stabilized reduced state after 1 hour of spontaneous reduction in vacuum. Obviously, the WL intensity evolves gradually with time from the upper to the lower boundary (Figure 7.2). Also, the considerable discrepancy between the two limits proves that the XANES WL intensity is sensitive to oxidation state changes of the Pt phase. Therefore, it should be possible to obtain more quantitative information on the degree of oxidation of an average cluster.

In both curves in Figure 7.11.c, the increase in WL intensity stabilizes and starts to decrease gradually between 0.5 and 1 nm. As indicated in Section 7.3.2, a linear relationship is established between the WL intensity and the x = O/Pt ratio for supported PtO_x clusters within the 1 – 5 nm range.[39, 40] The Pt oxidation state (oxidation state = 2x) can therefore be monitored through the WL intensity. All values of the WL intensity in Figure 7.11.c are rescaled to correspond to the Pt oxidation state within the 1 – 3 nm range. Within this range the WL intensity equals the Pt oxidation state. However, for the range below 1 nm, the effects mentioned earlier this section (support, size, …) lead to the breakdown of the linear relation between the WL intensity and the O/Pt ratio. Therefore, the latter region will not be considered in further calculations concerning the degree of cluster oxidation.

In an attempt to describe the previous trends, first, the oxidation state evolution after 1 hour in vacuum is modeled. This is done for the 1 – 3 nm range shown in Figure 7.11.c. The hemispherical (111)-truncated cuboctahedron can be used as a realistic cluster shape model

for this reduced state. First, it can be assumed that no oxygen atoms are adsorbed on the external surface of the Pt cluster, as proven by XANES analysis (Section 7.3.1 and 7.3.2, Figure 7.1 and Figure 7.2). Second, EXAFS and XRD prove that the Pt structure at the interior of the cluster is metallic fcc Pt, implying Pt^0 atoms. Since the cluster shape is known, the average oxidation state of the Pt atoms at the cluster-support interface can now be estimated. During the optimization procedure, the latter parameter is kept identical for all sizes. It is found that in order to describe the oxidation state evolution in an optimal way, a Pt interface atom should have an average oxidation state of $Pt^{4/3+}$. Therefore, a Pt_3O_2 interface stoichiometry is obtained. As can be seen in Figure 7.11.c, the implemented model describes the data in a satisfactory way (dotted curve).

In an attempt to simulate the oxidation state evolution immediately after the ozone pulse, first, the same cluster shape model is used again. At the cluster-support interface, the Pt_3O_2 interface stoichiometry is implemented since no change is expected at this point. Additionally, the Pt atoms residing at the cluster interior are set to a Pt^0 oxidation state. This time, the Pt atoms residing at the external cluster surface have the possibility to adsorb oxygen atoms. Therefore, the average oxidation state of Pt atoms at the cluster surface can be estimated. Again, during this optimization procedure, the latter parameter is kept identical for all sizes. A surface atom with oxidation state of Pt^{2+} yields the optimal description of the oxidation state evolution, corresponding to a PtO surface stoichiometry (solid dark grey curve, Figure 7.11.c).

As mentioned in Section 7.3.4, the cluster shape could alter through oxidation. A rounding of the original cluster shape has been observed.[49, 50] Considering a more spherical cluster shape model could therefore be useful. A spherical cuboctahedron is ideally suited for this. Thus, the spherical clusters are reconstructed with the same number of atoms as their hemispherical counterparts. The same interface stoichiometry is installed and an identical parameter is optimized using the same procedure as for the hemispherical shape. Now, a $PtO_{1.15}$ surface stoichiometry yields the optimal description of the oxidation state evolution

immediately after the ozone pulse (dashed curve, Figure 7.11.c). Therefore, an increased oxygen adsorption at the cluster surface is found compared to the hemispherical case. This can be clarified by the increased number of Pt atoms residing in the interior of the cluster. These internal Pt atoms possess a Pt^0 oxidation state and do not contribute anymore to the increase of the average oxidation state. This effect is corrected by the observed increase of the number of adsorbed oxygen atoms at the Pt cluster surface. Thereby, the same average oxidation state can be preserved.

Finally, some comments are worth mentioning. First, the XANES methodology applied in this section is sensitive to changes in the degree of cluster surface oxidation within the 1 – 3 nm range. To illustrate this, the Pt surface oxidation state is varied, i.e. $Pt^{1.5+}$, $Pt^{2.0+}$ and $Pt^{2.5+}$, using the hemispherical cuboctahedral cluster shape. In Figure 7.11.c, the result of this variation is shown in the solid lines with different grey shades. An increase (decrease) in the degree of cluster surface oxidation results in a considerable increase (decrease) in the WL intensity in the 1 – 3 nm range. The change of the oxidation state of the Pt surface atoms by ± 0.5 with respect to its optimal value results in a model curve located outside the uncertainty region of the data points, especially in the higher diameter range. The clear variation of these modeled curves, in response to the relatively small surface oxidation state changes (± 0.5), proves the sensitivity of the applied XANES methodology. Second, the degree of surface oxidation remains quasi-constant during deposition within the investigated 1 – 3 nm size range. Therefore, the decrease in oxidation state with size (Figure 7.11.c) is caused by a decreased surface-to-bulk ratio rather than a decreased surface oxidation. Third, based on considering the uncertainty area of the data points shown in Figure 7.11.c, the error bars on the modeled values of the cluster surface oxidation states are determined to be around ± 0.25. Therefore – fourth – the oxidation states of the Pt atoms residing at the surface of hemispherical and spherical clusters, i.e. $Pt^{2+(\pm 0.25)}$ and $Pt^{2.3+(\pm 0.25)}$, have overlapping uncertainty regions. Hence, the employed cluster shape models do not significantly alter the resulting degree of surface oxidation.

Table 7.1: The most relevant estimates of the structural parameters, obtained by EXAFS modelling, are listed. The tabulated quantities, given for 5 loadings below 1 EML, are defined and discussed in sections 7.3.3 and 7.3.6. The values in italic should be looked at as to give the reader a qualitative feeling. The remaining results are meant for quantitative use.

	0.007 EML	0.04 EML	0.16 EML	0.37 EML	0.71 EML
R-factor	*0.095*	0.032	0.017	0.012	0.008
$N_{O,NN1}$ [-]	*1.93 ± 0.34*	0.80 ± 0.18	0.45 ± 0.12	0.35 ± 0.12	0.30 ± 0.12
$N_{Pt,NN1}$ [-]	*4.08 ± 0.84*	5.88 ± 0.60	7.44 ± 0.36	8.52 ± 0.36	9.12 ± 0.36
$N_{Pt,NN2}$ [-]	-	0.72 ± 1.20	1.20 ± 0.72	2.58 ± 0.84	3.30 ± 0.78
$N_{Pt,NN3}$ [-]	-	3.36 ± 5.52	5.76 ± 2.88	11.28 ± 3.60	12.96 ± 3.36
$N_{Pt,NN4}$ [-]	-	0.84 ± 1.20	2.88 ± 0.96	4.20 ± 0.96	5.40 ± 0.96
$\sigma^2_{Pt,NN1}$ [10^{-3} Å²]*	*7.2 ± 1.5*	9.1 ± 0.8	7.8 ± 0.5	7.5 ± 0.4	7.1 ± 0.3
$\sigma^2_{Pt,NN2-4}$ [10^{-3} Å²]	-	11.9 ± 9.8	8.6 ± 2.5	9.1 ± 1.6	8.9 ± 1.2
$\sigma^{(3)}_{Pt,NN1}$ [10^{-4} Å³]	*18.8 ± 2.0*	5.9 ± 2.5	1.9 ± 0.9	2.7 ± 0.7	2.4 ± 0.5
$R_{O,NN1}$ [Å]	*1.995 ± 0.019*	1.984 ± 0.022	1.944 ± 0.026	1.918 ± 0.035	1.911 ± 0.039
$R_{Pt,NN1}$ [Å]	*2.742 ± 0.014*	2.719 ± 0.019	2.744 ± 0.006	2.761 ± 0.005	2.766 ± 0.004
$R_{Pt,NN2}$ [Å]	-	3.846 ± 0.027	3.881 ± 0.008	3.904 ± 0.007	3.912 ± 0.005
$R_{Pt,NN3}$ [Å]	-	4.710 ± 0.034	4.753 ± 0.010	4.782 ± 0.008	4.791 ± 0.007
$R_{Pt,NN4}$ [Å]	-	5.439 ± 0.039	5.489 ± 0.011	5.522 ± 0.009	5.533 ± 0.008
ΔE_0 [eV]	*2.78 ± 1.93*	3.75 ± 1.34	5.76 ± 0.51	6.38 ± 0.39	7.11 ± 0.34
N_{NN1} [-]	*6.01 ± 1.18*	6.68 ± 0.78	7.89 ± 0.48	8.87 ± 0.48	9.42 ± 0.48
$N_{O,NN1}/N_{NN1}$ [-]	*0.321 ± 0.057*	0.120 ± 0.027	0.057 ± 0.016	0.039 ± 0.014	0.032 ± 0.012
$N_{Pt,NN1}/N_{NN1}$ [-]	*0.679 ± 0.140*	0.880 ± 0.090	0.943 ± 0.046	0.961 ± 0.041	0.968 ± 0.038

* $\sigma^2_{Pt,NN1} = \sigma^2_{O,NN1}$

7.4 Conclusions

Combining XAS and XRF measurements under *in situ* conditions provides first-hand insights into the nucleation stage of the O_3-based Pt deposition process. By EXAFS modeling, in-depth structural information on the Pt clusters is gained. This information is directly used to obtain the cluster shape, diameter and lattice packing. XANES spectra yield the degree of oxidation during the deposition. XRF quantifies the amount of Pt deposited on the support, which can be expressed in equivalent monolayers (EML).

Crosslinking all these reveals interesting elements about the deposition process such as the evolution of cluster diameter and density with Pt loading and the degree of cluster surface oxidation with diameter. These refined details complete our picture about the design of Pt catalysts using sequential $MeCpPtMe_3/O_3$ pulses at 150°C.

During the nucleation regime of the deposition process, Pt clusters are deposited on the mesoporous SiO_2 support. At the very beginning of deposition, Pt adatoms cluster together to form more stable nuclei. From 0.04 up to 0.71 EML, these clusters grow linearly with Pt loading. They have an fcc packing and their cluster shape matches most closely to a hemispherical (111)-truncated cuboctahedron in the reduced state. Immediately after the ozone pulse, the degree of oxidation of the cluster at the surface corresponds to an average oxidation state around Pt^{2+} within the 1 – 3 nm cluster diameter range. This surface oxygen is necessary for further growth during the Pt deposition process. The nucleation of new clusters is dominant up to 0.16 EML, after which the coalescence of existing nuclei occurs.

These conclusions prove the synergy of performing XAS and XRF simultaneously under *in situ* conditions. The presented methodology exploits a detailed evolutional picture of the catalyst state during deposition and can be applied systematically for a diverse range of future studies.

7.5 References

(1) Puurunen, R. L. J. *Appl. Phys.* **2005**, *97*, 121301.

(2) Miikkulainen, V.; Leskela, M.; Ritala, M.; Puurunen, R. L. *J. Appl. Phys.* **2013**, *113*, 101.

(3) George, S. M. *Chem. Rev.* **2010**, *110*, 111.

(4) Detavernier, C.; Dendooven, J.; Sree, S. P.; Ludwig, K. F.; Martens, J. A. *Chem. Soc. Rev.* **2011**, *40*, 5242.

(5) Baker, L.; Cavanagh, A. S.; Seghete, D.; George, S. M.; Mackus, A. J. M.; Kessels, W. M. M.; Liu, Z. Y.; Wagner, F. T. *J. Appl. Phys.* **2011**, *109*, 084333.

(6) Lee, H. B. R.; Bent, S. F. *Chem. Mat.* **2012**, *24*, 279.

(7) Sree, S. P.; Dendooven, J.; Masschaele, K.; Hamed, H. M.; Deng, S. R.; Bals, S.; Detavernier, C.; Martens, J. A. *Nanoscale* **2013**, *5*, 5001.

(8) Lei, Y.; Liu, B.; Lu, J. L.; Lobo-Lapidus, R. J.; Wu, T. P.; Feng, H.; Xia, X. X.; Mane, A. U.; Libera, J. A.; Greeley, J. P.; Miller, J. T.; Elam, J. W. *Chem. Mat.* **2012**, *24*, 3525.

(9) Lee, H. B. R.; Mullings, M. N.; Jiang, X. R.; Clemens, B. M.; Bent, S. F. *Chem. Mat.* **2012**, *24*, 4051.

(10) Enterkin, J. A.; Setthapun, W.; Elam, J. W.; Christensen, S. T.; Rabuffetti, F. A.; Marks, L. D.; Stair, P. C.; Poeppelmeier, K. R.; Marshall, C. L. *ACS Catal.* **2011**, *1*, 629.

(11) Christensen, S. T.; Feng, H.; Libera, J. L.; Guo, N.; Miller, J. T.; Stair, P. C.; Elam, J. W. *Nano Lett.* **2010**, *10*, 3047.

(12) Li, J. H.; Liang, X. H.; King, D. M.; Jiang, Y. B.; Weimer, A. W. *Appl. Catal. B-Environ.* **2010**, *97*, 220.

(13) King, J. S.; Wittstock, A.; Biener, J.; Kucheyev, S. O.; Wang, Y. M.; Baumann, T. F.; Giri, S. K.; Hamza, A. V.; Baeumer, M.; Bent, S. F. *Nano Lett.* **2008**, *8*, 2405.

(14) Aaltonen, T.; Ritala, M.; Sajavaara, T.; Keinonen, J.; Leskela, M. *Chem. Mat.* **2003**, *15*, 1924.

(15) Kessels, W. M. M.; Knoops, H. C. M.; Dielissen, S. A. F.; Mackus, A. J. M.; van de Sanden, M. C. M. *Appl. Phys. Lett.* **2009**, *95*, 013114.

(16) Mackus, A. J. M.; Leick, N.; Baker, L.; Kessels, W. M. M. *Chem. Mat.* **2012**, *24*, 1752.

(17) Knoops, H. C. M.; Mackus, A. J. M.; Donders, M. E.; van de Sanden, M. C. M.; Notten, P. H. L.; Kessels, W. M. M. Electrochem. *Sol. St. Lett.* **2009**, *12*, G34.

(18) Longrie, D.; Deduytsche, D.; Van den Berghe, S.; Driesen, C.; Detavernier, C. *Solid State Sci. Technol.* **2012**, *1*, Q123-Q129.

(19) Dendooven, J.; Ramachandran, R. K.; Devloo-Casier, K.; Rampelberg, G.; Filez, M.; Poelman, H.; Marin, G. B.; Fonda, E.; Detavernier, C. *J. Phys. Chem. C* **2013**, *117*, 20557.

(20) Mostafa, S.; Behafarid, F.; Croy, J. R.; Ono, L. K.; Li, L.; Yang, J. C.; Frenkel A. I.; Cuenya, B. R. *J. Am. Chem. Soc.* **2010**, *132*, 15714.

(21) Yoshida, H.; Nonoyama, S.; Yazawa, Y.; Hattori, T. Cat. Tod., 153 (2010) 156.

(22) Koningsberger, D. C.; Mojet, B. L.; van Dorssen, G. E.; Ramaker, D. E. *Top. Catal.* **2000**, *10*, 143.

(23) Setthapun, W.; Williams, W. D.; Kim, S. M.; Feng, H.; Elam, J. W.; Rabuffetti, F. A.; Poeppelmeier, K. R.; Stair, P. C.; Stach, E. A.; Ribeiro, F. H.; Miller J. T.; Marshall, C. L. *J. Phys. Chem. C* **2010**, *114*, 9758.

(24) Devloo-Casier, K.; Dendooven, J.; Ludwig, K. F.; Lekens, G.; D'Haen J.; Detavernier, C. *Appl. Phys. Lett.* **2011**, *98*, 231905.

(25) Sree, S. P.; Dendooven, J.; Smeets, D.; Deduytsche, D.; Aerts, A.; Vanstreels, K.; Baklanov, M. R.; Seo, J. W.; Temst, K.; Vantomme, A.; Detavernier C.; Martens, J. A. J. *Mater. Chem.* **2011**, *21*, 7692.

(26) Briois, V.; Fonda, E. ; Belin, S. ; Barthe, L. ; La Fontaine, C. ; Langlois, F.; Ribbens M.; Villain, F. UVX 2010; Applications et Développements Récents: 41-47. EDP Sciences. (2011). http://dx.doi.org/10.1051/uvx/2011006

(27) Ravel B.; Newville, M. *J. Synchrot. Radiat.* **2005**, *12*, 537.

(28) Bus, E.; Miller, J. T.; Kropf, A. J.; Prins R.; van Bokhoven, J. A. *Phys. Chem. Chem. Phys*. **2006**, *8*, 3248.

(29) Rehr, J. J.; Deleon, J. M.; Zabinsky S. I.; Albers, R. C. *J. Am. Chem. Soc.* **1991**, *113*, 5135.

(30) Ravel, B. (2000) EXAFS Analysis with FEFF and FEFFIT: Part 2: Commentary. http://cars9.uchicago.edu/~ravel/course/notes.pdf

(31) Scherrer, P. *Nachr Ges Wiss Göttingen* **1918**, *28*.

(32) Mackus, A. J. M.; Leick, N.; Bol, A. A.; Kessels, W. M. M. *Chem. Mat.* 2013, *25*, 6.

(33) Lei, Y.; Jelic, J.; Nitsche, L. C.; Meyer R.; Miller, J. *Top. Catal.* **2011**, *54*, 334.

(34) Ichikuni, N.; Iwasawa, Y. *Catal. Lett.* **1993**, *20*, 87.

(35) Asakura, K.; Kubota, T.; Chun, W. J.; Iwasawa, Y.; Ohtani K.; Fujikawa, T. *J. Synchrot. Radiat.*, **1999**, *6*, 439.

(36) Ramaker, D. E.; Koningsberger, D. C. *Phys. Chem. Chem. Phys.* **2010**, *12*, 5514.

(37) Ramaker, D. E.; Oudenhuijzen M. K.; Koningsberger, D. C. *J. Phys. Chem. B* **2005**, *109*, 5608.

(38) Mansour, A. N.; Sayers, D. E.; Cook, J. W.; Short, D. R.; Shannon R. D.; Katzer, J. R. *J. Phys. Chem*. 1984, *88*, 1778.

(39) Yoshida, H.; Nonoyama, S.; Yazawa Y.; Hattori, T. *Phys. Scr*. **2005**, *T115*, 813.

(40) Yazawa, Y.; Yoshida H.; Hattori, T. *Appl. Catal. A-Gen*. **2002**, *237*, 139.

(41) Ono, L. K.; Croy, J. R.; Heinrich H.; Cuenya, B. R. *J. Phys. Chem. C* **2011**, *115*, 16856.

(42) Hamalainen, J.; Munnik, F.; Ritala M.; Leskela, M. *Chem. Mat*. **2008**, *20*, 6840.

(43) Frenkel, A. I.; Hills C. W.; Nuzzo, R. G. *J. Phys. Chem. B* **2001**, *105*, 12689.

(44) Clausen B. S.; Norskov, J. K. *Top. Catal.* **2000**, *10*, 221.

(45) Christensen, S. T.; Elam, J. W.; Rabuffetti, F. A.; Ma, Q.; Weigand, S. J.; Lee, B.; Seifert, S.; Stair, P. C.; Poeppelmeier, K. R.; Hersam M. C.; Bedzyk, M. J. *Small* **2009**, *5*, 750.

(46) Beale A. M.; Weckhuysen, B. M. *Phys. Chem. Chem. Phys.* **2010**, *12*, 5562.

(47) Frenkel, A. I.; Yevick, A.; Cooper C.; Vasic, R. *Ann. Rev. Anal. Chem.* **2011**, *4*, 23.

(48) Jentys, A. *Phys. Chem. Chem. Phys*. **1999**, *1*, 4059.

(49) Mittendorfer, F.; Seriani, N.; Dubay O.; Kresse, G. *Phys. Rev. B* **2007**, *76.*

(50) Nolte, P.; Stierle, A.; Jin-Phillipp, N. Y.; Kasper, N.; Schulli, T. U.; Dosch, H. *Science* **2008**, *321*, 1654.

(51) Wynblatt, P. *Acta Metallurgica* **1976**, *24*, 1175.

(52) Bus, E.; Miller, J.T.; van Bokhoven, J. A. *J. Phys. Chem. B* **2005**, *109*, 14581.

(53) Cohen, J. B. *Ultramicroscopy* **1990**, *34*, 41.

Chapter 8. Bimetal ALD: the formation of Pt-In alloys

Abstract

$MeCpPtMe_3/O_3$ and $In(TMHD)_3/O_2$ plasma ALD processes were combined for the production of Pt/In_2O_3 and $In(Pt)O_x$ nanosized layers. By means of *ex situ* XAS and *in situ* XRD, the structural evolution of these layers was monitored during H_2 temperature programmed reduction. The mechanisms of Pt-In alloying are discussed for both Pt/In_2O_3- as well as $In(Pt)O_x$-type samples. In addition, the controllability of the Pt-In alloy composition for bilayers is investigated as a case study. These investigated materials can serve as starting point for the fundamental study of Pt-promoted In reduction, Pt-In alloying, etc., but also show great potential for application in catalysis and gas sensing applications.

8.1 Introduction

Recent literature exemplifies the broad interest in bimetal ALD as a tool for tailoring the nanoparticle size, composition and morphology.[1-5] Pt-Pd[4, 5] and Pt-Ru[2, 4] bimetallic catalysts have been produced with randomly mixed and core-shell cluster morphologies depending on the implemented cycle sequence during ALD. This type of bimetal ALD relies on the selective reaction of a metal precursor with the pre-deposited metal phase. Such selectivity can be achieved by choosing a metal precursor type which exhibits negligible reactivity towards the support as compared to the metal cluster surface.[1] The proper selection of the metal precursor and the reaction sequence can then yield core-shell or perfectly mixed bimetallic nanoparticles.

A different approach, which – to the best of our knowledge – has not been studied before, consists of joining non-selective bimetal ALD. Here, $MeCpPtMe_3/O_3$ and $In(TMHD)_3/O_2$ plasma ALD processes, yielding fcc Pt and crystalline In_2O_3 respectively, are combined for depositing nanosized films of Pt/In_2O_3 and Pt-doped $In(Pt)O_x$. When the deposited nanosized films are treated by H_2 temperature programmed reduction, Pt-In intermetallic compounds can be obtained with controllable alloy composition.

Two distinct ALD sequences are investigated, resulting in two sample configurations which exhibit different behaviour upon Pt-In alloying. First, In_2O_3 and Pt are deposited separately, yielding a metallic fcc Pt phase on top of a crystalline In_2O_3 films (Pt/In_2O_3, termed 'bilayer'). Second, In_2O_3 and Pt ALD are combined by depositing In_2O_3 and Pt alternately, yielding a Pt-doped In_2O_3 film ($In(Pt)O_x$, 'multilayer'). These bi- and multilayer sample configurations exhibit strong similarities to $Pt/Mg(M)(Al)O_x$ (M = Ga, In, Chapter 3, 4, 5) and one-pot synthesized $Mg(Pt)(In)(Al)O_x$ (Chapter 6) materials, respectively. For Pt/In_2O_3 bilayers and $Pt/Mg(M)(Al)O_x$, the element which alloys with Pt is extracted from the support during H_2 reduction. For $In(Pt)O_x$ multilayers and $Mg(Pt)(In)(Al)O_x$, on the other hand, Pt and In are both residing in the same support structure and undergo reduction and

alloying, resulting in separate Pt-In alloyed phases (see below). The mechanisms of reduction and alloying in ALD- and LDH-derived materials can therefore be linked to increase the general understanding of the ongoing atomic scale processes.

8.2 Experimental

An ALD setup with a 150 °C heated doubly walled chamber (base pressure 5.10^{-4} Pa) was utilized for depositing the samples. The solid $MeCpPtMe_3$ precursor (99% Strem Chemicals) was contained in a stainless steel bubbler and heated above its melting point of 30°C. The container was connected to the vacuum chamber by a delivery line, which was heated at 60°C. An OzoneLab^{TM} OL100 ozone generator was employed for producing O_3 from pure O_2. The O_3 concentration yielded was 175 µg/mL. Another bubbler, containing solid $In(TMHD)_3$ (99%, Strem Chemicals) was heated to 130 °C to obtain an adequate vapor pressure, while its delivery lines were heated to 135 °C for preventing condensation of precursor molecules. For the remote plasma process, O_2 gas was fed into the plasma source at 0.01 mbar, and the RF plasma was operated at 300 W. Ar gas (99.999% purity) was employed as carrier gas for the precursors. For the $MeCpPtMe_3/O_3$ ($In(TMHD)_3/O_2$ plasma) process, a static exposure mode was applied during both ALD half-cycles, meaning that the valves to the pumping system were closed, while exposing the sample to the precursor or the reactant gas. The pulse time of the $MeCpPtMe_3$ ($In(TMHD)_3$) precursor was 6 (5) s, after which the valves to the pumping system were kept closed for another 9 (15) s, resulting in a total exposure time of 15 (20) s. For O_3 (O_2 plasma), the pulse time was 6 (5) s and the total exposure time was 12 (20) s. During the precursor and reactant exposures, the pressure in the chamber increased to ca. 50 Pa and 100 Pa, respectively. In total, the ALD cycle hence took 27 (50) s. The sample chamber contained a heated substrate holder and all depositions were performed at 150 °C.

Two different types of samples were produced: ‘bilayers’ and ‘multilayers’. For bilayers, a pure In_2O_3 layer was first deposited upon a SiO_2/Si substrate, after which Pt was

deposited, i.e. n x $In(TMHD)_3/O_2$ plasma + m x $MeCpPtMe_3/O_3$. For multilayers, alternating In_2O_3 and Pt depositions were performed, i.e. p x (a x $In(TMHD)_3/O_2$ plasma + b x $MeCpPtMe_3/O_3$). Five samples were prepared for discussion in this work:

1. 10.6 nm of pure In_2O_3: 100 at% In, 725 cycles $In(TMHD)_3/O_2$ plasma.
2. 6 nm Pt on top of 5.5 nm In_2O_3 (termed 'In-poor bilayer'): 72 at% Pt, 28 at% In, 375 cycles $In(TMHD)_3/O_2$ plasma + 120 cycles $MeCpPtMe_3/O_3$.
3. 6 nm Pt on top of 10.5 nm In_2O_3 (termed 'In-rich bilayer'): 58 at% Pt, 42 at% In, 725 cycles $In(TMHD)_3/O_2$ plasma + 120 cycles $MeCpPtMe_3/O_3$.
4. 6 nm Pt on top of 16 nm In_2O_3: 45 at% Pt, 55 at% In, 1100 cycles $In(TMHD)_3/O_2$ plasma + 120 cycles $MeCpPtMe_3/O_3$.
5. alternating In_2O_3 and Pt depositions yielding a 18.5 nm layer (termed 'multilayer'): 16 at% Pt, 84 at% In, 100 x (10 x cycles $In(TMHD)_3/O_2$ plasma +1 x cycles $MeCpPtMe_3/O_3$). In addition, a similar 'multilayer' sample was produced to perform *in situ* XRD by depositing 60 x (10 x cycles $In(TMHD)_3/O_2$ plasma +1 x cycles $MeCpPtMe_3/O_3$).

The film thickness for all samples was measured by X-ray reflectivity (XRR) using a Bruker D8 Discover system with Cu Kα radiation. X-ray fluorescence (XRF) measurements were performed using a Mo X-ray source (at an angle of 45° with the sample surface) and a silicon drift detector placed at an angle of 52° with respect to the sample surface. The fluorescence signal was integrated over a period of 100 s and calibrated to obtain the Pt and In atomic percentages (at%) of the ALD deposited samples.

In situ XRD was performed in a Bruker-AXS D8 Discover instrument (Cu Kα, 0.154 nm). The reactor has a Kapton window for X-ray transmission. The setup is equipped with a linear detector covering a 20° range in 2θ with a resolution of 0.1°. Gases were regulated by a rig with calibrated mass-flow controllers. H_2/He temperature programmed reduction (TPR) treatments were performed on the as deposited ALD samples. A heating ramp of 0.2 °C/s was implemented during which *in situ* XRD spectra were collected.

Ex situ XAS measurements were recorded at the SAMBA beam line of the 2.75 GeV SOLEIL synchrotron (Saint-Aubin, France) using a top-up X-ray beam of 430 mA. All experiments were performed in fluorescence mode at the Pt L_{III} edge (E = 11564 eV) and In K edge (= 27940 eV) using a 35-element Ge detector. The investigated *ex situ* XAS samples were produced at home and reduced in the in-house XRD setup. XAS data reduction and analysis were executed with the Demeter 0.9.13 software package by following the methodology of Koningsberger et al..[6-8] For EXAFS modeling, the FEFF 6.0 code was applied to calculate the phase shifts and backscattering amplitude functions of Pt-In and Pt-Pt contributions to the EXAFS signal.[7] The minimization of the objective function, carried out by IFEFFIT, yielded estimates for the structural parameters by multiple shell fitting in *R*-space using multiple *k*-weightings.[6] The estimated parameters resulting from EXAFS modeling are tabulated in Appendix E.1. Wavelet transformed (WT) XAS analysis was performed using the HAMA Fortran code in which a Cauchy wavelet order of 50 was selected to perform analysis.[9]

8.3 Results and discussion

8.3.1 Bilayer methodology

Figure 8.1.a displays time resolved *in situ* XRD patterns recorded during H_2 TPR on an ALD-deposited 10.6 nm In_2O_3 layer. Below 420 °C, a typical In_2O_3 (222) diffraction can be observed at a 2θ angle around 31°. When the temperature exceeds 420 °C this In_2O_3 (222) diffraction disappears, suggesting that the reduction of In_2O_3 results in the formation of metallic In. Indeed, above 300 °C In_2O_3 is known to reduce to metallic In^0, the latter being in a liquid aggregation state at the investigated temperature.[10, 11]

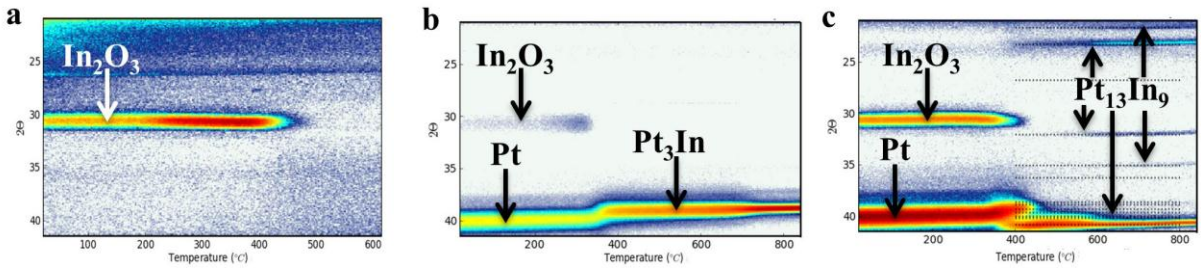

Figure 8.1: *in situ* XRD patterns during H_2 TPR of (a) 10.6 nm In_2O_3; (b) 6 nm Pt on top of 5.5 nm In_2O_3 ('In-poor' sample); (c) 6 nm Pt on top of 10.6 nm In_2O_3 ('In-rich' sample). The phases are indicated on each plot.

ALD deposition of Pt on top of an In_2O_3 layer induces significant changes in the observed XRD patterns. Two samples with different In/Pt ratios are monitored by *in situ* XRD during H_2 TPR: (1) 6 nm Pt deposited on top of 5.5 nm In_2O_3 (termed 'In-poor', Figure 8.1.b, 72 at% Pt), and (2) 6 nm Pt deposited on 10.6 nm In_2O_3 (termed 'In-rich', Figure 8.1.c, 58 at% Pt). As before, a In_2O_3 (222) diffraction is present at room temperature (~ 31°), though quite weak for the In-poor sample. This indicates that the In_2O_3 crystals of the latter sample are at the detection limit of X-ray diffraction (~ 3 nm). In addition to In_2O_3, clear Pt (111) diffraction peaks are observed around 40° for both samples, confirming that nanosized fcc packed metallic Pt is deposited.

Upon H_2 TPR treatment, the Pt (111) peaks of both samples gradually shift to lower 2θ angles, being indicative of the progressive insertion of In in the fcc Pt structure (Figure 8.1.b and Figure 8.1.c, ~ 360 – 400 °C). Indium incorporation causes the fcc lattice to expand which results in a concomitant decrease of the Pt (111) 2θ angle. For the In-poor sample, the end point of In-enrichment of the Pt phase is when the original Pt (111) peak stabilizes at the Pt_3In diffraction angle (~ 39°). Just like metallic Pt, Pt_3In intermetallic compounds exhibit face centered cubic lattice packing, though with increased lattice spacing. The Pt L_{III} XANES spectrum of the In-poor sample reduced to 820 °C confirms the formation of a Pt-In alloyed phase: the edge shift to higher energies – compared to bulk Pt – is a sensitive feature for Pt-In alloying (Figure 8.2.a).[12, 13] Complementary Fourier transformed (FT) EXAFS evidences the formation of a Pt-In alloyed phase with fcc packed crystal structure (Figure 8.2.b). More precisely, EXAFS modeling between R = 2 – 3 Å shows that both Pt and In neighbors coordinate Pt (parameter estimates are given in Appendix E.1). The higher shells around Pt (>

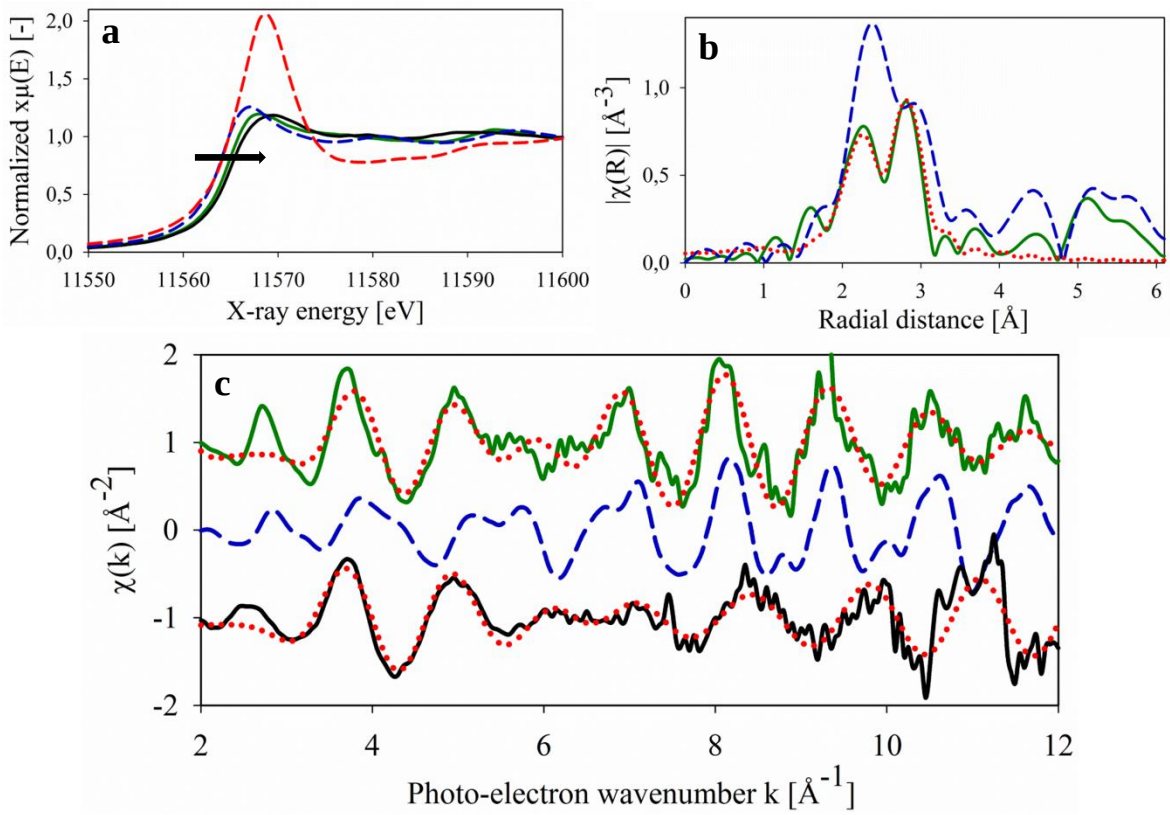

Figure 8.2: Pt L_{III} edge (a) XANES spectra of 820 °C reduced In-poor sample (solid green line), 670 °C reduced In-rich sample (solid black line), metallic fcc Pt (dashed blue line) and bulk PtO_2 (dashed red line) references; (b) k^2-weighted Fourier transformed EXAFS magnitude of 820 °C reduced In-poor sample (solid green line), metallic fcc Pt reference (dashed blue line), Pt-In + Pt-Pt shell model fit (dotted red line); (c) k^2-weighted EXAFS spectra of (top) 820 °C reduced In-poor sample (solid green line), (middle) metallic fcc Pt reference (dashed blue line), (bottom) 670 °C reduced In-rich sample (solid black line). The dotted red lines correspond to the model fit to the data using a Pt-In + Pt-Pt shell model. The estimated parameters resulting from EXAFS modeling are tabulated in Appendix E.1.

3 Å) then again show clear resemblance with the peak features of fcc packed Pt. Also, the k-space EXAFS signal of the 820 °C reduced In-poor sample shows strongly similar oscillations with the k-space signal of a Pt reference (Figure 8.2.c).

For the In-rich sample, the Pt_3In phase is not the end point. From the start of Pt_3In alloy formation (~ 360 °C), diffractions corresponding to $Pt_{13}In_9$ are also observed (Figure 8.1.c, dotted lines). This more In-rich Pt-In alloy could be the result of the higher abundance of In in this In-rich sample. A plausible explanation for the co-existence of Pt_3In and $Pt_{13}In_9$ is that $Pt_{13}In_9$ is formed at the interface between In_2O_3 and the Pt layers, whereas Pt_3In is more abundant further away from this interface, as also observed for Pd-In alloys.[14] The $Pt_{13}In_9$ alloy persists up to high temperature in contrast to the initially formed Pt_3In phase, which

vanishes at In_2O_3 reduction temperatures (~ 420 °C, see above). As mentioned before, the reduction of In_2O_3 results in the formation of metallic In. The high availability of metallic In could therefore further enrich and saturate the pre-existing Pt_3In alloys, which then collapse to the more In-rich $Pt_{13}In_9$ intermetallics. Other preliminary *in situ* XRD data on samples with different In/Pt ratio (not shown) also display intermetallic transformations into more In-rich alloy phases at the same temperature as In_2O_3 reduction.

In agreement with XRD, Pt L_{III} XANES shows a higher edge energy for the reduced In-rich sample as compared to the reduced In-poor sample and Pt/PtO_2 references – a higher shift being indicative of more deep Pt-In alloying (Figure 8.2.a). The k-space EXAFS signals of the reduced In-rich sample shows significant differences compared to the reduced In-poor sample and the Pt reference (Figure 8.2.c). As confirmed by EXAFS modeling, the bimodal envelope of the In-rich k-space EXAFS signal is typical of the presence of In around Pt (Appendix E.1).[12] The In-poor EXAFS signal shows similar k-space envelope as compared to the In-rich sample. However, its oscillations are in phase with the ones of the Pt reference, whereas the oscillations of the In-rich signal are in anti-phase with the Pt k-space signal. These anti-phase oscillations are caused by the more dominant presence of In around Pt for the In-rich as compared to the In-poor sample.

The described mechanisms of Pt-In phase formation can be understood by considering the Pt-In phase diagram (Figure 8.3).[11] In the as deposited samples, a pure Pt phase is present on top of an In_2O_3 layer (100 at% Pt, 0 at% In in Figure 8.3). At the start of Pt-In alloying (~ 360 °C), Pt promotes the reduction of the In_2O_3 phase: Pt-dissociated H species spill over to reducible In_2O_3 and decrease the reduction temperature of In_2O_3 by 60 °C (420 °C – 360 °C). Reduced In species then alloy with Pt by In-insertion in the Pt fcc lattice. Indeed, as derived from the phase diagram, fcc Pt can stabilize up to 10 at% of In by forming a Pt-In solid solution. The gradual insertion of In in the fcc Pt phase yields the observed Pt (111) peak angle shift towards lower values. Around 90 at% Pt, further In-enrichment of the Pt phase results in the formation of a Pt_3In intermetallic phase in addition to the Pt-In solid

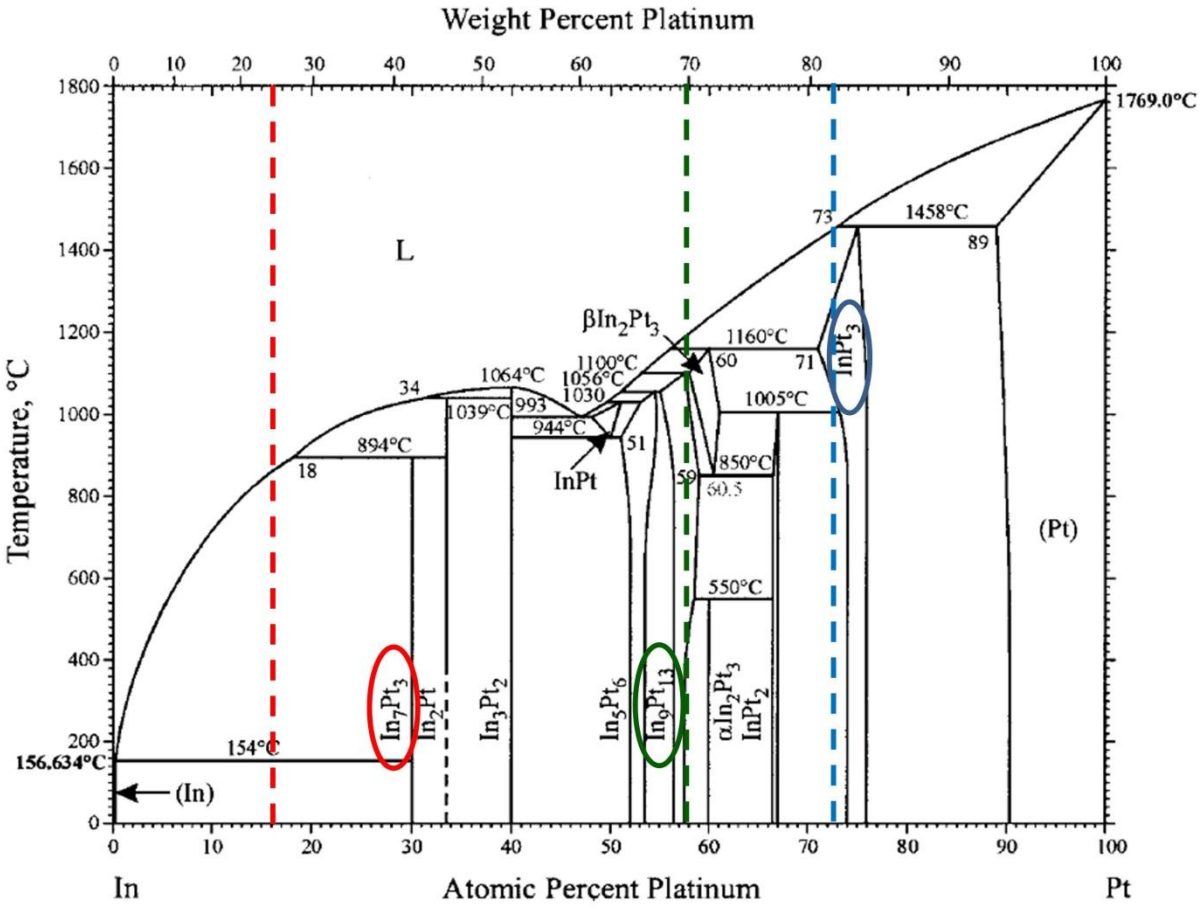

Figure 8.3: Pt-In phase diagram. The initial sample concentrations of the ALD deposited samples are indicated (dashed line), as well as the resulting Pt-In phase after H2/He temperature programmed reduction treatment (circles): blue = In-poor bilayer; green = In-rich bilayer; red = multilayer.[11]

solution. When the global In-concentration in the Pt phase increases above 90 at%, the fraction of the Pt-In solid solution phase shrinks while the share of the Pt_3In intermetallic increases. For the In-poor sample, the end point is at the Pt_3In intermetallic region of the phase diagram, as the XRD Pt peak angle coincides with the one of a Pt_3In intermetallic. The Pt-In phase in the In-rich sample undergoes more In-enrichment compared to the In-poor sample, which results in the sudden collapse of the Pt_3In intermetallic into a $Pt_{13}In_9$ alloy. The wide availability of metallic In at In_2O_3 reduction temperatures and the related In-enrichment of the Pt phase is likely the underlying cause for the latter phase transformation. Notably, the composition of the formed alloy phases, i.e. $Pt_{13}In_9$ and Pt_3In, corresponds to the composition of the initially deposited film, i.e. 58 at% Pt and 72 at Pt%, respectively (see Figure 8.3). This implies that no significant material loss occurs during Pt-In alloying, as confirmed by preliminary XRF data.

8.3.2 **Multilayer methodology**

A multilayer sample is deposited by alternating ALD deposition of In_2O_3 and Pt in the following sequence: 100 x (10 cycles of In_2O_3 + 1 cycle of Pt), yielding 16 at% Pt and 84 at% In containing 18.5 nm thick layer. The wavelet transformed (WT) XAS contour plot of the resulting as deposited sample is depicted in Figure 8.4.a, together with the PtO_2 reference signal in Figure 8.4.b. An intense WT XAS peak is observed at R ~ 1.5 Å and k ~ 5 $Å^{-1}$ for both the as deposited sample and the PtO_2 reference, being characteristic of Pt-O bonds. In the higher shells around Pt (higher R-values – vertical axis – in the WT XAS plot), a subtle peak is suggested in a k-region where In typically appears. In any case, the presence of Pt neighbors around Pt can be excluded: no WT XAS intensity is observed in higher k-regions (R ~ 3 Å, k ~ 9 $Å^{-1}$), as would be the case if Pt were present – such as for PtO_2 (Figure 8.4.b). These results suggest that Pt atoms are incorporated inside the oxide structure of In_2O_3 during alternating In_2O_3 and Pt ALD deposition.

Complementary to WT XAS, the Pt L_{III} edge XANES spectrum of the as deposited sample exhibits a white line feature which exceeds the one of PtO_2 (Figure 8.2.a, red dashed line). This implies that the density of unoccupied 5d states of Pt is higher compared to PtO_2.[8] It is therefore suggested that the In_2O_3 oxide structure induces a strong withdrawal of Pt 5d electrons. Similarly high white line intensities were also observed for Pt-doped SnO_2, an oxide material which displays properties similar to In_2O_3.[15] The withdrawal of Pt 5d electrons and their concomitant donation to hybridized SnO_2 resulted in superior properties during gas sensing applications. The high white line intensity of the as deposited sample thus strongly indicates that fully oxidized Pt atoms are doped inside the In_2O_3 structure.

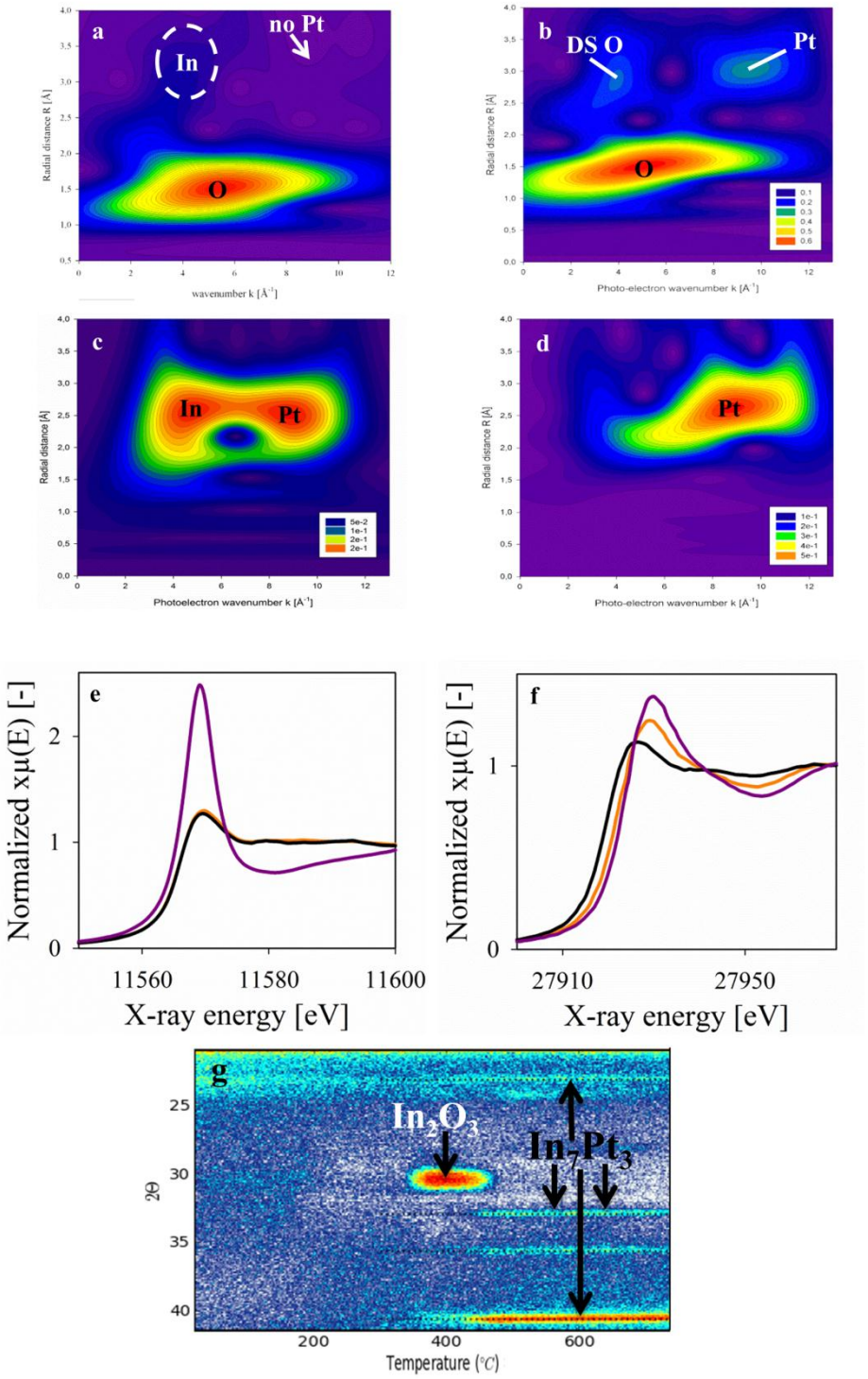

Figure 8.4: Pt L_{III} edge (a) Wavelet transformed (WT) XAS modulus of the as deposited multilayer; (b) WT XAS modulus of PtO_2 reference; (c) WT XAS modulus of 360 °C reduced multilayer sample; (d) WT XAS modulus of pure Pt reference; (e) Pt L_{III} and (f) In K edge XANES spectra of as deposited (purple), 360 °C (orange) and 650 °C (black) reduced multilayer samples; (g) *in situ* XRD patters during H_2 TPR of as deposited multilayer sample.

The In K edge XANES spectrum of the as deposited film shows a typical In_2O_3 profile (Figure 8.4.f).[16] However, XRD patterns of a similar multilayer sample (60 sequences

of (10 In_2O_3 + 1 Pt) cycles instead of 100) do not exhibit any significant In_2O_3 or Pt peaks at low temperature (Figure 8.4.g). The absence of a Pt phase is not surprising since distinct Pt atoms are expected to be incorporated in the In_2O_3 structure during alternating In_2O_3/Pt ALD deposition. In contrast, the absence of crystalline In_2O_3 is remarkable, since the $In(TMHD)_3$/ O_2 plasma ALD process yields crystalline In_2O_3 when deposited in its pure state (see Figure 8.1.a).[17] This suggests that the Pt-containing In_2O_3 layer has an amorphous structure due to the incorporation of Pt atoms inside the In_2O_3 structure. The deposited film thickness amounts to around 10 nm, which is definitely above the detection limit of XRD. The structural disorder caused by the amorphous nature of the film can cause the faint intensity of the In peak in the WT XAS signal (Figure 8.4.a), as well as the non-oscillatory XANES profile above the Pt L_{III} white line of the as deposited film (Figure 8.4.e).

H_2 TPR to 360 °C of the as deposited sample results in significant changes in the Pt L_{III} edge XANES spectra (Figure 8.4.e). The white line height strongly decreases and the edge position shifts to higher energies, indicative of Pt-In alloying.[12] The WT XAS contour plot of the 360 °C reduced sample (Figure 8.4.c) shows both In and Pt peaks as compared to a pure Pt reference (Figure 8.4.d), confirming that Pt-In alloying indeed occurs. For bilayer samples, Pt is shown to promote the reduction of In, resulting in Pt-In alloy formation at temperatures as low as 360 °C (Figure 8.1.b and Figure 8.1.c). Apparently, Pt-promoted Pt-In alloying also takes place in the present multilayer sample, as evidenced by XAS (~ 360 °C instead of 420 °C).

In situ XRD shows the appearance of multiple peaks around 360 °C (Figure 8.4.g): a high-intensity In_2O_3 diffraction at 31°, and multiple low-intensity In_7Pt_3 diffractions around 23°, 33°, 36° and 41° (dotted lines). The simultaneous appearance of In_2O_3 and In_7Pt_3 diffractions strongly indicates that Pt-In alloying is accompanied by a transformation of the original amorphous $In(Pt)O_x$ layer into crystalline In_2O_3 and intermetallic In_7Pt_3.

The fact that In_7Pt_3 diffractions have low intensity indicates that In_7Pt_3 alloys have nanosized morphology. In the as deposited (unreduced) material, Pt is completely surrounded

by In_2O_3, which facilitates the formation of In-rich Pt-In nanoalloys upon H_2 reduction. In fact, In_7Pt_3 is the most In-rich intermetallic compound that can be formed between Pt and In (phase diagram, Figure 8.3: 30 at% Pt and 70 at% In).[11] One can conclude that the dominant presence of In in the environment of Pt in the as deposited sample leads – upon reduction – to Pt-In nanoalloys which are saturated in In.

XANES data support these findings: the In K edge XANES spectrum shows a decreased white line height after 360 °C reduction as compared to the original as deposited sample spectrum. Apart from newly formed crystalline $In^{3+}{}_2O_3$, part of the In phase undergoes reduction upon alloying with Pt, which reduces the average white line height.

Further temperature increase in H_2 induces additional changes in the time resolved *in situ* XRD patterns. Around 420 °C, crystalline In_2O_3 reduces, causing its (222) diffraction peak to vanish – as observed in Figure 8.1.a too. When the sample is further reduced to 650 °C, the Pt L_{III} XANES spectrum does not show any changes compared to reduction to 360 °C (Figure 8.4.e). This implies that the Pt-In alloy composition remains constant upon In_2O_3 reduction to (liquid) metallic In at 420 °C: the In-satured In_7Pt_3 intermetallics cannot incorporate more In. Preliminary XRF results show that some In evaporates to the gas phase during reduction, presumably because In species cannot be stabilized through incorporation inside In-saturated In_7Pt_3 alloys.

8.3.3 **ALD-based Pt-In alloy composition control: a proof-of-principle**

The ultimate goal in the field of catalyst synthesis is the tailored design and fabrication of novel high-performing catalysts, departing from a fundamental understanding of the catalyst functioning.[1] To reach this goal, exploiting deeper insights should go in parallel with the development of novel synthesis techniques which can provide high control over the catalyst active sites. Although ALD for catalysis applications is still a field under strong development, it has potential for atomically precise engineering of these catalyst active sites.

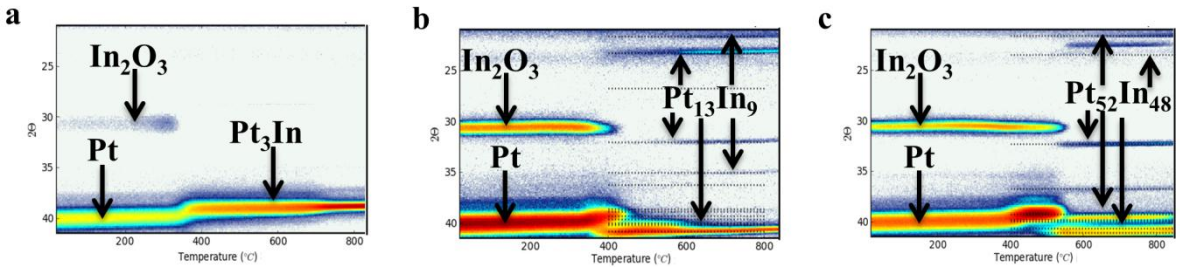

Figure 8.5: *in situ* XRD patters during H_2 TPR of (a) 6 nm Pt on top 5.5 nm In_2O_3; (b) 6 nm Pt on top 10.6 nm In_2O_3; (c) 6 nm Pt on top of 16 nm In_2O_3. The dotted horizontal lines represent the expected diffractions of $Pt_{13}In_9$ and $Pt_{52}In_{48}$ in plots (b) and (c) respectively.

A first step in this direction is shown in Figure 8.5. *In situ* XRD patterns during H_2 TPR for three Pt/In_2O_3 bilayer samples with differing Pt/In ratio are shown, namely 72 at% Pt (Figure 8.5.a), 58 at% Pt (Figure 8.5.b) and 45 at% Pt (Figure 8.5.c). Three different alloys are formed after H_2 TPR treatment, being Pt_3In, $Pt_{13}In_9$ and $Pt_{52}In_{48}$ (or ~ PtIn), respectively. The Pt and In concentrations within the resulting Pt-In intermetallic compounds correspond to their initial concentrations after film deposition. Consequently, ALD is able to control the Pt-In alloy composition in a good way by varying the Pt/In ratio in the bilayers. Here, this has been achieved by changing the In_2O_3 thickness from 6 (Pt_3In) to 10 ($Pt_{13}In_9$) and 16 nm ($Pt_{52}In_{48}$), while keeping the Pt thickness constant at 6 nm. Further investigation in this topic can pave the way to more controlled ALD-based catalyst design.

8.4 Conclusions

The mechanisms of Pt-In alloy formation are investigated during H_2 temperature programmed reduction of ALD-deposited Pt,In-nanocomposites. Two deposition sequences are utilized, yielding two types of sample configuration with different alloying behavior. First, separate deposition of In_2O_3 and Pt is established, yielding fcc metallic Pt on a crystalline In_2O_3 layer (Pt/In_2O_3, 'bilayer'). Second, In_2O_3 and Pt ALD are alternated during deposition, yielding an amorphous Pt-doped In_2O_3 layer ($In(Pt)O_x$, 'multilayer'). For both nanocomposites, Pt promotes the reduction of In_2O_3, which results in the formation of Pt-In alloys below the reduction temperature of In_2O_3.

For Pt/In_2O_3, initial Pt-In alloying originates from the gradual insertion of In in the original fcc structure of Pt, yielding a Pt-In solid solution. Further In-enrichment of this solid solution leads to the formation of Pt_3In intermetallic compounds. Around 420 °C, In_2O_3 reduces to metallic In. The high availability of In^0 presumably causes further In-enrichment and -saturation in the pre-existing Pt_3In alloys, which then collapse to the more In-rich intermetallics, e.g. $Pt_{13}In_9$, depending on their initial Pt/In ratio.

For $In(Pt)O_x$, the most In-rich intermetallic compounds (In_7Pt_3) are formed upon initial Pt-In alloying owing to the high abundance of In around Pt in the $In(Pt)O_x$ layer. This Pt-In alloying process is accompanied by the structural transformation of amorphous Pt-doped In_2O_3 into crystalline In_2O_3 and nanocrystalline In_7Pt_3. Reduction of In_2O_3 does not induce further In-enrichment of the In_7Pt_3 intermetallics, because the latter are already saturated in In.

First results are presented on the tunability of the Pt-In alloy composition using ALD-deposited Pt/In_2O_3 samples. It is confirmed that different intermetallic compounds can be obtained when the Pt/In ratio is varied – here by changing the In_2O_3 thickness.

Finally, it should be mentioned that the ALD technique has the potential to make catalysts with tunable properties, such as the alloy composition. However, more is to be

investigated: (1) how to downscale this approach to the atomic scale level? (2) what are the maximal/minimal In concentrations in the Pt-In alloys for the bilayer and multilayer methodologies? (3) which support material yields most stability against sintering during H_2 temperature programmed reduction? Notably, the currently deposited Pt-In layers are very useful from a fundamental point of view, for example to study the reduction and alloy mechanisms of different types of elements as well as the behavior of H in the alloy formation process.

8.5 References

(1) O'Neill, B. J.; Jackson, D. H. K.; Lee, J.; Canlas, C.; Stair, P. C.; Marshall, C. L.; Elam, J. W.; Kuech, T. F.; Dumesic, J. A.; Huber, G. W. *ACS Catal.* **2015**, *5*, 1804−1825.

(2) Christensen, S. T.; Feng, H.; Libera, J. L.; Guo, N.; Miller, J. T.; Stair, P. C.; Elam, J. W. *Nano Lett.* **2010**, *10*, 3047−3051.

(3) Johansson, A. C.; Larsen, J. V.; Verheijen, M. A.; Haugshoj, K. B.; Clausen, H. F.; Kessels, W. M. M.; Christensen, L. H.; Thomsen, E. V. *J. Catal.* **2014**, *311*, 481−486.

(4) Lu, J.; Low, K.-B.; Lei, Y.; Libera, J. A.; Nicholls, A.; Stair, P. C.; Elam, J. W. *Nat. Commun.* **2014**, 5, 4264.

(5) Lei, Y.; Liu, B.; Lu, J.; Lobo-Lapidus, R. J.; Wu, T.; Feng, H.; Xia, X.; Mane, A. U.; Libera, J. A.; Greeley, J. P.; Miller, J. T.; J. T. Elam, J. T. *Chem. Mater.* **2012**, *24*, 3525−3533.

(6) Ravel B.; Newville, M. *J. Synchrot. Radiat.* **2005**, *12*, 537.

(7) Rehr, J. J.; Deleon, J. M.; Zabinsky S. I.; Albers, R. C. *J. Am. Chem. Soc.* **1991**, *113*, 5135.

(8) Koningsberger, D. C.; Mojet, B. L.; van Dorssen, G. E.; Ramaker, D. E. *Top. Catal.* **2000**, *10*, 143.

(9) Funke, H.; Chukalina, M. Wavelet Transform for EXAFS: http://www.esrf.eu/UsersAndScience/Experiments/CRG/BM20/Software/Wavelets

(10) Bielz, T.Lorenz, H.; Jochum, W.; Kaindl, R.; Klauser, F.; Klötzer, B.; Penner, S. *J. Phys. Chem. C* **2010**, *114*, 9022.

(11) Okamoto, H. *J. Phase Equilib. Diffus.* **2005**, *26*, 399.

(12) Filez, M.; Redekop, E. A.; Poelman, H.; Galvita, V. V.; Marin, G. B. *Anal. Chem.* **2015**, *87*, 3520- 3526.

(13) Filez, M.; Redekop, E. A.; Poelman, H.; Galvita, V. V.; Ramachandran, R. K.; Dendooven, J.; Detavernier, C.; Marin, G. B. *Chem. Mater.* **2014**, *26*, 5936-5949.

(14) Lorenz, H.; Turner, S.; Lebedev, O.; Van Tendeloo, G.; Klötzer, B.; Rameshan, C.; Pfaller, K.; Penner, S. *Appl. Cat. A-General* **2010**, *374*, 180.

(15) Hübner, M.;Koziej, D.; Bauer, M.; Barsan, N.; Kvashnina, K.; Rossell, M. D.; Weimar, U.; Grunwaldt, J.-D. *Angew. Chem. Int. Ed.* **2011**, *50*, 2841.

(16) Proffit, D. E.;Buchholz, B. D.; Chang, R. P. H.; Bedzyk, M. J.; Mason, T. O.; Ma, Q. *J. Appl. Phys.* **2009**, *106*, 113524.

(17) Ramachandran, R. K.; Dendooven, J.; Poelman, H.; Detavernier, C. *J. Phys. Chem.* **2015**, DOI: 10.1021/acs.jpcc.5b03255.

Chapter 9. General conclusions

In this work, two strategies were explored and investigated for the alternative design of Pt-based alkane dehydrogenation catalysts: catalyst formation based on (1) the synthesis of layered double hydroxide (LDH) materials, and (2) via the method of atomic layer deposition (ALD). The family of LDH-derived catalysts studied here consisted of Pt-M alloy nanoparticles on basic Mg,Al-based mixed metal oxide supports, as these exhibit high propylene selectivity and activity during propane dehydrogenation (M = In, Ga). Their conventional formation relies on the successive impregnation of Pt and M species on $Mg(Al)O_x$ supports, $Mg(Al)O_x$ being obtained through calcination of Mg,Al-LDH support precursors. After H_2 reduction of calcined $M/Pt/Mg(Al)O_x$, Pt-M alloyed nanoparticles are formed on the $Mg(Al)O_x$ support. In the present thesis work, a simplified 'one-pot' methodology was developed in which both Pt and the alloying element M are incorporated inside the original Mg,Al-LDH structure in a single synthesis step, yielding Mg,Al,Pt,M-LDHs. After calcination and H_2 reduction, well-dispersed Pt-M nanoparticles decorate the $Mg(Pt)(M)(Al)O_x$ surface ($Pt\text{-}M/Mg(Pt)(M)(Al)O_x$). As an intermediate step to the one-pot and conventional double impregnation approaches, only the alloying element M was incorporated inside the Mg,Al-LDH lattice, yielding $Mg(M)(Al)O_x$ after LDH calcination, on which $Pt(acac)_2$ was subsequently deposited on top. The behavior of Pt, H, and M was extensively studied during calcination and H_2 reduction treatment of $Pt(acac)_2/Mg(M)(Al)O_x$, eventually yielding $Pt\text{-}M/Mg(M)(Al)O_x$ catalysts ('multi-step' methodology). In parallel to LDH-derived $Pt/Mg(M)(Al)O_x$ 'multi-step' and $Mg(Pt)(M)(Al)O_x$ 'one-pot' synthesized materials, the alloying behavior of their ALD-derived Pt/In_2O_3 and $In(Pt)O_x$ structural analogs was studied during H_2 reduction. These nanocomposites were obtained by combining $MeCpPtMe_3/O_3$ and $In(TMHD)_3/O_2$ plasma ALD processes. For producing Pt/In_2O_3, Pt was deposited on top of a separately deposited In_2O_3 layer (n x In_2O_3 + m x Pt). In contrast,

$In(Pt)O_x$ is obtained by alternating deposition of In_2O_3 and Pt, yielding a Pt-doped In_2O_3 layer (a x [b x In_2O_3 + c x Pt). The nanocomposites were used to explore the potential of bimetal ALD.

Advanced XAS-based methodologies were developed in order to more efficiently unravel the mechanistic events influencing catalyst formation. First, multi-resolution wavelet transformed (WT) XAS was applied for the first time to follow up on *in situ* formation of catalysts. Wavelet-based analysis provides simultaneous k- and R-space resolution in the XAS signal. The k-space location of each R-space peak can then be directly observed and linked to a specific atomic type. As a consequence, WT XAS allows for the simultaneous elemental discrimination and spatial localization of the X-ray absorber's neighbors. Especially when multiple atomic types are located around the X-ray absorber, WT XAS is shown to be a rapid tool for triggering profound XAS analysis. Second, an *in situ* XRF-XAS methodology was developed to probe the structural properties of Pt nanoparticles during the initial stages of Pt ALD. XAS provides detailed structural information on the Pt nanoparticles size, shape, lattice packing and surface oxidation state. XRF monitors the number of equivalent monolayers (EML) of Pt deposited during Pt ALD. In combination, *in situ* XRF-XAS provides an evolutional picture of the Pt nanoparticle size and support surface density as a function of the number of equivalent monolayers of Pt. These first-hand insights resulted in the direct observation of the phenomena taking place during the initial stages of Pt ALD on SiO_2 supports, including nucleation, sintering and cluster growth.

The formation process of catalytic Pt-Ga bimetallic nanoparticles on MgO-type $Mg(Ga)(Al)O_x$ mixed metal oxides (MMOs) was studied, starting from $Pt(acac)_2$ wet impregnated $Mg(Ga)(Al)O_x$ supports (4.4 wt% Pt). Calcination to 350 °C leads to the decomposition of the acac precursor ligands and results in the full oxidation of Pt. This yields five/six fold O-coordinated Pt^{4+} species which are atomically dispersed on $Mg(Ga)(Al)O_x$. Further calcination at 650 °C (2.25 h) leads to the scission of strong Pt-O(-Mg) support bonds, causing Pt species to gain mobility and migrate over the support surface. This results in the

formation of sub-nanometer fcc Pt clusters with oxidized surface, which exhibit relatively weak 2.5 Å Pt^0-$(OH)^-$ interfacial bonds. Switching to H_2 and heating to 450 °C causes these Pt^0-$(OH)^-$ bonds to be replaced by common 2 Å Pt-O bonds and induces further nanoparticle sintering into larger reduced Pt clusters. By increasing the temperature to 650 °C, Ga cations from the framework are mobilized, undergo transport from the support to Pt clusters, and form 1.5 nm Pt-Ga alloyed nanoparticles.

This process of Pt-Ga alloying was utilized as a probe reaction to study the mobility, nature and behavior of H and Ga, starting from pure Pt clusters on $Mg(Ga)(Al)O_x$ (calcined state). During H_2 treatment to 650 °C, Pt-dissociated H species spill over from the Pt cluster surface to non-reducible $Mg(Al)O_x$ and partially reducible $Mg(Ga)(Al)O_x$ surfaces. Spilled over H undergoes long range transport over the support surface towards reducible Ga^{3+} sites from the support. Subsequently, these Pt-dissociated H species partially reduce Ga^{3+} cations into moderately mobile $Ga^{\delta+}O_x$ which can only undergo short range transport towards Pt clusters below 650 °C. Only at the Pt cluster surface, $Ga^{\delta+}O_x$ is fully reduced to metallic Ga^0 on condition of immediate stabilization inside Pt-Ga alloyed nanoparticles. Notably, the $Mg(Ga)(Al)O_x$ support surface itself also dissociates significant amounts of H as compared to Pt. However, no (partial) reduction of Ga^{3+} is observed on Pt-free $Mg(Ga)(Al)O_x$ supports below 650 °C, suggesting that $Mg(Ga)(Al)O_x$ dissociates H species with differing reductive ability as compared to Pt-dissociated H.

The catalyst formation process of bimetallic Pt-In/$Mg(In)(Al)O_x$ catalysts – starting from $Pt(acac)_2$/$Mg(In)(Al)O_x$ – is governed by similar atomic scale processes as for their Pt-Ga analogs. However, two major differences should be noted. First, no Pt cluster formation occurs after a 20 min calcination treatment of $Pt(acac)_2$/$Mg(In)(Al)O_x$ (1.0 wt% Pt) at 650 °C. Instead, only 2 Å Pt-O bonds are observed in the first shell around Pt whereas no prolonged 2.5 Å Pt^0-$(OH)^-$ bonds can be detected between Pt and the support. These observations suggest that the calcination period of 20 minutes did not result in sufficient Pt-O support bond scission, inhibiting Pt migration and subsequent cluster formation. Second, In_2O_3 is known to

reduce at lower temperatures as compared to Ga_2O_3, implying that Pt cluster formation and Pt-In alloying could be simultaneously established during H_2 reduction of Pt/Mg(In)(Al)O_x up to 650 °C. In addition, Pt-In alloying could – besides the alloying mechanisms explained above for Pt-Ga – also be driven by liquid/gas phase transport of In^0.

Besides the multi-step synthesized Pt-M catalysts discussed above (M = Ga, In), the one-pot synthesis of Mg,Al,Pt,In-LDH catalyst precursors was developed, yielding Pt-In alloyed nanoparticles on Mg(Pt)(In)(Al)O_x after calcination and H_2 reduction. This one-pot procedure is based on the single-batch intercalation of $[PtCl_1(OH)_5]^{2-}$ complexes in the interlayer galleries of precipitated $[(Mg)_{1-a}^{2+}(Al/In)_a^{3+}(OH)_2]^{a+}$ layers. Calcination of the original Mg,Al,Pt,In-LDH to 650 °C results in the collapse of the layered hydrotalcite structure, yielding MgO-type Mg(Pt)(In)(Al)O_x MMOs with a minority of amorphous or nano-crystalline (mixed) metal oxide phases. Upon H_2 reduction to 650 °C, well-dispersed Pt-In nanocatalysts are formed on the Mg(Pt)(In)(Al)O_x support, which exhibit superior activity during propane dehydrogenation as compared to their multi-step synthesized analogs. As a consequence, this one-pot synthesis method allows for a facile and scalable production of bimetallic Pt-based nanocatalysts, which is not only cost efficient during catalyst synthesis, but also during dehydrogenation reaction.

Parallel to LDH-derived Pt/Mg(In)(Al)O_x (multi-step) and Mg(Pt)(In)(Al)O_x (one-pot) pre-catalysts, ALD-derived Pt/In_2O_3 and In(Pt)O_x nanocomposites were deposited and subjected to a H_2 reduction treatment to study their Pt-In alloy behavior, respectively. For both ALD-derived sample configurations, Pt promotes the reduction of In_2O_3 (~ 360 °C), inducing Pt-In alloying below In_2O_3 reduction temperatures (~ 420 °C). For Pt/In_2O_3 materials, Pt-In alloy formation is established by the gradual In-enrichment of the Pt phase during temperature programmed H_2 reduction treatment. During initial Pt-In alloying, In is gradually inserted in the pure fcc Pt structure, resulting in a Pt-In solid solution. Further In-enrichment of this solid solution leads to the formation of Pt_3In intermetallic compounds. At In_2O_3 reduction temperatures, In_2O_3 reduces to metallic liquid In. The high availability of this

metallic In presumably increases the In concentration in these Pt-In alloys which causes restructuring of Pt_3In into more In-rich intermetallics, the composition of which depends on their initial Pt/In ratio. For $In(Pt)O_x$, the most In-rich intermetallic compound (In_7Pt_3) is formed at the initial start of Pt-In alloying, due to the high abundance of In around Pt inside $In(Pt)O_x$. This Pt-In alloying is accompanied by the structural transformation of the $In(Pt)O_x$ layer into crystalline In_2O_3 and nanocrystalline In_7Pt_3. Full reduction of In_2O_3 does not result in further In-enrichment of In_7Pt_3 intermetallics, as these alloys are already saturated in In.

The behavior, nature and mobility of Ga, In and H have been extensively discussed in this work as they strongly determine the process of Pt-M alloy formation. Based on the combined research of LDH- and ALD-derived materials described in this chapter, the behavior and mobility of Pt can also be evaluated. The results exemplify that the Pt mobility is affected by (1) the calcination time, (2) the gas environment and (3) the support material. In oxygen environment, fully oxidized Pt^{4+} species on/in LDH-derived MMO supports are mainly anchored by strong Pt-O-Mg bonds. Only after sufficiently long calcination times, Pt species gain mobility through Pt-O support bond scission as suggested by the occurrence of Pt^0-$(OH)^-$ interfacial bonds for Pt clusters on $Mg(Ga)(Al)O_x$ (135 min calcination). In contrast, shorter calcination treatments decrease the probability of thermally activated Pt-O support bond cleavage, inhibiting Pt migration and Pt cluster formation on $Mg(In)(Al)O_x$ supports (20 min calcination). When however the calcined $Pt/Mg(In/Ga)(Al)O_x$ materials are treated during H_2 reduction, H-assisted Pt-O support bond scission is suggested as Pt clustering/sintering is observed. Finally, the strong impact of the support interaction with Pt should not be forgotten. Even at 650 °C in O_2, MgO-based MMO supports can atomically disperse Pt species on the support surface. In contrast, rapid Pt cluster formation is observed during Pt/O_3 ALD on SiO_2 surfaces at temperatures as low as 150 °C and Pt loadings (0.007 EML) much smaller than on LDH-derived materials. This indeed shows that the nature of the support can have a major influence on the state of the Pt phase, ranging from atomically

dispersed Pt^{4+} species on the support to strongly clustered Pt nanoparticles with an oxidation state approaching Pt^0.

Although some pieces of the metal catalyst design puzzle are put together by this research, a multitude of questions remain unanswered. As detailed above, the synthesis and formation process of LDH-derived bimetallic catalysts has a major influence on the eventually formed Pt-M nanoparticles on the MMO support. Hence, a major task in future research is to establish the link between the Pt-M nanocatalyst structure and its influence on the catalyst performance. Some intermediate challenges lie in pointing out the Pt-M nanoparticle (surface) composition and the Pt-In alloying phase, and its direct influence on the dehydrogenation activity, selectivity and the rate of coke formation. In addition, the catalyst stability during multiple C_3H_8/O_2 redox cycles – for coke burn-off after reaction – should be systematically studied in order to address the performance changes which occur during the catalyst lifetime.

For ALD-derived bimetallic Pt-based systems, significant efforts are required to downscale the deposition approach for achieving tailored Pt-M nanoparticles. In addition, a more clear control over the Pt-M alloyed phase composition could be achieved, and the effect of the support surface on the nanoparticle structure should be investigated. Once these challenges are solved, ALD-based catalyst synthesis is a very promising approach to deliver a model catalyst, which can aid in answering multiple fundamental questions, ranging from the behavior, nature and mobility of Pt, H and M, to the mechanisms of Pt-M alloy formation in LDH-derived catalysts. To date, LDH-derived Pt-M catalysts are most attractive for industrial use owing to their simple/scalable formation and superior alkane dehydrogenation performance. However, future tailored ALD-based model catalysts could pave the way towards a more deep understanding of the fundaments of metal catalysis in general.

Appendix A

Appendix A.1: EXAFS modeling details

The Pt coordination numbers N_{Pt-X}, interatomic distances R_{Pt-X}, Debye-Waller disorder factors σ^2_{Pt-X} and energy origin corrections ΔE_0 are reported (X = O, Mg, In, Pt), resulting from multiple k-weight R-space EXAFS modeling of the following experimental spectra:

$Pt(acac)_2$-toluene solution wet impregnated on $Mg(In)(Al)O_x$ and dried at 110 °C (Figure 3.1.b).

Table A-1: structural parameters obtained by EXAFS modeling using a single Pt-O shell model

N_{Pt-O}	[-]	3.8 ± 0.8
R_{Pt-O}	[Å]	1.97 ± 0.02
σ^2_{Pt-O}	[10^{-3} x Å²]	2.6 ± 2.4
ΔE_0	[eV]	8.3 ± 2.9

$Pt(acac)_2/Mg(In)(Al)O_x$ calcined to 650 °C (Figure 3.2.b).

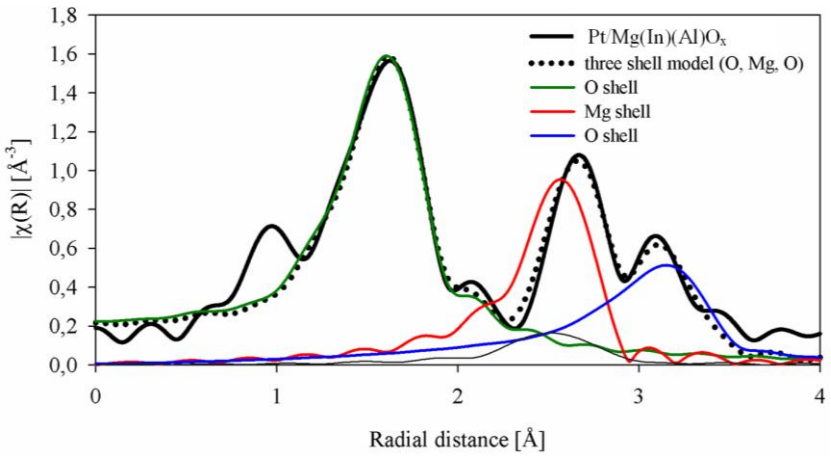

Figure A-1: experimental k²-weighted Fourier transformed EXAFS signal of $Pt(acac)_2/Mg(In)(Al)O_x$ calcined to 650 °C (full, black), fit of three shell model (dotted, black) containing Pt-**O**, Pt-O-**Mg** and Pt-O-Mg-**O** shells, separate shell contributions of Pt-**O** (full, green), Pt-O-**Mg** (full, red) and Pt-O-Mg-**O** (full, blue).

The feature around R ~ 1 Å is a non-physical peak resulting from atomic background subtraction. Therefore, it doesn't correlate with the presence of atomic species around Pt.

Table A-2: structural parameters obtained by EXAFS modeling using a three shell model containing Pt-**O**, Pt-O-**Mg** and Pt-O-Mg-**O** shells

$N_{Pt\text{-}\mathbf{O}}$	[-]	5.0 ± 0.4
$N_{Pt\text{-}O\text{-}\mathbf{Mg}}$	[-]	4.1 ± 0.7
$N_{Pt\text{-}O\text{-}Mg\text{-}\mathbf{O}}$	[-]	12.6 ± 4.1
$R_{Pt\text{-}\mathbf{O}}$	[Å]	2.01 ± 0.01
$R_{Pt\text{-}O\text{-}\mathbf{Mg}}$	[Å]	2.97 ± 0.01
$R_{Pt\text{-}O\text{-}Mg\text{-}\mathbf{O}}$	[Å]	3.64 ± 0.02
$\sigma^2_{Pt\text{-}\mathbf{O}}$	[10^{-3} x Å²]	5.6 ± 1.2
$\sigma^2_{Pt\text{-}O\text{-}\mathbf{Mg}}$	[10^{-3} x Å²]	2.6 ± 1.4
$\sigma^2_{Pt\text{-}O\text{-}Mg\text{-}\mathbf{O}}$	[10^{-3} x Å²]	10.3 ± 5.3
ΔE_0	[eV]	6.4 ± 1.1

The structural parameters obtained by EXAFS modeling of the $Pt(acac)_2/Mg(In)(Al)O_x$ (650 °C calcined) signal using a PtO_2 structural model (Figure 3.2.b – dashed line) show non-physical negative values in the Pt-Pt coordination numbers and Debye-Waller disorder factors, in addition to parameters approaching 0. This clearly shows that the PtO_2 structure is not appropriate for modeling the higher shells around Pt.

Pt/Mg(In)(Al)O_x reduced to 650 °C in H_2/He (Figure 3.3.b).

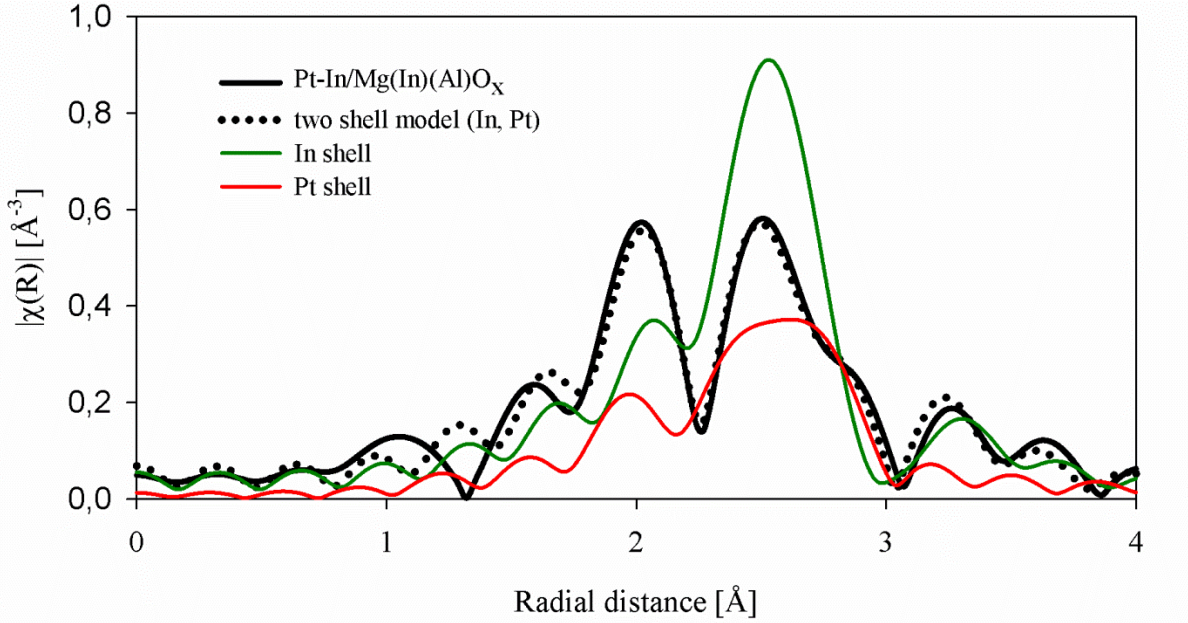

Figure A-2: experimental k²-weighted Fourier transformed EXAFS signal of Pt/Mg(In)(Al)O_x reduced to 650 °C in H_2/He (full, black), fit of two shell model (dotted, black) containing Pt-**In** and Pt-**Pt** shells, separate shell contributions of Pt-**In** (full, green) and Pt-**Pt** (full, red).

Table A-3: structural parameters obtained by EXAFS modeling using a two shell model containing Pt-**In** and Pt-**Pt** shells

N_{Pt-In} [-]	4.4 ± 0.7
N_{Pt-Pt} [-]	2.4 ± 0.8
R_{Pt-In} [Å]	2.69 ± 0.01
R_{Pt-Pt} [Å]	2.73 ± 0.01
σ^2_{Pt-In} [10^{-3} x Å²]	5.1 ± 1.7
σ^2_{Pt-Pt} [10^{-3} x Å²]	8.1 ± 1.1
ΔE_0 [eV]	-0.9 ± 1.1

Appendix A.2: PtO_2 EXAFS magnitude signal

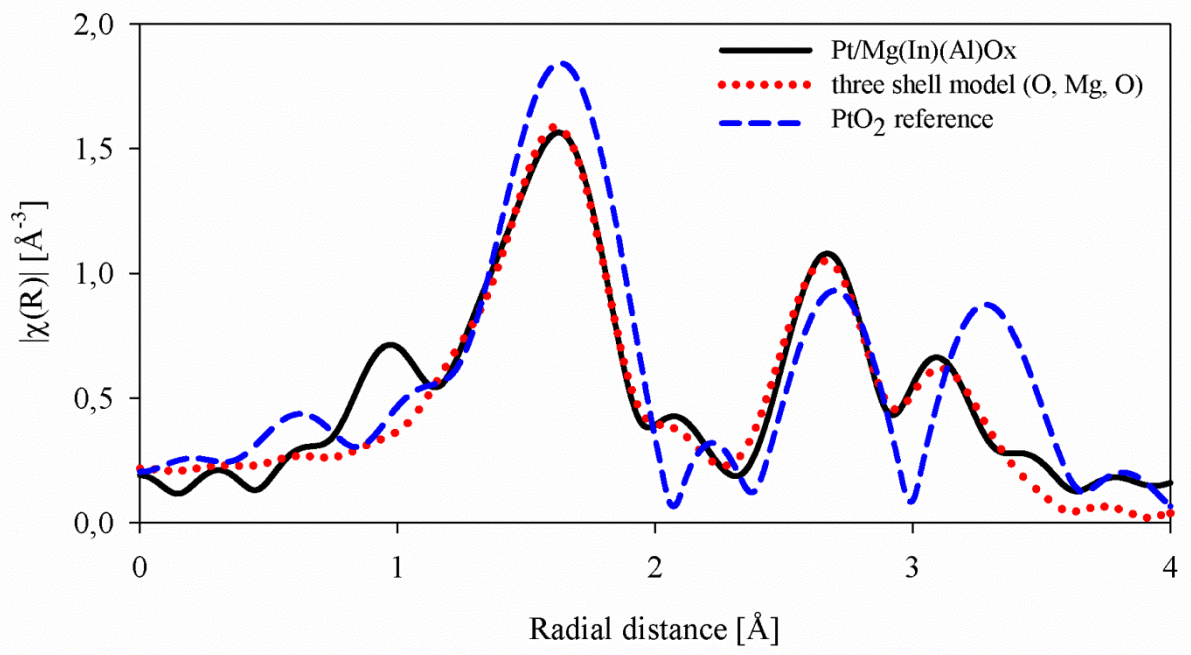

Figure A-3: experimental k²-weighted Fourier transformed EXAFS signal of $Pt(acac)_2/Mg(In)(Al)O_x$ calcined to 650 °C (full, black), fit of three shell model (dotted, red) containing Pt-**O**, Pt-O-**Mg** and Pt-O-Mg-**O** shells, PtO_2 reference signal (dashed, blue).

The k²-weighted Fourier transformed EXAFS signal of $Pt(acac)_2/Mg(In)(Al)O_x$ calcined to 650 °C and bulk PtO_2 reference show similar profiles. However, the PtO_2 structure is inadequate to model this experimental signal, in contrast to a three shell model containing a Pt-O, Pt-O-Mg and Pt-O-Mg-O shell. This three shell model is derived from wavelet transformed XAS analysis, which allows for the rapid determination of the location and the atomic type of the neighbors surrounding the X-ray absorber. Wavelet-based XAS analysis can therefore be a helpful tool for achieving more efficient structural identification.

Appendix A.3: Wavelet transformed XAS; the allocation of atomic elements

Determining the nature of the absorber's neighbors by wavelet transformed XAS requires knowledge on the k-space region where these neighbors generate EXAFS signal amplitude. This information is contained in the effective backscattering function of the involved atoms, representing the degree of photoelectron backscattering as a function of photoelectron wavenumber k.

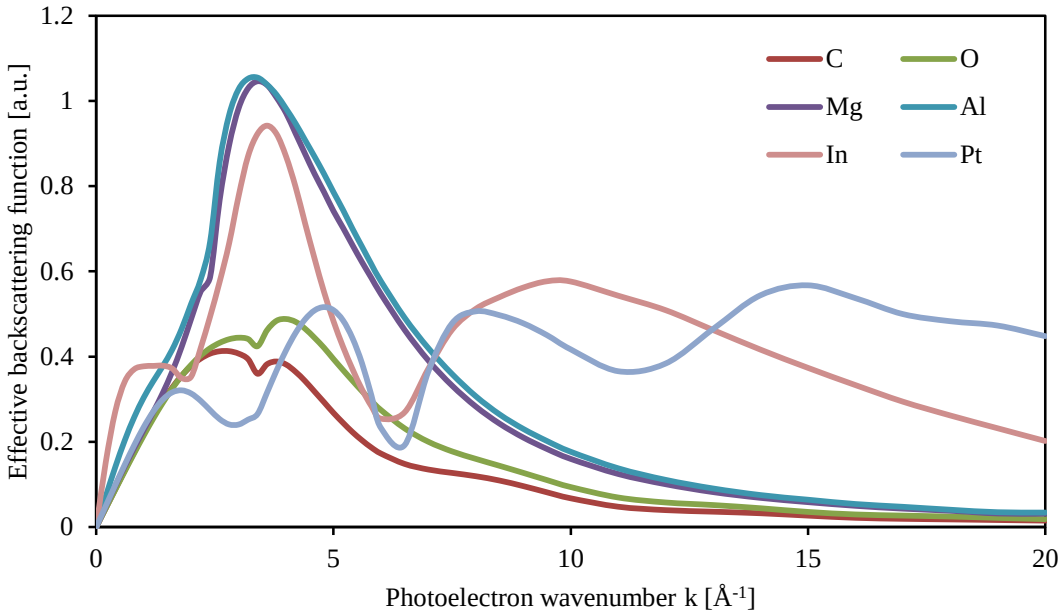

Figure A-4: effective backscattering functions of Pt-C, Pt-O, Pt-Mg, Pt-Al, Pt-In and Pt-Pt scattering paths as a function of the photoelectron wavenumber k.

Considerable changes in the k-space backscattering function are observed for atoms with significantly differing atomic mass. C, O, Mg and Al atoms surrounding Pt give rise to EXAFS signals in similar k-regions, having maxima around 4 – 5 $Å^{-1}$, as their atomic masses are similar. Indium creates a bimodal EXAFS contribution, with a maximum amplitude around 4 $Å^{-1}$ as well as a more subtle peak in the higher k-range (~ 9 $Å^{-1}$). As also observed from the Pt reference wavelet transformed XAS signal (Figure 3.3.c), Pt atoms surrounding Pt result in a single EXAFS peak between 8 and 10 $Å^{-1}$.

Appendix B

Appendix B.1: Cauchy order determination

An optimal balance between a reasonable k- and R-space resolution should be obtained in order to adequately pinpoint the k-region of backscattering for each specific R-space peak. The order of the Cauchy wavelet during wavelet transformation controls the resolution in both k- and R-space, respectively Δk and ΔR. The latter two quantities are constrained by the Heisenberg inequity $\Delta k.\Delta R \geq 1/4$[1] and are therefore inversely proportional. From Funke et al.[2], it is known that Δk behaves proportional to the Cauchy order. As a consequence, high (low) Cauchy order leads to a large (small) Δk and small (large) ΔR. Equivalently, a low (high) k-space resolution and high (low) R-space resolution is obtained when a high (low) Cauchy order is used.

In Figure A-5, a series of Cauchy wavelet transformed EXAFS contour plots are shown with different order, i.e. 800, 400, 200, 50, 20, 5. As expected, the plot with the highest Cauchy order yields a high R-space resolution. In the higher R-range, two separate peak maxima are detected at ~ 2.4 and 2.8 Å, as in the Fourier transformed R-space EXAFS signal (Figure 4.3.b). Despite the good R-space resolution, all peaks are broadly stretched over a wide k-range, lacking a proper k-space resolution. When the order is decreased to 400 and subsequently to 200, the R-space resolution decreases gradually leading to a single peak in the higher R-range around 2.4 Å. In addition, the k-space resolution improves, resulting in less asymmetric and more narrow peaks. Decreasing the Cauchy order to 50 further decreases the R-space resolution which causes the peak R ~ 1.5 Å and the peak at R ~ 2.4 Å to merge to one major peak. Finally, decreasing the resolution up to order 5 results in the loss of R-space resolution. All peaks evolve to a single surface with several vertically shaped foothills,

appearing at k-values corresponding to the peak maxima of the k-space EXAFS signal (not shown).

When the order of the Cauchy wavelet evolves towards a limit, i.e. one or infinity, the wavelet transformed EXAFS signal boils down to the respective k- or R-space signal. The information from the latter two signals is already available from the conventional EXAFS analysis. Therefore, simultaneous k- and R-space resolution is pursued, which is possible by selecting an intermediate value of 200 for the order of the Cauchy wavelet. For this value of the Cauchy order, two single peaks can still be resolved with a reasonable k- and R-space resolution.

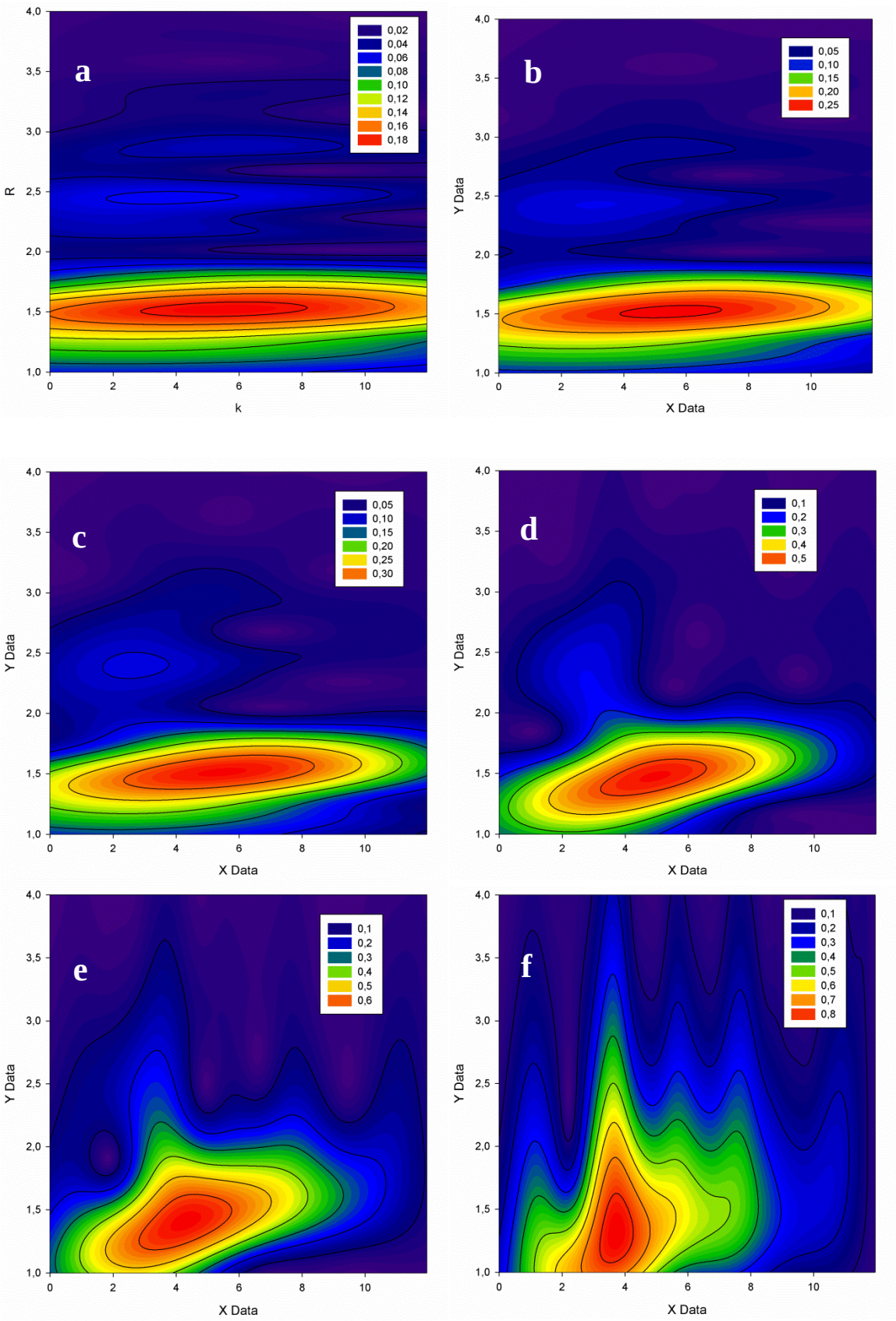

Figure A-5: WT different cauchy order (a) 800, (b) 400, (c) 200, (d) 50 (e) 20 (f) 5.

Appendix B.2: Influence of temperature on wavelet transformed XAS signal.

In Figure A-6.a-c, the k^2-weighted EXAFS signals of respectively single O, Ga and Pt around Pt are shown. The region of backscattering in k-space shifts to higher k-values as the atomic mass A increases (A_O = 16, A_{Ga} = 70, A_{Pt} = 195). This is also reflected in the wavelet transformed EXAFS contour plots (Figure A-6.d-f): the peak maximum gradually shifts to higher k-values for respectively O, Ga and Pt. Therefore, it is possible to discriminate between different atomic species if the atomic masses differ significantly. Heavier elements generally backscatter in a higher k-region compared to lighter elements.

The EXAFS signal in k-space contains information on the backscattering region of the atomic species, i.e. on their actual nature.[3] When only one backscattering atom is present around Pt, a simple analysis of the k-space EXAFS signal can reveal the nature of this atomic species. However, when multiple neighbors are present in the local environment of Pt, the k-space contributions are superimposed in k-space. Unraveling the k-space EXAFS signal with multiple backscatterers to elucidate which of the atomic species are present is challenging. Wavelet transformed XAS resolves this issue since it is capable of determining the k-region of backscattering for each R-space peak because of its simultaneous k- and R-space resolution.

It is widely established that a temperature increase leads to an increased (dynamic) Debye-Waller bond length disorder σ^2.[4] Since the EXAFS signal is proportional to $\exp(-2k^2\sigma^2)$, the temperature increase dampens the EXAFS oscillations, especially in the high k-range. The influence of an increasing temperature on the signals shown in Figure A-6.a-c is represented in Figure A-7.a-c for O, Ga and Pt respectively.

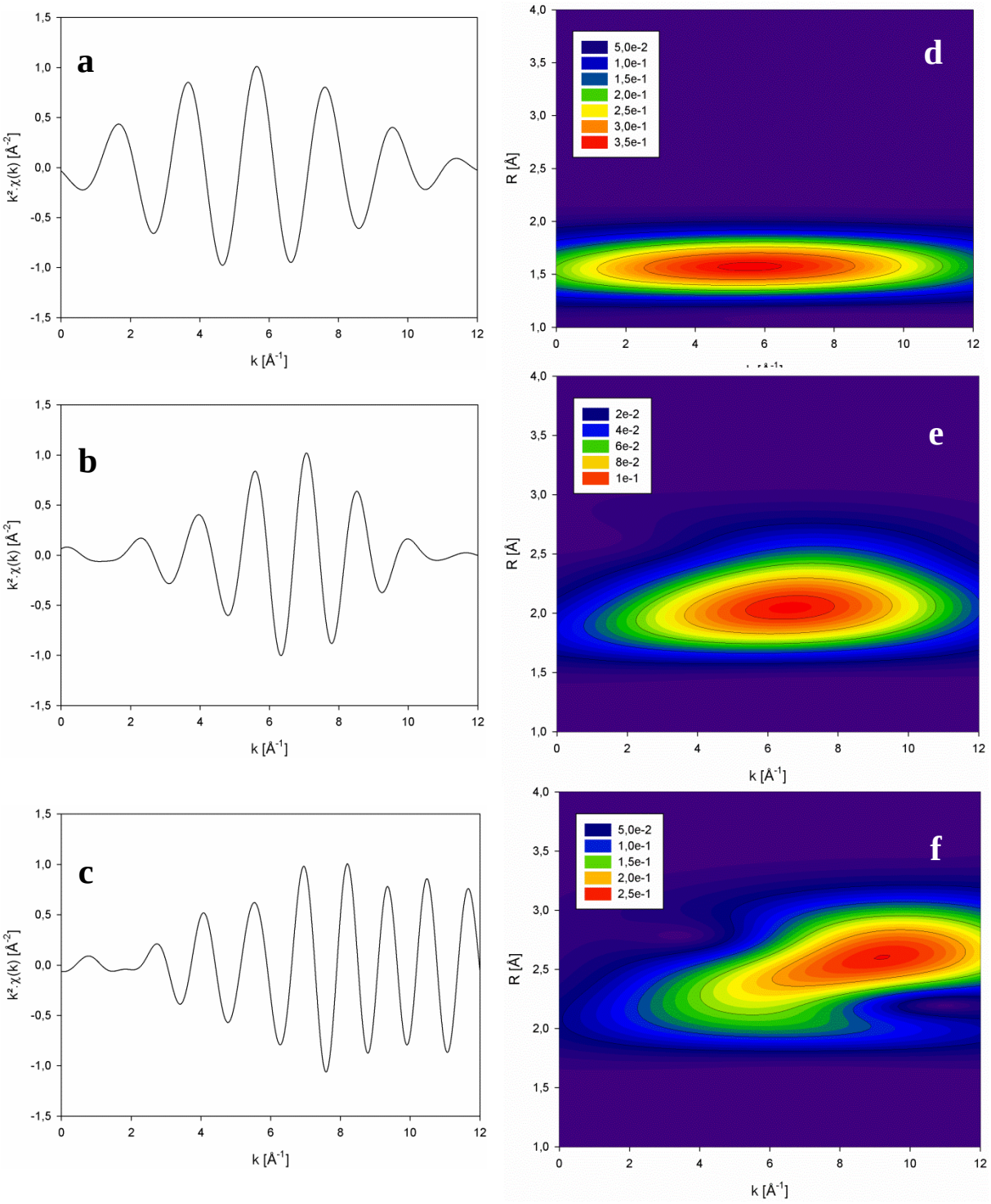

Figure A-6: k²-weighted EXAFS signals of (a) O, (b) Ga and (c) Pt; wavelet transformed EXAFS contour plots of (d) O, (e) Ga and (f) Pt, all with Cauchy order 200.

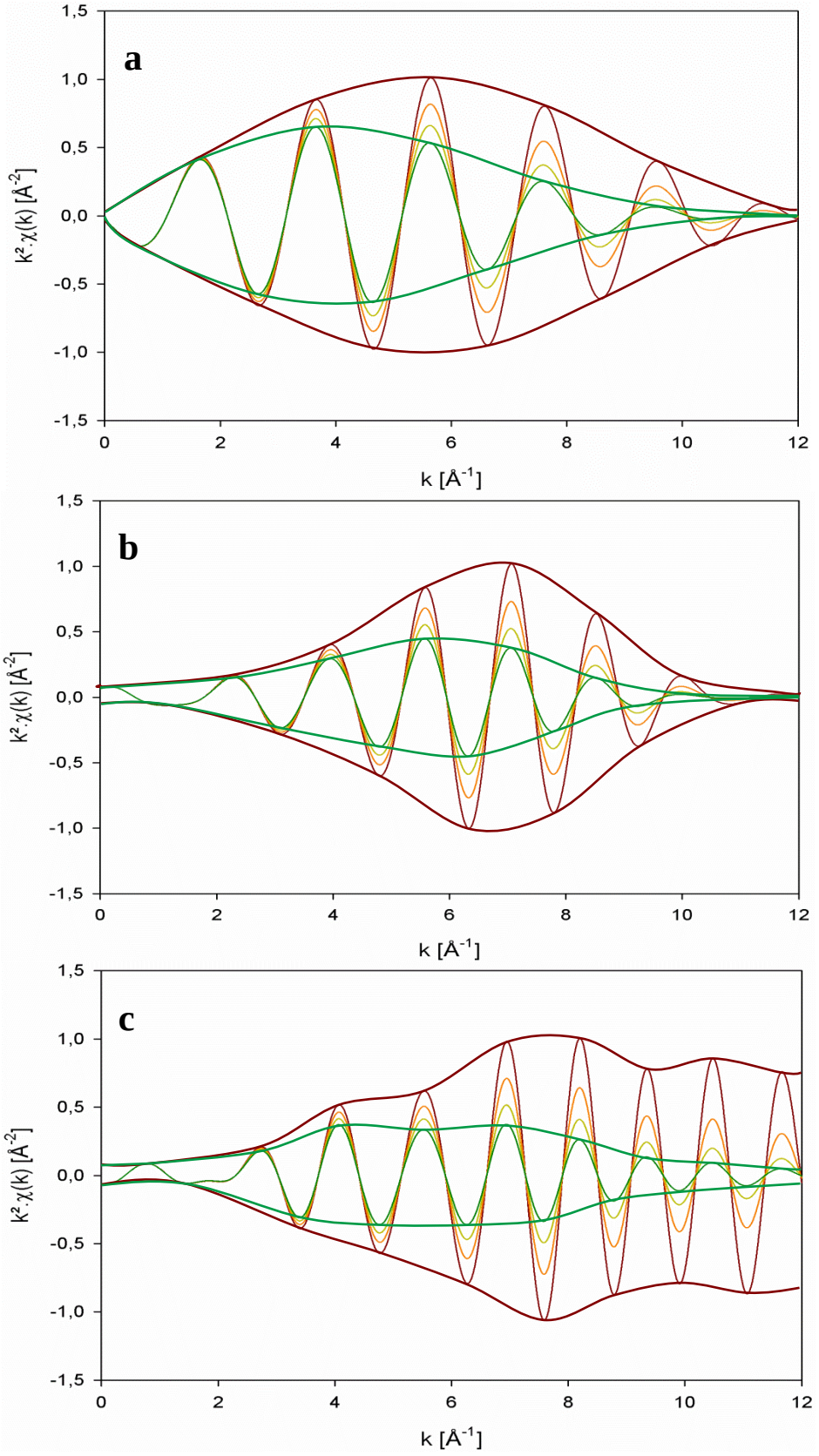

Figure A-7: k²-weighted EXAFS signals of (a) O, (b) Ga and (c) Pt with increasing temperatures (Debye-Waller factor): from red to green = from RT to ~1000°C.

The windowing functions surrounding the oscillatory EXAFS signals show changes upon temperature increase. At high temperatures, the higher k-range of the signal is damped, leading to a backscattering located in a lower k-region compared to the one at low temperatures. This induces a shift in the maximum of the windowing functions to lower k-values with temperature increase (Figure A-7.a-c). This shift will also affects the position of the peak maximum of the wavelet transformed EXAFS signal. The evolution of the wavelet transformed EXAFS signals with increasing temperature/disorder is shown for O and Pt respectively in Figure A-8.a-d and Figure A-9.a-d.

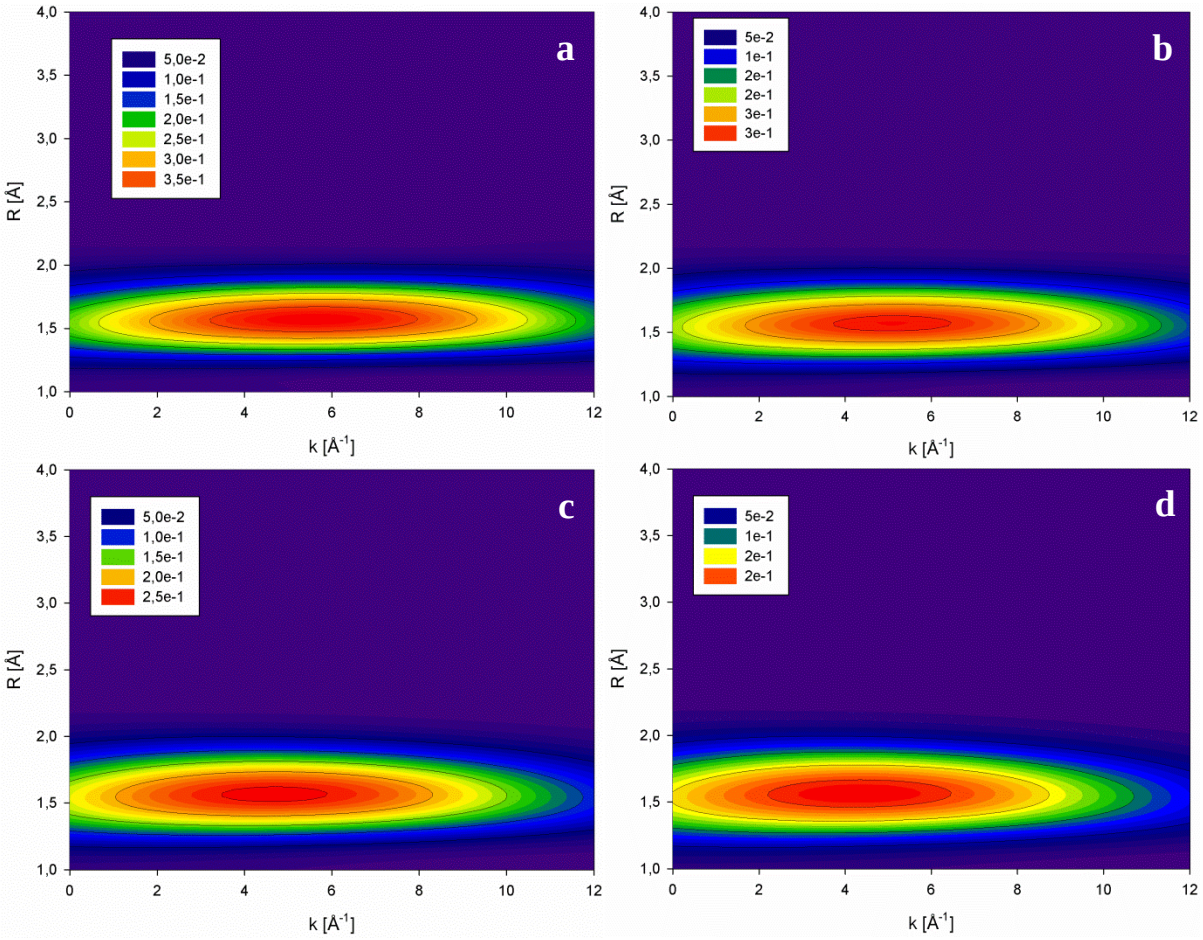

Figure A-8: wavelet transformed EXAFS signals of O with increasing temperature (disorder): (a) σ^2(RT), (b) σ^2(RT) + 0.0025 Å², (c) σ^2(RT) + 0.005 Å², (d) σ^2(RT) + 0.0075 Å².

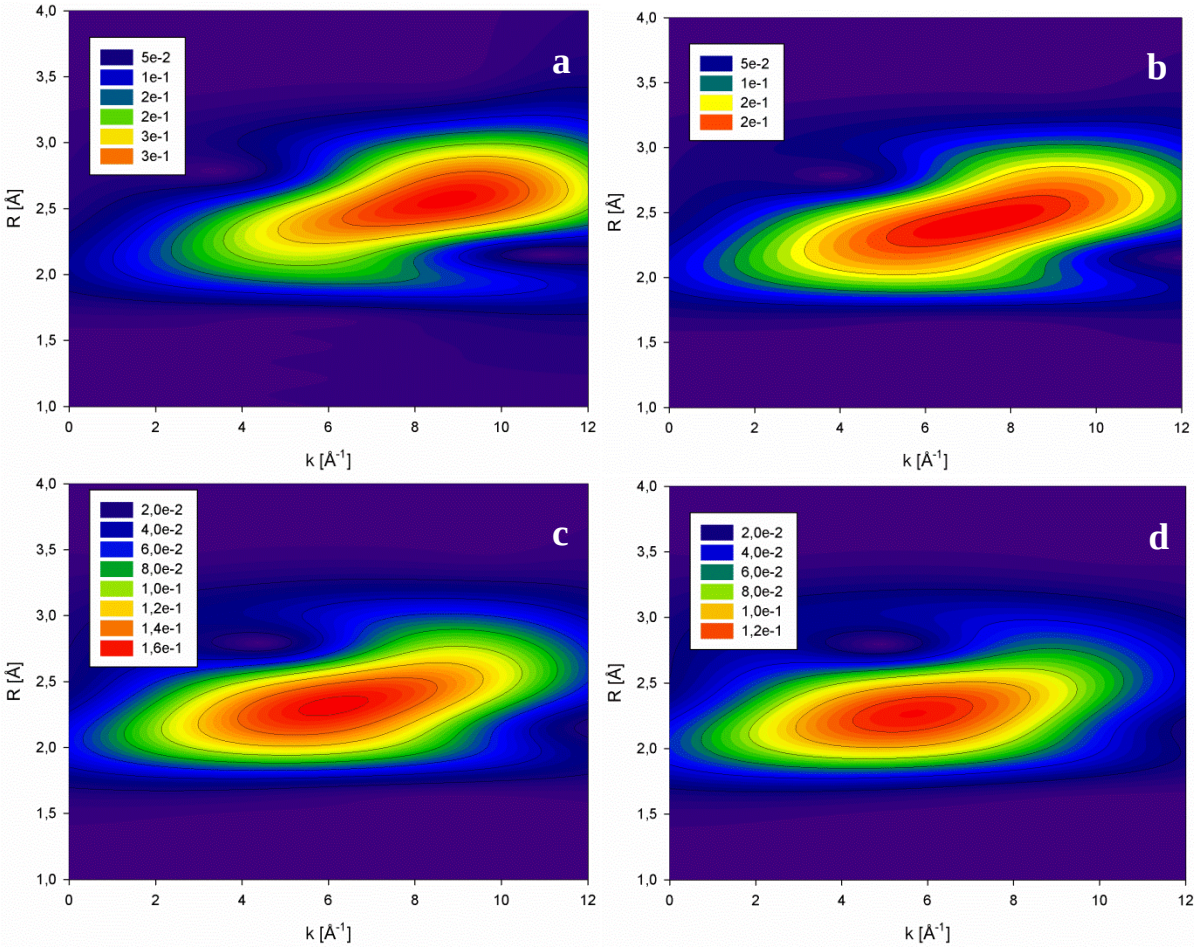

Figure A-9: wavelet transformed EXAFS signals of Pt with increasing temperature (disorder): (a) σ^2(RT), (b) σ^2(RT) + 0.0025 Å², (c) σ^2(RT) + 0.005 Å², (d) σ^2(RT) + 0.0075 Å².

As expected, the wavelet transformed peak maximum of the O peak shifts from k ~ 5.5 Å^{-1} towards ~ 4.5 Å^{-1} with increasing temperature/disorder ($\Delta\sigma^2$ = 0.0075 Å², Figure A-8.a-d). For the same temperature/disorder increase as for O, i.e. $\Delta\sigma^2$ = 0.0075 Å², a Pt peak shift occurs from k ~ 9 Å^{-1} to ~ 6 Å^{-1} (Figure A-9.a-d). Therefore, the discrepancy between the peak maxima of Pt and O, i.e. $\Delta max_{Pt\text{-}O} = max_{Pt} - max_{O}$, decreases from ~ 3.5 Å^{-1} to ~ 1.5 Å^{-1} with increasing temperature/disorder ($\Delta\sigma^2$ = 0.0075 Å²).

This behavior clarifies the difference between Figure 4.6.d (450 °C) and Figure 4.7.c (room temperature). Both these contour plots of the wavelet transformed EXAFS signal correspond to the same pre-catalyst state, i.e. 450°C H_2/He reduced Pt/Mg(Ga)(Al)O_x. However, the temperature difference of 425°C introduces different degrees of disorder,

leading to a decreased $\Delta max_{Pt\text{-}O}$ upon temperature increase. The O and Pt peaks in Figure 4.7.c are therefore more separated compared to Figure 4.6.c.

Superposition of the wavelet transformed EXAFS signals of the single O and Pt shells at the highest temperature/disorder displayed in Figure A-8.d and A-9.d, largely corresponds to the wavelet transformed EXAFS signal of the pre-catalyst in Figure 4.6.d. This shows that, indeed, both O and Pt atoms are present around the central Pt absorber during reduction up to 450°C. In addition, after 650°C calcination and cool down to 250°C, the Pt and O peak positions in Figure 4.5.c are somewhat shifted to higher k-values compared to the peak positions in Figure 4.6.d because of the temperature differences (250°C instead of 450°C). The observed peak shifts in Figure 4.5.c (250°C, O_2) and Figure 4.6.d (450°C, H_2) are therefore induced by the temperature increase, leading to an increased disorder.

Appendix B.3: Support characterization by XRD

In Figure A-10, the X-ray diffraction (XRD) patterns for five different samples are shown: (a) HT, (b) HT-Ga, (c) Mg(Al)O_x, (d) Mg(Ga)(Al)O_x and the (e) 650°C calcined 'as prepared material' (Pt/Mg(Ga)(Al)O_x). The XRD pattern of the HT sample is typical of a hydrotalcite. The (00*l*) diffractions in this pattern reflect the interlayer spacing, broad and asymmetric non-basal reflections and a typical intralayer doublet.[5] Addition of Ga to this uncalcined hydrotalcite material, yielding the HT-Ga sample, results in the same pattern with some subtle shifts in peak position and intensity (Figure A-10.b). Therefore, the introduction of Ga into the hydrotalcite framework preserves the lamellar structure of the original hydrotalcite.

Table A-4 displays crystallographic parameters determined from the XRD pattern for several samples, more specifically the unit cell parameters and particle sizes. The interlayer spacing c_{HT} follows from the (003) basal plane diffraction as $c_{HT} = 3\ d_{003,HT}$, assuming a hexagonal 3R stacking of the layers.[6] Based on a brucite-like layer thickness of 0.48 nm[7], the interlayer distance h_{HT} can be calculated as $d_{003,HT} - 0.48$ nm. Finally, the (110) diffraction gives the cell parameter $a_{HT} = 2\ d_{110,HT}$, which equals to the average metal-metal distance within the brucite-like layer.

The introduction of Ga into the hydrotalcite framework leads to a reduced interlayer spacing and distance, c_{HT} and h_{HT}, but does not affect the metal-metal distance a_{HT}. The crystallinity of the HT-Ga sample is higher than the one for HT, as evidenced from the more intense and sharp diffractions, leading to a larger crystallite size for the HT-Ga sample.

After calcination of the HT and HT-Ga samples up to 650°C, both mixed oxide Mg-Al-O and Mg-Ga-Al-O support types are obtained showing new strong lines around 44° and 62° (Figure A-10.c and Figure A-10.d for Mg(Al)O_x and Mg(Ga)(Al)O_x samples). These lines are typical of the collapsed hydrotalcite structure, where a mixed oxide Mg(-Ga)-Al-O is formed showing MgO as the only XRD phase.[6] The lattice parameter derived by averaging both (200) and (220) diffractions yields 0.4149 nm and 0.4176 nm for Mg(Al)O_x and

$Mg(Ga)(Al)O_x$ samples respectively, i.e. slightly lower than the bulk value for MgO (periclase): 0.4211 nm. This is due to the incorporation of Al^{3+} and/or Ga^{3+} into the MgO lattice, which have a smaller ionic radius than Mg^{2+}, resulting in lattice contraction.[6] Hence, the Mg(-Ga)-Al-O mixed oxide phases can be written as $Mg(Al)O_x$ or $Mg(Al)(Ga)O_x$. In addition to the mixed oxide, weak hydrotalcite diffractions persist. This indicates that either the layered structure of hydrotalcite is not entirely destroyed or it is reconstructed to some extent after the calcination from contact with CO_2 from air. The latter reconversion is known as 'memory effect'.[8, 9] As the applied calcination temperature lies well below 1000°C, no $MgAl_2O_4$ spinel diffractions are found.[9, 10] The particle size for $Mg(Al)O_x$ has considerably changed due to the combined effect of layer collapse and sintering. The Ga insertion decreases the particle size along the [001] direction after calcination. Both samples $Mg(Al)O_x$ and $Mg(Al)(Ga)O_x$ contain mixed oxide particles of a size similar to those of hydrotalcite.

The last sample that is characterized by XRD is a $Mg(Al)(Ga)O_x$ support upon which $Pt(acac)_2$ precursor is impregnated and subsequently calcined at 650°C in air to form Pt nanoparticles ($Pt/Mg(Ga)(Al)O_x$, Figure A-10.e). From comparison between patterns d and e in Figure A-10, the structure of the support remains the same, i.e. weak hydrotalcite and mainly mixed oxide $Mg(Al)(Ga)O_x$, with similar particle size. The Pt particles give rise to faint diffractions around 39.7° (111) and 46.2° (200) in Figure A-10.e. The intensity is however too low to accurately determine the particle size. XRD is therefore not suitable to follow the transformations occurring in the Pt phase during the catalyst formation process. However, XAS can provide results in this prospect (see Section 4.2.).

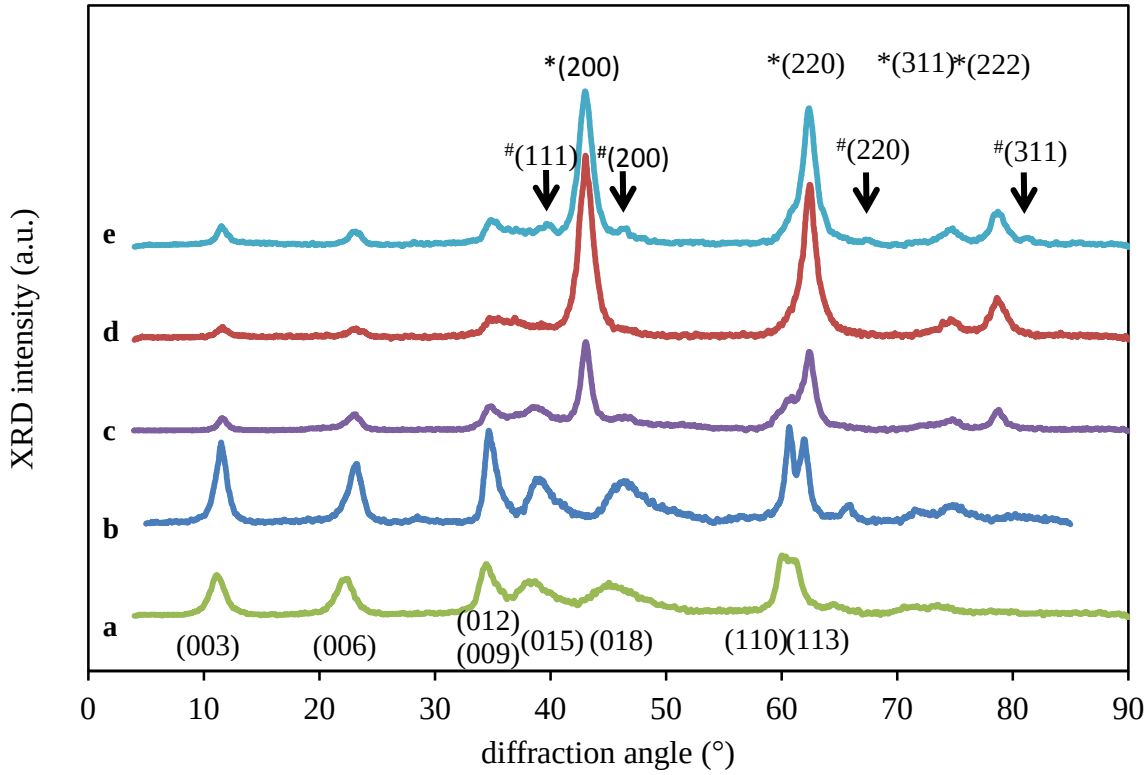

Figure A-10: XRD patterns for materials in different stages of preparation; **a**: HT, **b**: HT-Ga, **c**: $Mg(Al)O_x$, **d**: $Mg(Ga)(Al)O_x$, **e**: $Pt/Mg(Ga)(Al)O_x$ (*: MgO diffractions, #: Pt diffractions).

Table A-4: lattice parameters and crystallite sizes obtained from XRD for the hydrotalcite support in subsequent stages of preparation and for calcined Pt/Mg(Ga)(Al)O_x.

	$d_{003,HT}$ [nm]	$d_{110,HT}$ [nm]	c_{HT} [nm]	h_{HT} [nm]	a_{HT} [nm]	a_{MgO} [nm]	Crystallite size		
							MgO [nm]	HT-d_{003} [nm]	HT-d_{110} [nm]
HT	0.7906	0.1539	2.3718	0.3106	0.3079	-	-	5.50	9.34
HT-Ga	0.7689	0.1525	2.3066	0.2889	0.3050	-	-	9.94	12.73
Mg(Al)O_x	0.7561	0.1521	2.2683	0.2761	0.3041	0.4149	9.55	9.07	4.52
Mg(Ga)(Al)O_x	0.7605	0.1474	2.2816	0.2805	0.2949	0.4176	4.36	6.71	-
Calcined Pt/Mg(Ga)(Al)O_x	0.7621	0.1488	2.2862	0.2821	0.2975	0.4200	6.56	7.60	-

Appendix B: References

(1) Funke, H.; Chukalina, M.; Scheinost, A. C. *J. Synchr. Rad.* **2007**, *14*, 426.

(2) Funke, H.; Scheinost, A. C.; Chukalina, M. *Phys. Rev. B* **2005**, *71*, 9.

(3) Antoniak, C. *Beilstein J. Nanotechnol.* **2011**, *2*, 237.

(4) Frenkel, A. I.; Hills, C. W.; Nuzzo, R. G. *J. Phys. Chem. B* **2001**, *105*, 12689.

(5) Bellotto, M.; Rebours, B.; Clause, O.; Lynch, J.; Bazin, D.; Elkaim, E. *J. Phys. Chem.* **1996**, *100*, 8527.

(6) Valente, J. S.; Rodriguez-Gattorno, G.; Valle-Orta, M.; Torres-Garcia, E. *Mater. Chem. Phys.* **2012**, *133*, 621.

(7) Cavani, F.; Trifiro, F.; Vaccari, A., *Catal. Today* **1991,** *11*, 173.

(8) Virnovskaia, A.; Jorgensen, S.; Hafizovic, J.; Prytz, O.; Kleimenov, E.; Havecker, M.; Bluhm, H.; Knop-Gericke, A.; Schlogl, R.; Olsbye, U. *Surf. Sci.* **2007**, *601*, 30.

(9) Rives, V. *Mater. Chem. Phys.* **2002**, *75*, 19.

(10) Rocha, J.; del Arco, M.; Rives, V.; Ulibarri, M. A. *J. Mater. Chem.* **1999**, *9*, 2499.

Appendix C

Appendix C.1: Temporal Analysis of Products (TAP) experiments

Experimental details

Table A-5: Experimental details

Material	**Zone 1 (SiO_2), mm**	**Zone 2 (sample), mm**	**Zone 3 (SiO_2), mm**	**ε^***	**Sample mass, mg**	**T °C**	**$^{**}D_{ref} \cdot 10^2$ m^2/s**	**$^{**}N_p \cdot 10^8$ mol/pulse**
SiO_2	57.5	-	-	0.5	-	650	1.20	4.35
$Mg(Al)O_x$	32.9	1.5	23.1	0.5	8.8	650	1.32	4.32
$Mg(Al,Ga)O_x$	33	1.1	23.5	0.5	7.1	650	1.30	5.67
$5\%Pt/Mg(Al)O_x$	33.5	1.0	23.0	0.5	8.6	650	1.31	5.59

[*] characteristic value for 250<d<500 μm particles
[**] estimated by regression from He response

Data analysis

To calibrate the sensitivities of the QMS towards He and H_2, a series of 1000 H_2/He (1:1) pulses was injected into the microreactor packed with SiO_2 from a fixed (V_f = 6.8 ml) feed volume which was kept at 75°C. The pressure drop in the feed volume was measured as 11.7 kPa. The sensitivities of He and H_2 were calculated based on the recorded responses as $5.8 \cdot 10^6$ and $14.0 \cdot 10^6$ V/mol, respectively. The following formula based on the ideal gas law was used:

$$c_f^i = \frac{m_0^i \cdot 1000 \cdot R \cdot T}{\Delta P \cdot 0.5 \cdot V_f}$$

where R = 8.314, J/mol/k is the universal gas constant.

To quantify the transport of gases through the microreactor packing, the reference effective diffusion coefficient was estimated for each experiment from the He response using a standard 1D Knudsen model (see ref. 51 in Chapter 5). The reference effective diffusion coefficient is defined as diffusion coefficient of a reference gas, in this case He, measured at room temperature (298.15 K). The diffusion coefficient at any temperature (T) and for any gas with molecular mass (M) can then be calculated using this reference according to

$$D_i(T) = D_{ref}(T_{ref}) \sqrt{\frac{T}{T_{ref}}} \sqrt{\frac{M_{ref}}{M_i}}$$

Simultaneously, the total pulse intensity was also estimated from the He response using the He QMS sensitivity. Estimated reference diffusion coefficients and pulse intensities are listed for all samples in Table A-5. To illustrate the quality of the fit, Figure A-11.a depicts experimental and fitted He responses over the 5%Pt/Mg(Al)O_x sample. The obtained estimates were used to scale the exit-flow rate curves presented in Figure 5.3.a. Furthermore, they were used to simulate how the H_2 response would look like in the absence of chemical reactions (diffusion-only). Figure A-11.b depicts simulated diffusion-only and experimental responses for He and H_2 pulsed over the 5% Pt/Mg(Al)O_x sample.

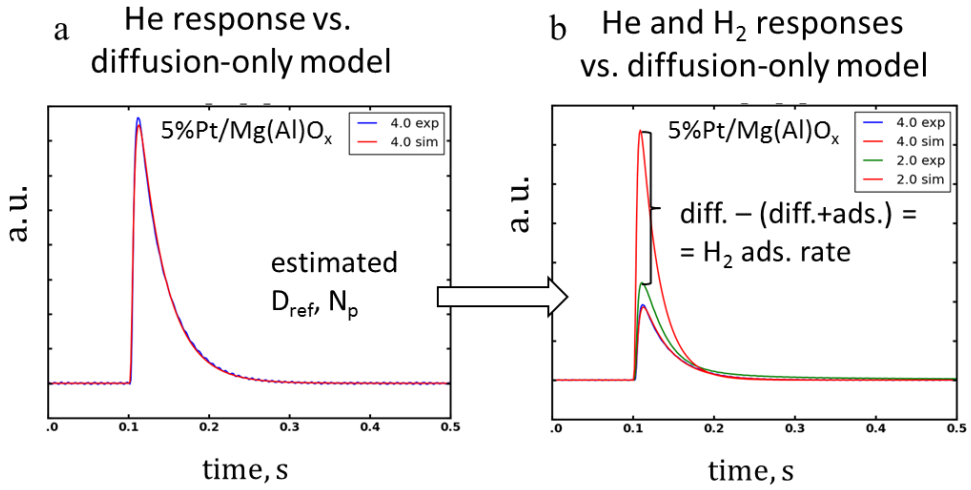

Figure A-11: (a) Regression of the experimental He response; (b) simulation of the diffusion-only H_2 response based on the estimated diffusion coefficient of He.

From the difference between the simulated diffusion-only and the actual experimental (diffusion + reaction) response of H_2, the rate of H_2 consumption by the sample can be reconstructed with no additional kinetic assumptions using the Y-Procedure (see ref. 52 in Chapter 5). The reconstructed adsorption rates for all investigated samples are plotted in Figure A-12. The rate peaks very early during the pulse, when adsorption dominates desorption. Then, the rate decreases and becomes negative, when desorption begins to dominate. In the tail of the curve, the rate very slowly approaches zero from below as a result of slow desorption. These rates were subsequently integrated in time and normalized by the catalyst mass and the BET surface area to yield the surface coverage presented in Figure 5.3.b:

$$\theta_H(t) = \int_0^t \frac{2R_{H_2}(t')}{W_{cat} \cdot BET} dt'$$

It should be noted that the 0.1 s lag before the pulse, which is clearly visible in Figure A-11, was cut out in Figure A-12 for proper time integration of the rates.

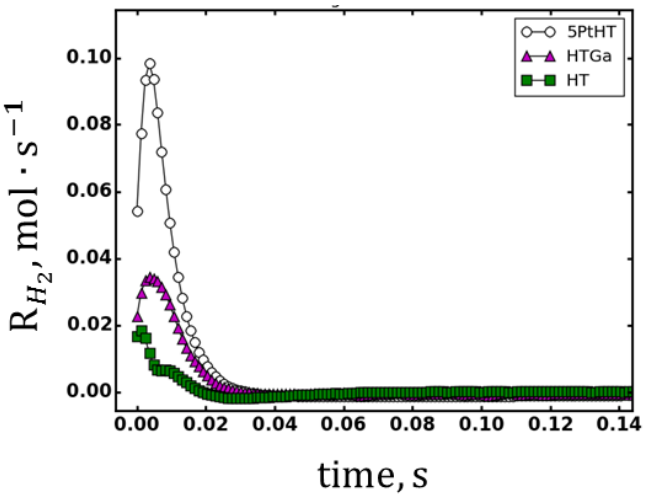

Figure A-12: Adsorption rates of H_2 over different materials reconstructed via the Y-Procedure from the difference between experimental and diffusion-only H_2 response.

Appendix C.2: XANES during H_2 TPR to 750 °C on a physical mixture of Pt/Mg(Al)O_x and Mg(Ga)(Al)O_x.

The XANES profiles depicted in Figure A-13 are recorded during H_2/He TPR treatment from 650 °C to 750 °C on a physical mixture of Pt/Mg(Al)O_x and Mg(Ga)(Al)O_x. Below 650 °C, no Pt-Ga alloying is observed (Figure 5.1.e) due to the limited mobility of partially reduced Ga species on Mg(Ga)(Al)O_x. However, thermal activation from 650 °C to 750 °C in H_2/He environment results in a significant Pt L_{III} XANES edge shift and white line decrease, characteristic for Pt-Ga alloying. This strongly suggests that partially reduced Ga species gain mobility upon temperature increase and migrate to Pt to form Pt-Ga nano-alloys.

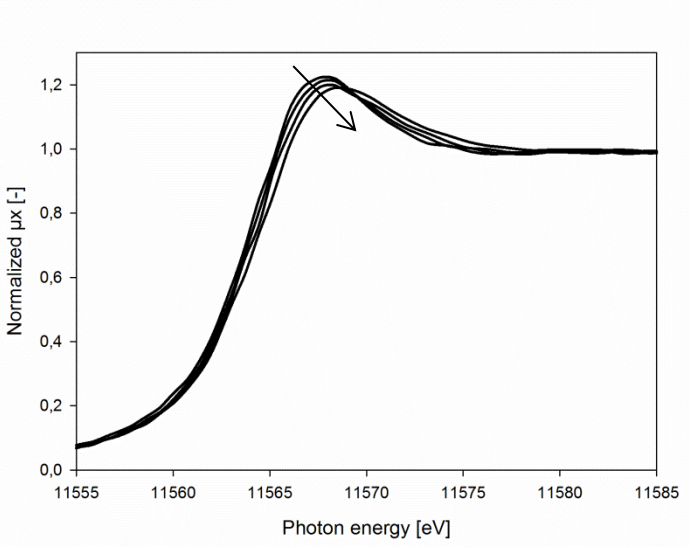

Figure A-13: Pt L_{III} edge XANES spectra recorded during H_2/He TPR from 650 °C to 750 °C of a physical mixture of Pt/Mg(Al)O_x + Mg(Ga)(Al)O_x.

Appendix D

Appendix D.1: Performance of Pt/Mg(Pt)(Al)O_x monometallic and Pt-Ga/Mg(Ga)(Al)O_x bimetallic catalysts

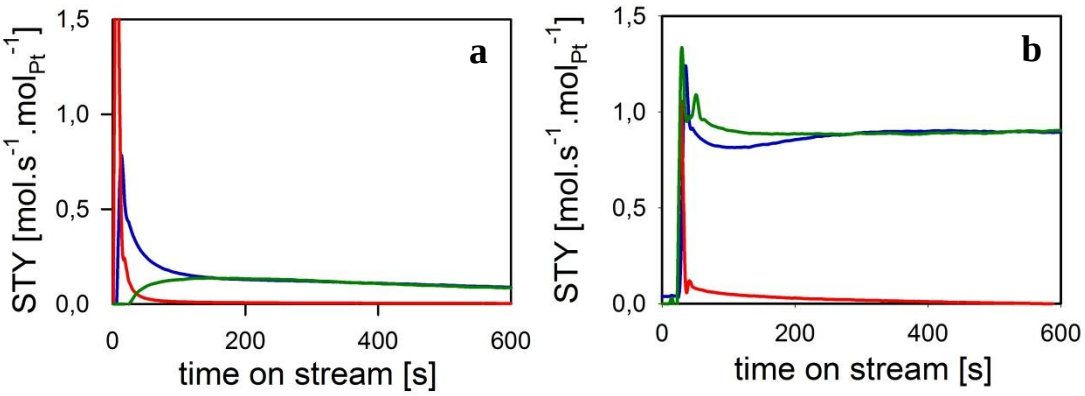

Figure A-14: Catalytic propane dehydrogenation at 600 °C ($W_{cat}/F_{propane,0}$ = 4 kg_{cat}·s·mol^{-1} and $P_{propane,0}$ = 5 kPa at a total pressure of 101.3 kPa): site-time yield (STY) vs. time on stream: (a) one-pot synthesized Pt/Mg(Pt)(Al)O_x and (b) one-pot synthesized Pt-Ga/Mg(Pt)(Ga)(Al)O_x (red = CH_4, blue = H_2, green = C_3H_6).

Appendix E

Appendix E.1: Estimated parameters resulting from EXAFS modeling

Table A-6: structural parameters obtained by EXAFS modeling of the 'In-poor bilayer' sample which is reduced to 820 °C, by using a two shell model containing Pt-In and Pt-Pt shells (R-factor = 0.032). Fit is displayed in Figure 8.2.b and Figure 8.2.c.

N_{Pt-In}	[-]	4.2 ± 2.4
N_{Pt-Pt}	[-]	6.2 ± 3.2
R_{Pt-In}	[Å]	2.81 ± 0.04
R_{Pt-Pt}	[Å]	2.82 ± 0.04
$\sigma^2_{Pt-In/Pt}$	[10^{-3} x Å²]	6.2 ± 5.2
ΔE_0	[eV]	5.1 ± 3.8

Table A-7: structural parameters obtained by EXAFS modeling of the 'In-rich bilayer' sample which is reduced to 670 °C, by using a two shell model containing Pt-In and Pt-Pt shells (R-factor = 0.015). Fit is displayed in Figure 8.2.c.

N_{Pt-In}	[-]	4.3 ± 0.5
N_{Pt-Pt}	[-]	3.8 ± 0.7
R_{Pt-In}	[Å]	2.73 ± 0.01
R_{Pt-Pt}	[Å]	2.84 ± 0.01
$\sigma^2_{Pt-In/Pt}$	[10^{-3} x Å²]	6.8 ± 0.9
ΔE_0	[eV]	0.9 ± 0.9

It should be noted that the binary correlation coefficients between the coordination numbers and the Debye-waller factor for the fit of the In-poor sample are relatively high (maximum of 0.93 for N_{Pt-In} - $\sigma^2_{Pt-In/Pt}$ pair) relative to the ones for the In-rich sample (maximum of 0.73 for N_{Pt-In} - $\sigma^2_{Pt-In/Pt}$ pair). The estimated parameters for the In-rich bilayer are therefore more reliable than for the In-poor bilayer, which is clearly observed in the error bars of the estimates.

Glossary

Active sites

Functional groups at the surface of a solid, where catalytic reaction takes place, responsible for catalytic activity.

Adsorption

Adhesion of atoms, ions or molecules from a gas, liquid, or dissolved solid to a surface.

Atomic layer deposition (ALD)

A thin film deposition technique which uses sequential self-saturating reactions between gaseous precursor molecules and a solid surface to grow thin films in a layer-by-layer fashion. The self-saturating nature of the reactions allows to deposit material with an atomic layer precision in a conformal way.

Catalysis

Process of changing the rate of a chemical reaction due to the participation of a substance called catalyst.

Catalyst

A substance, usually used in small amounts relative to the reactants, that modifies the reaction path and increases the rate of a reaction without being consumed in the process.

Catalyst oxidation

The act of taking up oxygen from the gas phase by a catalyst resulting in an increase in oxidation state of the metals constituting the catalyst.

Catalyst reduction

The act of losing oxygen from a catalyst resulting in a decrease in oxidation state of the metal constituting the catalyst.

Dehydrogenation

The endothermic reaction which involves the removal of hydrogen from a molecule.

Dispersion

The fraction of atoms exposed on the surface of a catalyst.

Extended X-ray absorption fine structure (EXAFS)

The oscillatory features in the XAS signal above the edge position which contain detailed structural information on the local environment around the X-ray absorber. Fourier transformation of the EXAFS signal results in a radial structure function which can be correlated to the radial distribution function around the X-ray absorbing element.

Heterogeneous catalysis

Catalysis where the phase of the catalyst differs from that of the reactant.

Intercalation

The reversible inclusion or insertion of molecules or ions into compounds with layered structures.

Intermetallic compound

Solid-state phase involving different metals which are ordered into different sites in the structure, with distinct local environments and often a well-defined, fixed stoichiometry.

Layered double hydroxide (LDH)

Material consisting of cationic 2D $[M_{1-a}^{2+}M_a^{3+}(OH)_2]^{a+}$ layers, containing octahedrally OH-coordinated di- and trivalent metal cations. By electrostatic interaction with charge-compensating anions A and water, these 2D layers self-assemble into a stacked configuration of alternating cationic layers and anionic interlayer galleries, yielding $[M_{1-a}^{2+}M_a^{3+}(OH)_2]^{a+}[A^{n-}]_{a/n}^{a-}.mH_2O$.

Metal alloy

A material composed of two or more metals. An alloy can be a solid solution of the elements in a single phase, a mixture of metallic phases composed of two or more solutions, or an intermetallic compound with no distinct boundary between the phases.

Mixed metal oxide (MMO)

An oxide which contains cations of more than one chemical element. It can be considered as the oxide analog of a metal solid solution.

Nanoparticle sintering

Temperature-induced average size increase of nanoparticles without melting it to its liquefaction point, resulting in loss of active surface area.

One-pot synthesis

Material synthesis route in which the reactants are subjected to a set of successive chemical reactions within one reactor.

Solid solution

A solid-state solution of one or more solutes in a solvent. Such mixture is considered a solution rather than a compound as the crystal structure of the solvent remains unchanged by addition of the solutes, and the mixture remains in a single homogeneous phase.

Spill over

The transport of a species, adsorbed or formed on a surface, to another surface, which does not adsorb or form this species under the same conditions.

Temporal analysis of products (TAP)

A transient kinetic experiment performed on a continuously evacuated microreactor loaded with a fixed catalyst bed, in which the response to a pulse of reactants is recorded.

Transmission electron microscopy (TEM)

A technique in which a beam of electrons is transmitted through an ultra-thin specimen, interacting with the specimen as it passes through. An image is formed from the interaction of matter with the electrons transmitted through the specimen.

Wavelet transformed (WT) XAS

Transformation of the XAS signal above the edge position by using of a finite wave packet. The resulting wavelet transformed XAS signal allows for the simultaneous elemental discrimination and spatial localization of the X-ray absorber's neighbors.

X-ray absorption near edge structure (XANES)

The fine structural features contained within the XAS signal around the rising edge position which contain information on the geometry and average oxidation state of the X-ray absorber.

X-ray absorption spectroscopy (XAS)

Excitation of a core-electron to an electron state above Fermi level, resulting from the absorption of X-rays with variable energy. The energy dependence of the X-ray absorption coefficient yields electronic information on the X-ray absorbing element, as well as structural information on its local environment.

X-ray diffraction (XRD)

An analytical technique primarily based on elastic X-ray scattering used for phase identification of a crystalline material which can provide information on unit cell dimensions.

List of publications

1. J. Dendooven, R.K. Ramachandran, K. Devloo-Casier, G. Rampelberg, M. Filez, H. Poelman, G.B. Marin, E. Fonda, C. Detavernier, Low temperature atomic layer deposition of platinum using (methylcyclopentadienyl)-trimethylplatinum and ozone. *J. Phys. Chem. C* **2013**, *117*, 20557.

2. V. Galvita, M. Filez, H. Poelman, V. Bliznuk, G.B. Marin, The role of different types of CuO in CuO-CeO_2/Al_2O_3 for total oxidation. *Catal. Lett.* **2014**, *144*, 32.

3. M. Filez, H. Poelman, R.K. Ramachandran, J. Dendooven, K. Devloo-Casier, E. Fonda, C. Detavernier, G.B. Marin, *In situ* XAS and XRF study of nanoparticle nucleation during O_3-based Pt deposition. *Catal. Today* **2014**, *229*, 2. (Chapter 7)

4. M. Filez, E.A. Redekop, H. Poelman, V.V. Galvita, R.K. Ramachandran, J. Dendooven, C. Detavernier, G.B. Marin, Unraveling the formation of Pt-Ga alloyed nanoparticles on calcined Ga-modified hydrotalcites by *in situ* XAS. *Chem. Mater.* **2014**, *26*, 5936. (Chapter 4)

5. M. Filez, E.A. Redekop, H. Poelman, V.V. Galvita, G.B. Marin, Advanced elemental characterization during Pt-In catalyst formation by wavelet transformed X-ray absorption spectroscopy. *Anal. Chem.* **2015**, *87*, 3520. (Chapter 3)

6. M. Filez, E.A. Redekop, V.V. Galvita, H. Poelman, M. Meledina, S. Turner, G. Van Tendeloo, A.T. Bell, G.B. Marin, The role of hydrogen during Pt-Ga nanocatalysts formation. (submitted, Chapter 5)

7. M. Filez, E.A. Redekop, H. Poelman, V.V. Galvita, M. Meledina, S. Turner, G. Van Tendeloo, C. Detavernier, G.B. Marin, One-pot synthesis of Pt-based mono- and multimetallic catalysts derived from layered double hydroxides. (submitted, Chapter 6)